A PROPOSED DAMAGE MODEL FOR R/C BRIDGE ELEMENTS UNDER CYCLIC LOADING

by

RIYADH A. HINDI

B.Sc. (Civil), University of Baghdad, 1988

M.Sc. (Structures), Saddam University for Engineering and Science, 1992

A THESIS SUBMITTED IN PARTIAL FULFILMENT OF

THE REQUIREMENTS FOR THE DEGREE OF

DOCTOR OF PHILOSOPHY

in

THE FACULTY OF GRADUATE STUDIES

Department of Civil Engineering

We accept this thesis as conforming

to the required standard

THE UNIVERSITY OF BRITISH COLUMBIA

AUGUST 2001

In presenting this thesis in partial fulfilment of the requirements for an advanced degree at the University of British Columbia, I agree that the Library shall make it freely available for reference and study. I further agree that permission for extensive copying of this thesis for scholarly purposes may be granted by the head of my department or by his or her representatives. It is understood that copying or publication of this thesis for financial gain shall not be allowed without my written permission.

Department of Civil Engineering

The University of British Columbia
Vancouver, Canada

Date Aug. 31, 01

DE-6 (2/88)

ABSTRACT

Analytical damage models provide a way to have an index to create a single measure that fairly represents the damage sustained under seismic loading in reinforced concrete structures. Damage indices are important tools to quantify the consequences of a structural decision.

A damage model is proposed for reinforced concrete elements. The model yields a damage index at a point in the time history for the load on the element, based on the predicted monotonic response from the point in time to failure. The model takes into account the parameters that describe the hysteretic behavior: stiffness degradation, strength deterioration, and ultimate displacement reduction. The model is cumulative and it combines energy, ductility, and low-cycle accumulation. The model is based on the work needed to fail the element monotonically after it experiences cyclic loading and takes the energy under the monotonic load-deformation envelope for the virgin state of the element as a reference capacity. The model modifies the ultimate displacement that the element can achieve, due to low-cycle accumulated damage at the longitudinal reinforcement using the Coffin-Manson rule in combination with Miner's hypothesis.

Most of this study is applied specifically to reinforced concrete columns and column-like elements, but the application is also demonstrated for a coupling beam in a coupled shear wall system.

A layers analysis program is written to predict the monotonic force-displacement envelope based on plane sections remaining plane, accounting for concrete confinement, elastic shear deformation, elastic and inelastic flexural deformation, and bond slip deformation.

The proposed model is applied to 12 bridge columns tested by others. The proposed model gave a realistic prediction of the damage throughout the loading cycles for the test

specimens investigated. The results are also compared to two existing damage models; the Park and Ang (1985) and the low-cycle damage model by Mander and Cheng (1995).

An experimental test for a full-scale coupling beam is conducted in this study in order to observe the damage due to cyclic loading. A theoretical prediction of the monotonic force-displacement response of a diagonally reinforced coupling beam is proposed based on a truss model. The model considers the confined concrete between the diagonal reinforcement in the compression direction in addition to the diagonal reinforcement, while only the diagonal reinforcement is considered in the tension direction. The proposed damage model is applied to predict the damage and is compared to the observed damage and to other existing models. The damage prediction of the proposed model compared very well with the observed damage and showed the ability of the proposed model in describing the damage of elements other than bridge columns.

The proposed damage model is applied to two existing bridges in Vancouver area. The piers of these bridges consist of a spread footing, a single column and a cap beam. The bridge piers are modeled as cantilevers with lumped mass. A bilinear monotonic force-displacement response for each pier was predicted using the layer analysis program. A nonlinear dynamic analysis is performed using the CANNY structural program (CANNY-E, 1996). CANNY sophisticated hysteresis model is used to model stiffness degradation, strength deterioration and pinching behavior. A series of nonlinear dynamic analyses were performed using records from the 1971 San Fernando, 1989 Loma Prieta, 1978 Miyaki-Oki (Japan), and 1999 TW (Taiwan) earthquakes fitted to Vancouver firm ground spectrum with 2% probability of exceedance in 50 years. A comparison between the proposed model, the Park and Ang model, and the low-cycle damage model by Mander and Cheng is performed. This study showed that the proposed model is applicable to real bridge columns under real seismic loading.

A risk-based retrofit decision is briefly demonstrated for an existing bridge in Vancouver using the proposed damage as a tool. This is done to demonstrate how the damage index can be useful as a measure of consequences.

TABLE OF CONTENTS

LIST OF TABLES

CHAPTER FOUR

CHAPTER FIVE

CHAPTER SIX

CHAPTER SEVEN

APPENDIX A

LIST OF FIGURES

CHAPTER TWO

CHAPTER THREE

CHAPTER FOUR

CHAPTER FIVE

CHAPTER SIX

CHAPTER SEVEN

APPENDIX A

APPENDIX B

LIST OF SYMBOLS AND ABBREVIATIONS

θ	angle
ϕ	curvature
ϕ_{ult}	ultimate curvature
ϕ_y	yield curvature
μ	ductility
ε	strain at a point
ε'_c	concrete strain at maximum stress
ε'_{cc}	confined concrete strain at maximum strength
ε_c	concrete strain
ε_{ccu}	crushing strain of confined concrete
ε_o	strain at the centroid at ordinate y_o
ε_p	plastic strain
ε_y	yield strain
Δ_b	bond slip displacement
Δ_e	elastic flexural displacement
Δ_f	failure displacement
Δ_{fn}	failure displacement after n cycles
Δ_p	plastic flexural displacement
Δ_{pn}	plastic flexural displacement after n cycles
Δ_{se}	elastic shear displacement
Δ_y	yield displacement
Δ_{y2}	second yield displacement
$\int dE$	absorbed hysteretic energy
β_e	energy parameter
δ_m	maximum displacement reached
δ_{strn}	reduction in strength after n cycles
δ_u	monotonic ultimate displacement

ρ_v	volumetric ratio of shear reinforcement
$2N_f$	number of complete cycles to fatigue
A_c	concrete area
A_g	gross area
A_g	reinforcement area
A_n	area under monotonic load-deformation envelope after n cycles
A_n	nominal area
A_o	area under initial monotonic load-deformation
C	low-cycle fatigue test factor
CSA	Canadian Standards Association
C_u	ultimate compressive force
D	damage magnitude
D′	concrete core dimension
d_b	bar diameter
D_n	damage after n cycles
E	modulus of elasticity
E_c	concrete modulus of elasticity
E_s	steel modulus of elasticity
F	flexure capacity
f'_c	concrete compressive strength
f'_{cc}	confined concrete compressive strength
f_c	concrete stress
FD	displacement reduction factor
FDR	flexure damage ratio
ft	feet
F_y	yield force
h	section height
I	moment of inertia
in.	inches
K_n	stiffness after n cycles
K_o	initial stiffness

K_{vcr}	cracked shear stiffness
K_{vun}	uncracked shear stiffness
L	length (from maximum moment to infliction point)
l_d	bar development length
L_p	length of plastic hinge
LVDT	linear voltage displacement transducer
M_{cr}	cracking moment
mm	millimeters
M_{ult}, M_u	ultimate moment capacity
M_y	yield moment
n	number of cycles
P	axial force
r	displacement range
S	bar slip
s	stirrups spacing
T_u	ultimate tensile force
UBC	University of British Columbia
V	shear force capacity
V_c	concrete shear force strength
V_f	shear force capacity at ultimate ductility
V_p	axial shear force strength
V_s	stirrups shear force strength
y	ordinate from the bottom fiber of the section
z	distance c/c between top and bottom longitudinal reinforcement

ACKNOWLEDGMENTS

This research was funded by the National Sciences and Engineering Research Council of Canada. This support is gratefully acknowledged.

I would like to express my great debt for help beyond measure to my supervisor, Dr. Robert Sexsmith, for the excellent guidance, endless support, valuable advice he has given me during this research. His comments and suggestions during the preparation of this thesis are sincerely appreciated.

Special gratitude goes to Dr. Perry Adebar for his help and guidance during my years at UBC. I want to thank him for giving me the opportunity to work with him on the experimental test of a coupling beam and for permission to use his test results.

I would like to thank Dr. Sashi Kunnath at the University of Central Florida for permission to use his test results.

Special thank and appreciation to Dr. Donald Anderson for his help and technical advice on the nonlinear analysis. I would also like to express my appreciation to Dr. Ricardo Foschi and Dr. N. Banthia for their comments and suggestions during this research.

The experimental part of this research would not have been possible without the assistance of the Laboratory technicians. Special Thanks go to Doug Smith, Doug Hudniuk and John Wong for their help with building and testing the coupling beam specimen.

Last, but certainly not the least, I would like to thank my wife Luma and my parents for their support and encouragement. Luma is given special thanks for the patience and care she has had for me during my study and work at UBC.

CHAPTER ONE

INTRODUCTION

The design criteria adopted by current seismic bridge codes generally requires the structure to resist minor ground motions with no inelastic damage, moderate ground motions with minor inelastic structural damage, and major ground motions without collapse. The primary seismic design goal is to ensure life-safety. To achieve this at reasonable cost, the bridge codes specify that the bridges should be designed to resist moderate ground motions, or a fraction of the maximum probable ground motion, in the elastic range, while providing sufficient ductility to dissipate the energy of a major earthquake in the inelastic range. This requires that the structural strength be proportioned to ensure the formation of a desirable mechanism.

There were a number of failures in the 1971 San Fernando earthquake in the United States that showed the need for a ductile design of bridge structural systems. This led to upgrades in the Canadian Standards Association, Design of Highway Bridges (CAN/CSA S6). Prior to 1971, bridges in Canada were generally designed predominantly for gravity loads. Although the CAN/CSA S6 code includes wind, centrifugal and hydrodynamic loads, these are generally small compared to earthquake lateral loads, and the design philosophy used to provide lateral strength for these loads is inherently different from the ductile inelastic strength principles associated with seismic design.

One of the major problems facing bridge engineers in seismically active areas is the assessment of existing bridge structures for earthquake loading. Many such bridge structures were designed with little or no provision for lateral load resistance; therefore, they fall well below the performance criteria set for new bridges. Therefore, decisions must be made over which bridges should be retrofitted, and what level of retrofit is appropriate.

While some routine retrofit decisions can be carried out following predetermined guidelines such as FEMA (The Federal Emergency Management Agency) (FEMA 306 and FEMA 307 ATC 1999), formal decision analysis should be applied to important or unique situations. In this way optimal choices can be made that aim to minimize present expected value of retrofit costs and damage consequences. Decision analysis requires that the consequences of any decision be quantified. In order to quantify the consequences of a structural decision, a measure of the damage due to seismic events has to be available. One class of methods to quantify damage is the use of a "damage index" to create a single measure that fairly represents the complex hysteretic behavior. Damage indices are important tools to provide a means of quantifying numerically the damage sustained under cyclic loading in concrete structures. Damage indices may be based on the results of a non-linear dynamic analysis, on the measured response of a structure during an earthquake, or on a comparison of a structure's physical properties before and after an earthquake.

Damage in reinforced concrete bridge columns during an earthquake may be due to excessive deformation, or it may be accumulated damage sustained under repeated load reversals. Damage is usually expressed in term of ductility, stiffness softening, absorbed energy during the loading cycles, or/and low-cyclic accumulation. Damage due to low-cycle accumulation at the reinforcing steel can be excessive depending on the number of cycles in an earthquake and the displacement amplitude of these cycles. There are numerous damage indices that have been proposed as summarized later in Chapter 2, but engineers and researchers are still in need of a damage model that can simply combine and consider all the important parameters in the hysteretic response.

Laboratory model tests can be performed to evaluate the capacity of the existing structures for lateral earthquake load. Obviously, such testing is expensive and time-consuming, and could not be performed for all the existing bridges. Therefore, there is a need for analytical approaches for assessing existing bridges. Damage indices provide simple numerical indicators of the damage during an earthquake loading, which can be computed from the results of a non-linear dynamic analysis.

In addition to retrofit and repair decision making, damage indices are useful tools in:

- Performance based seismic design of bridges; damage indices can be used to define the damage states in order to help engineers set seismic design criteria.
- Disaster planning; indices can be used to estimate the likely extent of bridge damage caused by a seismic event, enabling planners to predict the likely cost and response strategies for the earthquake.
- Post-earthquake assessment; damage indices can be used to assess vulnerability to aftershocks, enabling authorities to decide whether or not a bridge is safe to stay opened for traffic immediately after a seismic event. In the longer term, damage indices can be used as an aid to decide whether the bridge is repairable or not.

Earthquakes can have a seriously negative impact on society by causing human suffering and economic losses. Reliable rehabilitation decisions require sufficient information on the degree of structural damage. Relationship between earthquake ground motion severity and structural damage along with seismic site hazard analysis can be used to asses extensive damage, collapse casualties and subsequent long term economic losses due to earthquakes. The motion-damage relationships obtained in the form of probability distributions of damage at specified ground motion intensities are usually expressed by means of fragility curves and damage probability matrices. The fragility curves and damage probability matrices describe the conditional probabilities of reaching different damage states for specified ground motion levels. ATC-13 (Applied Technology Council, 1983) provides motion-damage relationships for different types of buildings in the form of damage probability matrices; however, these matrices are subjective in nature because they are based only on expert opinion. Analytical damage models are needed to develop such relationships empirically in order to identify the different damage states based on suitable structural response parameters.

1.1 OBJECTIVES

The following are the main objectives of this thesis:

1. Develop a theoretical damage model that is able to represent a measure of the damage due to the complex hysteretic behavior of a structural element under cyclic loading at any point in the load history. The damage measure serves as a measure of the damage consequences. In order to develop such a model, the following are considered:
   (i) The model is based on force-displacement response and not on moment-curvature response. This is meant to capture the effect of other actions, such as shear and bond slip actions. Shear failure, which is not considered in almost all existing damage models, is a brittle action and should be considered;
   (ii) The model is cumulative and capable of combining ductility, absorbed energy, stiffness, and low-cycle accumulation. Damage in reinforced concrete bridge columns during an earthquake may be due to excessive deformation, or it may be accumulated damage sustained under repeated load reversals due to losses in the strength and stiffness, and/or low-cycle accumulated damage;
   (iii) It can be used directly to evaluate the overall damage of entire structure; therefore, it serves as a local and global damage index in the same time.

2. Compare the proposed model with existing damage models that are widely used to examine its ability in predicting the damage and in showing the progression of damage during the loading cycles.

3. Compare the model to different test observations in order to calibrate it and to establish damage classification that can be used by a practicing engineer to assess structural integrity following a seismic event.

4. Apply the model to real bridge columns that have experienced or might experience seismic events to compare the predicted damage with the observed damage and to verify the model in real life.

5. Apply the model as a tool in a retrofit decision analysis study.

1.2 SCOPE AND ORGANIZATION

The approach followed in this thesis is to first develop a damage model, define the tools and assumptions to evaluate it's parameters, apply the model to structural elements that are experimentally tested by others and by the author, and, finally, apply the model to existing bridge columns.

A relevant literature survey is made in Chapter 2 on topics related to damage indices for structural elements due to cyclic loading. This chapter focuses on local damage indices since they are the basis for most available global indices. Existing damage models are classified into four categories: non-cumulative models, deformation-based cumulative models, energy-based cumulative models, and combined models.

Chapter 3 describes in detail the development of the proposed damage model and the assumptions involved in defining its parameters. A description of the theory and assumptions used in developing a layer analysis program to predict the monotonic force-displacement envelope of a reinforced concrete column is also presented in this chapter.

A comparison between the proposed model, the Park and Ang damage index by Park and Ang (1985), and the low-cycle damage model by Mander and Cheng (1995) for six specimens of circular reinforced concrete columns that were tested by Kunnath et al. (1997), and six square columns that were tested by Adebar and Roux (1998) is presented in Chapter 4. Chapter 4 focuses on applying the proposed damage model to tested columns under reversed cyclic loading with controlled displacement. This is the simplest appropriate loading history, and it avoids the many complexities of dynamic behavior, to be treated subsequently. The comparison is meant to cover as much as possible the different aspects that play a major role in the behavior of bridge columns, such as; shear, flexure, confinement, axial load, stirrups spacing, number of cycles, and displacement amplitude. The chosen tests by Kunnath et al. (1997) and Adebar and Roux (1998) covered most of the above aspects. The loading scheme applied to the chosen tested

columns consists of a standard reversed cyclic loading. The controlled displacement amplitude of the loading cycles is either constant or different from one cycle to another.

This study is conducted to compare the proposed model to other existing models in order to evaluate the ability of the proposed model in describing the damage during controlled cycles. The damage prediction is also discussed and compared to the available observed damage from the tests in terms of photos and damage descriptions in order to relate the proposed model to the actual damage. This is used to calibrate the proposed damage model and to establish damage classification.

Chapter 5 describes in detail the experimental program and damage analysis of a full-scale coupling beam that is typically used in high-rise buildings in Vancouver area. The coupling beam was experimentally tested as a part of this thesis for the purpose of damage computations. The objective is to briefly explore the use of the proposed damage model for a structural element other than bridge columns. A comparison between the observed damage and the predicted damage by the proposed model, the Park and Ang model and low-cycle damage model by Mander and Cheng is also presented in this chapter.

The damage prediction is discussed and compared to the observed damage from the test in terms of photos and damage descriptions in order to verify the proposed model in describing the actual damage of such a structural element based on the damage classification as concluded in Chapter 4.

Chapter 6 presents the analysis of seismic damage of two bridges in Greater Vancouver area. The objective is to apply the proposed damage model to existing bridge columns, that might experience real earthquake loading anytime in the future, to evaluate the model's ability in describing the seismic damage of the bridge columns during earthquake loading. A comparison between the proposed model, the Park and Ang model, and the low-cycle damage model is also presented in this chapter as part of the evaluation of the proposed damage model. The damage prediction is discussed and

compared only to existing damage models and to the damage classification as suggested in Chapter 4 since no observed damage is available for these bridges.

A risk-based retrofit decision is demonstrated through an existing bridge in Vancouver in Chapter 7. The objective of this study is to demonstrate the use of the damage index as a measure of consequences in decision analysis. An expected value decision is constructed as a decision tree. Fully effective retrofit and no retrofit actions make up the two main branches of the decision tree. Six earthquake records with different probability of exceedance in 50 years are selected and scaled for use in the damage analysis. The damage cost depends on the seismic damage level as estimated by the proposed damage model. Comparing the net present costs of the two actions reveals whether a seismic retrofit is advisable.

Finally, Chapter 8 provides a summary of the conducted research and a discussion of the conclusions drawn. This investigation has shed some light into the need for some well-planned analytical and experimental studies to look into the behavior of some specific variables. A recommendation for further research, both analytical and experimental, is outlined.

CHAPTER TWO

LITERATURE REVIEW

A literature survey is presented in this chapter on topics related to damage indices for structural elements due to cyclic loading. There are various ways of categorizing the numerous damage indices that have been proposed, but one of the most fundamental distinctions is between local indices, which quantify the level of damage in individual elements, and global indices, which describe the state of a large part of a structure. Taking a weighted average of the local indices calculated for constituent elements usually derives the global indices, but some are formulated directly from the overall structural characteristics. This survey focuses only on local indices since they are the basic to calculate the global indices and bridge columns are single elements.

2.1 CATEGORIZATION OF DAMAGE

Many attempts to categorize damage by observation use a simple classification based on visual signs of damage. For example, Park et al. (1987) use:

- None - no damage or localized minor cracking
- Minor - minor cracking throughout
- Moderate - severe cracking and localized spalling
- Severe - crushing of concrete and exposure of reinforcing bars
- Collapse

Such a categorization is obviously easy to apply in experimental observation and in post-earthquake inspections, though it would be helpful if the categories were defined rather more rigorously.

A different approach to classify damage is to relate the damage to the repairability of the structure. Bracci et al. (1989) and Stone and Taylor (1993) use the following categorization:

- Undamaged or minor damage
- Repairable

- Irrepairable
- Collapsed

While this scale may be harder to apply in practice, it is perhaps more helpful as a tool for retrofit decision making, or for outline planning and cost of post-earthquake reconstruction. An important limitation is that it implies that consequences are primarily related to repair costs.

2.2 DAMAGE INDICES

The categories listed in the foregoing provide a simple description of damage. There have been a number of proposals to provide a quantified measure of damage, a *damage index*. In most cases damage indices are dimensionless parameters intended to range between 0.0 for an undamaged element and 1.0 for a completely failed element, with intermediate values giving some measure of the degree of damage.

Damage in reinforced concrete bridge columns during an earthquake may be due to excessive deformation, or it may be accumulated damage sustained under repeated load reversals. The damage may involve the concrete, the reinforcement or a combination of both. Cyclic loading may accumulate damage in the member in terms of strength deterioration, stiffness degradation, and low-cycle accumulation; however, small amplitude cycles within the elastic limit cause insignificant and negligible damage in terms of minor cracking. The accumulated damage is expressed in terms of plastic deformation or in terms of hysteretic energy absorbed during the loading. Low-cycle accumulated damage can be an important issue depending on the amplitude and number of inelastic cycles since earthquake loading induces large inelastic reversals. Obviously, if a single index is required to predict all forms of seismic damage, it must include inelastic deformation and cyclic loading effect.

Researchers have proposed a number of damage models and attempted to include as much as possible of the aspects that represent the complex hysteretic behavior of a reinforced concrete member. Existing damage models can be classified into:

2.2.1 Non-Cumulative Models

The earliest and simplest damage model was ductility index. The ductility ratio can be defined in terms of rotation, curvature or displacement. The rotational ductility, μ_θ, for a member is defined as the ratio of the maximum rotation in the member, θ_m, to the yield value, θ_y:

$$\mu_\theta = \frac{\theta_m}{\theta_y} \tag{2-1}$$

Banon et al. (1981) suggested that yield rotation θ_y is calculated assuming that the element yields in antisymmetric bending. The need for this assumption can be eliminated by defining ductility in terms of curvature, μ_ϕ:

$$\mu_\phi = \frac{\phi_m}{\phi_y} \tag{2-2}$$

Where ϕ_y is the yield curvature and ϕ_m is the maximum curvature along the element. Obviously, this ratio applies only to the most damaged section along the element and not to the entire element. Another common approach is to use some characteristic member displacement, δ, as a ductility parameter:

$$\mu_\delta = \frac{\delta_m}{\delta_y} \tag{2-3}$$

Where μ_δ is the displacement ductility, δ_y is the yield displacement and δ_m is the maximum displacement.

Another widely used damage model is the drift. Attempts have been made to relate damage from an earthquake to both the maximum drift and the permanent drift remaining after the earthquake (Toussi and Yao, 1983). As with ductility, simple drift measures fail to take account of the effects of repeated cycling that occurs under seismic loading, but nevertheless remain quite widely used because of their simplicity and ease of interpretation.

In an attempt to overcome some of the deficiencies of these traditional damage models, a number of models related to stiffness degradation have been proposed. As shown in

Figure 2.1 (where M_y, M_m and M_f are the yield moment, the maximum moment reached in the loading, and the moment at failure respectively, and ϕ_f is the curvature at failure), Banon et al. (1981) defined the flexural damage as:

$$FDR = \frac{k_o}{k_m} \tag{2-4}$$

Where k_o and k_m are the initial and maximum element stiffness respectively as shown in Figure 2.1. This is an improvement on a ductility ratio as it takes some account of the stiffness and strength degradations that occur under cyclic loading. Banon et al. (1981) suggested that k_o be calculated using the assumption of antisymmetric bending as it was assumed for the rotational ductility. In comparisons with test data, it was found that neither ductility nor the flexural damage ratio, FDR, give a consistent indication of failure, but they suggested that FDR is a preferable indicator as it gives more information on the degradation of member properties.

Roufaiel and Meyer (1987) suggested a modified form of the flexural damage ratio, defined as the increase in flexibility between the initial condition and the instant of maximum deformation divided by the increase in flexibility at failure. This can be expressed in terms of stiffnesses as:

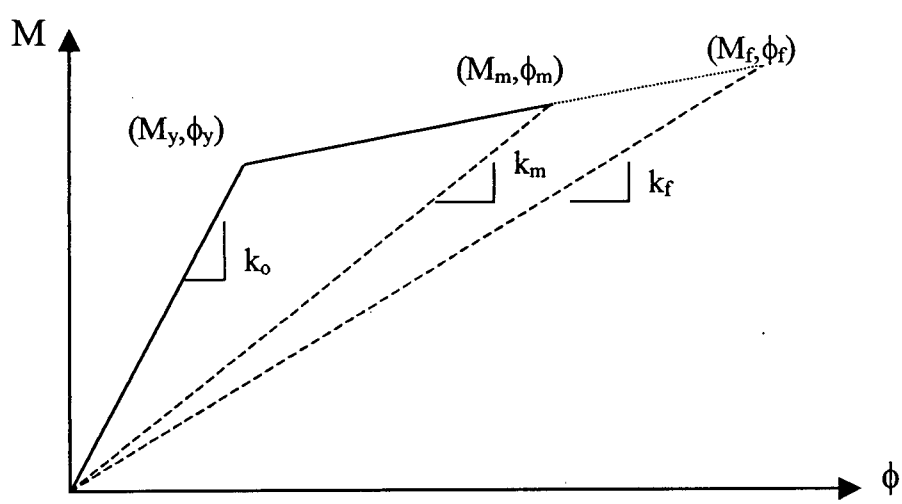

Figure 2.1: Definition of stiffness degradation

$$FDR = \frac{k_f}{k_m}\frac{(k_m - k_o)}{(k_f - k_o)} \tag{2-5}$$

Where k_f is the element stiffness at failure. The FDR is taken as the largest of values achieved during positive and negative loading cycles. This parameter showed a good correlation with the residual strength and stiffness of laboratory test specimens tested in flexure. Some of the tests also included significant shear and axial actions.

2.2.2 Deformation-Based Cumulative Models

Modeling of the accumulation of damage which occurs under cyclic loading is usually performed either by using a deformation-based formulation, in which damage is taken as a function of the accumulated plastic deformation, or by incorporating a term related to the hysteretic energy absorbed during the loading.

Early deformation-based cumulative damage model simply attempted to extend the ductility concept to cover repeated loading. Banon et al. (1981) used a normalized cumulative rotation, NCR:

$$NCR = \frac{\sum\left|\theta_m - \theta_y\right|}{\theta_y} \tag{2-6}$$

This model was applied to a wide range of cyclic load tests, mostly flexure dominated, with some also including significant axial load. This damage index showed considerable scatter at failure.

Stephens and Yao (1987) developed a cumulative damage model based on the displacement ductility. With positive and negative displacement as shown in Figure 2.2, the damage index is:

$$D = \sum\left(\frac{\Delta\delta^+}{\Delta\delta_f}\right)^{1-br} \tag{2-7}$$

Where $r = \Delta\delta^+/\Delta\delta^-$, $\Delta\delta_f$ is the value of $\Delta\delta^+$ in a single-cycle test to failure and b is a constant. Stephens and Yao recommended taking $\Delta\delta_f$ as 10% of the column height and b

as 0.77. The index was used to assess two test structures, and showed moderate correlation with the observed damage, the degree of scatter increasing with damage level.

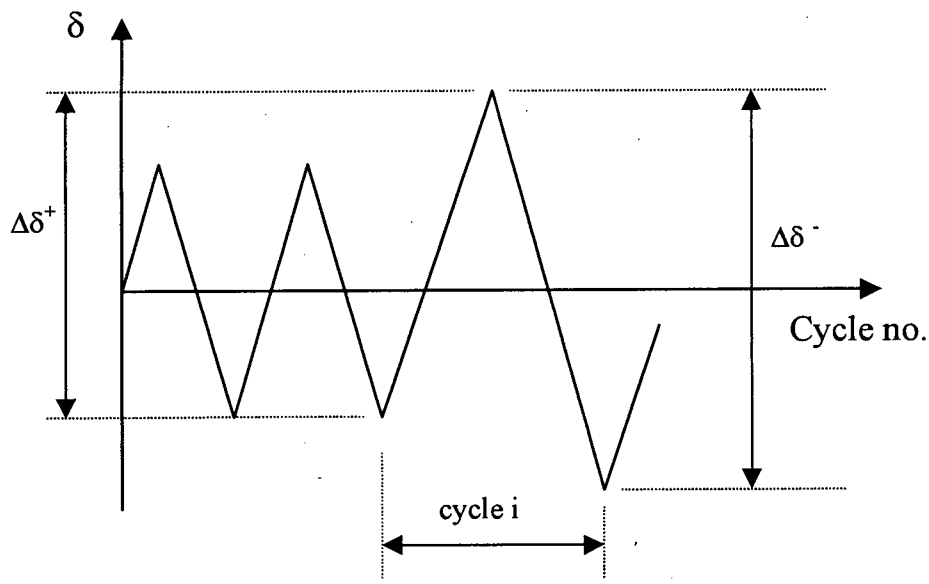

Figure 2.2: Plastic displacement increments (Stephens and Yao, 1987)

Wang and Shah (1987) assumed that the development of damage depends on the maximum deformation occurring in a cycle, and that the rate of accumulation of damage is proportional to the damage already incurred, as shown in the following damage index:

$$D = \frac{\exp(sb) - 1}{\exp(s) - 1}, \qquad b = c\sum_i \frac{\delta_{m,i}}{\delta_f} \tag{2-8}$$

Where s and c are user-defined constants, the parameter b is a scaled cumulative displacement ductility and δ_f is the failure displacement. The index is basically a measure of strength degradation. The yield load in a deformation cycle is given by the maximum load in the previous cycle multiplied by (1-D) as shown in Figure 2.3. Wang (1994) stated that the model is of limited use due to the need for calibration against observed seismic damage.

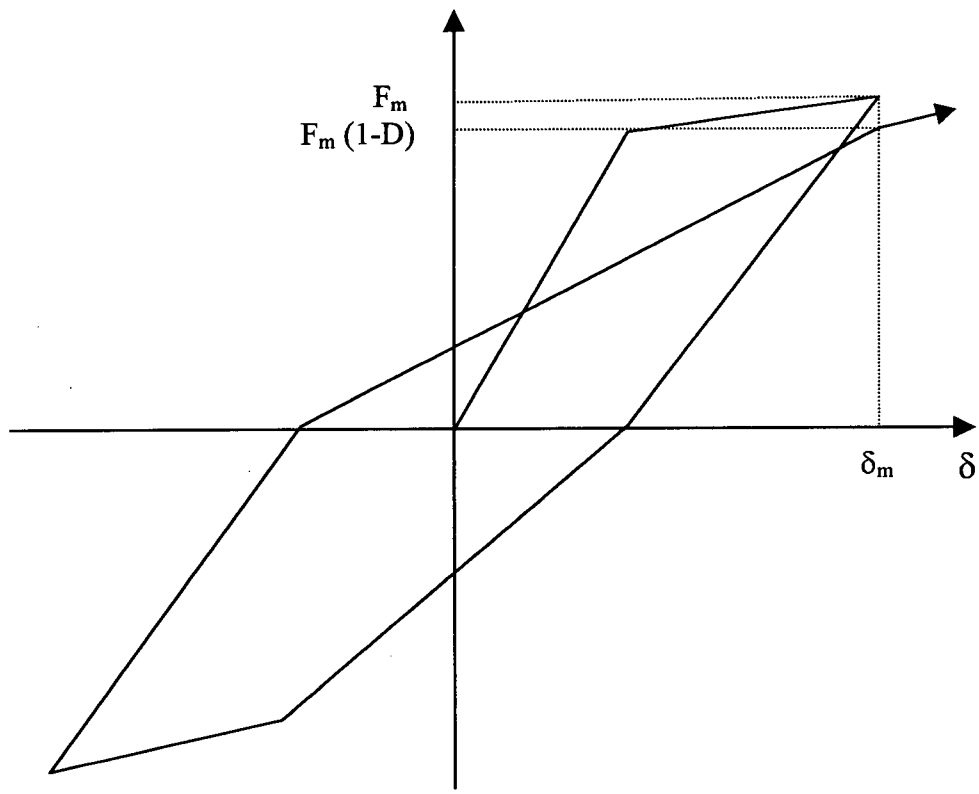

Figure 2.3: Physical meaning of Wang and Shah (1987) damage model

Since seismic loading of reinforced concrete elements results in several inelastic cycles at relatively large ductility demands, the idea of using a classical low-cycle damage formulation is logical. Though fatigue of metals and concrete have been evaluated in the past, few have attempted to extend these concepts to evaluating seismically induced fatigue damage. Chung et al. (1987, 1989) combined Miner's rules (1945) with an assumed failure criteria, which states that failure occurs when the degraded moment-curvature curve intersects the failure envelope as shown in Figure 2.4:

$$D = \sum_i \left(w_i^+ \frac{n_i^+}{n_{f,i}^+} + w_i^- \frac{n_i^-}{n_{f,i}^-} \right) \tag{2-9}$$

Where positive and negative deformation cycles are considered separately, w_i is a weighting factor that depends on degraded stiffness, n_i is the number of cycles at a given displacement level, and $n_{f,i}$ is the number of cycles to fatigue at the same level of displacement. The model defines the strength reduction due to cyclic loading as a

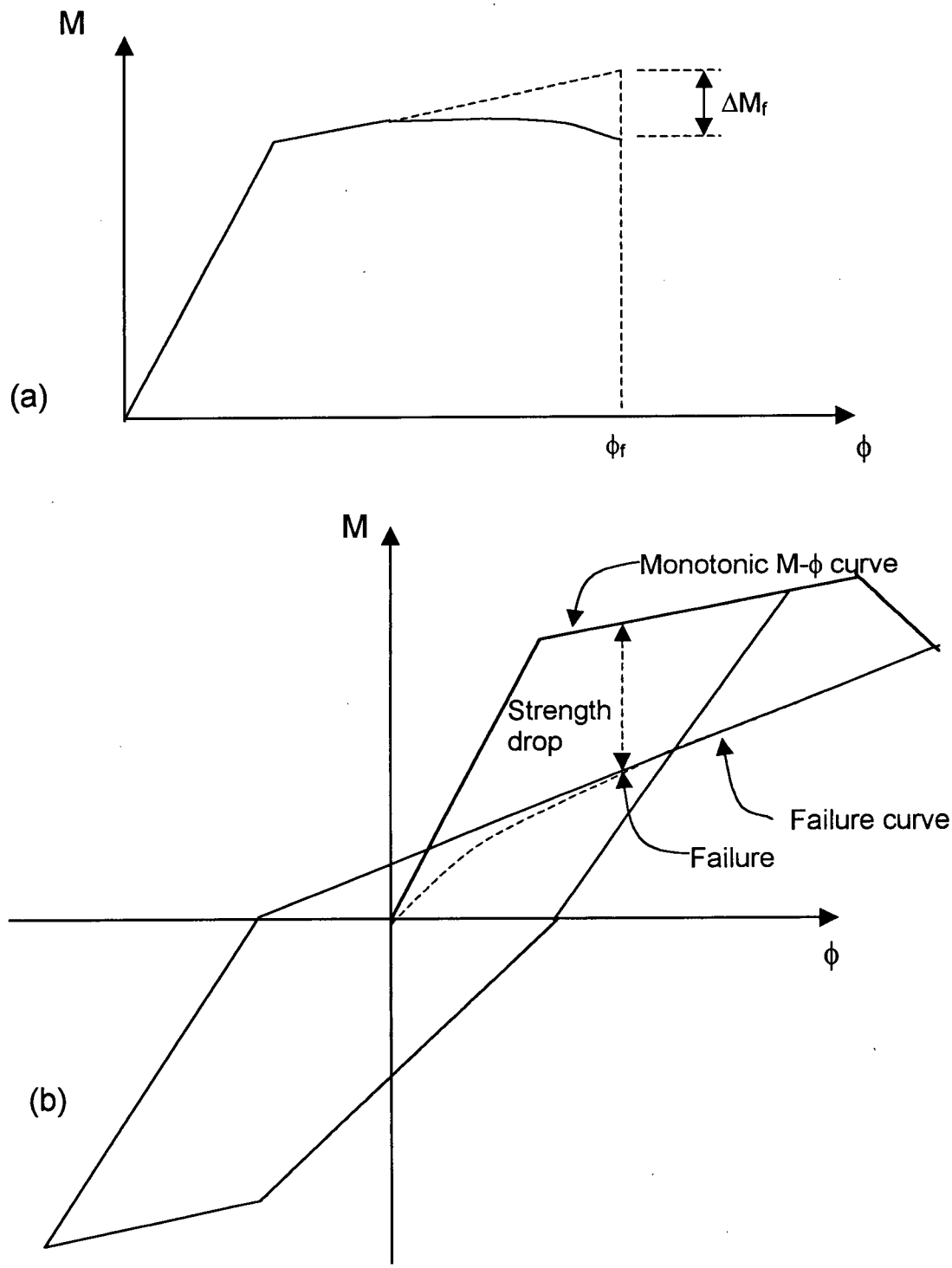

Figure 2.4: Definition of flexural failure under (a) monotonic and (b) cyclic loading (Chung et al., 1987).

function of the reduction at failure due to monotonic loading. The degradation in the hysteretic behavior giving by this model has shown good agreement with several flexural tests; however, calibration of the damage index against observed damage seems to be limited. Chung et al. (1990) derived an automated design procedure based on this index, in which a design is considered acceptable if a column for example has a damage, D, less than 0.01.

Jeong and Iwan (1988) combine Miner's rules with the well-known Coffin-Manson law:

$$D = \sum_i \frac{n_i \mu_i}{c} \tag{2-10}$$

where $c = n_f \mu$ and n_f is the number of cycles to failure at a specified ductility μ.

In seismic event, the longitudinal reinforcement in concrete elements may undergo large strain reversals of typically one to five fully reversed equiamplitudes (Mander et al., 1994). Experimental fatigue test data for this low-cycle fatigue do not seem to exist as stated by Mander et al. (1994) because the majority of existing fatigue tests are generally conducted for mechanical engineering applications that mostly deal with medium to high-fatigue. Therefore, Mander et al. (1994) tested reinforcing bars to evaluate the parameters of low-cycle accumulated damage. No other similar tests have been found in the literature.

Mander and Cheng (1995) have derived a very practical low-cycle damage model for reinforced concrete columns. They related local section curvature at the plastic hinge region directly to the strain in the longitudinal reinforcement. The following derivation (Equations 2-11 to 2-17) is a variation, developed by Kunnath et al. (1997), of the procedure derived by Mander and Cheng (1995). It is shown herein in detail because it is adopted and utilized in this research. The low-cycle behavior of the longitudinal reinforcement under reversed cyclic loading is formulated in terms of Coffin (1954) – Manson (1953) equation.

$$\varepsilon_p = \varepsilon_f (2N_f)^c \tag{2-11}$$

Where: ε_p = Plastic strain amplitude

ε_f = A material constant
$2N_f$ = Number of complete cycles to failure

Mander et al. (1994) obtained an experimental fit to Equation 2-11 to relate plastic strain, ε_p, that will result in fracture of the longitudinal steel, to the number of complete cycles, $2N_f$,

$$\varepsilon_p = 0.08(2N_f)^{-0.5} \tag{2-12}$$

Mander et al. (1994) also developed a similar expression using total strain, ε_t, instead of plastic strain,

$$\varepsilon_t = 0.08(2N_f)^{-0.33} \tag{2-13}$$

The plastic strain in the longitudinal reinforcement, ε_p, of a symmetric column section can be related to the plastic curvature, ϕ_p, as shown in Figure 2.5.

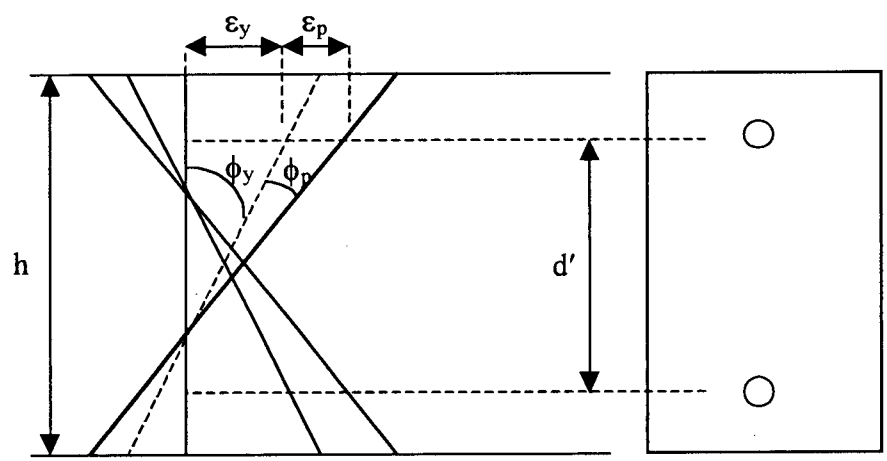

Figure 2.5: Strain distribution (Mander et al., 1994)

$$\varepsilon_p = \phi_p \frac{d'}{2} \tag{2-14}$$

The plastic curvature is assumed to be constant over the plastic hinge length, L_p, as shown in Figure 2.6.

$$\Delta_p = \phi_p L_p (L - L_p/2) \tag{2-15}$$

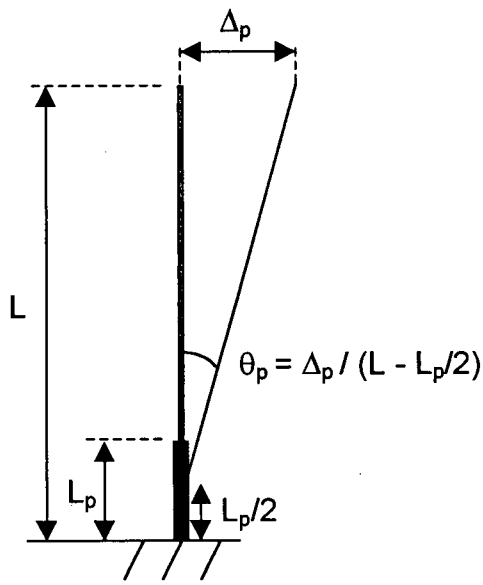

Figure 2.6: Plastic displacement

Where the equivalent plastic hinge length (L_p) can be estimated as suggested by Paulay and Priestley (1992),

$$L_p = 0.08L + 4400\varepsilon_y d_b \tag{2-16}$$

L is the length of the column in millimeters (from the maximum moment to the inflection point). Δ_p (plastic displacement = Δ_n- Δ_y), where Δ_y is the yielding displacement of the column, and Δ_n is the total displacement at cycle n. ε_y is the yield strain of steel, and d_b is the bar diameter in millimeters.

Therefore, the number of complete cycles to low-cycle failure ($2N_f$) can be found now at any plastic displacement level (Δ_p) from the above equations. Following Miner's rules (Miner 1945), the low-cycle damage model can be derived:

$$D_{fatigue} = \sum \frac{1}{2N_f} \tag{2-17}$$

A modified low-cycle damage model was proposed by Kunnath et al. (1997) based on experimental fitting of the Coffin-Manson fatigue expression using results from constant-amplitude testing of four columns. The test was limited to circular columns with a predominantly flexural response. The plastic and total strains in the longitudinal

reinforcement are calculated following the Mander et al. (1994) expressions as shown in Equations 2-14 and 2-15. Kunnath et al. (1997) proposed the following expressions instead of Equations 2-12 and 2-13 respectively:

$$\varepsilon_p = 0.065(N_{2f})^{-0.436} \tag{2-18}$$

$$\varepsilon_t = 0.060(N_{2f})^{-0.360} \tag{2-19}$$

It was concluded that low-cycle failure at the longitudinal steel bars is more likely to occur when the column is subjected to high amplitude inelastic cycles, while it is more probable that the confinement will fail when low amplitude cycles are predominating.

2.2.3 Energy-Based Cumulative Models

Gosain et al. (1977) were the first to adopt energy absorption. They proposed a simple cumulative energy ratio:

$$D = \sum_i \frac{F_i \delta_i}{F_y \delta_y} \tag{2-20}$$

Where F_i and F_y are the force of cycle i and the yield force respectively, and δ_i and δ_y are the displacement of cycle i and the yield displacement respectively. Only cycles with $F_i/F_y \geq 0.75$ are considered in the calculation, because they assumed that the remaining capacity becomes negligible when it is 25% less than the initial capacity. Gosain et al. introduced modification terms to account for the effect of shear and axial load. It was observed that this damage index correlated very closely with normalized cumulative rotation, NCR, Equation 2-6. Darwin and Nmai (1986) suggested a similar energy index, but they included a modification factor to account for the reinforcing arrangement.

Kratzig and Meskouris (1987) developed a more complex energy model. Figure 2.7 illustrates the terminology used in this model. A primary half cycle (PHC) is defined as the first half cycle of loading at a given displacement level. Other half cycles are treated as followers (FHC) unless they induce higher displacement than the previous primary half cycle. Positive and negative displacements are treated separately, accumulated damage for the positive part of the hysteretic behavior is calculated as:

$$D^{+} = \frac{\sum E_{p,i}^{+} + \sum E_{i}^{+}}{E_{f}^{+} + \sum E_{i}^{+}} \tag{2-21}$$

Where $E_{p,i}$ is the energy in a PHC, E_i is the energy in an FHC, and E_f is the energy absorbed in a monotonic force-displacement envelope to failure. A similar damage is calculated for negative displacements, then the total damage is defined as:

$$D = D^{+} + D^{-} - D^{+}D^{-} \tag{2-22}$$

The follower half cycles contribute less than the primary half cycles since they are included in both numerator and denominator. Calibration of the index against observed damage in flexure dominated tests showed that the index reliably converged to a value of unity at failure, but a detailed assessment of the significance of intermediate values does not appear to have been made.

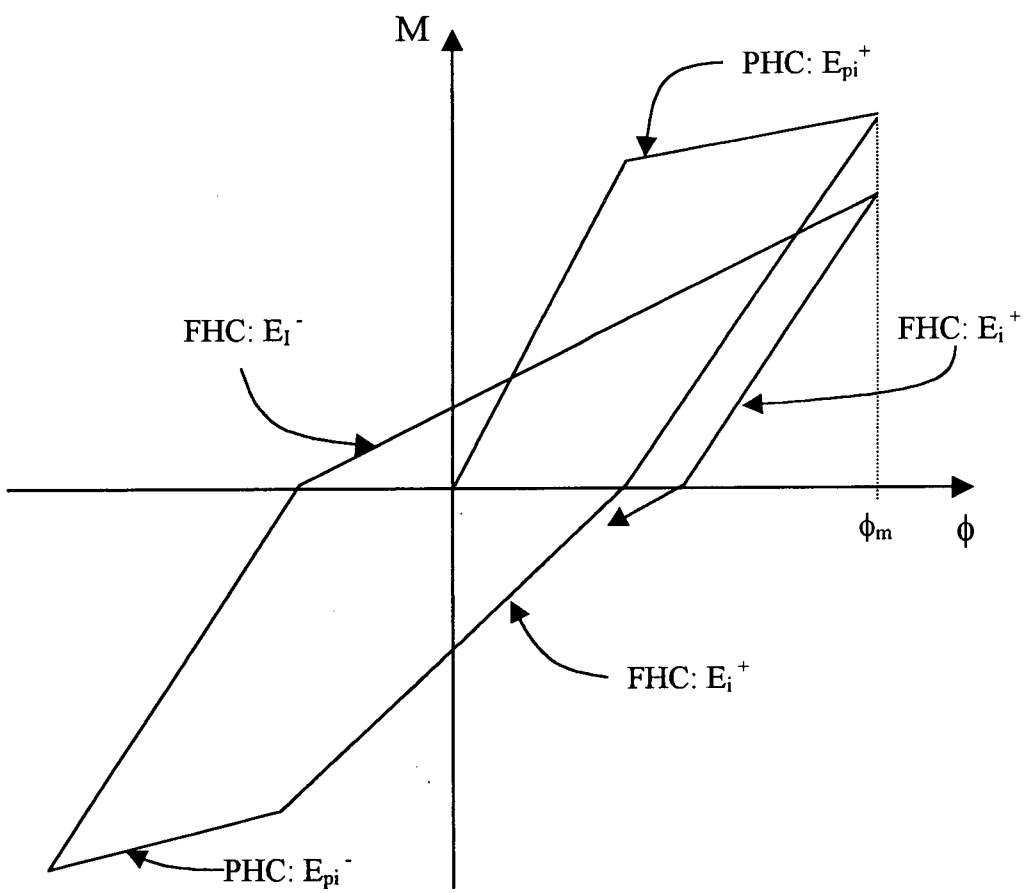

Figure 2.7: Parameters used in Kratzig model (1987)

2.2.4 Combined Models

The Park and Ang (1985) model is the best known and most widely used damage index. This model consists of a simple linear combination of normalized deformation and energy absorption:

$$D = \frac{\delta_m}{\delta_u} + \beta_e \frac{\int dE}{F_y \delta_u} \tag{2-23}$$

Where δ_m is the maximum displacement reached in the loading, δ_u is the monotonic ultimate displacement, F_y is the yield force, $\int dE$ is the absorbed hysteretic energy, and β_e is an energy parameter. The first term is a pseudo static displacement measure, the second term is an energy term accounting for accumulated damage. The advantages of this model are its simplicity, and the fact that it has been calibrated against a significant amount of observed seismic damage. Park et al. (1987) suggested the following damage classification:

$D < 0.1$	No Damage or localized minor cracking
$0.1 \leq D < 0.25$	Minor Damage- light Cracking throughout
$0.25 \leq D < 0.4$	Moderate damage- severe cracking, localized spalling
$0.4 \leq D < 1.0$	Severe damage – concrete crushing, reinforcement exposed
$D \geq 1.0$	Collapse

D = 0.4 was suggested by the same authors as a threshold value between repairable and irrepairable damage. Ang et al. (1993) suggested a value of D = 0.8 to represent complete collapse.

A modified version of this index was used by Kunnath et al. (1992), where the yield deformation is removed from the first term, and moment and curvature are used instead of force and displacement:

$$D = \frac{\phi_m - \phi_y}{\phi_u - \phi_y} + \beta_e \frac{\int dE}{M_y \phi_u} \tag{2-24}$$

This form of the index was applied by Stone and Taylor (1993) to 82 tests on CALTRANS circular bridge columns. They proposed the following damage classification:

$D < 0.11$	No Damage or localized minor cracking
$0.11 \leq D < 0.4$	Repairable – extensive spalling but inherent stiffness remains
$0.4 \leq D < 0.77$	Irrepairable – still standing but failure imminent
$D \geq 0.77$	Collapse

Park and Ang (1985) have proposed regression equations to compute β_e and δ_u or ϕ_u in terms of several variables, including shear to span ratio, axial load, longitudinal and confinement reinforcement, and material strengths. The equations for β_e yielded very small values, so that the energy term made a negligible contribution to the damage. Kunnath et al. (1990) and Stone and Taylor (1993) proposed other regression equations with a more substantial energy term. Ciamopli et al. (1989) utilized a probabilistic approach, where β_e is assumed as a random variable. Nevertheless, there is a degree of arbitrariness in the choice of β_e, which is undesirable.

Williams et al. (1997) studied and evaluated eight damage models by applying them to six specimen that were tested by Adebar and Roux (1998). Most of the specimens were shear dominated with different shear span and stirrups spacing. It was concluded that all the considered damage models are prone to quite a high degree of scatter, with non of them showing shear dependent trends. It was also concluded that the damage in shear dominated elements is mainly dependent on the level of ductility with small effect of the number of cycles. The above conclusion means that the relatively simple, predominantly deformation-based models, such as the Park and Ang model, provide more reliable indication of the various damage levels than many of the apparently more sophisticated models.

Singhal and Kiremidjian (1995) developed fragility curves and damage probability matrices for reinforced concrete frame structures based on characterization of ground motion and the identification of different degrees of structural damage. Three different classes of reinforced concrete frames based on story heights were considered. They used spectral acceleration and root mean square acceleration as ground motion characterization parameters. At a given ground motion parameter, an ensemble of ground motions were required to evaluate the conditional probabilities of the different degrees of damage. They identified different degrees of structural damage based on the structural damage models. The Park and Ang damage model was used for the development of fragility curves and damage probability. Constrained Monte Carlo simulation techniques were used to evaluate the fragility curves. This is an illustration of the use of damage index as a basis for decision models. Singhal and Kiremidjian (1995) compared the damage probability matrices with those in ATC-13 (Applied Technology Council, 1985). It was concluded that the ATC-13 potentially underestimates the damage to reinforced concrete structures since it is based on experts opinion and not on actual damage.

CHAPTER THREE

THEORETICAL DAMAGE MODEL

This chapter describes in detail the development of the proposed damage model and its parameters. The following goals are set to develop a damage model that can overcome some of the disadvantages of the existing damage models as stated in Chapter Two (Literature Review):

1. The model is based on force-displacement response and not on moment-curvature response in order to capture any shear action in the cyclic response;
2. It is cumulative and capable of combining ductility, absorbed energy, stiffness, and low-cycle accumulation;
3. The model minimizes the number of parameters that have to be assumed by the user and the degree of arbitrariness in choosing them;
4. It can be used directly to evaluate the overall damage of the entire structure (global index).

The model proposed herein takes as a reference capacity the energy under a monotonic load-displacement curve up to failure, A_o, as shown in Figure 3.1. With the actual load history up to point n (after n cycles of load-displacement), followed by a monotonic load-displacement history from the end of last cycle n (zero force point) to failure, total energy for the damaged state is A_n. The damage index D_n is the ratio;

$$D_n = \frac{(A_o - A_n)}{A_o} \tag{3-1}$$

The monotonic load-displacement relationship following the cyclic load to point n is determined taking account of degradation in strength, stiffness, and low-cycle accumulated damage. Most of the other damage indices are defined as functions only of the history up to the point n. Thus the index defined herein is a measure of damage with respect to the remaining degraded monotonic load-displacement capacity.

The proposed damage model considers all the parameters in the hysteretic behavior; stiffness degradation, strength deterioration, and ultimate displacement reduction due to low-cycle accumulated damage at the longitudinal reinforcement. Therefore, this damage model is accumulative, and it is capable of combining energy, ductility, and low cycle accumulation.

Given the hysteretic behavior of a structural element due to an earthquake loading, the proposed damage model can be used:

- To predict damage and remaining monotonic behavior of that element after it experienced any real seismic event or cyclic loading.
- As an analysis tool to predict damage and remaining monotonic response at any time during or after any prescribed earthquake that the element might experience.

3.1 MODEL DEFINITION

To fail a R/C column monotonically as shown in Figure 3.1, the tip of the column has to be displaced until it reaches the ultimate deformation Δ_f. The amount of energy needed to damage the column completely is the area A_o under the monotonic force-displacement envelope as shown in Figure 3.1. In this case the damage is complete and the damage index is equal to one (D=1.0). The monotonic Force-Displacement envelope can be generated theoretically using a layers analysis program based on plane sections remaining plane, accounting for elastic shear deformation, elastic and inelastic flexural deformation, and bond slip deformation (as discussed later). The theoretical monotonic ultimate displacement is defined by rupture of longitudinal reinforcement, crushing of confined concrete, or rupture of hoop reinforcement (confining steel). The Mander model for confined concrete, Mander et al. (1988), is utilized herein. The theoretical monotonic yield displacement is generated from the yield curvature, which is defined by applying a bilinear approximation to the moment-curvature response as suggested by Park and Paulay (1975).

In cyclic loading there is damage due to each cycle of loading and the damage accumulates until it reaches 1.0 (D=1.0) for complete failure. To measure the damage after any cycle, we need the entire history of loading and response (hysteretic behavior) prior and including that cycle, and the monotonic response following that cycle to failure.

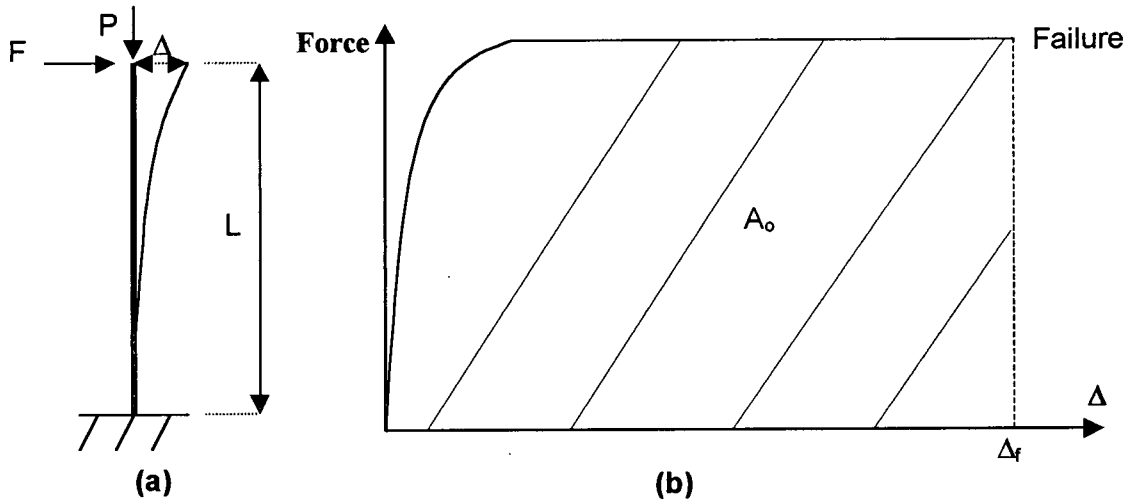

Figure 3.1: (a) Loaded column and (b) monotonic force-displacement envelope

It is assumed here that there is no damage if the cycle displacement is less than the yield displacement; therefore, damage starts when the cycle deformations get into the inelastic region. The definition of yield displacement is discussed later in this chapter.

Figure 3.2 shows a sample of displacement-controlled load history for a column. The loading starts at point A. There is loading until a displacement of Δ_1 is reached at point B, then unloading to point C, then reversal loading to point D, where the displacement reaches $-\Delta_1$, then unloading again to point E which is the end of the first cycle of force. For the type of displacement-controlled loading used here, the first displacement cycle is finished when the displacement equals zero at point F. We keep loading and then unloading until we reach a zero-force point H (passing through point G in order to capture the damage- the deterioration in strength, the degradation in stiffness, and the permanent plastic deformation that has occurred due to cyclic loading prior to point H, which is equivalent to one and a half load cycle). Point H is defined in this model as the

original point to start loading the column monotonically after it experienced one and a half load cycles as shown in Figure 3.2. Therefore, the proposed damage model calculates the damage at each time the hysteresis loops intersect the Δ-axis (In the direction of first loading from point A). The properties of the column until this point of

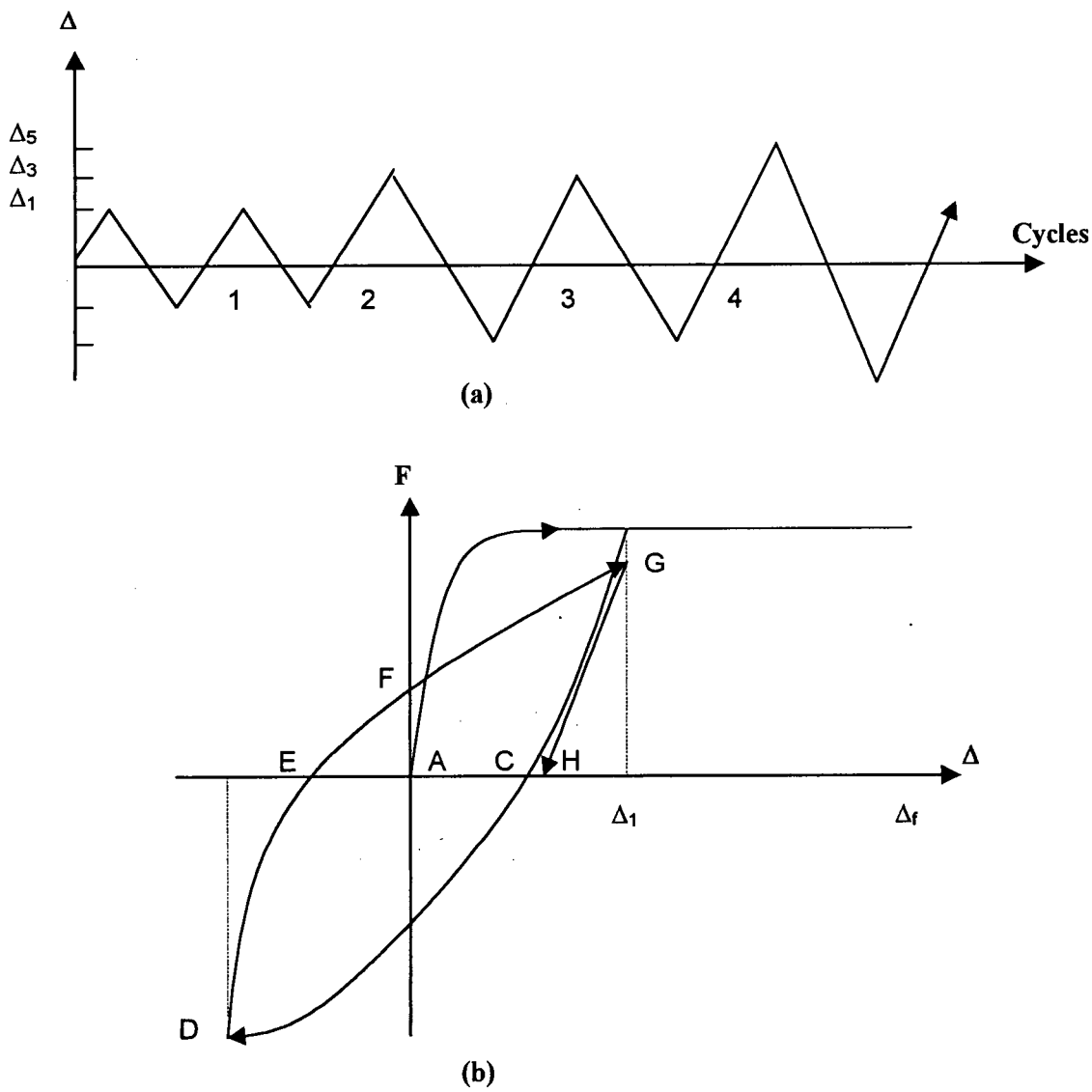

Figure 3.2: (a) Displacement-controlled cyclic loading (b) force-displacement response

loading are different than the virgin state. As shown in Figure 3.3a, the column has permanent deformation (plastic deformation Δ_{p1}) and stiffness, K_1, that is smaller than the initial stiffness, K_o, and a reduction in the strength, δ_{str1}.

In case the cycle stops at point E (Figure 3.2), which might happen during earthquake loading, point E will be the starting point to load the column monotonically after cycling. The monotonic loading will be toward point D (negative direction).

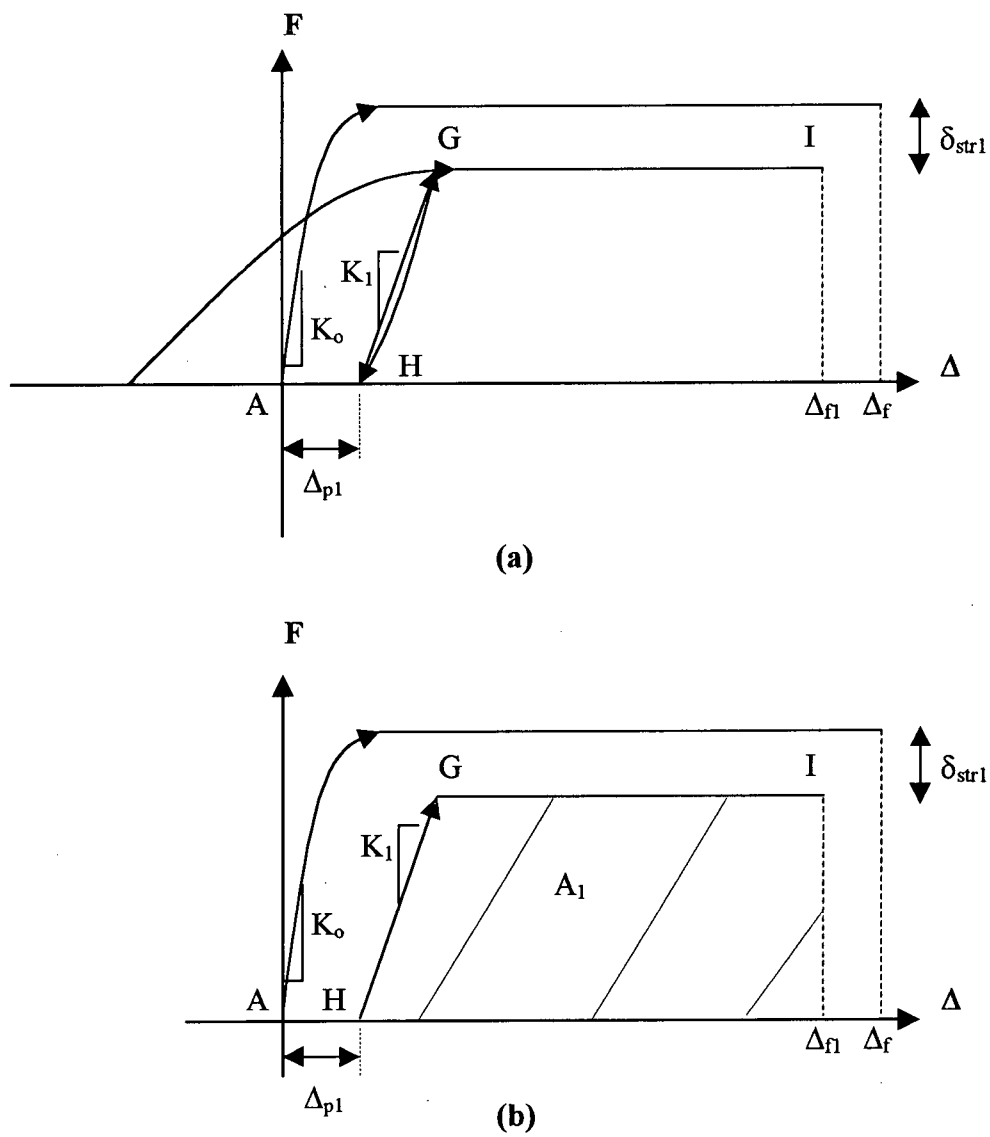

Figure 3.3: (a) Degraded column properties and (b) degraded monotonic energy.

To start monotonic loading from point H, assume that the new stiffness is the slope K_1 that connects point H and G as shown in Figure 3.3a. Figure 3.3b shows the energy needed to damage the column completely if it is loaded from point H. The new stiffness is K_1, the capacity is reduced by δ_{str1}, and the ultimate displacement is Δ_{f1}, which is less than the ultimate displacement, Δ_f, of the virgin state. This reduction in the ultimate displacement depends on the damage due to low-cycle accumulation as discussed later in section 3.4. Based on these new values, the energy to damage the column now is the area A_1 under the curve HGI as shown in Figure 3.3b, while A_o was the energy needed to damage the virgin state completely. Therefore, according to Equation 3-1, the damage that the column experienced until this point of loading is D_1 and equals to:

$$D_1 = \frac{(A_o - A_1)}{A_o} \tag{3-1}$$

The damage D_1 is calculated at point H, but it has already occurred in the column at the end of the first displacement cycle prior to point F.

As derived above, the proposed damage model takes into account all the parameters in the hysteretic behavior; stiffness degradation, strength deterioration, and ultimate displacement reduction due to low-cycle accumulation at the longitudinal reinforcement. The complete damage occurs at D=1.0 when A_n=0 as shown in Equation 3-1.

Figure 3.4 shows two cases where the damage reaches a value of 1.0 at the end of loading. Case a represents a state when the column is loaded monotonically to failure at point E, where it lost all the strength capacity; therefore, if the column is loaded now from point E, the degraded monotonic energy is A_n and is equal to zero because the loading path will follow the Δ-axis. This leads to a damage, D, of 1.0 according to Equation 3-1. Case b describes a state where the column is loaded cyclically, under constant displacement amplitude, n cycles until it fails and losses all the capacity at point E. Loading the column now monotonically from this complete failure point (E) results in a degraded energy, A_n, of zero value because the loading path will also follow the Δ–axis.

The damage is calculated at any cycle n by loading the column monotonically from its permanent deformed position (zero force) until it fails, taking into account stiffness degradation, strength deterioration, and ultimate displacement reduction due to low-cycle accumulated damage at the longitudinal reinforcement.

When the above is done analytically, it provides a damage model that can be used as a partial measure of consequences of a load history to a structural element, and of remaining capacity of a structural element.

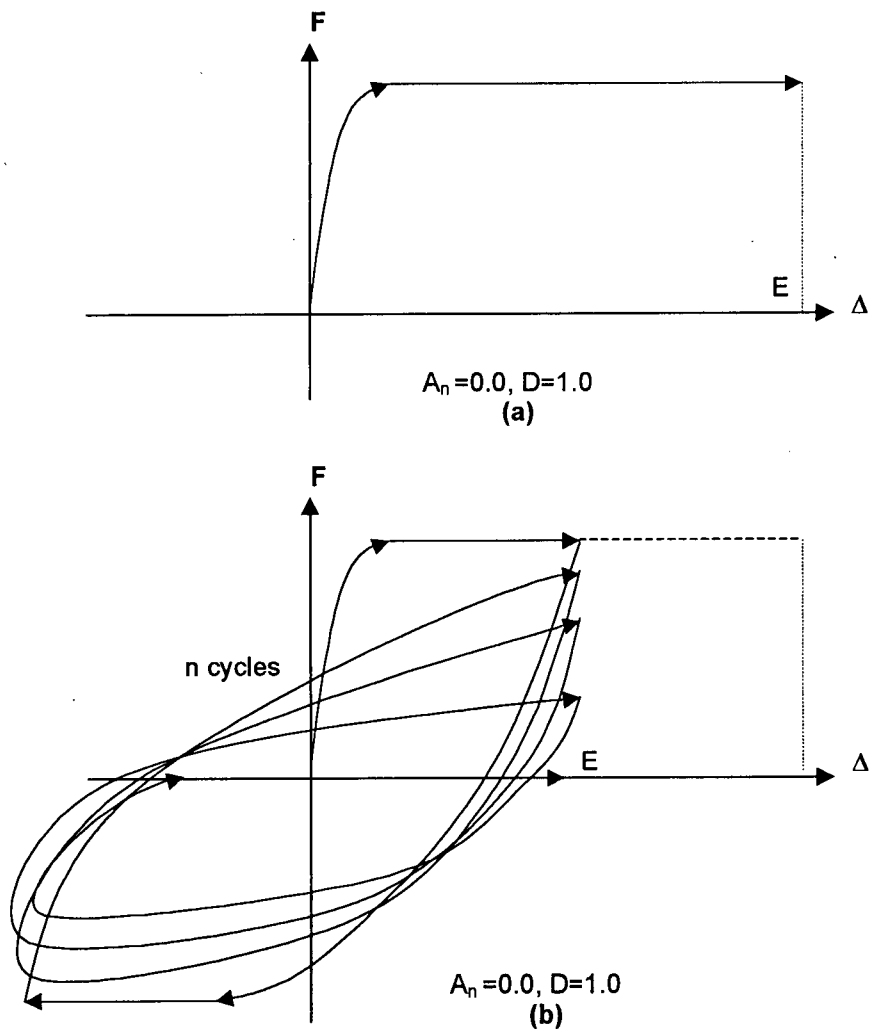

Figure 3.4: (a) Monotonic loading to failure (b) cyclic loading (n cycles) to failure.

3.2 MONOTONIC MOMENT-CURVATURE RESPONSE

The monotonic force-displacement behavior to failure for the virgin state of a reinforced concrete column is needed to predict the damage as discussed in the previous section, which mainly depends on the moment-curvature distribution along the height of the column. Layers analysis theory is adopted herein to predict the monotonic moment-curvature response of a section, following Bernoulli's assumption where plane sections remain plane, thus the strain at any fiber, as shown in Figure 3.5, is given by:

$$\varepsilon = \varepsilon_o + \phi(y_o - y) \tag{3-2}$$

Where: ε_o = Strain at the centroid at ordinate y_o

y = Ordinate from the bottom fiber

ε = Strain at any ordinate y

ϕ = Section's curvature

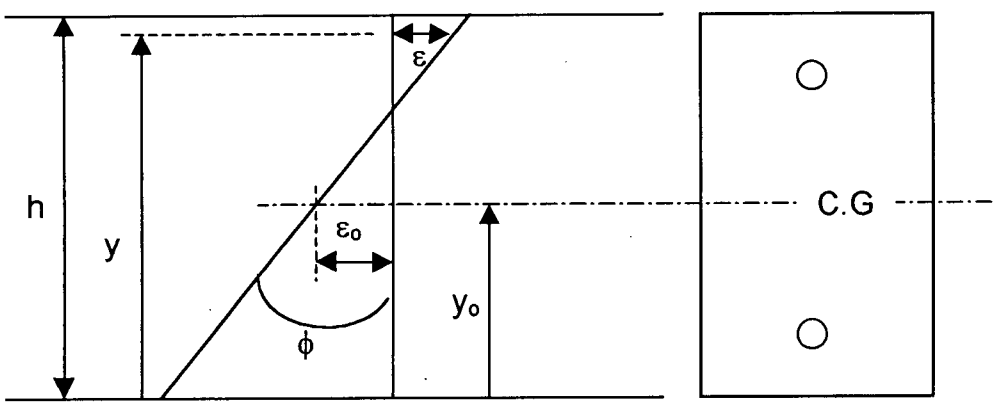

Figure 3.5: Strain distribution.

The column cross section is divided into concrete layers, steel rebars layers, and prestressing layers if any. At each curvature level, the strain at the centroid is assumed depending on the initial axial load, then the strain in each layer is calculated from Equation 3-2 and assuming no bond slip to occur. A corresponding stress at each layer is obtained using adopted constitutive material models as described later, then integrating over the entire section to predict the axial force and the bending moment, and iterating the above by changing the strain at the centroid until equilibrium is satisfied. Complete

moment-curvature response can be generated using the above layers analysis method. Concrete crushing or longitudinal steel rupture will stop the analysis and determine the curvature at failure (ultimate curvature, ϕ_{ult}).

A complete monotonic stress-strain model for concrete by Chang and Mander (1994) is adopted herein. The concrete model is based on Tsai's equation:

$$y = \frac{nx}{1 + \left(n - \frac{r}{r-1}\right)x + \frac{x^r}{r-1}} \tag{3-3}$$

Where $x = \varepsilon_c/\varepsilon'_c$, $y = f_c/f'_c$, n and r are parameters to control the shape of the curve and they are defined by Chang and Mander (1994). A comprehensive review of existing concrete models can be found in Chang and Mander (1994). Equation 3-3 can be used for both confined and unconfined concrete, as the parameters r and n shift the descending branch either upward or downward. Figure 3.6 shows a plot of different concrete strengths using the Chang and Mander concrete model. The concrete of the section is treated as confined and/or unconfined, concrete covers are treated as unconfined concrete while the core of the section is treated as confined concrete. The confinement model proposed by Mander et al. (1988) is adopted herein, as it is a generalized model that is applicable to all section shapes. The Mander confinement model has control on the strength, ductility, and on the descending branch of the curve as shown in Figure 3.6.

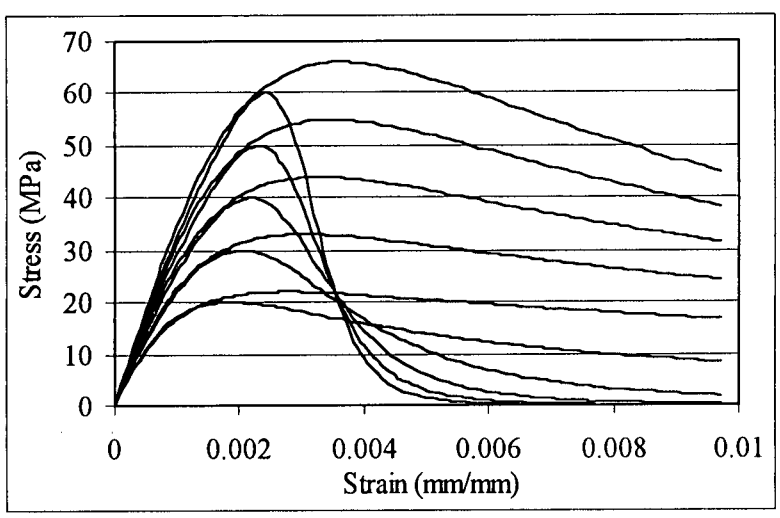

Figure 3.6: Concrete stress-strain relationship (Chang and Mander, 1994)

A simple bilinear stress-strain model is adopted for the steel reinforcement since ignoring the strain hardening is considered conservative. This is considered to be a reasonable assumption since the strain hardening starts to kick in at a strain ductility of about 5.0 which can be reached by just a very few cycles in a seismic event.

The moment-curvature response is then approximated to a bilinear envelope for simplicity. The approximation is done following the procedure suggested by Park and Paulay (1975) as shown in Figure 3.7. The yield capacity, M_y, is estimated as a percentage of the ultimate capacity, M_{ult}, depending on the concavity of the original moment-curvature envelope. Then the yield curvature, ϕ_y, is estimated as the curvature corresponding to (1/0.75) of the elastic curvature corresponding to 0.75 M_y, as shown in Figure 3.7.

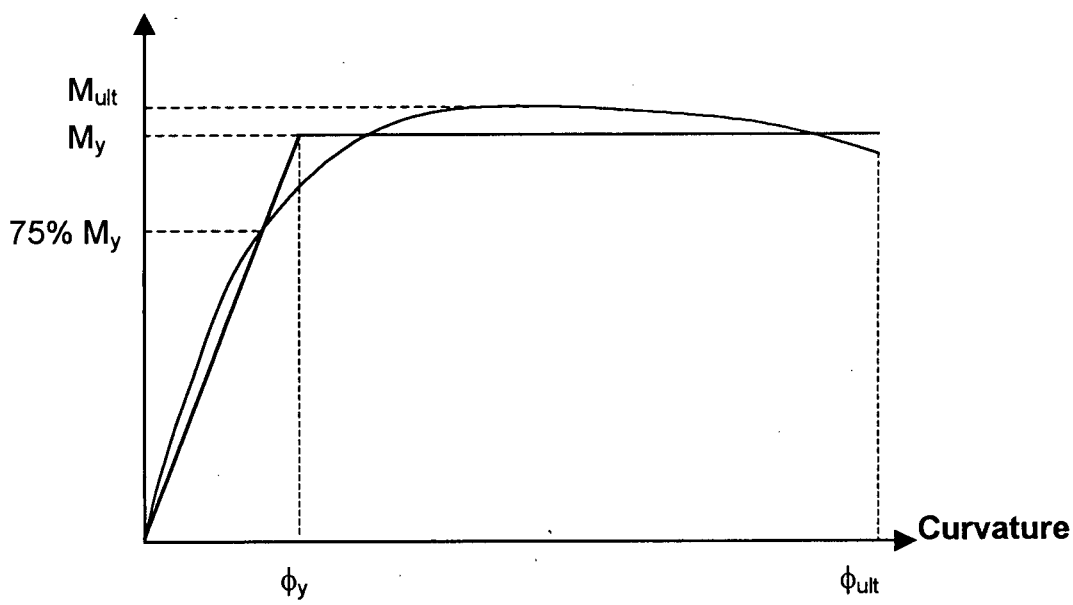

Figure 3.7: Bilinear moment-curvature approximation (Park and Paulay, 1975)

After defining the bilinear approximation, we take the ultimate moment (M_{ult}) as equal to the yield moment (M_y). The yield curvature, ϕ_y, and the ultimate curvature, ϕ_{ult}, can be found now from the approximated bilinear moment-curvature response as shown in Figure 3.7. These values will be used in integrating the curvature over the height of the column to calculate the displacement.

3.3 FORCE-DISPLACEMENT ANALYSIS

3.3.1 Displacement

The following shows a methodology adopted here to assess the displacement of a column. The total displacement, Δ, is assumed to be expressed in terms of various components as:

$$\Delta = \Delta_e + \Delta_p + \Delta_{se} + \Delta_b, \tag{3-4}$$

where; Δ_e = elastic flexural displacement

Δ_p = plastic flexural displacement

Δ_{se} = elastic shear displacement

Δ_b = bond slip displacement.

The following describes each of these displacement components to predict the monotonic force-displacement response:

3.3.1.1 Flexure deformation

By taking first moment of the curvature distribution along the column, the elastic flexural displacement can be calculated as:

$$\Delta_e = \phi_y \frac{L^2}{3} \tag{3-5}$$

where ϕ_y is the yield curvature.

The magnitude of the plastic curvature at the critical section is shown in Figure 3.8 and is given by:

$$\phi_p = \phi - \phi_y \tag{3-6}$$

If the plastic hinge length is defined as L_p, an expression for the plastic flexural displacement in terms of plastic curvature can be established (Paulay and Priestley, 1992) assuming that plastic rotation takes place about the center of the plastic hinge (Figure 2.6).

$$\Delta_p = \phi_p L_p (L - L_p / 2) \tag{3-7}$$

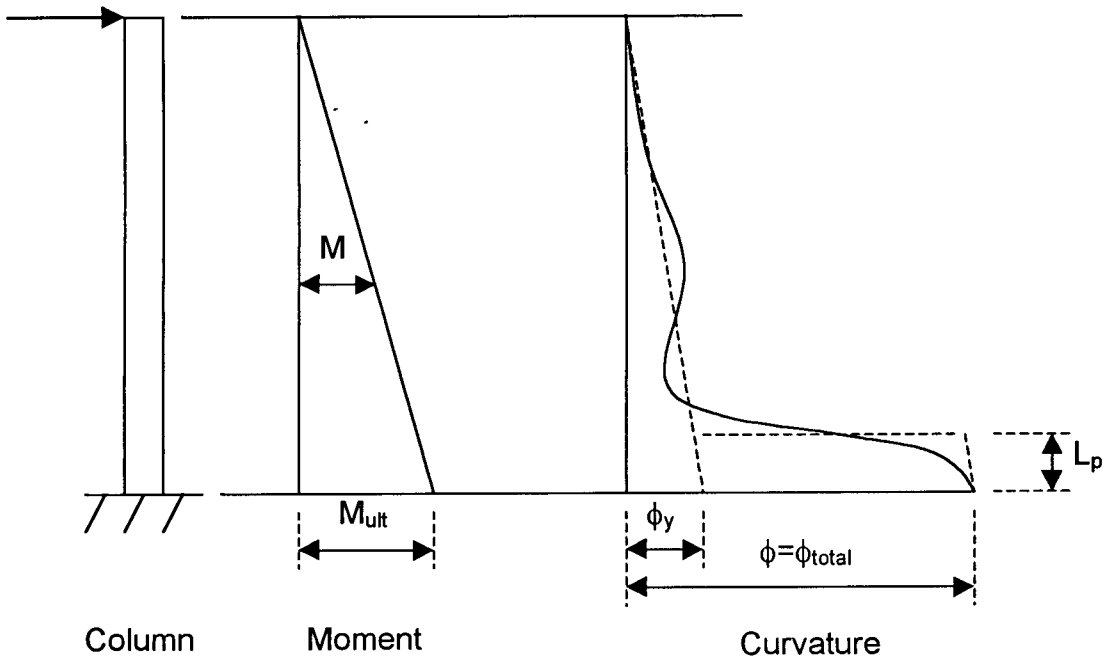

Figure 3.8: Moment and curvature distribution.

where the equivalent plastic hinge length, L_p, can be estimated as suggested by Paulay and Priestley (1992),

$$L_p = 0.08L + 4400\varepsilon_y d_b \tag{3-8}$$

L is the length of the column in millimeters (from the maximum moment to the inflection point), ε_y is the yield strain of steel = 0.002, and d_b is the bar diameter in millimeters.

3.3.1.2 Shear deformation

Elastic shear deformations for uncracked and cracked zones of the column, as shown in Figure 3.9, are calculated using the procedure suggested by Park and Paulay (1975). Prior to cracking the shear deformation can be computed as:

$$\Delta_{se} = \frac{VL}{K_{vun}} \tag{3-9}$$

Where V is the applied shear and K_{vun} is the uncracked shear stiffness as given by:

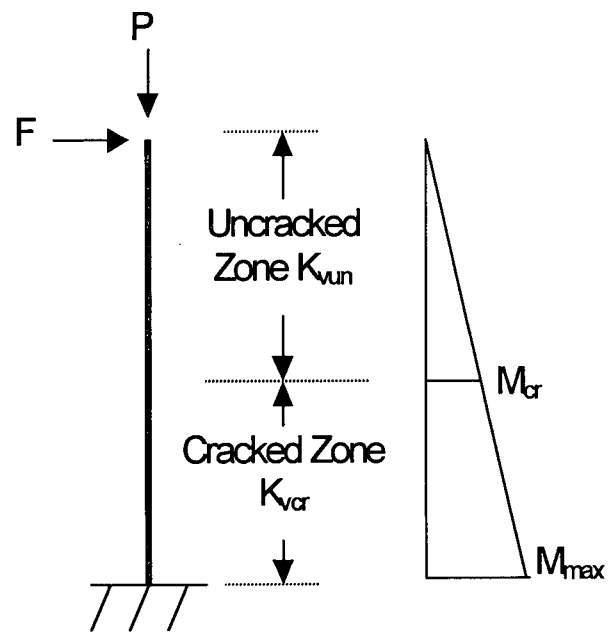

Figure 3.9: Elastic shear stiffness of a column

$$K_{vun} = \frac{0.4E_c A_g}{f} \tag{3-10}$$

When cracking exists over a portion of the column, the elastic shear deformation can be calculated following the truss action as:

$$\Delta_{se} = VL\left(\frac{1}{K_{vun}}\frac{M_{cr}}{M_{\max}} + \frac{1}{K_{vcr}}\left(1 - \frac{M_{cr}}{M_{\max}}\right)\right) \tag{3-11}$$

where M_{cr} is the cracking moment and K_{vcr} is the post-cracking shear stiffness. The post-cracking elastic shear stiffness is related to the inclination of the cracks, which is assumed 45°, and is calculated by the expression given by Park and Paulay (1975):

$$K_{vcr} = \frac{b_w d}{\frac{1}{E_s \rho_v} + \frac{4}{E_c}} \tag{3-12}$$

Where ρ_v is the web steel content = A_v/sb_w.

3.3.1.3 Bond slip deformation

Figure 3.10 shows the relation between the bond slip, S, and the deformation, Δ_b, assuming that deformation of concrete in the anchorage zone is negligible (Park and Ang, 1985):

$$\Delta_b = \frac{SL}{z} \tag{3-13}$$

Where L is the column length. S value was suggested by Park and Ang (1985) based on pullout tests by others.

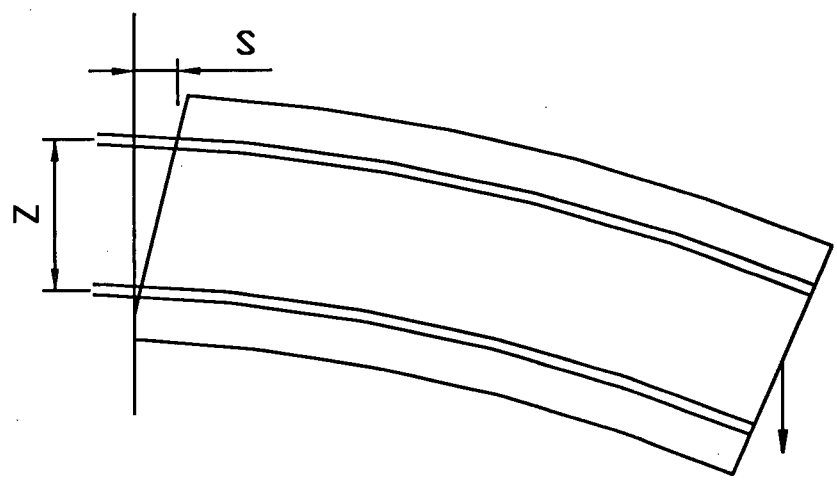

Figure 3.10: Bond slip deformation (Park and Ang, 1985)

3.3.2 Shear Force

The maximum shear force, F, is determined by dividing the moment, as shown in the approximated bilinear moment-curvature analysis in the previous subsection, by the height of the column (the length from the maximum bending moment to the inflection point),

$$F = \frac{M_y}{L} \tag{3-14}$$

Shear capacity can limit the ductility of a reinforced concrete column and may cause the column to fail prematurely before its flexural capacity is achieved. This will occur if the shear demand on a column exceeds its shear capacity. Many different models are available to predict the shear capacity of a reinforced concrete column.

The following traditional method is most often used to estimate the shear capacity (V), which is the sum of the shear capacities provided by concrete (V_c) and steel (V_s) as follows,

$$V = V_c + V_s \tag{3-15}$$

The above simplified method is used extensively by design engineers and forms the basis for the initial shear capacity referred to ATC-6-2 Code Criteria (Applied Technology Council, 1983), which is also included in the Canadian Concrete Code (CSA-A23.3, 1994) and the ACI-318 Code (American Concrete Institute, 1989). This method uses a 45 degree truss model to calculate the contribution of the transverse reinforcement as follows,

$$V_s = \frac{A_v f_{yh} d_s}{s} \qquad \text{tied columns} \tag{3-16a}$$

$$V_s = \frac{\pi}{2}\frac{A_b f_{yh} D'}{s} \qquad \text{columns with spiral or hoops} \tag{3-16b}$$

Where s is the spacing of stirrups or hoops, A_v the total area of transverse reinforcement, A_b the area of one leg of the spiral or hoops, f_{yh} the yield strength of the steel, d_s the effective depth, and D′ the core dimension from center to center of transverse reinforcement.

The contribution of concrete (V_c) is equal to the shear required to cause diagonal cracking. For bridge columns that usually have reasonable amount of longitudinal reinforcement, are under a compression axial force, and have minimum transverse reinforcement, the following is a simple formula for the concrete contribution as given by the ACI 318,

$$V_c = 0.17\left(1 + \frac{P}{13.8A_g}\right)\sqrt{f'_c}\, b_w d \qquad \text{(MPa units)} \tag{3-17}$$

Where P is the axial compression force applied to the column and A_g is the gross area of the column's cross section. Units of Equation 3-17 are Newton and millimeter.

Several methods are available to predict the shear and ductility capacity of columns at failure. These methods are conservative because they are mainly for design. The Applied Technology Council, for example, has set out guidelines for the shear resistance of reinforced concrete columns under seismic loading. It recommends that the column's shear capacity degrades with increases of the plastic displacement. In the ATC-6-2 model, the shear capacity of the column is degraded from its initial value as given by Equation 3-15 to a final value (V_f) that is equal to the contribution of the transverse reinforcement only, V_s, at a ductility level of 5.0 as shown in Figure 3.11.

Priestley et al. (1994b) found that the above approach and many other approaches for shear strength do not provide a particularly good estimate of the shear strength of columns. For low-ductility levels, the approach tends to be excessively conservative, while the degree of conservatism decreases with increasing ductility. Priestley et al. (1994b) proposed the following shear strength for columns,

$$V = V_c + V_s + V_p \tag{3-18}$$

where

$$V_c = k\sqrt{f'_c}A_e \tag{3-19}$$

$A_e = 0.8A_{gross}$, and k, with plastic end region, depends on the member displacement ductility μ, reducing from 0.29 MPa for $\mu \leq 2$ to 0.05 MPa for $\mu \geq 8$, as shown in Figure 3.12.

The truss mechanism strength of transverse reinforcement is given by

$$V_s = \frac{A_v f_{yh} d_s}{s}\cot\theta \qquad \text{for tied columns} \tag{3-20a}$$

$$V_s = \frac{\pi}{2}\frac{A_b f_{yh} D'}{s}\cot\theta \qquad \text{for columns with spiral or hoops} \tag{3-20b}$$

where D′ is the core dimension from center to center of transverse reinforcement as shown in Figure 3.13. The angle of the critical inclined flexure shear cracking to the column axis is taken as $\theta = 30^\circ$ as recommended by Priestley et al. (1996). The development of steeper angles of cracking than $\theta = 45^\circ$ assumed is well supported by experimental results (Priestely et al., 1996).

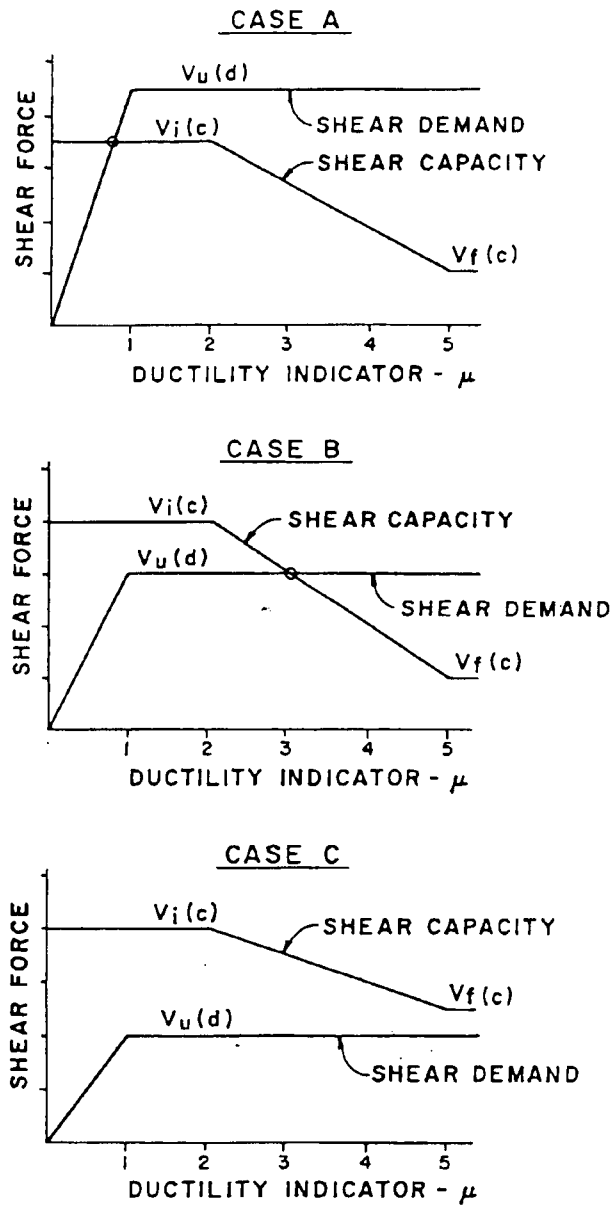

Figure 3.11: Resolution of shear demand and capacity (ATC-6-2, 1983)

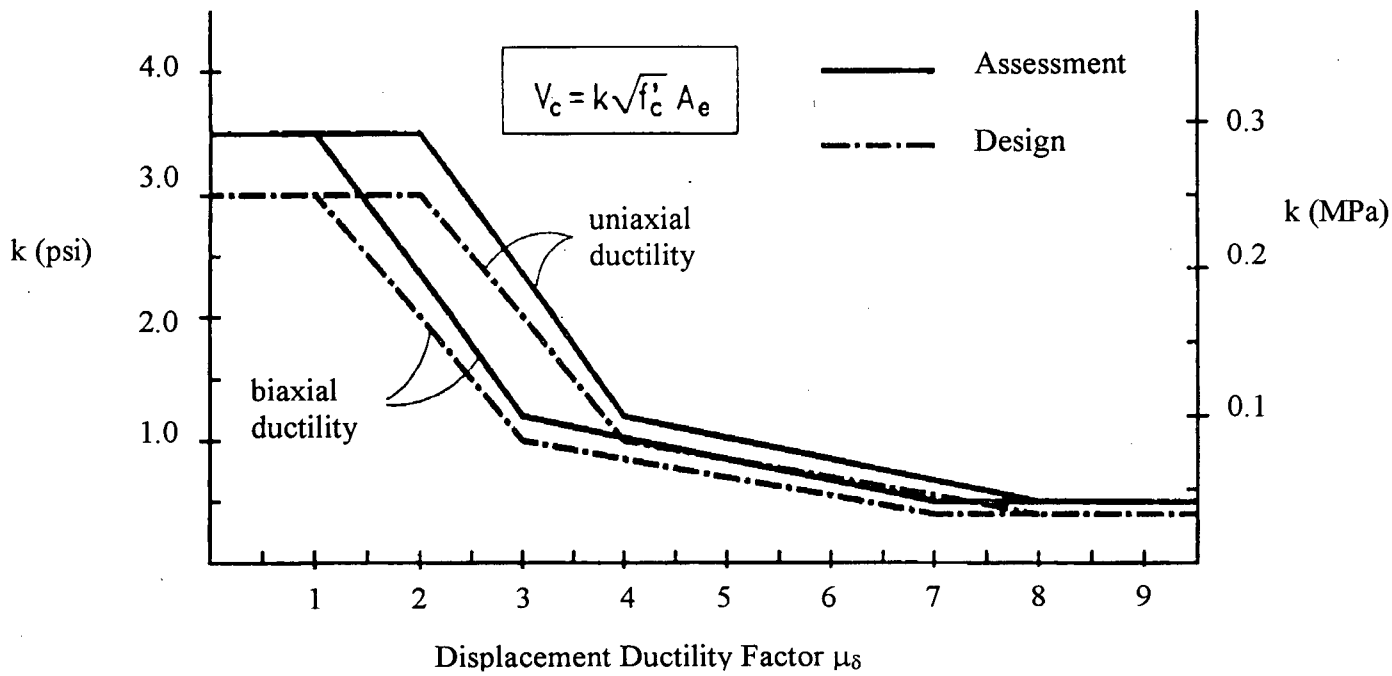

Figure 3.12: Shear strength of concrete (Priestley et al., 1994a)

The shear strength enhancement resulting from axial compression is considered as an independent component of shear strength, resulting from a diagonal compression strut, as shown in Figure 3.14, given by

$$V_p = P\tan\alpha \tag{3-21}$$

For a cantilever bridge column, α is the angle formed between the column axis and the strut from the point of axial load application to the center of the flexural compression zone at the column plastic hinge as shown in Figure 3.14(b).

In this study the Priestley approach is adopted to estimate the shear capacity. This is considered acceptable since the ATC-6-2 is conservative for assessment purposes like most available shear prediction methods.

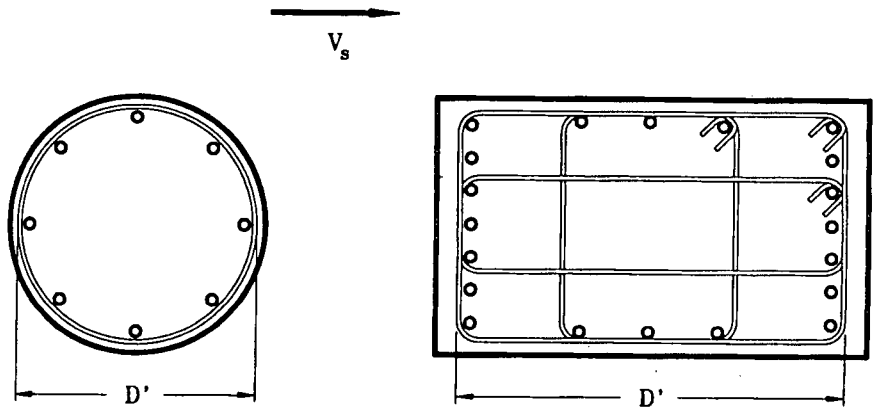

Figure 3.13: Definition of D′ for truss-mechanism strength (Priestley et al., 1996)

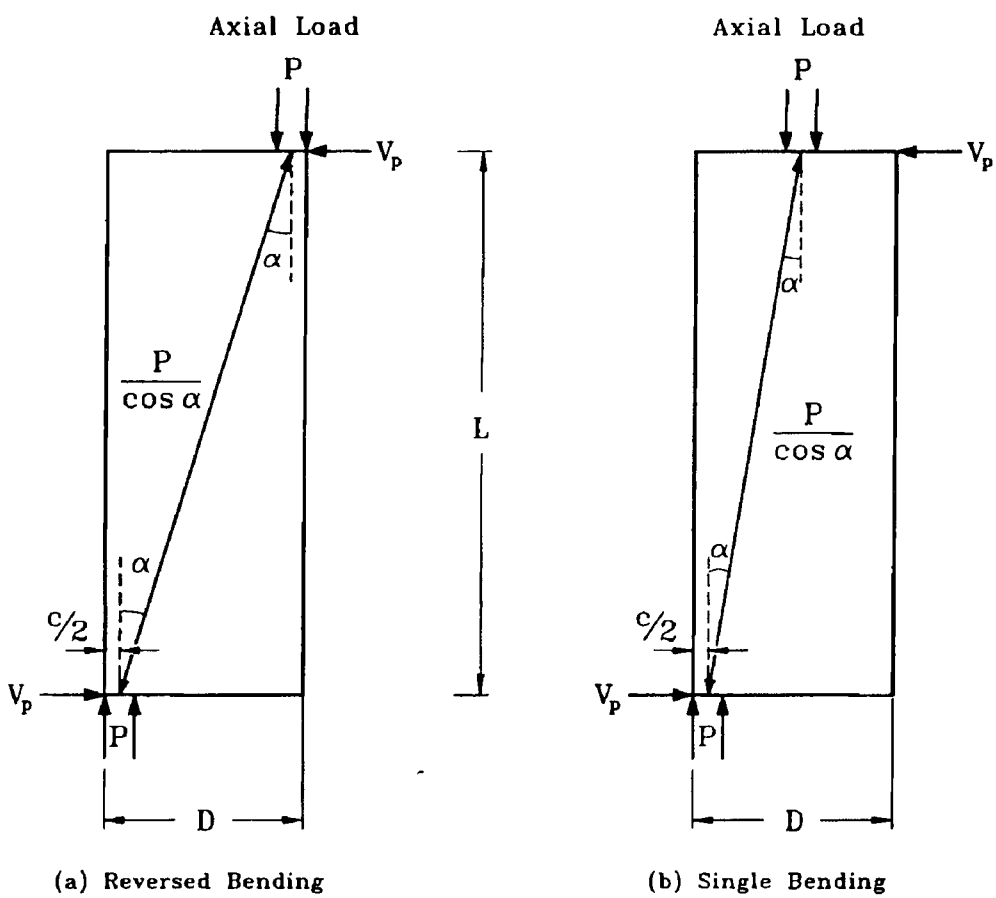

Figure 3.14: Contribution of axial force to column shear strength (Priestley et al., 1994b)

3.4 LOW-CYCLE ACCUMULATION

Since seismic loads induce several inelastic cycles at high ductility demands, the longitudinal reinforcement will experience strains beyond the yielding level. Such a case will expose the reinforcement to low-cycle accumulated damage due to repeated plastic strains. The amplitude of induced plastic strains at the longitudinal reinforcement and the number of cycles of each plastic strain level control the low-cycle accumulated damage.

According to Miner's rule (Miner, 1945), the low-cycle accumulated damage can be written as,

$$D_{low-cycle} = \sum_{i}^{n} \frac{1}{(2N_f)_i} \tag{3-22}$$

The low-cycle damage model by Mander and Cheng (1995) (Equations 2-11 to 2-15) in Chapter Two, as developed by Kunnath et al. (1997), is adopted herein to calculate the total number of complete cycles, $2N_f$, due to specified plastic strain amplitude, ε_p, and the low-cycle accumulated damage at the longitudinal reinforcement. They related local section curvature at the plastic hinge region directly to the strain in the longitudinal reinforcement (see derivation in Chapter Two).

Investigators have tested reinforced concrete columns under different number of cycles and different levels of plastic strain. After cyclically testing the columns, they were pushed monotonically to complete failure. It was concluded that the cyclic loading has no effect on the ultimate displacement. But most of these tests (i.e. by Kunnath et al., 1997) were under a low plastic strain level that produced a low damage according to the above formulation.

It is assumed in the proposed damage model that cycling will reduce the ultimate displacement. This would be the case when large plastic strains occur in some of the loading cycles. By increasing the plastic strain level we reduce the number of cycles to failure and; therefore, the ultimate displacement will be lower than that achieved by monotonic loading. The proposed model modifies the ultimate displacement of the

column to failure Δ_f after each cycle due to low-cycle accumulated damage at the longitudinal reinforcement.

The following criterion is proposed to calculate the reduction in the ultimate displacement based on the low-cycle accumulated damage as given in Equation 3-22. FD is the reduction factor after reversal cyclic loading and is assumed to vary with the number of cycles applied to the column and the plastic strain level, ε_p, that controls the number of complete cycles to failure, $2N_f$,

$$FD_n = \left[1 - \sum_i^n \frac{1}{(2N_f)_i}\right]^C \tag{3-23}$$

Where the number of complete cycles to low-cycle failure at the longitudinal reinforcement, $2N_f$, at any plastic strain amplitude, ε_p, is calculated using the procedure developed by Mander and Cheng (1995) as mentioned above. It was observed that the damage increases rapidly at the end of the cycles due to low-cycle accumulated damage; therefore, C is assumed to be 0.5 to represent the rapid increase in the low-cycle accumulated damage as the number of cycles increases.

The following equation is proposed to predict the modified ultimate displacement after n cycles.

$$\Delta_{fn} = FD_n R_n + P_n \tag{3-24}$$

For example, after one cycle of loading, Equation 3-25 shows the modified ultimate displacement.

$$\Delta_{f1} = FD_1 R_1 + P_1 \tag{3-25}$$

Where, R_1 and P_1 are shown in Figure 3.15.

Then by accumulating the effect of all cycles at different levels of plastic strain, we can calculate the modified ultimate displacement after a complete reversal cyclic loading.

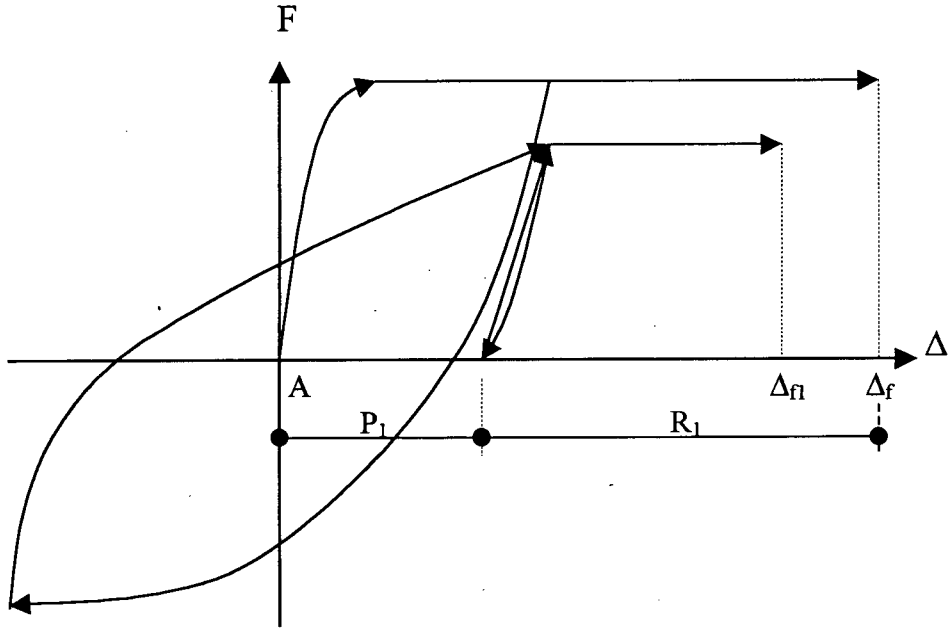

Figure 3.15: Reduction in ultimate displacement

CHAPTER FOUR

APPLICATIONS TO TESTED COLUMNS

A comparison between the proposed model, the Park and Ang damage index by Park and Ang (1985), and the low-cycle damage model by Mander and Cheng (1995) for six specimens of circular reinforced concrete columns that were tested by Kunnath et al. (1997), and six square columns that were tested by Adebar and Roux (1998) is presented in this chapter.

This chapter focuses on applying the proposed damage model to tested columns under reversed cyclic loading. This avoids all the parameters that have to be assumed for a real seismic event in order to examine the damage model under the control of the variables that formulate it. This limitation excludes the many complexities of dynamic behavior and the unsymmetry of real seismic loading. An application of the proposed model to real bridge columns under real seismic events is presented in Chapter 6.

This comparison is meant to cover as much as possible the different aspects that play a major role in the behavior of bridge columns, such as; shear action, flexure, confinement, axial load, stirrup spacing, number of cycles, and displacement amplitude. The chosen tests by Kunnath et al. (1997) and Adebar and Roux (1998) cover most of the above aspects. The loading scheme applied to the chosen tested columns consisted of a standard reversed cyclic loading. The displacement amplitude of the loading cycles is either constant or different from one cycle to another, and is controlled in the tests.

The first set of columns was tested by Kunnath et al. (1997). It includes six specimens of circular reinforced concrete bridge columns. These specimens are identical in everything except the loading, and they are flexure dominated tests, adequately designed for shear. An axial load of about $0.1f'_cA_g$ was applied to all the column specimens. The Kunnath test was done with the objective of studying seismic damage of bridge columns, and it is very well documented and observed. Kunnath et al. (1997) compared their observed tests with the Park and Ang model, a modified form of the softening index as suggested by Kunnath et al. (1997), the Kratzig model (Kratzig and Meskouris, 1987), and the low-cycle damage model

(Mander and Cheng, 1995). The comparison showed that the softening index is sensitive in the early stage of damage progression and showed little variation beyond this point to failure, making it difficult to calibrate. It was also concluded that the Kratzig model, which is an energy-based model and does not account for the level of ductility at which energy is dissipated, consistently over-predicted the damage. Therefore, the Kratzig model and the softening model are not considered in this comparison.

The second set of columns was tested by Adebar and Roux (1998) at the University of British Columbia. While the tests were not designed with damage computation in mind, they are ideal for this comparison since they provide simple, well defined cyclic loading with significant flexure and shear components, and they are well documented. Six rectangular specimens were tested with various combination of moment to shear ratio and stirrup spacing. The Adebar tests were also used by Williams et al. (1997) to evaluate several damage indices. It was concluded by Williams et al. (1997) that the damage for shear dominated columns is mainly dependent on the ductility level with a small effect of the number of cycles. The Park and Ang model is considered to be the more reliable damage model for the above conclusion.

The Park and Ang model (1985) and the low-cycle damage model by Mander and Cheng (1995) were selected to compare to the proposed damage model in order to examine it's ability in predicting damage during cycling loading. The Park and Ang (1985) model is the best known and most widely used damage index. This model consists of a simple linear combination of normalized deformation and energy absorption:

$$D = \frac{\delta_m}{\delta_u} + \frac{\beta_e \int dE}{F_y \delta_u} \tag{4-1}$$

Where δ_m is the maximum displacement reached in the loading, δ_u is the monotonic ultimate displacement, F_y is the yield force, $\int dE$ is the absorbed hysteretic energy, and β_e is an energy parameter.

The advantages of this model are its simplicity, and the fact that it has been calibrated against a significant amount of observed seismic damage. As indicated in Section 2.1, Park et al. (1987) suggested the following damage classification:

$D < 0.1$	No damage or localized minor cracking
$0.1 \leq D < 0.25$	Minor damage–light cracking throughout
$0.25 \leq D < 0.4$	Moderate damage–severe cracking, localized spalling
$0.4 \leq D < 1.0$	Severe damage–concrete crushing, reinforcement exposed
$D \geq 1.0$	Collapse

D = 0.4 was suggested by the same authors as a threshold value between repairable and irrepairable damage. The above damage classification will be referred to in the application and comparison in this chapter.

The Mander and Cheng model (1995) was derived from principles of low-cycle accumulated damage as discussed in Chapter 2 and it is logical since seismic loading induces several inelastic cycles at relatively large ductility demands. Other existing models are omitted from the comparison in this research because they are difficult to calibrate, and they failed to predict the damage and to show damage progression throughout the cycling, as concluded by others (i.e., Kunnath et al., 1997 and Williams et al., 1997).

In order to simplify the comparison between the selected existing models (the Park and Ang model and the low-cycle damage model by Mander and Cheng) and the proposed model, the following designations are made and they will be referred to in the remainder of this thesis:

E1	The Park and Ang damage model (1985).
E2	The low-cycle damage model by Mander and Cheng (1995).
P	The proposed damage model.

Where E stands for existing model and P stands for proposed model. However, the figures in the remainder of this thesis will show the full name of the models.

4.1 TESTS BY KUNNATH ET AL. (1997)

This section discusses the observed damage for six circular bridge piers tested by Kunnath et al. (1997), the predicted damage by E1, E2, and P models, and a comparison among them.

The damage was well documented by Kunnath et al. (1997) during the test. Table 4.1 summarizes the properties of the six specimens considered herein. The columns are identical in everything except the loading and slight differences in the materials properties. It is concluded from Table 4.1 that the Kunnath specimens can be classified in two sets of columns. First set includes columns A1, A2 and A3 and the second set includes A4, A5 and A6.

Theoretical monotonic force-displacement response was predicted for each of the two sets following the procedure discussed in Chapter 3. Figure 4.1 shows the predicted moment-curvature response for each set, accompanied by a bilinear approximation. Figure 4.2 summarizes the predicted force-displacement envelopes. The specimens were designed adequately for shear. Shear strength was checked following the procedure described in Chapter 3. Spiral shear strength, Vs, for both sets was calculated to be 218 kN, which is much higher than the shear demand as shown in Figure 4.2.

4.1.1 Specimen A1

Figure 4.3a shows a comparison between the experimental and theoretical monotonic behavior for specimen A1. Kunnath et al. (1997) tested specimen A1 monotonically until failure. It was found that the ultimate displacement at failure was 152 mm, and the maximum capacity reached was 66 kN. The complete failure was difficult to reach monotonically in this test due to the limitation of stroke capacity of the hydraulic actuator. Therefore, test stopped at this displacement level after the load capacity decreased significantly, on the order of 20-30%. The theoretical prediction, which is done using the layer analysis program as discussed in Chapter 3, of the monotonic force-displacement envelope agreed reasonably with the experiment as shown in Figure 4.3a. The failure in the theoretical response was due to fracture of the longitudinal reinforcements because of the limitation that was put on the strain to fracture the steel (fracture strain = 0.1). The predicted ultimate displacement is about 15% less than the observed value, a result of the low steel fracture strain used in the analysis compared to the tested one.

The predicted monotonic force-displacement envelope for each specimen was used for the damage analysis in order to calculate the energy needed to fail the column monotonically, A_o,

from the virgin state. However, the experimental monotonic ultimate displacement was used in the damage analysis instead of the predicted one.

Table 4.1: Summary of Kunnath et al. (1997) Tests.

Specimen	**A1**	**A2**	**A3**	**A4**	**A5**	**A6**
Diameter (mm)	305	305	305	305	305	305
Height (mm)	1372	1372	1372	1372	1372	1372
Cover (mm)	12.5	12.5	12.5	12.5	12.5	12.5
Long. Steel	21- # 3 (9.5 mm)	21- # 3 (9.5 mm)	21- # 3 (9.5 mm)	21- # 3 (9.5 mm)	21- # 3 (9.5 mm)	21- # 3 (9.5 mm)
f_y (Long. Steel) (MPa)	448	448	448	448	448	448
Spiral (Wire)	ϕ 4 mm	ϕ 4 mm	ϕ 4 mm	ϕ 4 mm	ϕ 4 mm	ϕ 4 mm
f_y (Spiral) (MPa)	434	434	434	434	434	434
Spiral Pitch (mm)	19	19	19	19	19	19
f'_c (MPa)	*29*	*29*	*29*	*35.5*	*35.5*	*35.5*
Axial Load (kN)	*200*	*200*	*200*	*222*	*222*	*222*
Maximum Displacement Level (mm)	*152*	*76*	*26*	*57*	*75*	*95*

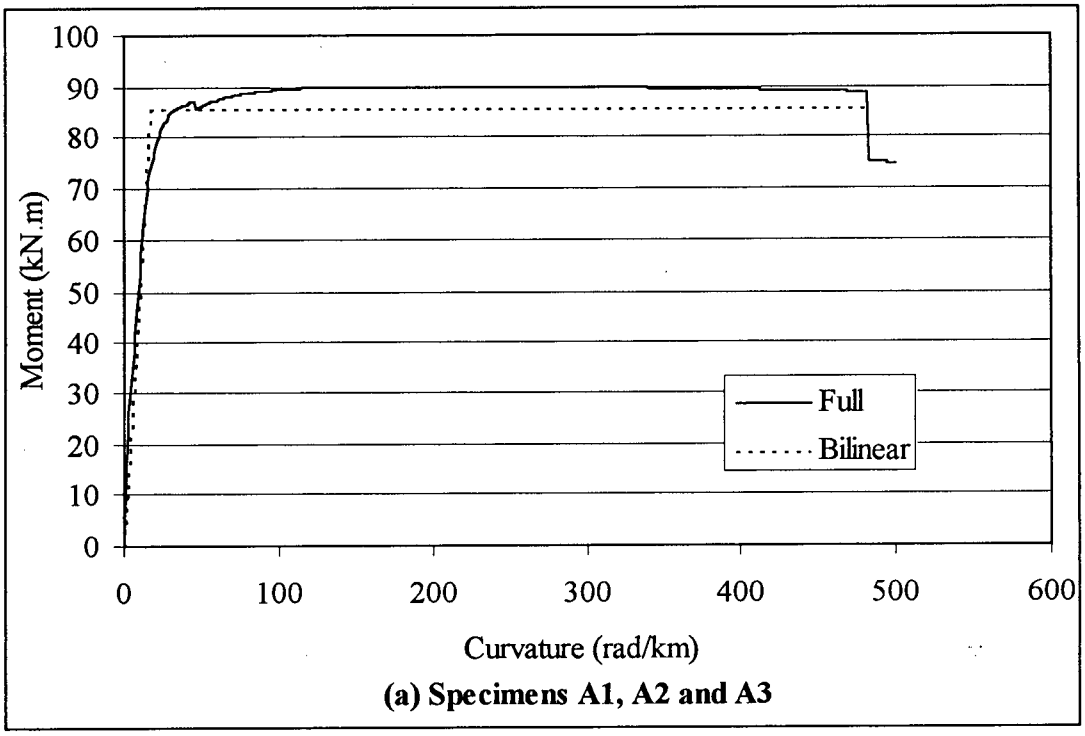

(a) Specimens A1, A2 and A3

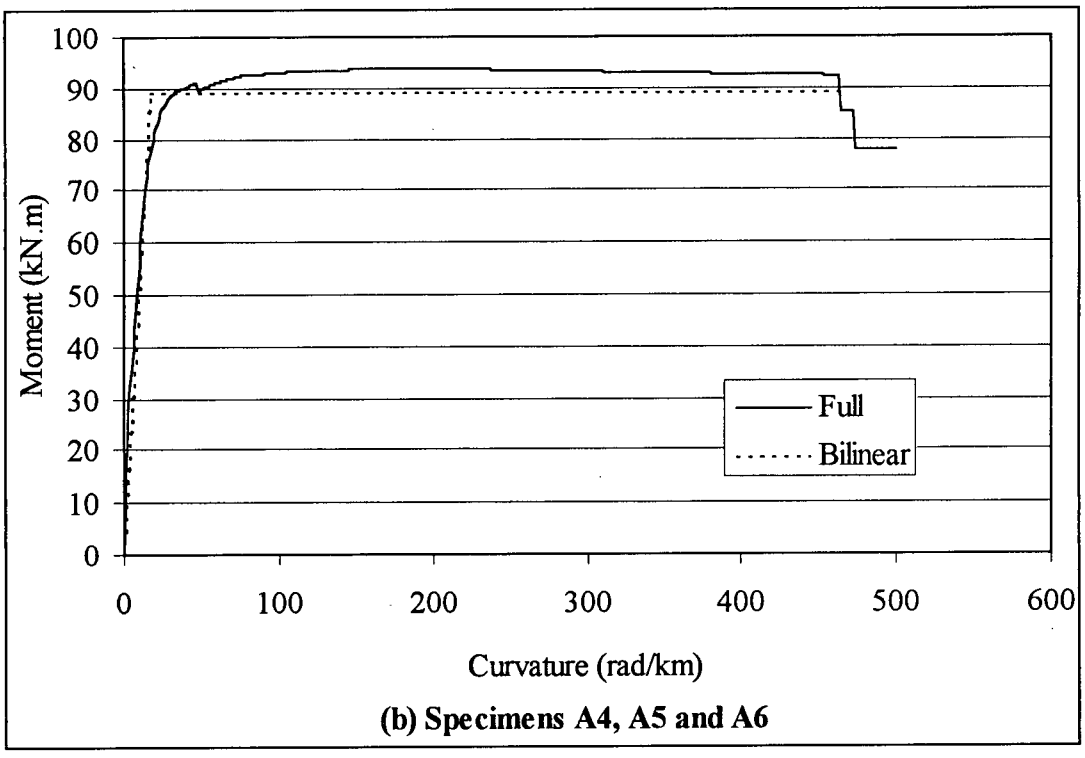

(b) Specimens A4, A5 and A6

Figure 4.1: Theoretical moment-curvature responses.

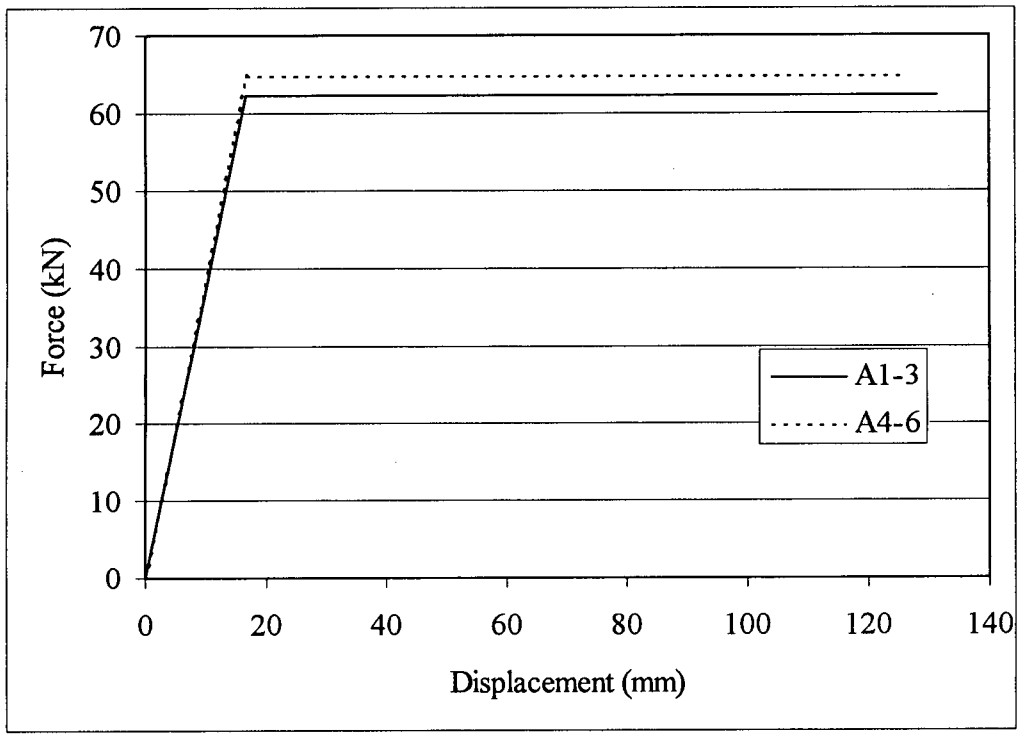

Figure 4.2: Predicted force-displacement envelopes.

Table 4.2: Observed damage for Specimen A1.

Cycle	Displacement (mm)	Comments
Monotonic	2.5-5.0	Very fine hair-line cracks
Monotonic	5.0	Cracks became significant
Monotonic	19	Yielding
Monotonic	33	Concrete cover spalling
Monotonic	60	Spalling became significant, signs of longitudinal bars buckling, significant strength deterioration
Monotonic	150	Failure

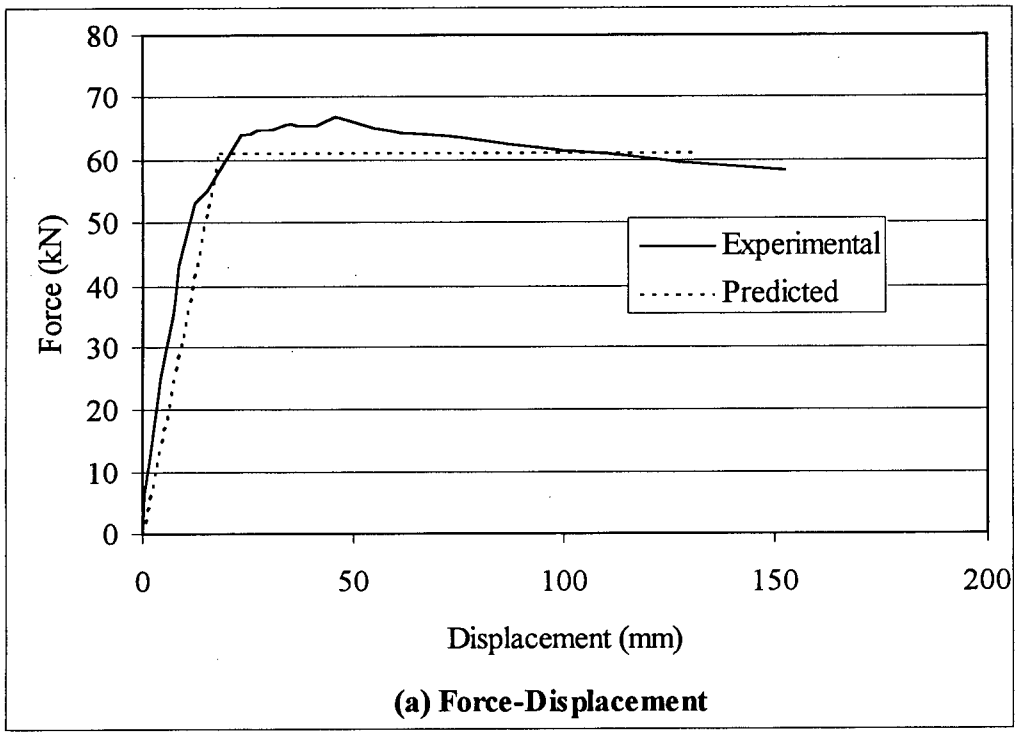

(a) Force-Displacement

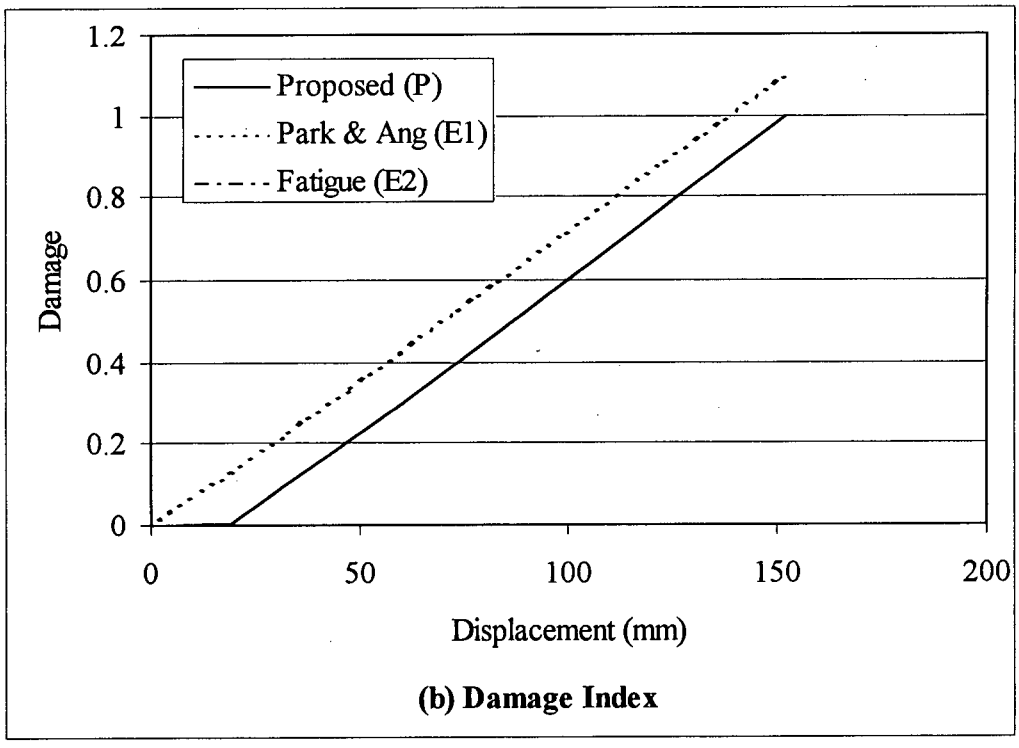

(b) Damage Index

Figure 4.3: Specimen A1.

Table 4.2 summarizes the observed damage. A value of 0.05 for the energy parameter, β_e, is assumed for E1 model as concluded from Kunnath et al. (1997). Figure 4.3b shows the predicted damage by E1, E2 and P models. As observed in the test, the damage at 33 mm displacement was initial spalling of the concrete cover. At a displacement of 60 mm the cover spalling became significant, and two longitudinal bars showed signs of buckling. The E1 model as shown in Figure 4.3b shows damage of more than 0.4, which would be irrepairable according to the damage classification given by Park et al. (1987) at 60 mm displacement. The damage classification and objectives suggested by Park et al. (1987), as stated in the beginning of this chapter, will be used here for the damage prediction by the E1 and P models. The P model predicted damage of 0.3 at this stage. At a displacement of 100 mm, the E1 model predicted severe damage of more than 0.7, while the test showed failure of the specimen at 152 mm of lateral displacement. At this level of displacement of 100 mm, the P model showed a damage of 0.6. At the end of the test, The E1 model gave damage of higher than 1.0 due to the energy term as shown in Equation 4-1, while the P model predicted damage of magnitude 1.0, which means complete failure. The E2 model is not suitable for this type of loading and gave no damage at all.

4.1.2 Specimen A2

This column was subjected to three cycles at each displacement amplitude as a function of lateral drift. Displacement amplitudes used in the testing consisted of three cycles each at 1.0% (14 mm), 1.5% (20 mm), 2% (28 mm), 2.5% (32 mm), 3.0% (40 mm), 4.0% (53 mm), 5.0% (65 mm), and 6.0% (76 mm). The smaller amplitude between each increase in amplitude was 0.5% drift. Table 4.3 summarizes the observed damage of this specimen.

Figure 4.4 shows the predicted damage. The E1 model showed a gradual progression of damage throughout the load history with increasing accumulation of damage at each increase in the displacement level. The E2 model showed little or no damage through the first 10 cycles where displacement ductilities are below 2. The E2 model suggested rapid deterioration of the specimen towards the end of the loading, while the damage is estimated to be in the repairable range after 24 cycles as shown in Figure 4.4. The actual observed damage was probably between the predictions of the E1 and E2 models (Kunnath et al., 1997). The P model as shown in Figure 4.4 predicted damage between the two existing

models E1 and E2, and appears reasonable with respect to the test observations, as shown in the photos in Figure 4.5 and in Table 4.3.

Table 4.3: Observed damage for Specimen A2.

Cycle	Displacement (mm)	Comments
1	2.5	Very fine hair-line cracks
1	5.0	Cracks became wider (0.2 mm)
10	28	Crack width almost 0.7 mm
13	32	Crack width almost 1.0 mm
15	32	Concrete cover spalling, significant cracking
19	40	Crack width almost 1.5 mm
22	65	Significant spalling, minor bar buckling
30	76	Failure of spiral, 180 mm plastic hinge length

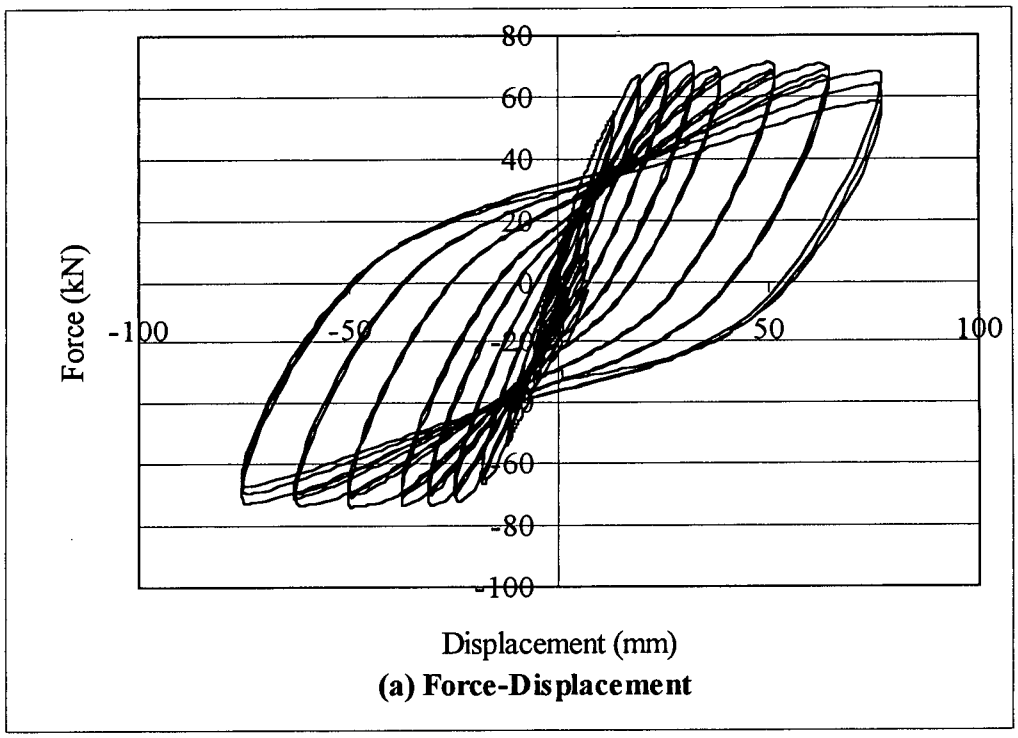

(a) Force-Displacement

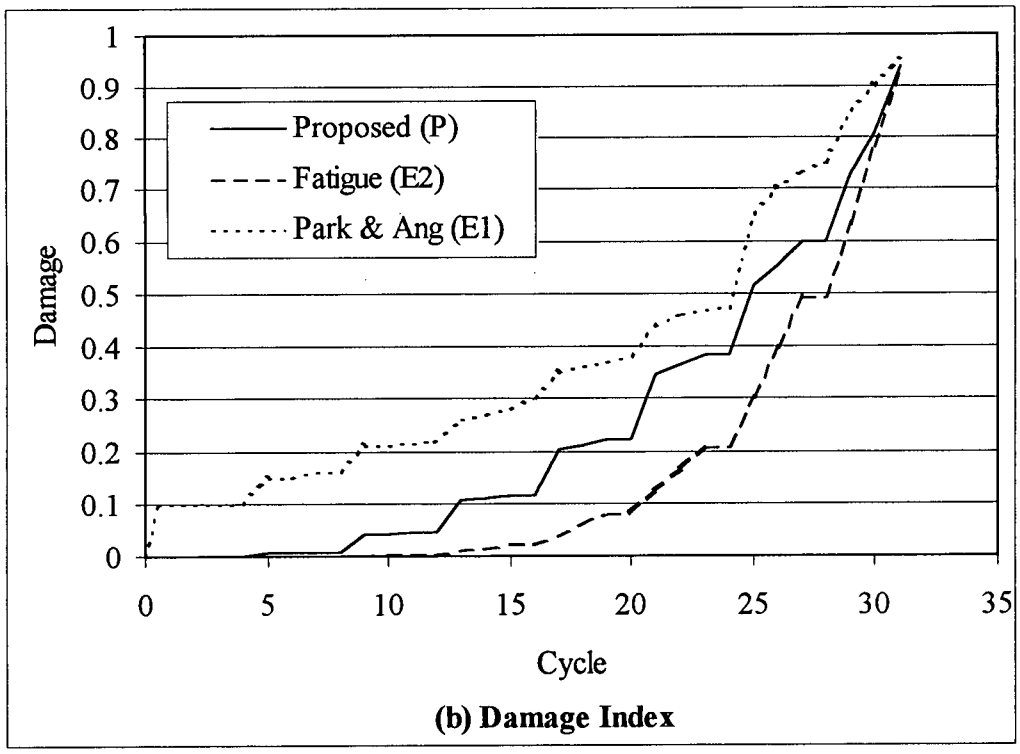

(b) Damage Index

Figure 4.4: Specimen A2.

(a) Displacement = 50 mm

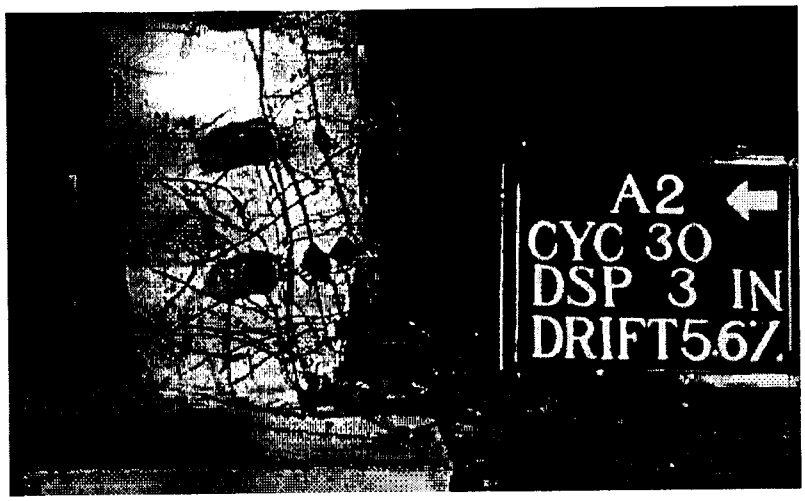

(b) Displacement = 75 mm

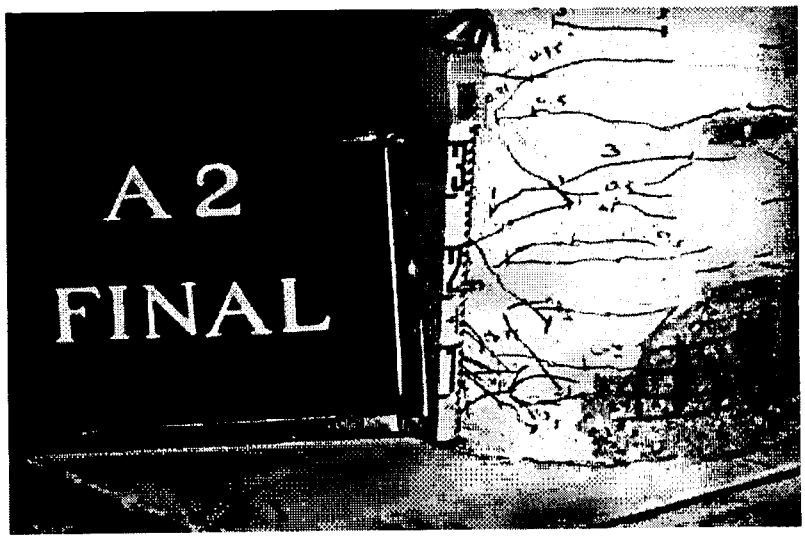

(c) Final

Figure 4.5: Damage to specimen A2 (Kunnath et al. 1997).

4.1.3 Specimen A3

This specimen was subjected to 150 cycles at a constant lateral drift of about 2.0% (26 mm) (Figure 4.6). Table 4.4 summarizes the test observations. The specimen sustained a final displacement of 155 mm after cycling as shown in Figure 4.6a. This suggested that the damage of the initial 150 cycles was negligible (Kunnath et al., 1997).

Table 4.4: Observed damage for Specimen A3.

Cycle	Displacement (mm)	Comments
1	26	Yielding, 0.5 mm crack width, minor spalling
3	26	0.8 mm crack width
19	26	No additional cracking and spalling
40	26	No further damage
95	26	Some loose concrete was picked off
150	26	No further damage, minor damage
Monotonic	155	Failure

Figure 4.6 shows the predicted damage. The E1 model failed to predict accurately the damage state of the specimen at the end of the 150 cycles. It gave a complete failure (D=1.0) at the end of 150 cycles, while these cycles produced only minor damage as observed (Kunnath et al., 1997). The E2 model performed better prediction compared to the test observation, while it gave almost no damage at the first few cycles as shown in Figure 4.6. The P model gave a damage of less than 0.5 after 150 cycles and showed good prediction of damage at all stages of loading compared to the observed damage.

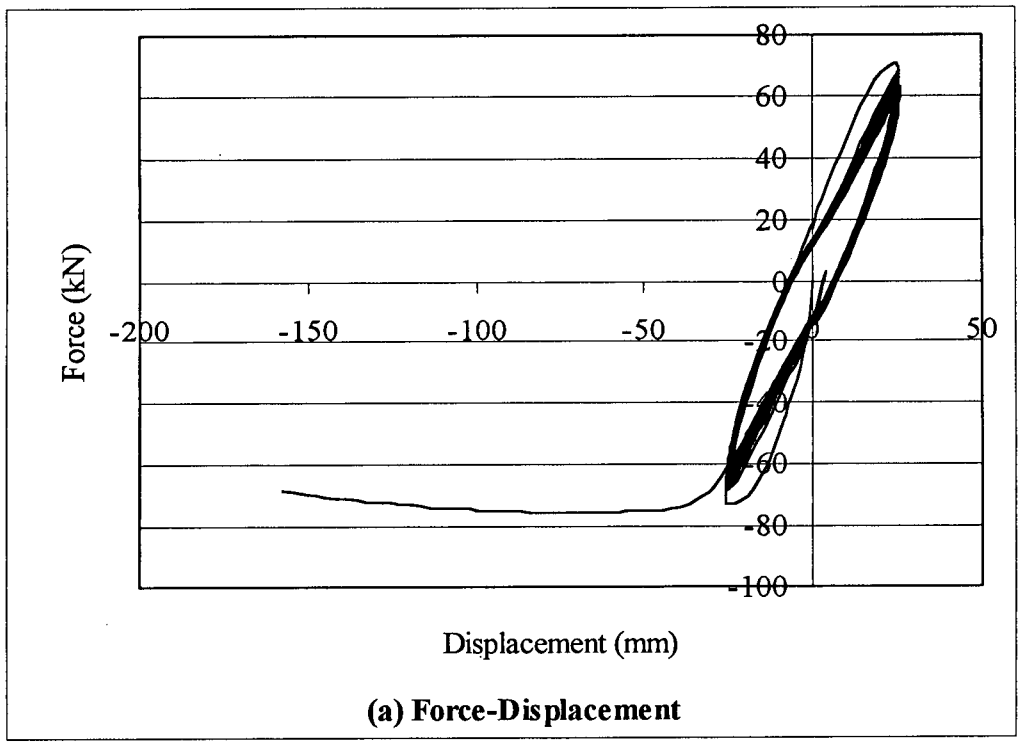

(a) Force-Displacement

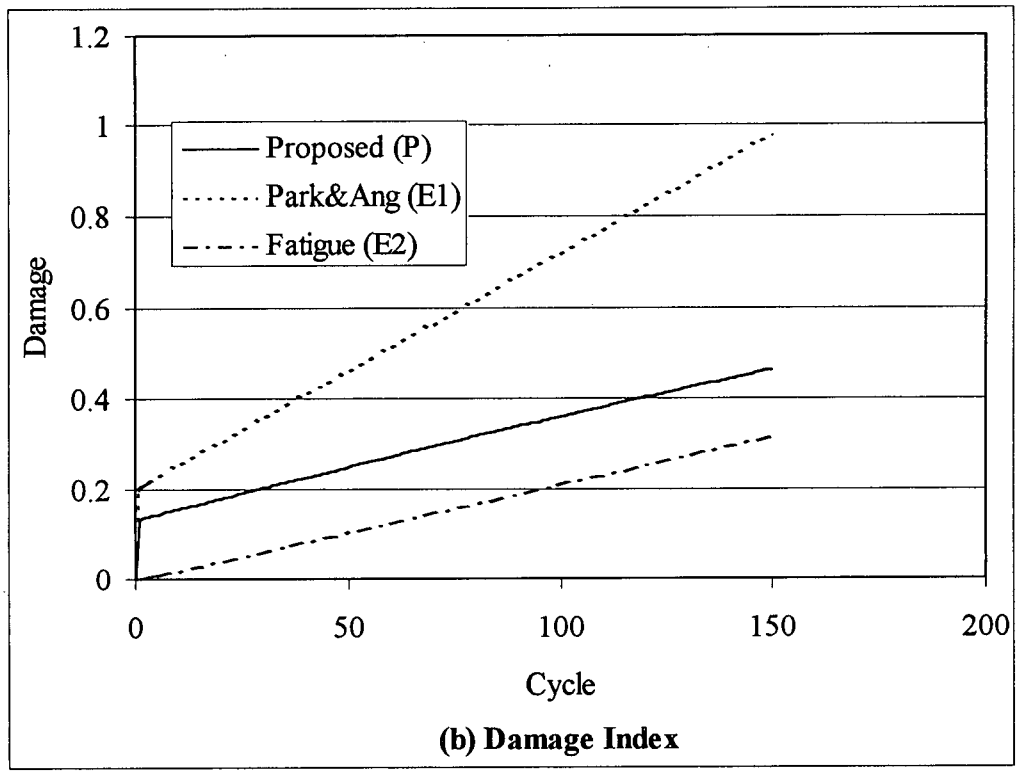

(b) Damage Index

Figure 4.6: Specimen A3.

4.1.4 Specimen A4

This specimen was tested under a much larger drift amplitude of approximately 4.0% (57 mm) until failure. Failure of the column was recorded through rupture of the hoop in the middle of plastic hinge at cycle 26. Table 4.5 summarizes the test observations of this specimen.

Table 4.5: Observed damage for Specimen A4.

Cycle	Displacement (mm)	Comments
1	57	Yielding, spalling of concrete cover
2	57	Cracks propagation
3	57	Spalling progressed to 150 mm from the base on both sides
5	57	1.5 mm crack width
6	57	2.0 mm crack width
8	57	150-160 mm plastic hinge length
9-17	57	Significant cracking and concrete spalling
18	57	Necking of spirals, some bar buckling
26	57	Hoop failure

Figure 4.7 summarizes the prediction of damage. Both E1 and E2 models gave full damage before the 26th cycle. The E1 model seems to perform better when the displacement amplitudes are significantly larger than the yield displacement. The E1 model

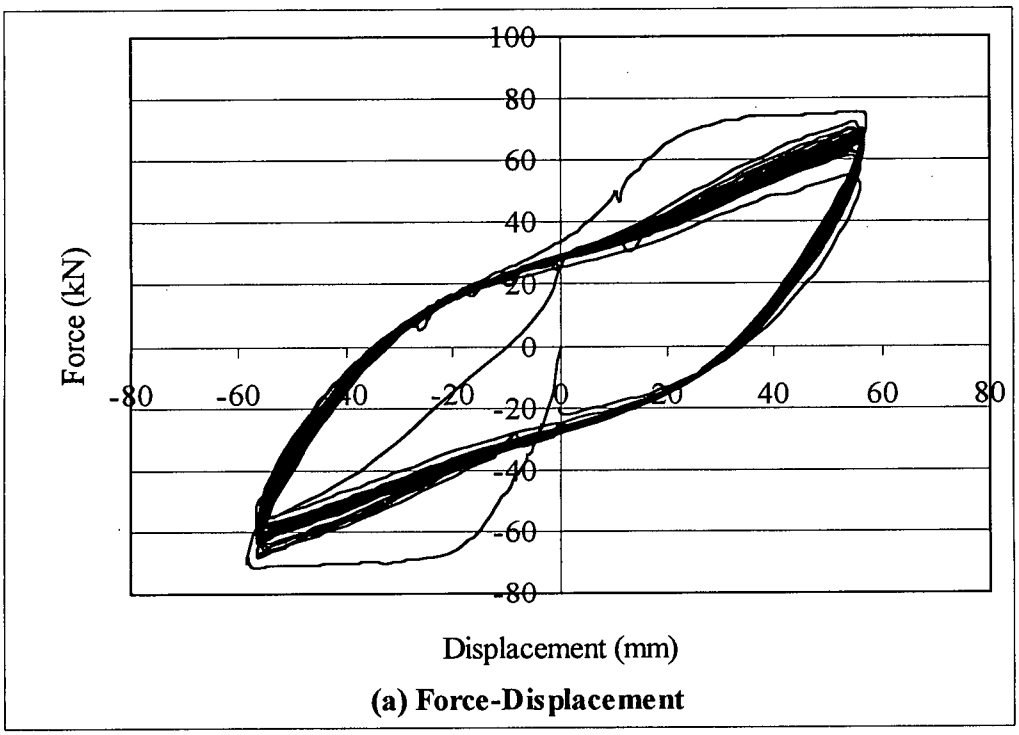

(a) Force-Displacement

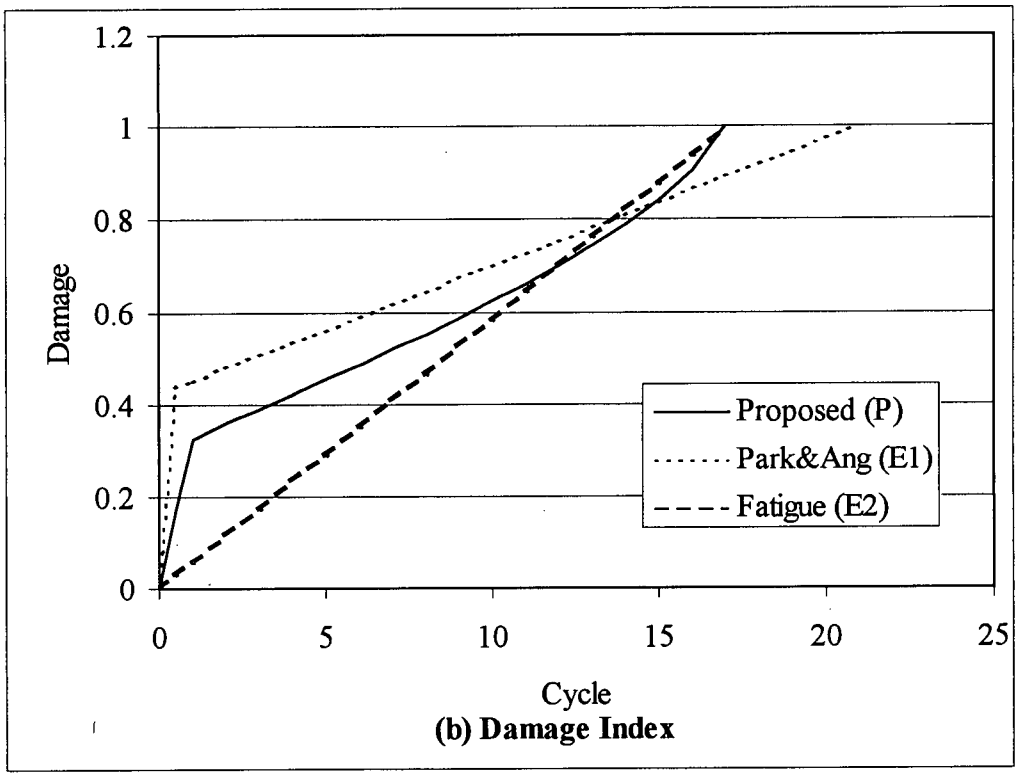

(b) Damage Index

Figure 4.7: Specimen A4.

overestimated the damage in the early cycles. The E2 and P models over predicted damage and gave failure at the 17th cycle through rupture of longitudinal steel. The reason for that is the assumption they use to estimate the plastic strain and the number of cycles to failure for given displacement level. The P model gave a good prediction compared to the observed damage in the first 5 cycles, while the E2 model underestimated the damage.

4.1.5 Specimen A5

This specimen was tested under repeated cyclic loading of drift of approximately 5.5% (75 mm). Table 4.6 summarizes the observed damage. The column failed in rupture of longitudinal reinforcement before cycle 10 was completed.

Table 4.6: Observed damage for Specimen A5.

Cycle	Displacement (mm)	Comments
1	75	Observation of cracking, yielding, and spalling of concrete cover
6	75	Crack width exceeded 2.5 mm, spalling progressed beyond 150 mm from the base, 175 mm plastic hinge length
9	75	Significant buckling of longitudinal bars on both sides, necking of the spiral
10	75	Failure

Figure 4.8 shows the predicted damage by the E1, E2, and P models. The E1 model gave a damage of more than 0.5 at the first cycle due to high displacement amplitude. The observed damage appeared to be repairable at this stage. The predicted damage by the E2 model progressed linearly to give a damage of 1.0 (complete failure) at cycle 8. The E2 model underestimated the damage in the first cycle compared to the test observation. The P model described the damage well through the first 5 cycles compared to Table 4.6 but it is limited to 1.0 at cycle 8 due to low-cycle accumulated damage.

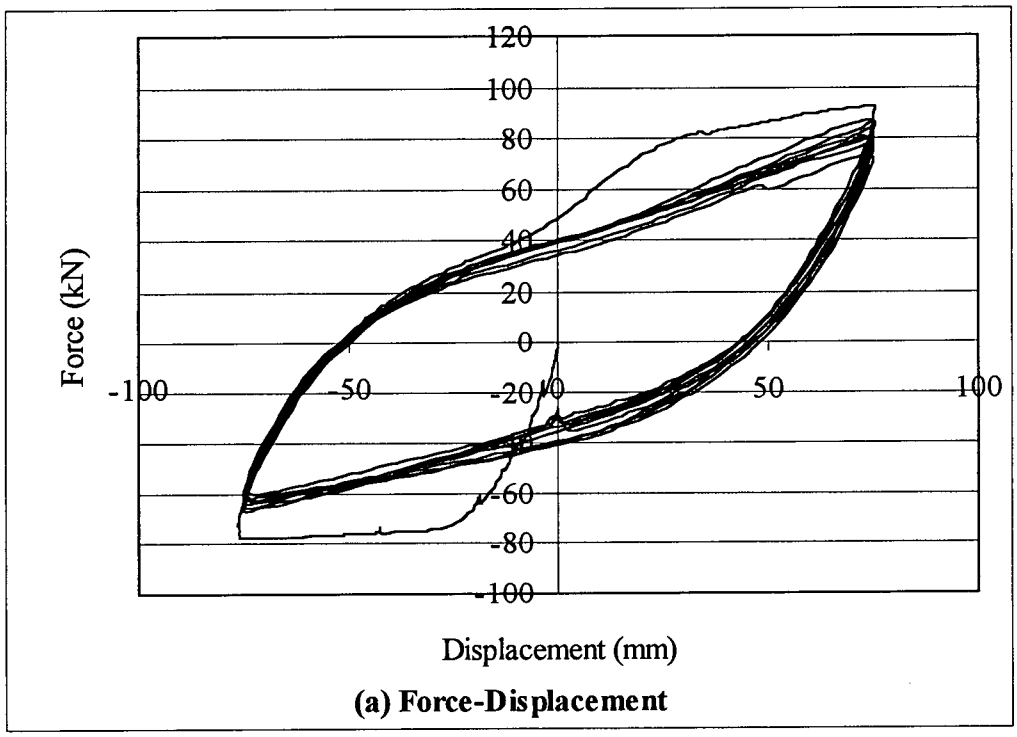

(a) Force-Displacement

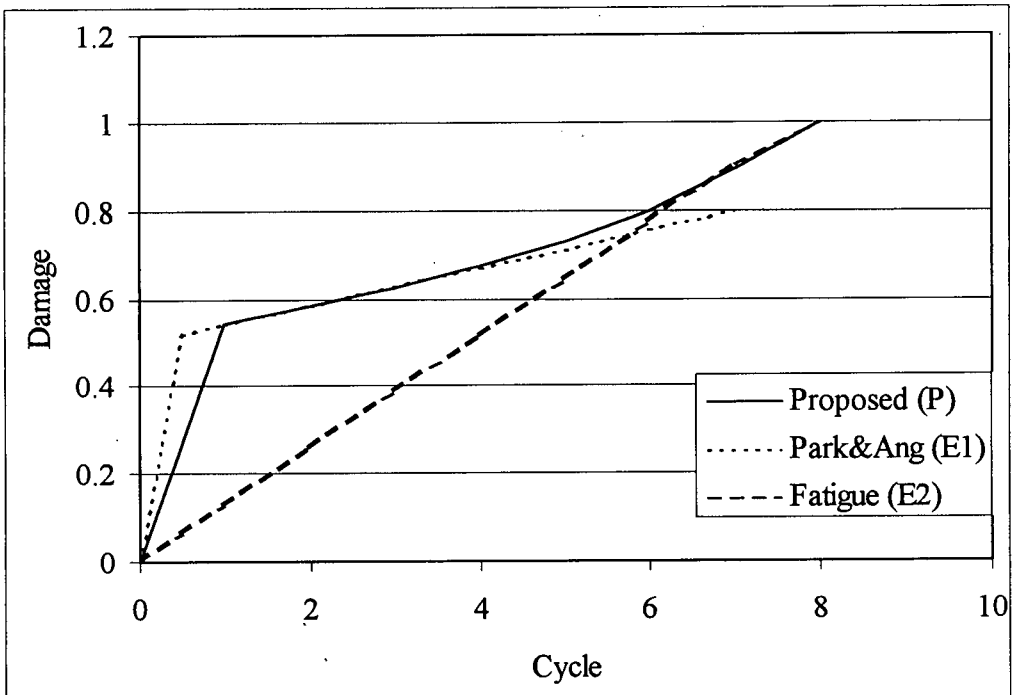

(b) Damage Index

Figure 4.8: Specimen A5.

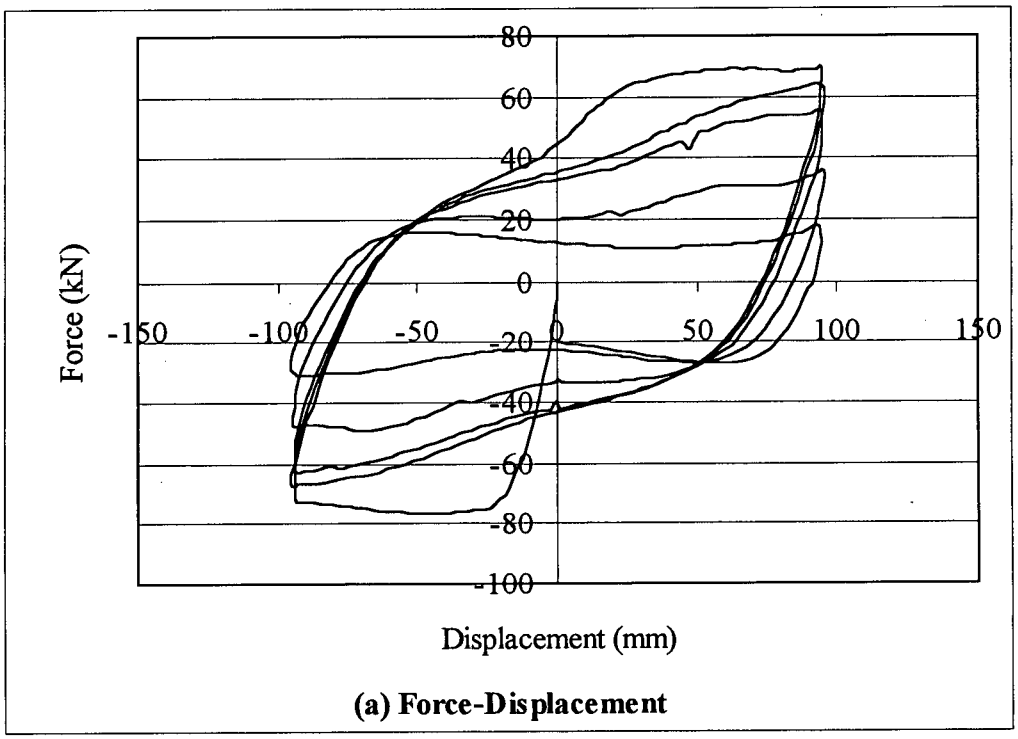

(a) Force-Displacement

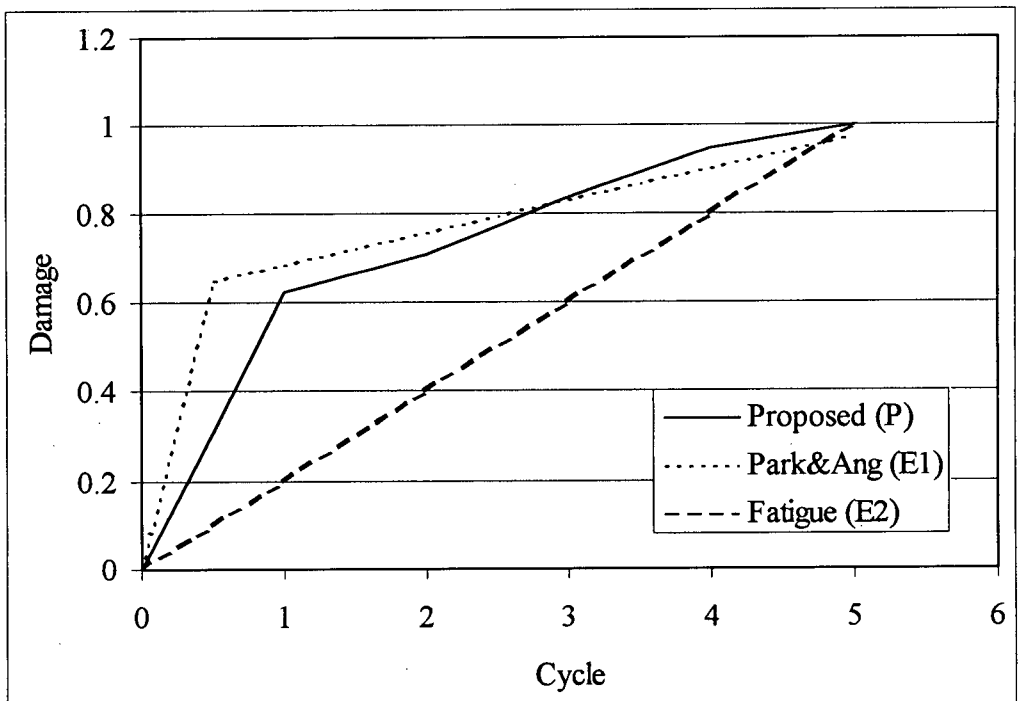

(b) Damage Index

Figure 4.9: Specimen A6.

4.1.6 Specimen A6

This column was subjected to repeated cycles of a drift slightly larger than 7.0% (95 mm). Table 4.7 summarizes the test observation. The column failed at the end of cycle 4 in rupture of a longitudinal bar.

Table 4.7: Observed damage for Specimen A6.

Cycle	Displacement (mm)	Comments
1	95	Yielding and spalling commenced well before the end of cycle
2	95	Significant spalling, necking of spirals, buckling of longitudinal bars, 250 mm plastic hinge length
3	95	Significant strength deterioration
4	95	Failure

Figure 4.9 shows the predicted damage by the E1, E2, and P models. The E2 model gave a good estimation of the number of cycles to complete rupture of longitudinal steel, which agreed with the test observation. The E2 model underestimated the damage through the loading history as shown in all specimens and specially in this specimen. The E1 and P models gave approximately the same prediction of damage and compared well with the observed damage.

4.2 TESTS BY ADEBAR AND ROUX (1998)

This section discusses the observed damage for six rectangular columns tested by Adebar and Roux (1998), the predicted damage by the E1, E2, and P models, and a comparison among them. These tests were not designed with damage computation in mind, but they are ideal for this purpose, since they provide simple, well-defined cyclic loading with significant flexural and shear components.

Each of the six specimens has different moment to shear ratio, and stirrups spacing. In all other aspects, the test specimens were identical as shown in Figure 4.10. The test parameters are summarized in Table 4.8. These tests are mostly shear dominated except specimen SR1 which is flexure dominated. Experimental force-displacement envelopes are not available for these specimens. A bilinear force-displacement envelope was predicted theoretically for each specimen, following the procedures discussed in Chapter 3, as shown in Figure 4.11.

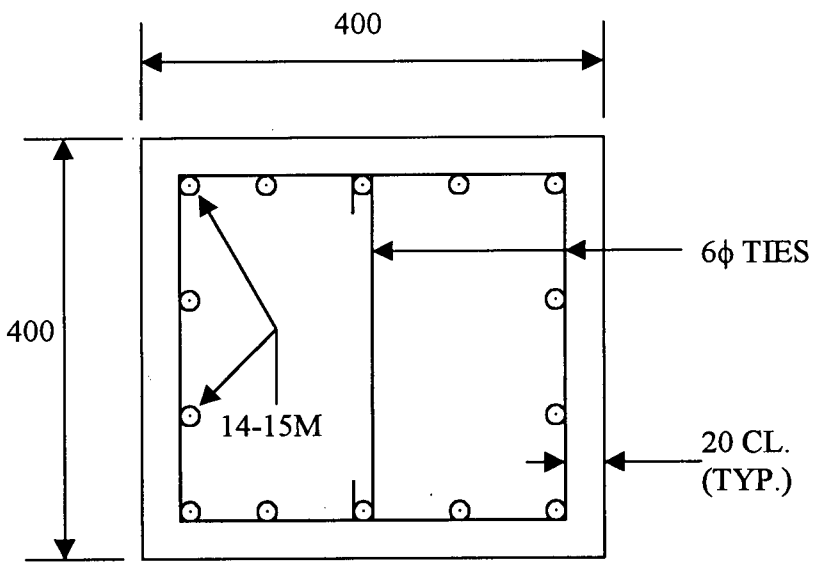

Figure 4.10: Cross-section of SR columns (Adebar and Roux, 1998).

In this study the shear capacities of the monotonic force-displacement envelopes are estimated following the procedures developed by Priestley et al. as discussed in Chapter 3. As shown in Figures 4.11a & b, the shear demands for specimens SR1, SR2 and SR5 are lower than the shear capacities at any ductility level. Therefore, the shear has no effect on the strength and ductility of these specimens. The initial shear capacity for specimens SR3,

SR4 and SR6 are higher than the shear demand as shown in Figures 4.11c & d. The shear capacities of these specimens become less than the demand at a ductility of about 3.5. This difference between the shear capacity and demand as shown in Figure 4.11 is assumed to be small and can be ignored since it is only for part of the envelope (higher ductilities). Therefore, no shear nor ductility reduction is considered due to shear capacity. This is considered reasonable as long as the hysteresis response has the ability to capture all the damage due to shear through the loading cycles. Therefore the flexural monotonic force-displacement response is followed for damage calculations without any reduction due to shear.

Table 4.8: Summary of Adebar and Roux (1998) Tests.

Specimen	Length M/V (mm)	M/Vd	Stirrup Spacing (mm)	f'_c (MPa)	f_y Long. (MPa)	f_y Stirrups (MPa)
SR1	1100	3.00	75	30	482	246
SR2	900	2.46	75	30	482	246
SR3	800	2.19	75	30	482	246
SR4	725	2.05	75	30	482	246
SR5	900	2.46	50	30	482	246
SR6	900	2.46	100	30	482	246

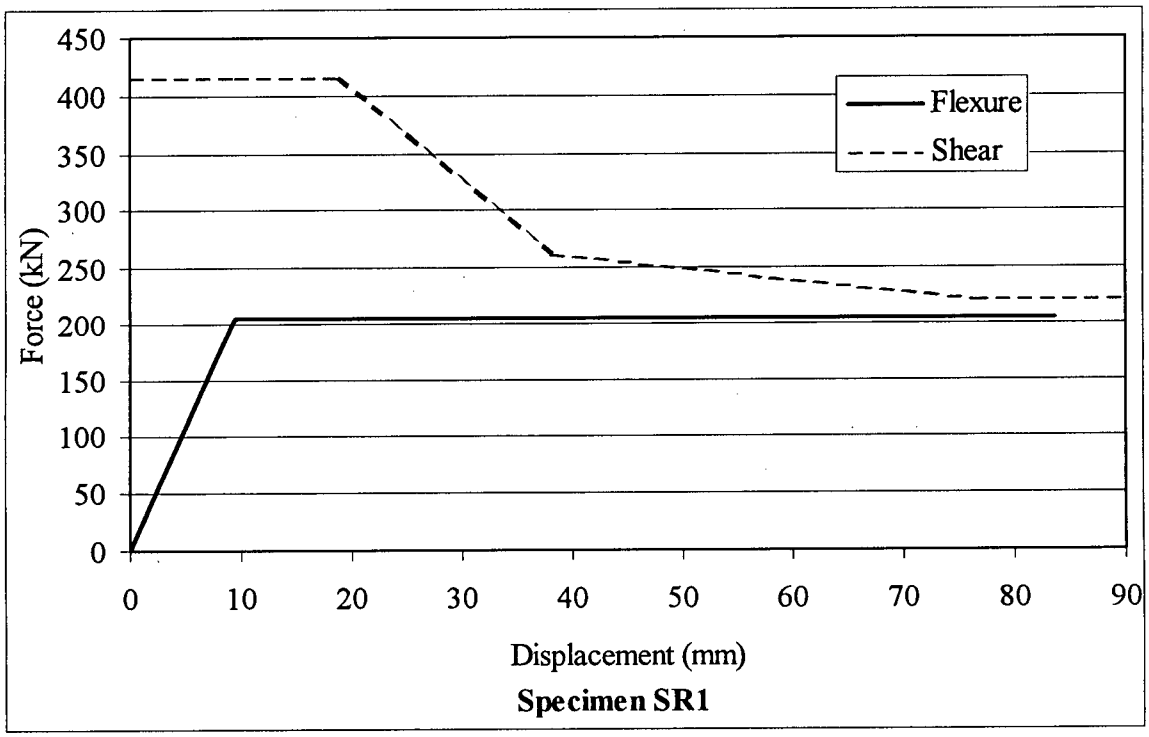

(a)

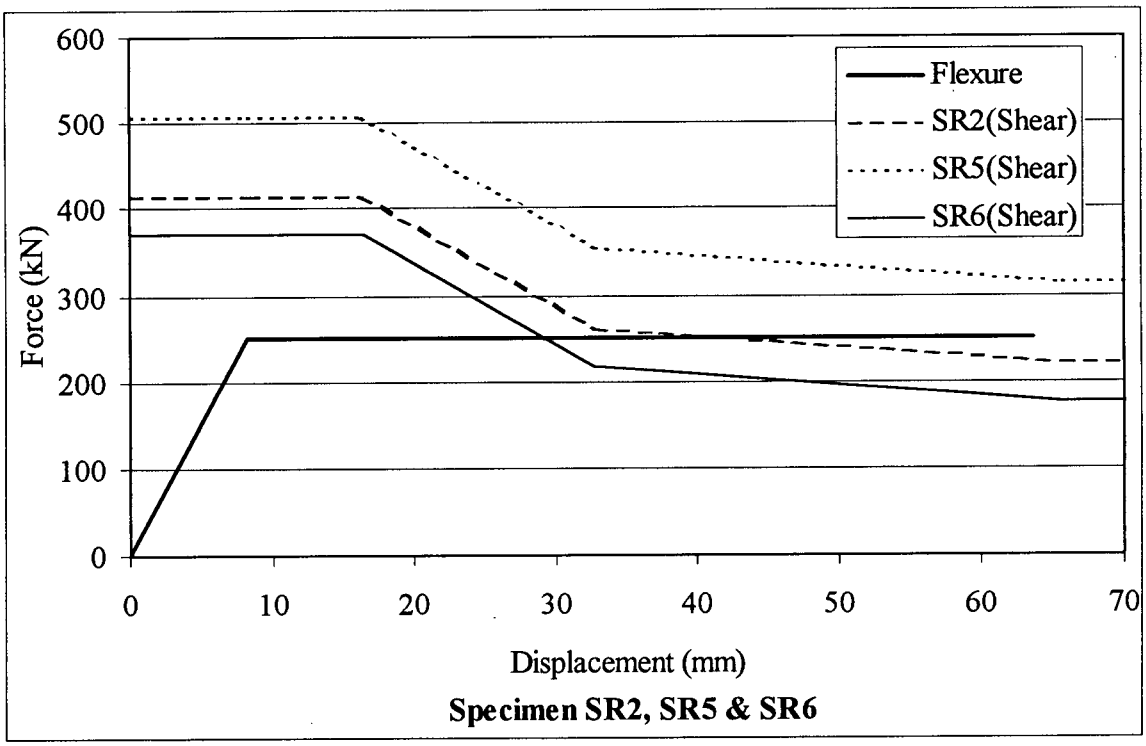

(b)

Figure 4.11. Theoretical force-displacement envelope.

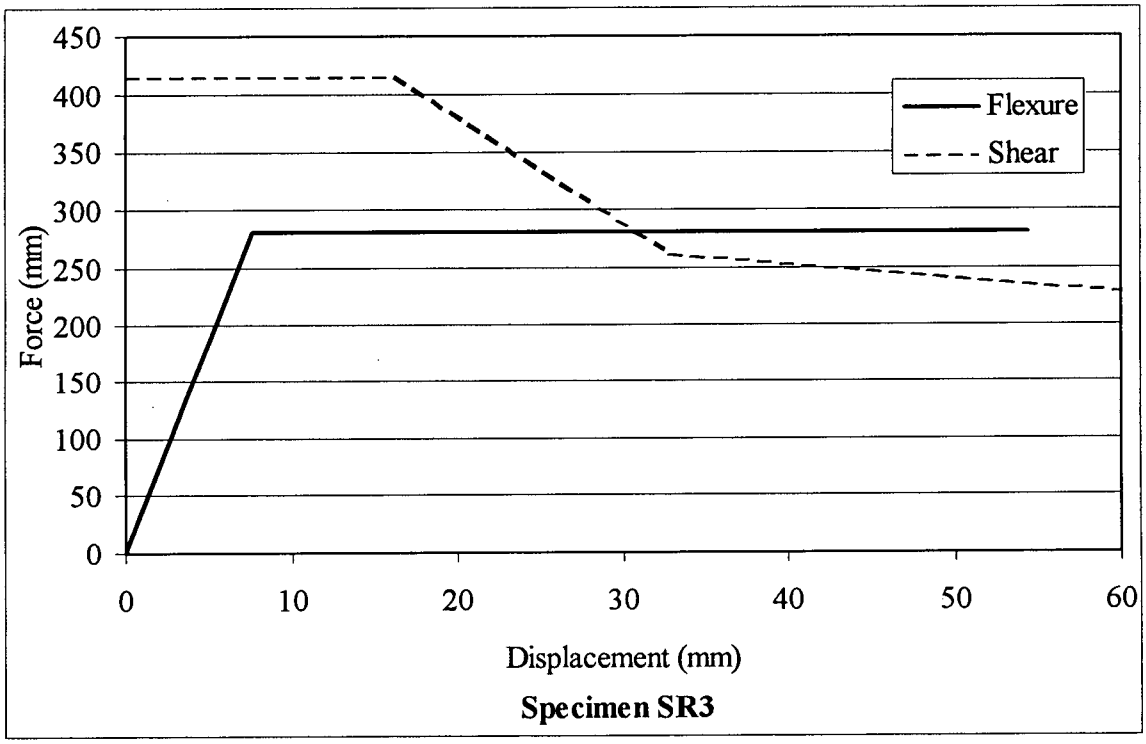

(c)

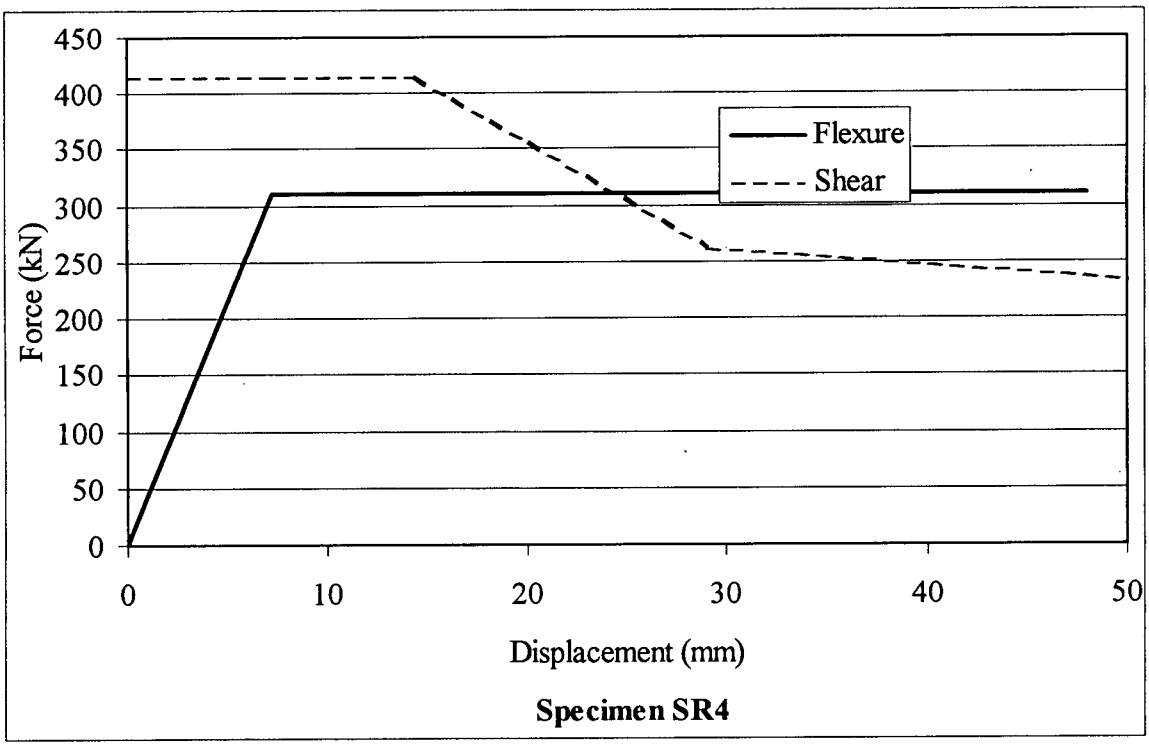

(d)

Figure 4.11 (continued). Theoretical force-displacement envelope.

A value of 0.1 for β_e is used for the E1 model calculations for this set of columns as suggested by Williams et al. (1997) since these columns are considered well reinforced.

4.2.1 Specimen SR1

This Specimen was subjected to 21 cycles, three cycles at each displacement amplitude. The displacement amplitudes used in the testing are 5 mm, 10.5 mm, 14 mm, 21 mm, 28 mm, 35 mm, and 42mm as shown in Figure 4.12.

Specimen SR1 is flexure dominated, but it ultimately failed in shear. At a displacement 21 mm (cycles 10-12), a 2 mm wide flexural crack and a 1.5 mm wide diagonal shear crack were observed. At a displacement level of 28 mm (cycles 13-15), not much damage occurred to the specimen since the last displacement level of 21 mm as observed. The shear strength started to deteriorate after cycle 15. Significant shear strength degradation occurred at cycle 19 when the displacement reached 42 mm as shown in Figure 4.12a.

Figure 4.12 shows the damage prediction by the E1, E2, and P models. The E1 and P models gave very close results. At a displacement level of 21 mm for cycles 10, 11, and 12, the P model gave a damage of 0.2. The P model gave a damage between 0.2 and 0.3 between cycles 13 and 15. The E1 model gave a higher estimation of damage for this loading stage, but still close to the P model. The P model gave a high damage of 0.6 at the end of cycle 18 (35 mm). The E2 model gave lower damage during the loading cycles compared to the E1 and P models due to the fact that it depends only on flexure, but it gave significant damage at the end of the test (D=0.63).

4.2.2 Specimen SR2

This Specimen was subjected to 18 cycles, three cycles at each displacement amplitude. The displacement amplitudes used in the testing are 5 mm, 9 mm, 12 mm, 18 mm, 24 mm, and 30 mm.

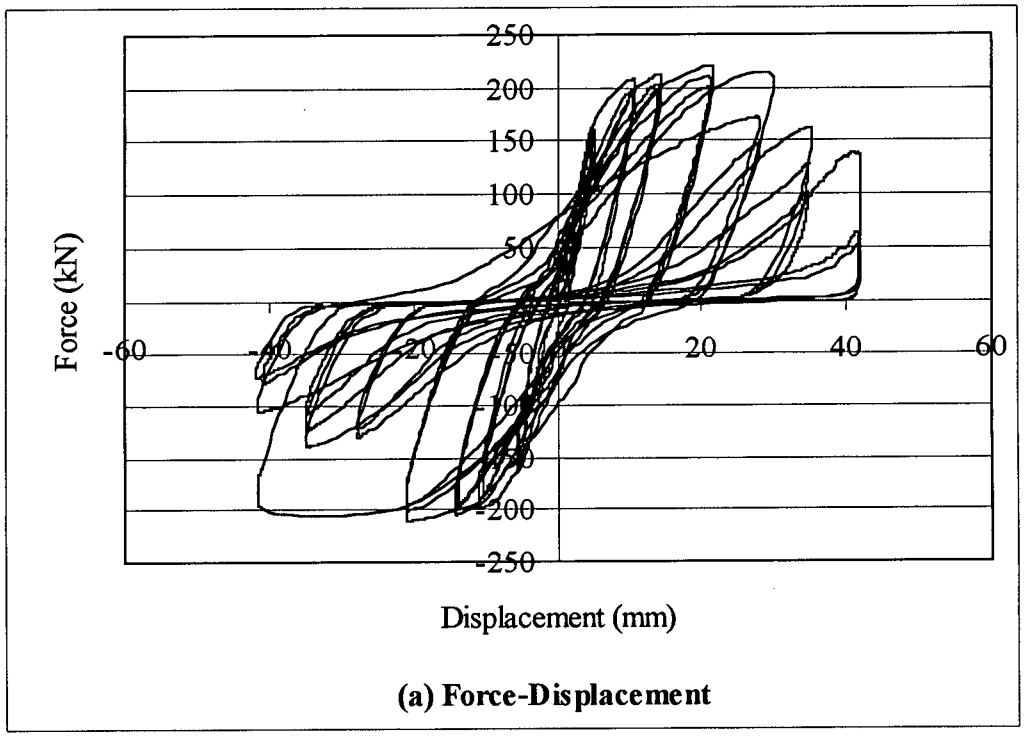

(a) Force-Displacement

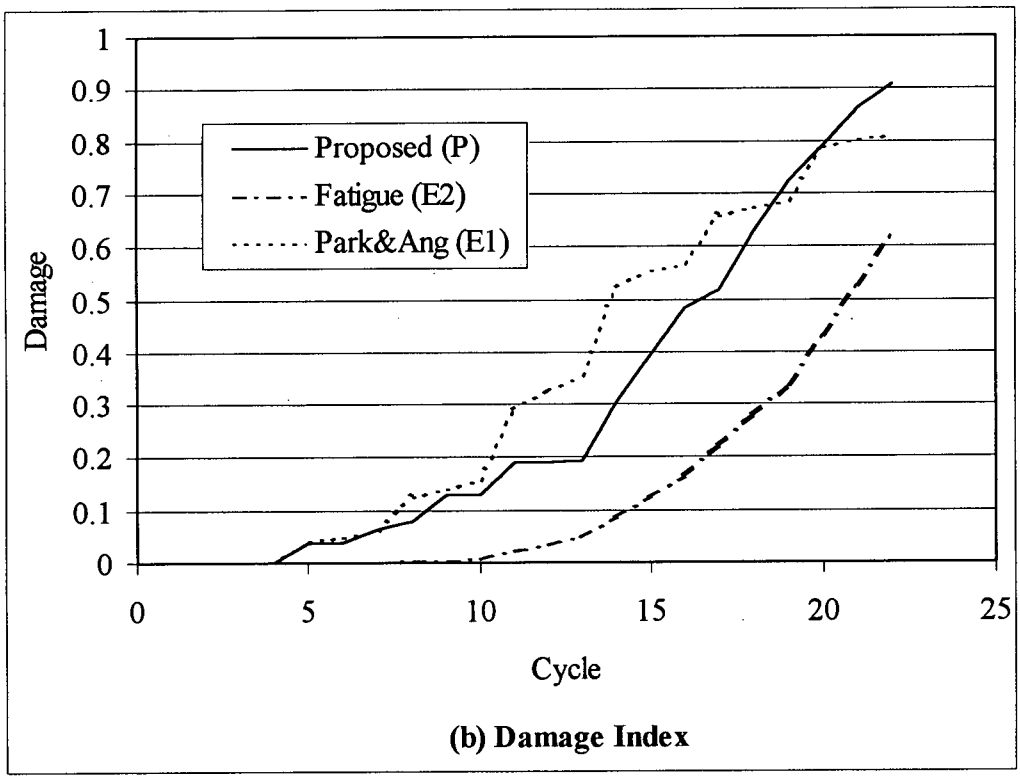

(b) Damage Index

Figure 4.12: Specimen SR1.

As shown in Figure 4.13, the observed test indicated that the specimen appeared to be repairable until the end of cycle 12, which showed a 4 mm wide shear crack and 18 mm displacement. While the damage was significant, but would still be repairable until the end of cycle 15, with a 5 mm wide crack and 24 mm displacement as shown in Figure 4.13b. The specimen was damaged beyond repair after cycle 16 (30mm of displacement) as shown in Figure 4.13c. The failure was definitely due to shear.

As shown in Figure 4.14, the E1 and P models gave close results for the damage during the first 13 cycles, while E1 damage seemed to be lower after that and did not predict the shear failure. The reason for that is the E1 model depends on the level of ductility and the hysteretic energy during the cycling, but for a shear dominated test, the hysteresis loops are pinched and the energy is small compared to flexure dominated loops. The P model gave a damage of less than 0.6 at the end of cycle 15, and a damage of higher than 0.6 (beyond repair) after cycle 15. Once again, the E2 model is incapable of describing the damage because it is a shear dominated test.

4.2.3 Specimen SR3

This Specimen was subjected to 9 cycles, three cycles at each displacement amplitude. The displacement amplitudes used in the testing are 5 mm, 14 mm, and 17 mm as shown in Figure 4.15. The specimen was then loaded monotonically until it failed in shear at a displacement of 33 mm.

At a displacement of 14 mm (Cycles 4 to 6), a diagonal shear crack widened to 4 mm. At a displacement of 17 mm (Cycles 7 to 9), the specimen shear capacity began to degrade considerably as shown in the hysteresis loops in Figure 4.15a. The damage at this stage was significant and appeared to be beyond repair.

As shown in Figure 4.15b, the E1 model gave very low damage during the cycling, while the damage was high at the failure stage because of the high ductility ratio. The E1 model underestimated the damage because it is a shear dominated test. The P model described the damage very close to what was observed above. It showed significant damage of 0.45 at the

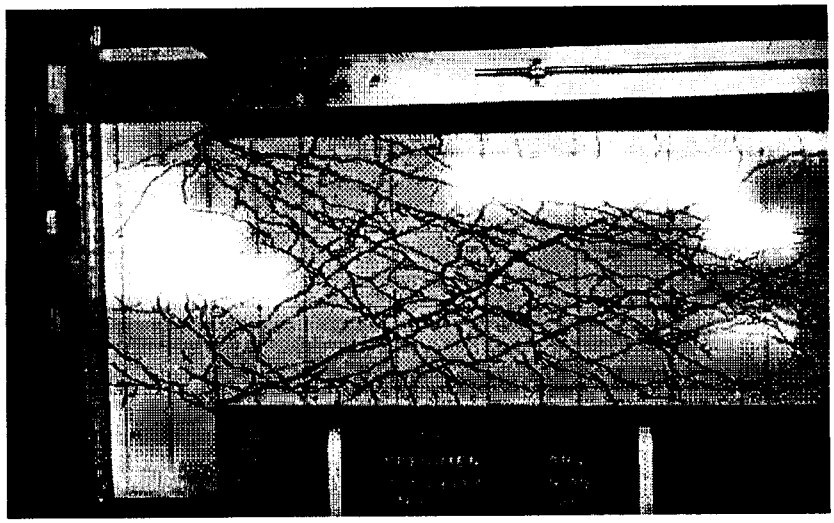

(a) Displacement = 18 mm.

(b) Displacement = 24 mm.

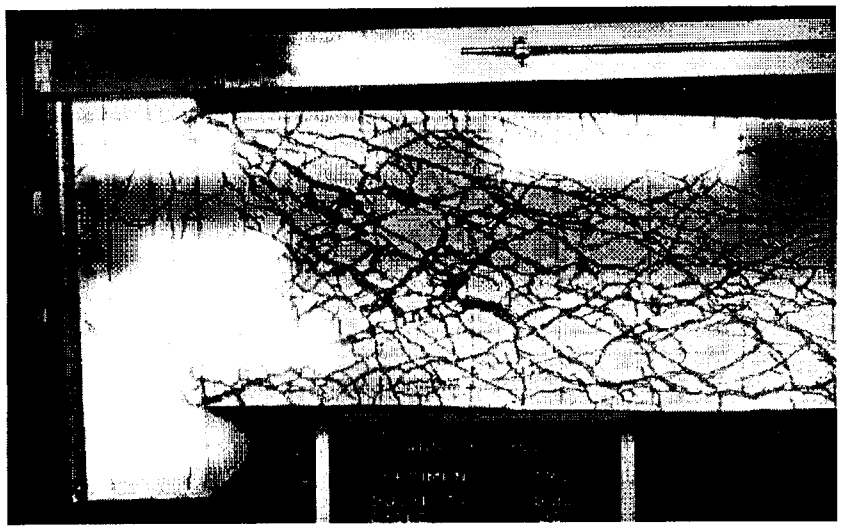

(c) Displacement = 30 mm.

Figure 4.13: Damage to specimen SR2 (Adebar and Roux, 1998).

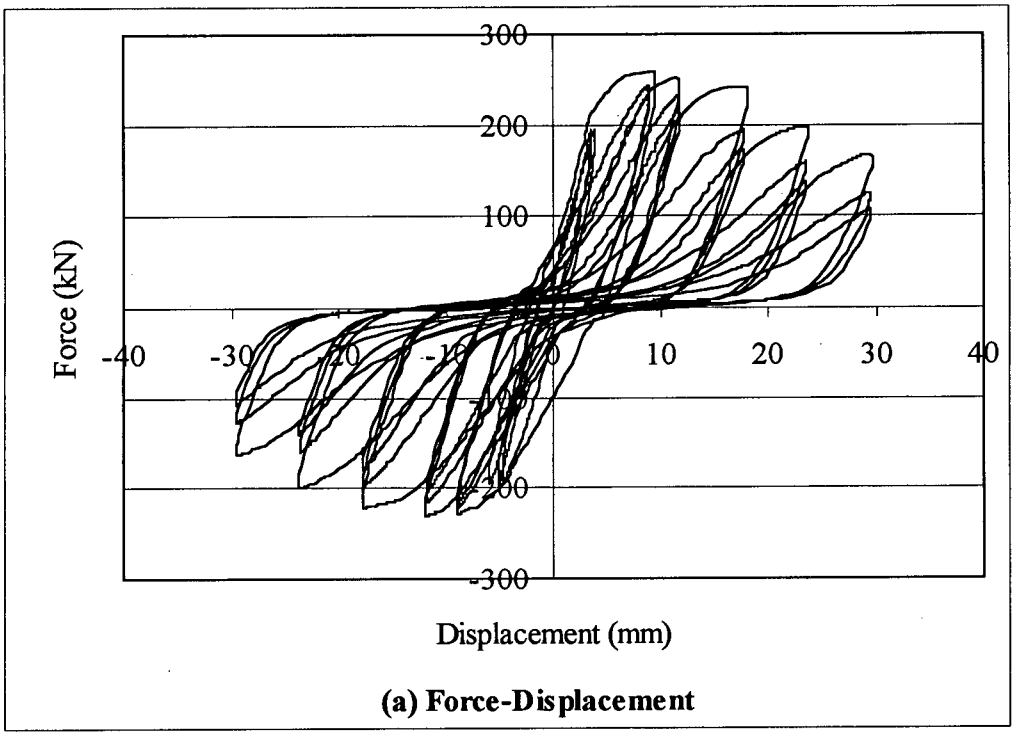

(a) Force-Displacement

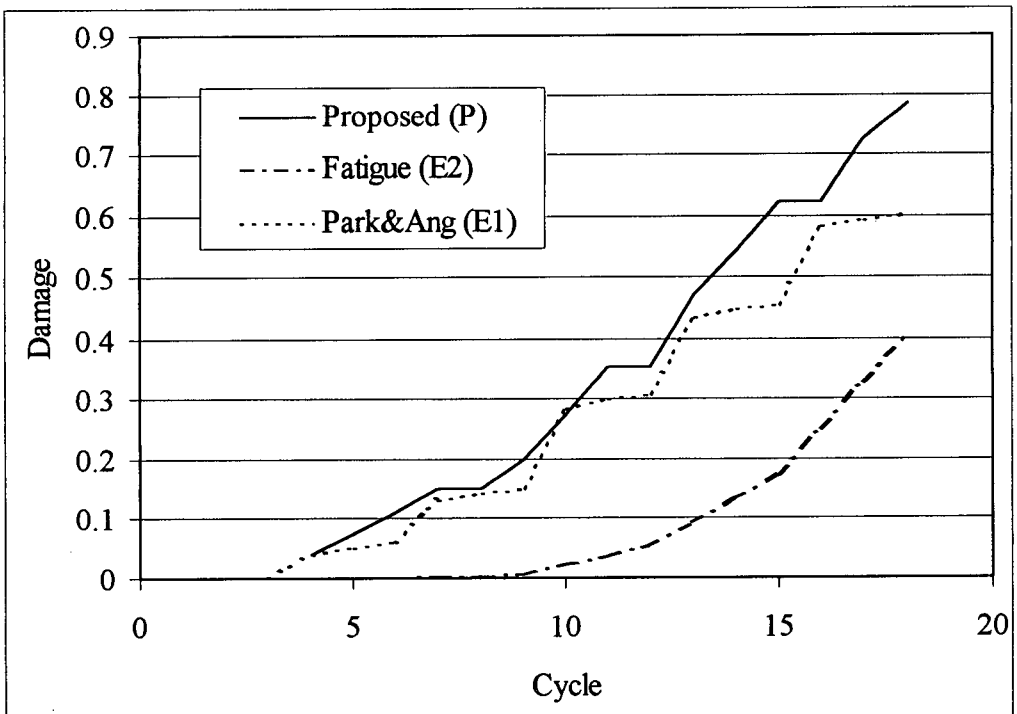

(b) Damage Index

Figure 4.14: Specimen SR2.

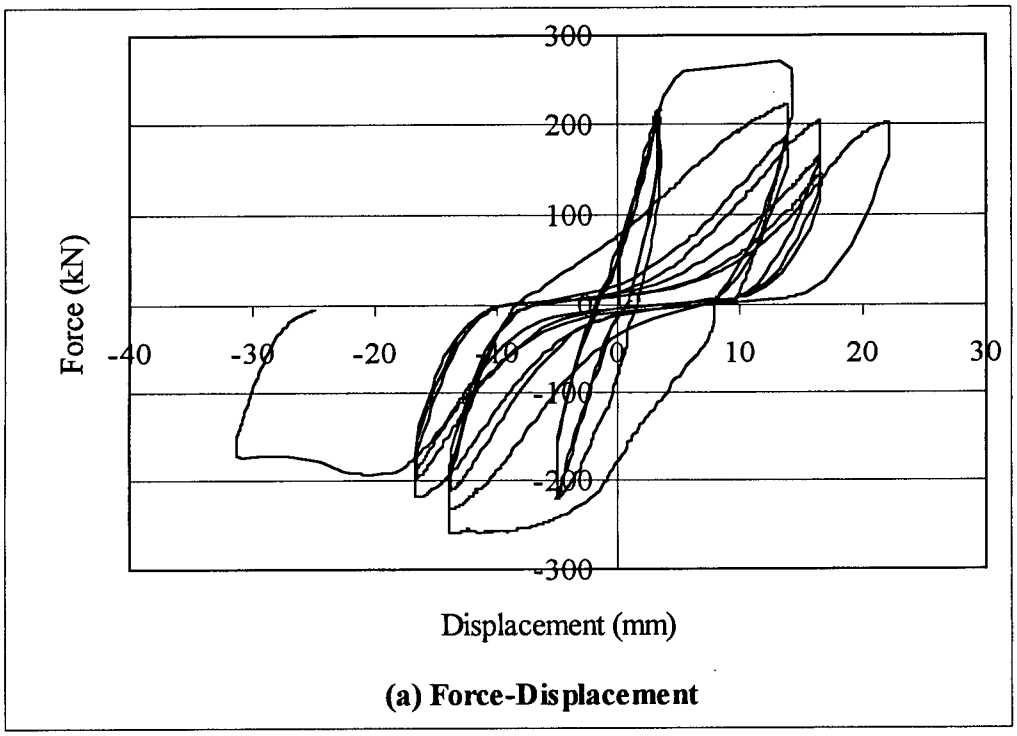

(a) Force-Displacement

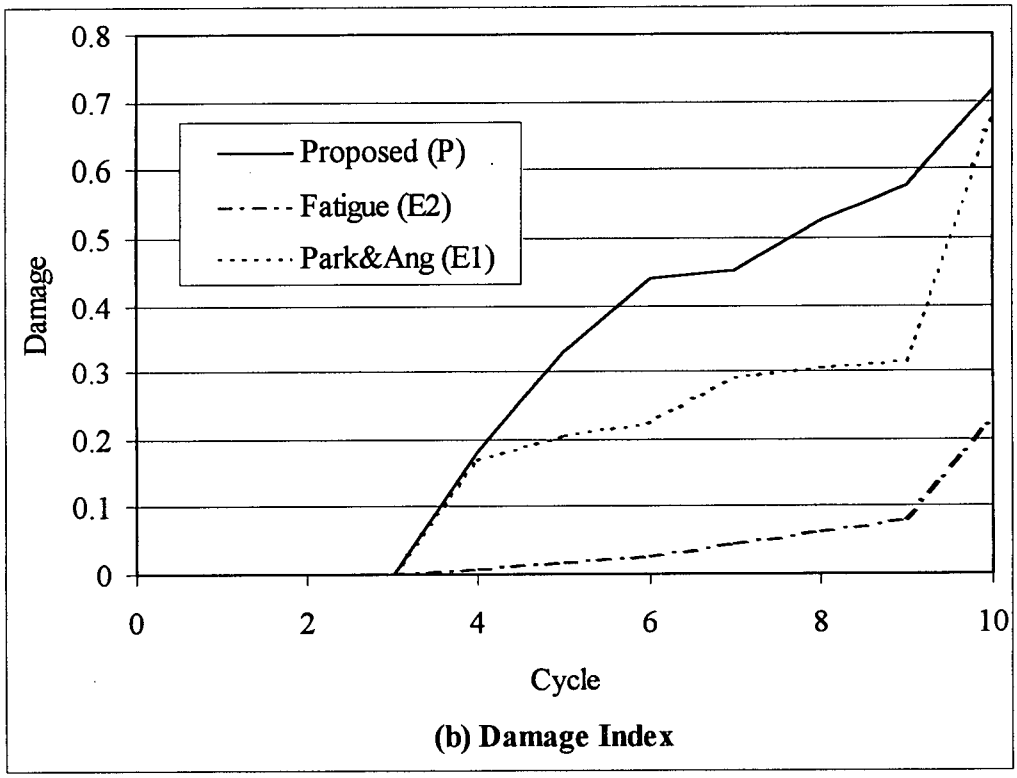

(b) Damage Index

Figure 4.15: Specimen SR3.

end of cycle 6. The P model gave a damage of more than 0.6 at the end of cycle 9.

4.2.4 Specimen SR4

This Specimen was subjected to 18 cycles, three cycles at each displacement amplitude. The displacement amplitudes used in the testing are 3 mm, 7 mm, 9 mm, 13 mm, 17 mm, and 22 mm as shown in Figure 4.16. This specimen was then loaded monotonically until it failed at a displacement of 46 mm.

The observed damage of this specimen showed minor cracks until the end of cycle 6 where the displacement was about 6.5 mm. At a displacement of 13 mm at the end of cycle 12, the cracks widened. At a displacement of 17 mm at cycles 13, 14, and 15, the cracks opened up to 6 mm, and the damage appeared to be difficult to repair. Three more cycles were followed at a displacement of 22 mm. The damage through these cycles was definitely irrepairable. Finally the specimen was loaded monotonically until failure.

Figure 4.16 shows the prediction of damage by the three models. The E1 model gave low damage because the test is shear dominated. The P model gave a damage of less than 0.2 until the end of cycle 6, a damage of less than 0.4 at the end of cycle 9, and a damage of less than 0.6 at the end of cycle 15. The damage was calculated to be between 0.6 and 0.8 during the cycles 16, 17, and 18. As discussed above, the P model agrees with the observed damage.

The P model predicted the ultimate displacement after cycling the column 18 cycles at different displacement level. The ultimate displacement was found to be 43 mm. This reduction (from 48 mm to 43 mm) in the ultimate displacement is due to low cycle accumulated damage at the longitudinal reinforcement.

Figure 4.16a shows the predicted monotonic envelopes for the virgin state, after 9 cycles and after 18 cycles (A_o, A_9, and A_{18}). These curves were used to calculate the damage by the P model.

4.2.5 Specimen SR5

This Specimen was subjected to 21 cycles, three cycles at each displacement amplitude. The displacement amplitudes used in the testing are 4 mm, 8 mm, 11 mm, 16 mm, 22 mm, 27 mm, and 34 mm as shown in Figure 4.17a.

The stirrup spacing of 50 mm is used here instead of 75 mm as in previous specimens. Considerable flexural action was present during the test. At a displacement of 16 mm until end of cycle 12, the specimen showed good crack control as cracks were extensive but not wide. This means that the damage was minor. Very little strength deterioration was evident until a displacement of 27 mm at the end of cycle 18 was reached.

As shown in Figure 4.17b, the E1 model overestimated the damage. The E2 model worked for this specimen and gave close results to the P model since it is a flexure dominated test. The P model described the damage very close to what was observed above. At cycle 12, the damage is less than 0.2, which indicates minor damage, as was observed in the test. At the end of cycle 18, the P model estimated a damage of 0.5.

4.2.6 Specimen SR6

This Specimen was subjected to 13 cycles, three cycles at each displacement amplitude except the first cycle. The displacement amplitudes used in the testing are 5 mm, 9 mm, 13 mm, 17 mm, and 22 mm as shown in Figure 4.18. The specimen was then loaded monotonically until it failed in shear at a displacement of 43 mm.

Stirrup spacing of 100 mm was used in this specimen; therefore, this specimen had the least shear resistance of the specimens mentioned above. Considerable shear action was present during the test. Considerable shear deterioration occurred at a displacement of 9 mm at cycles 7 to 9. At a displacement of 13 mm at the end of cycle 10, the specimen showed a 6 mm wide diagonal crack with considerable strength reduction. This means that the damage was significant at cycle 10. The specimen failed in shear after loading it monotonically as shown in Figure 4.18a.

As shown in Figure 4.18b, the E1 model underestimated the damage. The E2 model did not describe the damage properly because it is derived for flexural behavior. The P model described the damage very close to what was observed above. At cycle 10, the damage was more than 0.6.

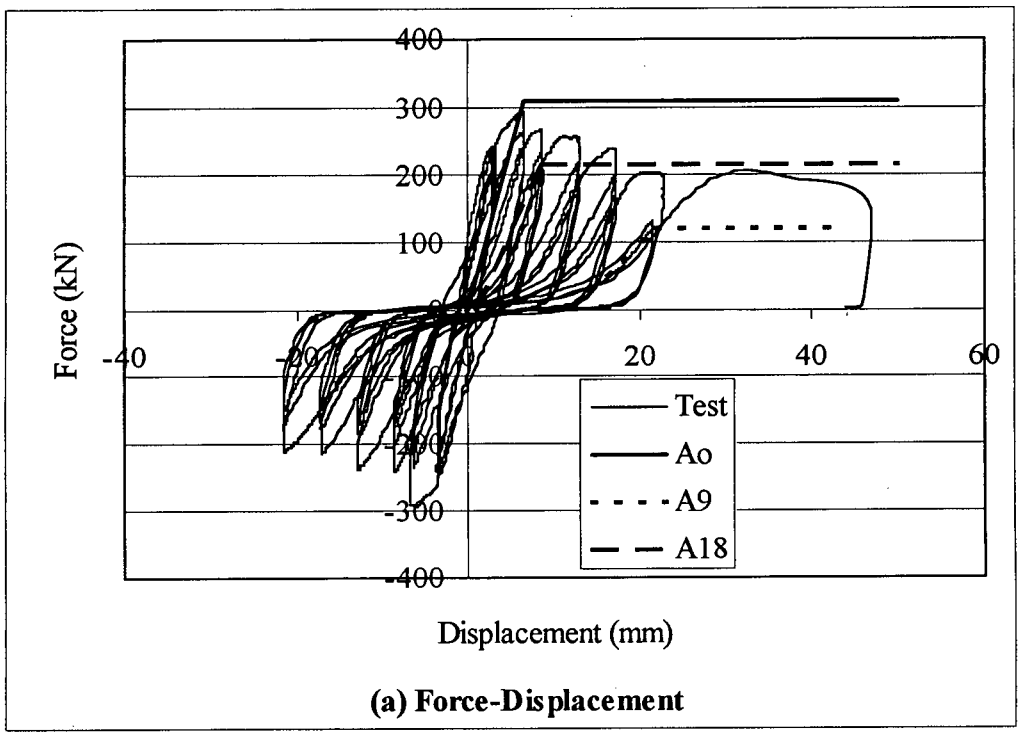

(a) Force-Displacement

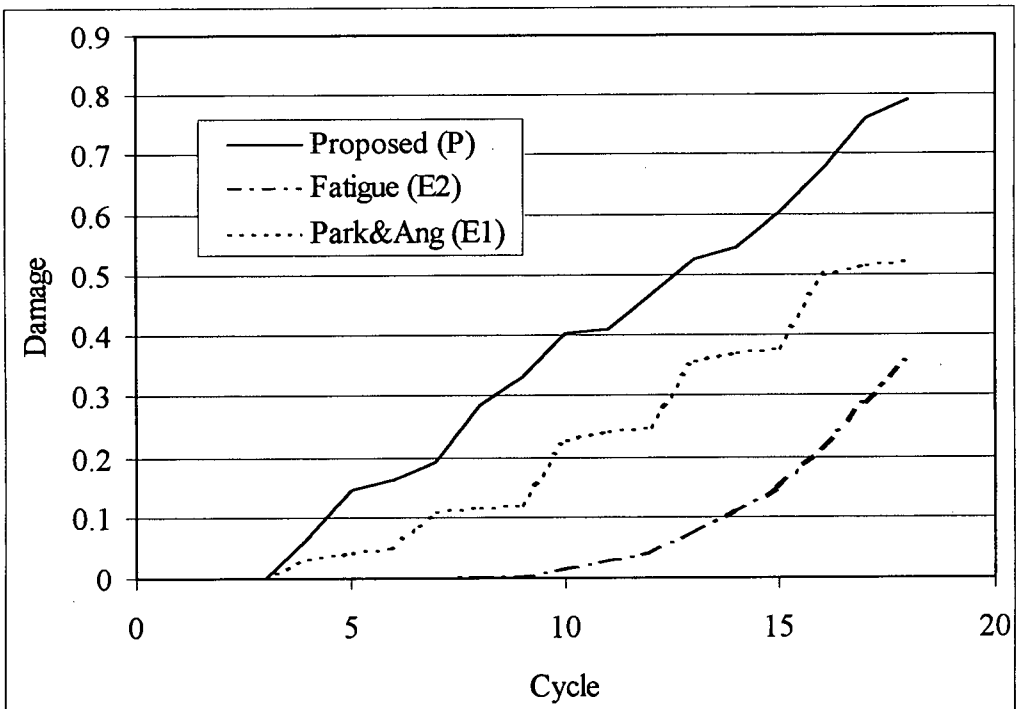

(b) Damage Index

Figure 4.16: Specimen SR4.

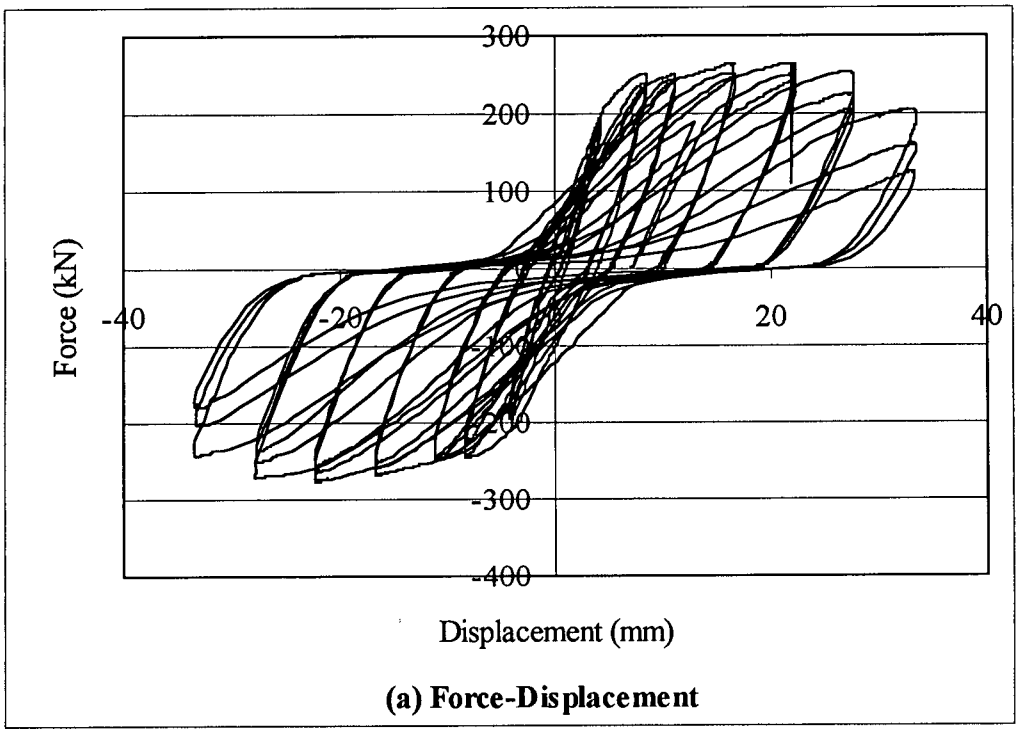

(a) Force-Displacement

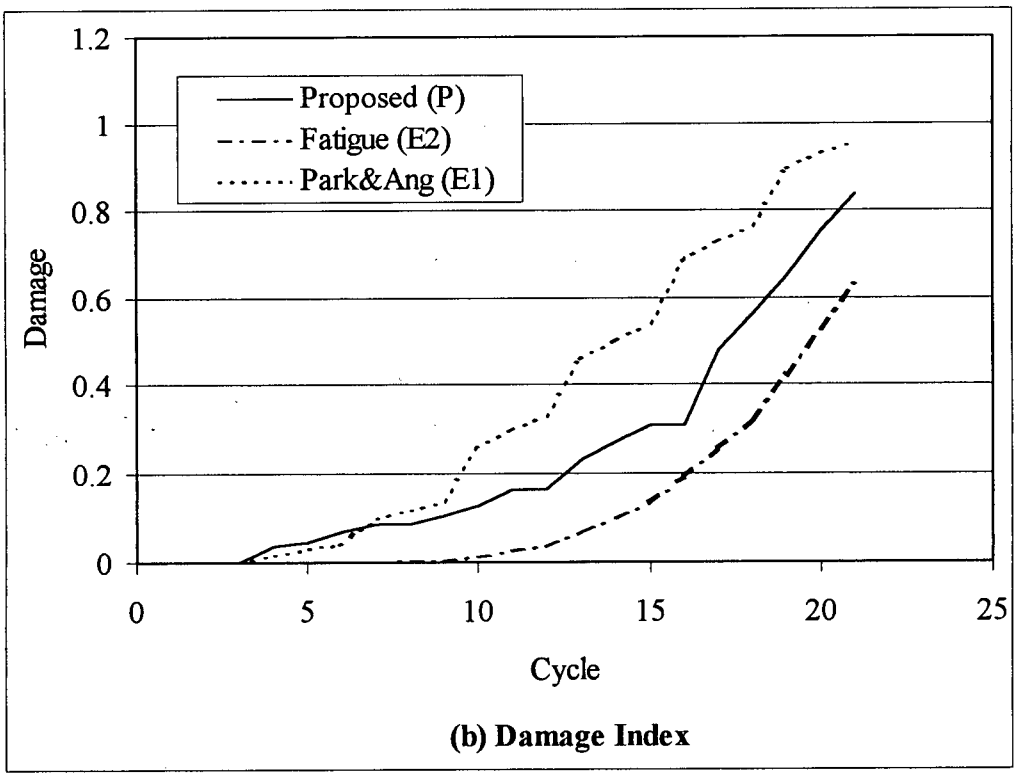

(b) Damage Index

Figure 4.17: Specimen SR5.

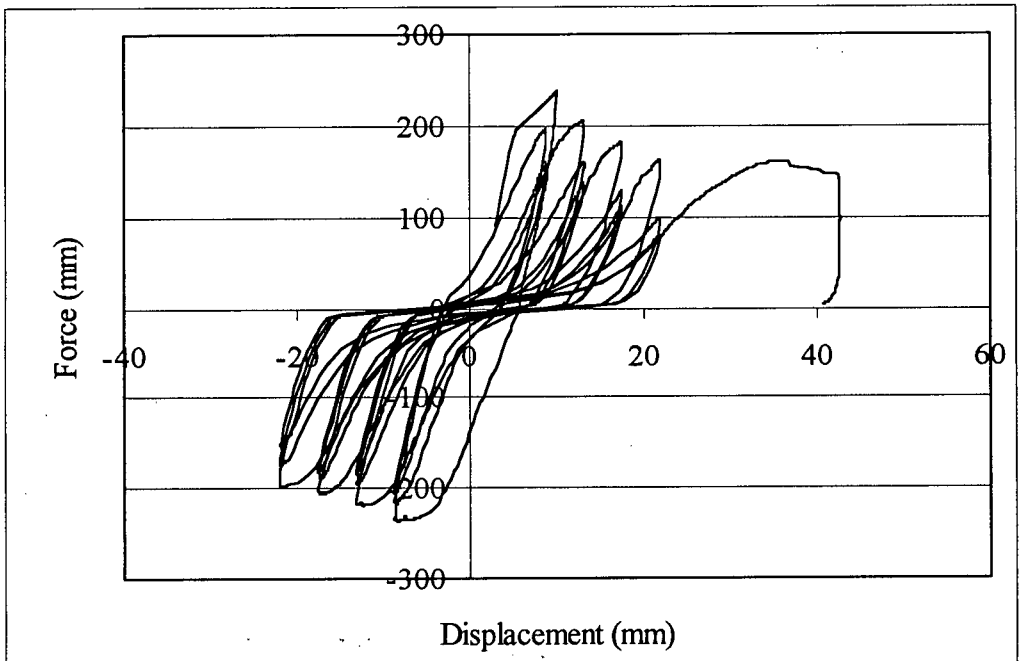

(a) Force-Displacement

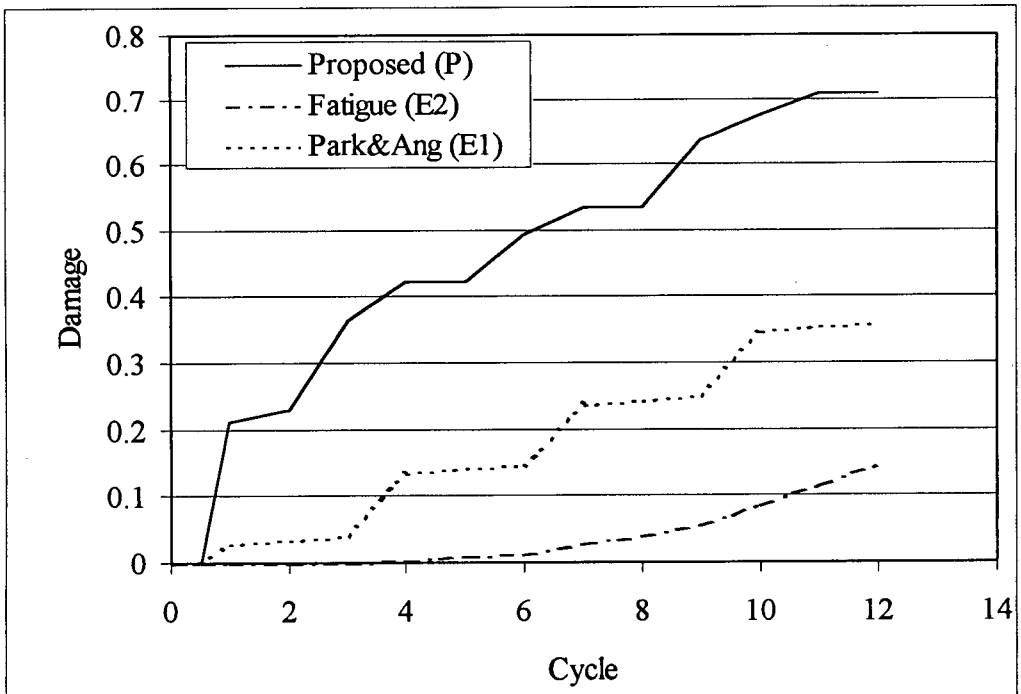

(b) Damage Index

Figure 4.18: Specimen SR6.

4.3 CONCLUSIONS

The results presented in this chapter showed that the E1 model sometimes overestimates damage at small inelastic amplitude and underestimates damage at large inelastic cycles. The E1 model is essentially derived for flexure dominated elements. On the other hand, the E2 model accounts only for low-cycle accumulated damage at the steel due to flexure and sometimes underestimates damage. It is concluded that the P damage model is a reasonable combination between ductility, energy and low-cycle accumulated damage and it gave good results compared to the observed damage for both flexure and shear dominated tests.

The previous damage application showed that a damage of 0.4 as suggested by Park et al. (1987) as a threshold value between repairable and irrepairable damage is considered conservative. The E1, E2, and P models seem to agree under medium inelastic cycles. The E2 model showed good ability in predicting the number of cycles at failure, but it sometimes underestimated the damage during early loading stages. The E2 and P models performed better than the E1 model at small inelastic cycles (specimen A3 from Kunnath et al. tests).

The following damage scale is concluded from the comparison between the P model and the observed damage, which suggests a value of 0.6 for the irrepairable damage.

$D < 0.1$	No damage.
$0.1 \leq D < 0.2$	Minor damage–light cracking–very easy to repair.
$0.2 \leq D < 0.4$	Moderate damage–severe cracking, cover spalling–repairable.
$0.4 \leq D < 0.6$	Severe damage–extensive cracking, reinforcement exposed–repairable with difficulties.
$0.6 \leq D < 1.0$	Severe damage–concrete crushing, reinforcement buckling–irrepairable.
$D = 1.0$	Complete collapse.

CHAPTER FIVE

DAMAGE OF A COUPLING BEAM

This chapter describes in detail the experimental program and damage analysis of a full-scale coupling beam. The objective of this study is to apply the proposed damage model to a structural element other than a bridge column, in order to explore the possibility of extending the application of the model.

Typical high-rise buildings in Vancouver have coupled walls to resist lateral loads due to earthquakes. Figure 5.1 illustrates a typical coupled wall system. The system is designed with the shear walls coupled by beams (the coupling beams) that are the weak ductile links to dissipate the energy from earthquakes. These beams are usually designed to sustain large displacement demands.

5.1 EXPERIMENTAL PROGRAM

The design and construction of the specimen was done by the author as part of this thesis, while the testing was done in collaboration with Gonzalez. The analysis of the data presented in this chapter and in Appendix A was done by Gonzales (Gonzales, 2001).

This section describes the experimental program including specimen geometry, materials properties, instrumentation, testing procedure, and experimental results and observations.

Many high-rise building in the Vancouver area are residential structures with 8 ft (2440 mm) clear floor to ceiling, 6 in. (150 mm) concrete plate, and 7 ft (2134 mm) high and 4 ft (1220 mm) long door openings, resulting in a beam of 18 in. (457 mm) deep that couples the shear walls. The specimen tested herein consists of a full scale coupling beam and portion of the shear walls as shown in Figure 5.2 to simulate the rigidity of the shear walls, which imposes rigid rotational stiffness of the beam to wall connections.

5.1.1 Test Specimen

The coupling beam has a rectangular cross section of 17.5 in. (445 mm) deep, 12 in. (305 mm) wide, and 48 in. (1220 mm) long. These dimensions result in a beam with a 2.75 span to depth ratio. Each of the end walls was 15 in. (381 mm) thick, 48 in. (1220 mm) wide and 45 in. (1143 mm) high as shown in Figure 5.2.

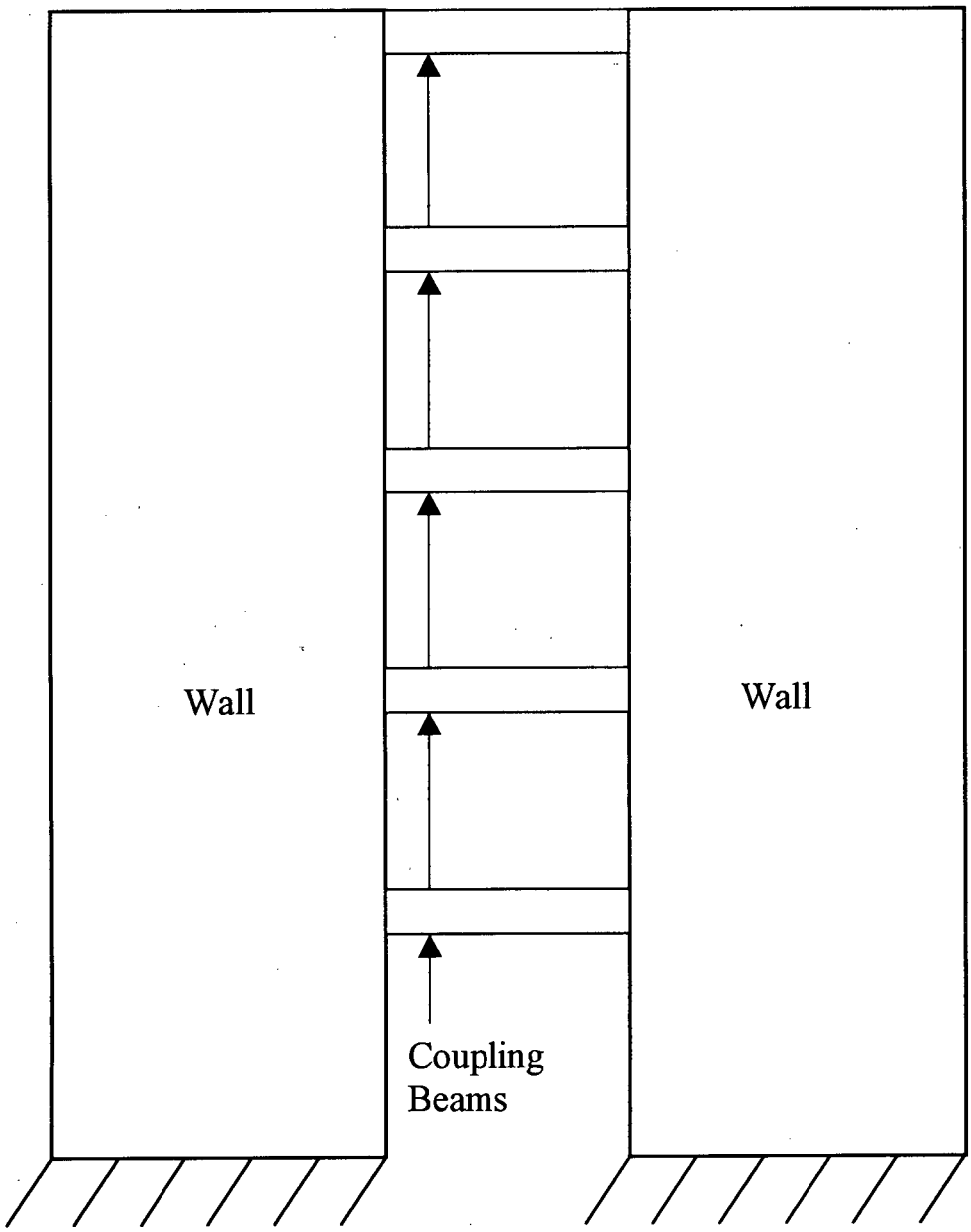

Figure 5.1: Coupled wall system.

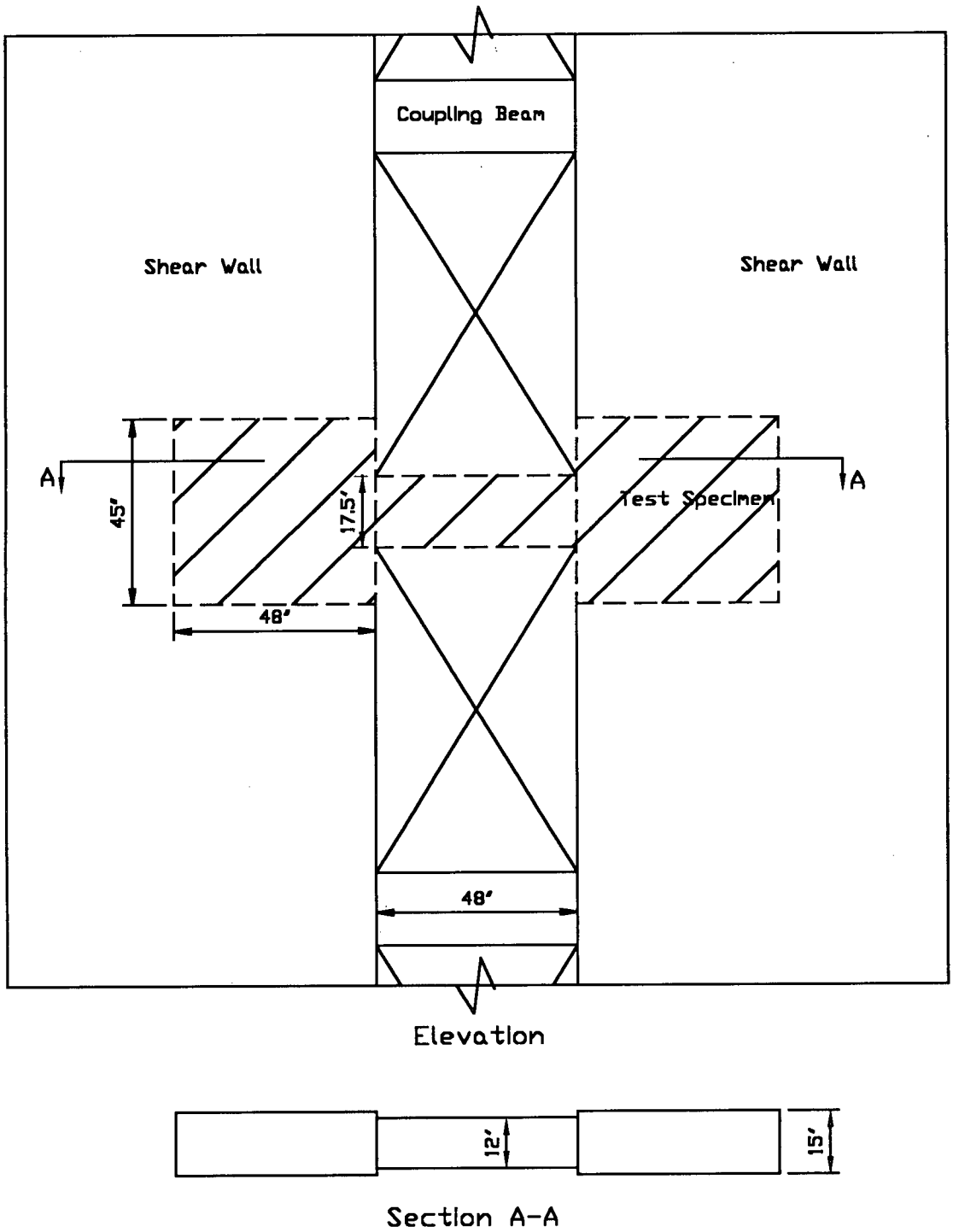

Figure 5.2: Location and dimensions of test specimen.

Figure 5.3 shows the reinforcement details of the specimen. The design of the coupling beam was in accordance with the provisions of Chapter 21 of the Canadian concrete code (CSA-A23.3, 1994). Four 30M weldable grade diagonal bars were provided in each direction. The centerline of the four diagonal bars was a distance of 3.5 in. (89 mm) from the face of the beam at the ends of the coupling beam to provide minimum clear cover of 1.0 in. (25 mm) as shown in Figure 5.3. The centerline of the reinforcement resulted in a diagonal angle of 12.3 degrees.

According to the Canadian concrete code (CSA-A23.3, 1994), the diagonal bars have to extend in the wall a minimum distance of 1.5 l_d (where l_d is the bar development length), which is 69.7 in. (1770 mm), while the available distance in the walls is only 49 in. (1250 mm). Thus the diagonal reinforcement continues through the walls and is welded to a steel plate to provide the required development length. 10M ties at 4 in. (100 mm) spacing, which is the minimum of 6 d_b (7 in.), 24 tie diameter (9.5 in.) and 4 in., as shown in Figure 5.3 were provided to tie the four diagonal bars in each direction within the coupling beam. Four 10M straight longitudinal reinforcement bars were provided in the coupling beam to support the stirrups. They extend about 7 in. (178 mm) into the end of the walls. Five 10M stirrups, spaced at 9.6 in. (244 mm) with the first one at s/2, were provided in the coupling beam as shown in Figure 5.2. This spacing corresponds to approximately h/2 as required by the Canadian concrete code (CSA-A23.3, 1994).

5.1.2 Material Properties

5.1.2.1 Concrete

The concrete was cast in July 1999 using one batch of concrete from a ready-mix supplier, while the specimen was tested in July 2000 and continued for three days; therefore, the concrete aged for about one year. The 28-day compressive strength of the concrete was specified to be 45 MPa. In order to obtain the actual compressive strength of the concrete, four standard cylinders with a 6 in. (152 mm) diameter and a 12 in. (305 mm) length were cast along with the specimen in July 1999. The cylinders were tested according to CSA A23.2-9C in UBC Materials Laboratory. All cylinders were tested a

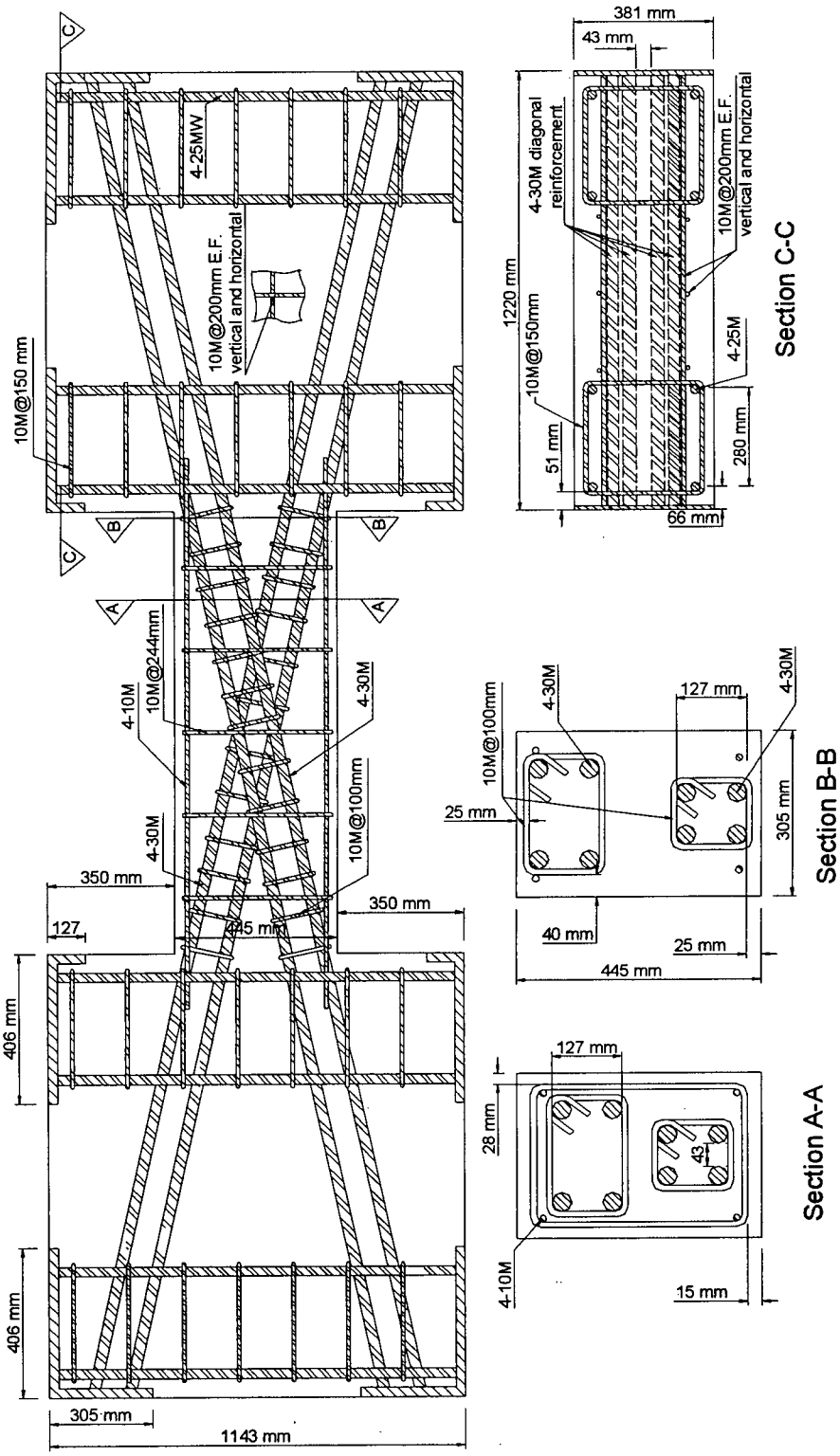

Figure 5.3: Reinforcement details.

few days after testing the specimen. The results of the four cylinder compression tests are shown in Table 5.1. Note that the measured average strength of the concrete (35.6 MPa) was considerably lower than the specified strength (45 MPa).

Table 5.1: Cylinder compression test results.

Cylinder	**f'_c (MPa)**
1	34.7
2	35.7
3	37.2
4	35.0
Average	*35.6*

5.1.2.2 Reinforcement

Reinforcement used in the test specimen consisted of weldable and regular deformed bars. The reinforcement was grade 400 MPa and met the requirement of CSA G30.18. The specified tensile property requirements are a minimum yield strength of 400 MPa and a minimum tensile strength of 600 MPa. 10M bars were used for ties, stirrups, and longitudinal reinforcement in the coupling beam, while 10M, and 25M weldable grade bars were used in the walls. 30M weldable grade bars were used for the diagonal reinforcements. The nominal area of 10M, 25M and 30M reinforcing bars is 100 mm^2, 500 mm^2 and 700 mm^2, respectively.

Two coupon tests were performed on the 30M diagonal reinforcing steel to determine the stress strain relationship, which is shown in shown in Figure 5.4a. Tests indicated

average yield stress, f_y, and average modulus of elasticity, E_s, of 490 MPa and 200,000 MPa respectively. The corresponding calculated yield strain $\varepsilon_y = f_y/E_s$, is 0.00245.

Two force-displacement tests were also performed on the 30M diagonal reinforcing steel to determine the effective yield strength, $f_{y\ eff}$, of the bar as shown in Figure 5.4b. Tests indicated an average yield force, F_y, of 325 kN. The corresponding calculated effective yield strength, using 700 mm^2 nominal area and 325 kN yield force, $f_{y\ eff} = F_y/A_n$ is 464 MPa.

5.1.3 Construction of Test Specimen

The specimen was constructed in the University of British Columbia Structures Laboratory. The procedure is briefly described below.

As shown in Figure 5.5, eight steel corner plates were constructed using ½ in (12.5 mm) thick steel plate, which were welded to the diagonal reinforcement (30M bars) to provide enough development length and also welded to the concentrated reinforcement in the walls (25M bars). The four exterior corner plates, which were located at the outside faces of the walls, were 16 × 12 × 15 in. (406 × 305 × 381 mm). The four interior corner plates, which were located at the inside faces of the walls, were 16 × 5 × 15 in. (406 × 127 × 381 mm).

The specimen was cast horizontally (lying down) for simplicity. Formwork was constructed for the bottom and side faces of the specimen. The steel corner plates were put in their places in the form and welded to the diagonal reinforcement (30M) of the coupling beam and the longitudinal concentrated reinforcement (25M) of the walls after all the pre-cut and pre-bent ties and stirrups were placed in their locations. Then the reinforcement with the corner plates were positioned vertically as shown in Figure 5.5 to tie all the reinforcement in the coupling beam and the walls. The complete reinforcement was then lifted and put in place in the form. Two steel hooks were inserted and

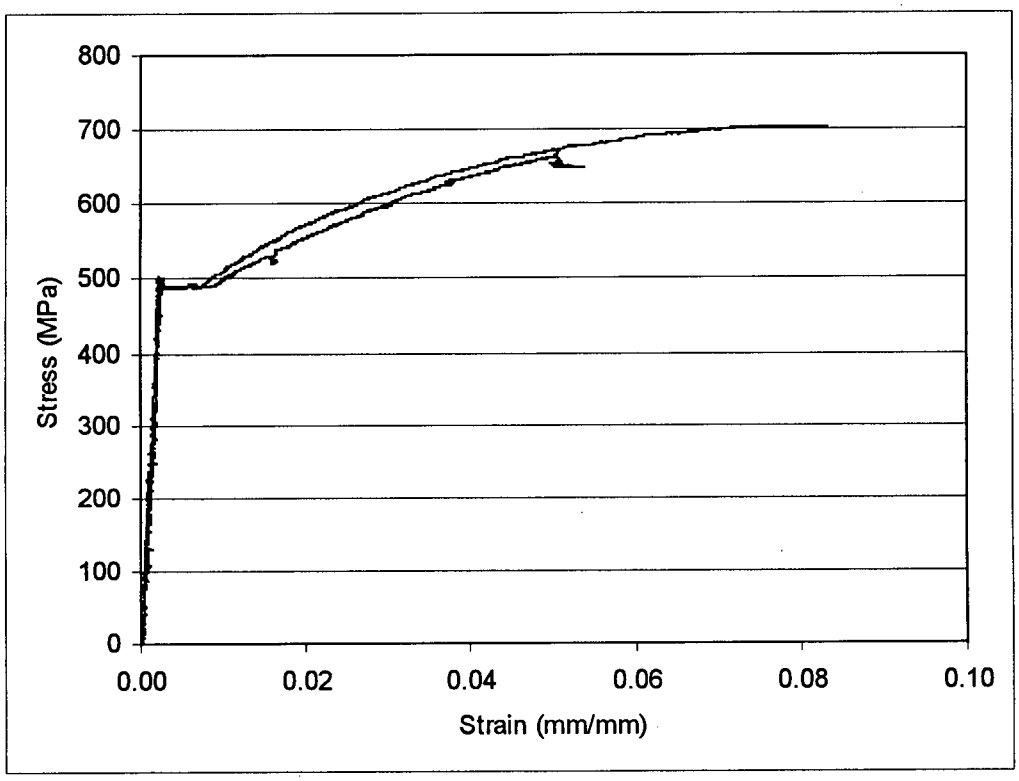

Figure 5.4a: Stress-strain relationships from coupon samples of 30M bars.

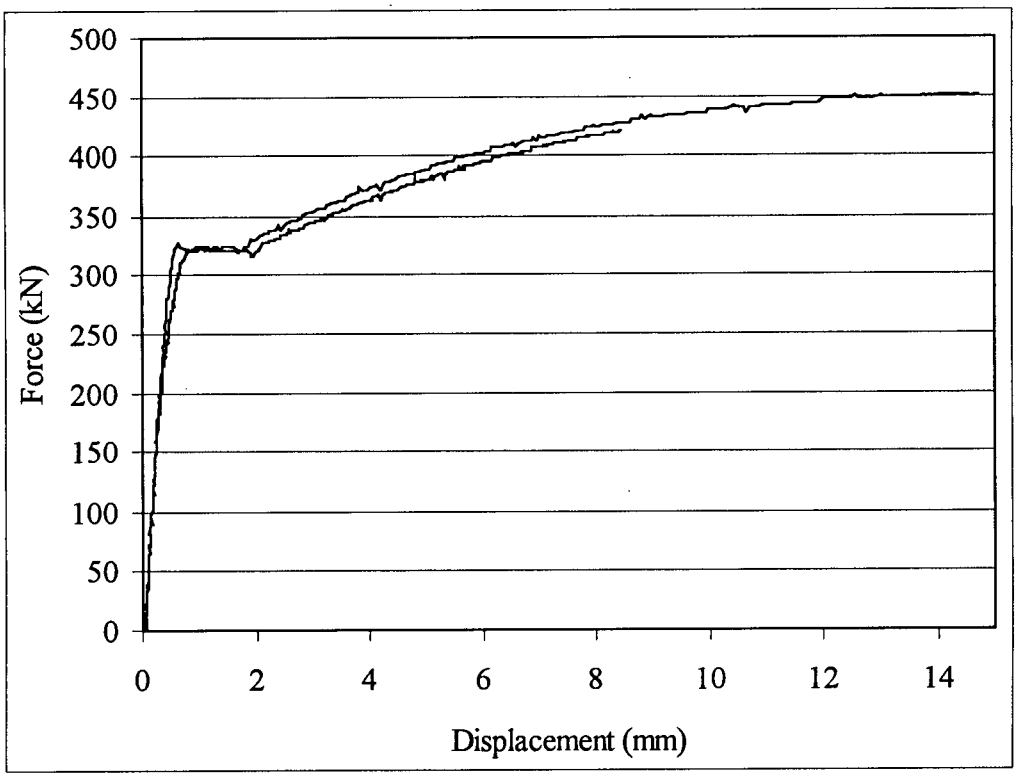

Figure 5.4b: Measured force-displacement relationships of 30M bars.

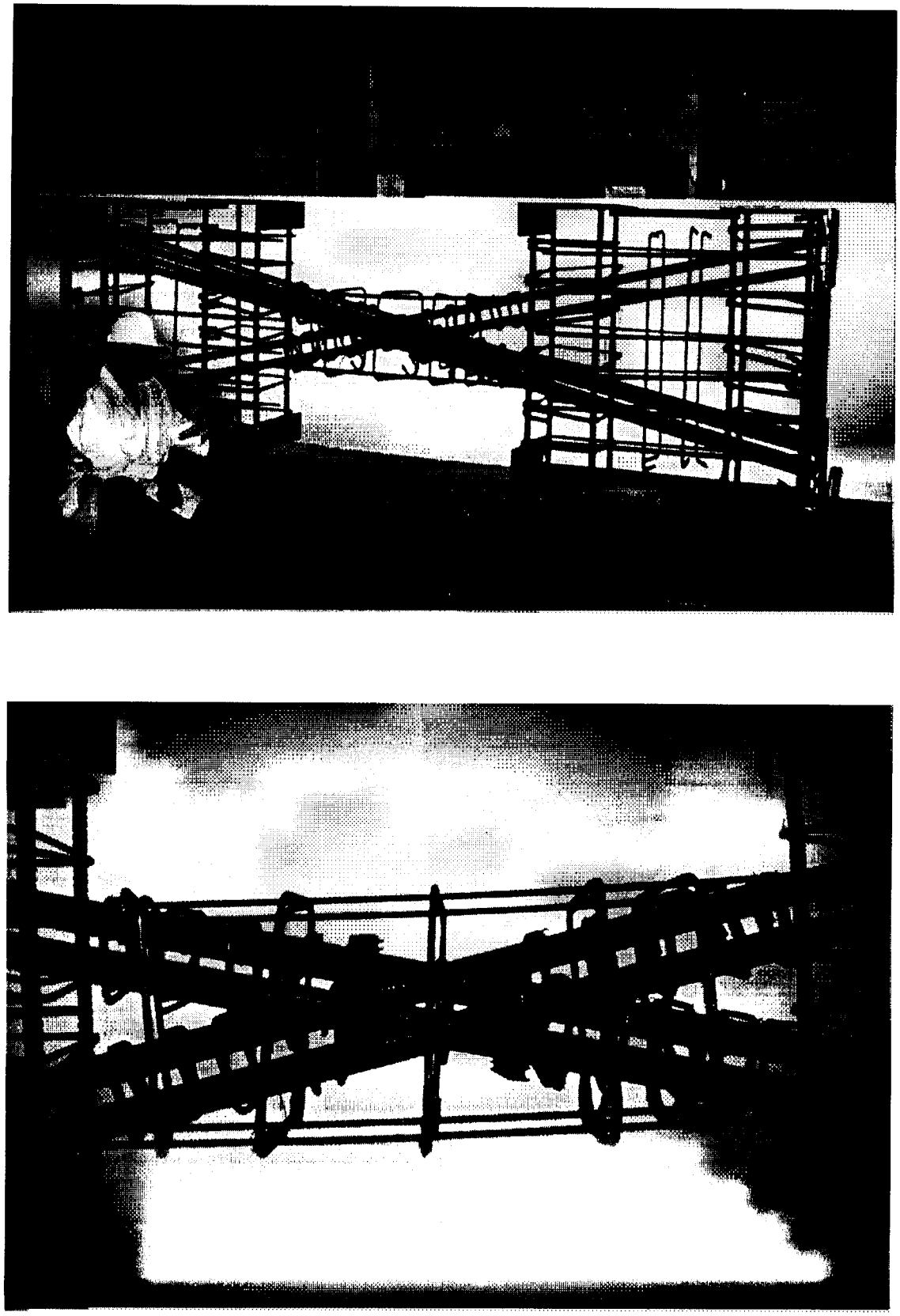

Figure 5.5: Reinforcement construction.

tied to the reinforcement in the top face of each wall. The hooks were later used to lift the specimen. Six strain gauges were placed on the diagonal reinforcement. The locations of the strain gauges are described later in this chapter.

Four sheet metal ducts, which had a 11 in. × 1.6 in. (275 × 40 mm) cross section, were constructed and placed inside the concentrated reinforcement of the walls and attached to holes in the steel corner plates to run Dywidag bars inside them in order to connect the specimen to the supporting system.

The ready-mix concrete was placed in the specimen form. The concrete was consolidated using an immersion type vibrator and then screeded to the specified thickness of the coupling beam and the walls. The concrete top surface was given a smooth finish using a wood trowel.

Two days after casting the concrete, the forms were removed from the sides of the specimen, while the specimen was removed from the casting bed after four weeks and placed horizontally on wood supports. The specimen was left to cure inside the Structures Laboratory for about one year.

5.1.4 Test Set-Up

Figure 5.6 shows the test set-up. Two steel plate beams were connected to the specimen using 1 3/8 in. (35 mm) diameter Dywidag bars. The first steel beam (supporting beam) was fixed to the floor using steel rods and concrete bases in order to prevent one of the walls from moving and rotating. Three hydraulic actuators were attached to the second steel beam (loading beam). The loading beam was supported vertically by a Teflon sliding bearing system to allow for horizontal movement and prevent any uplifting. The specimen self-weight was supported on Teflon bearings to reduce friction.

Each hydraulic actuator has a two-way capacity of 800 kN. As shown in Figure 5.7, the two actuators A and B were mainly used to apply the load, while the actuator C was used

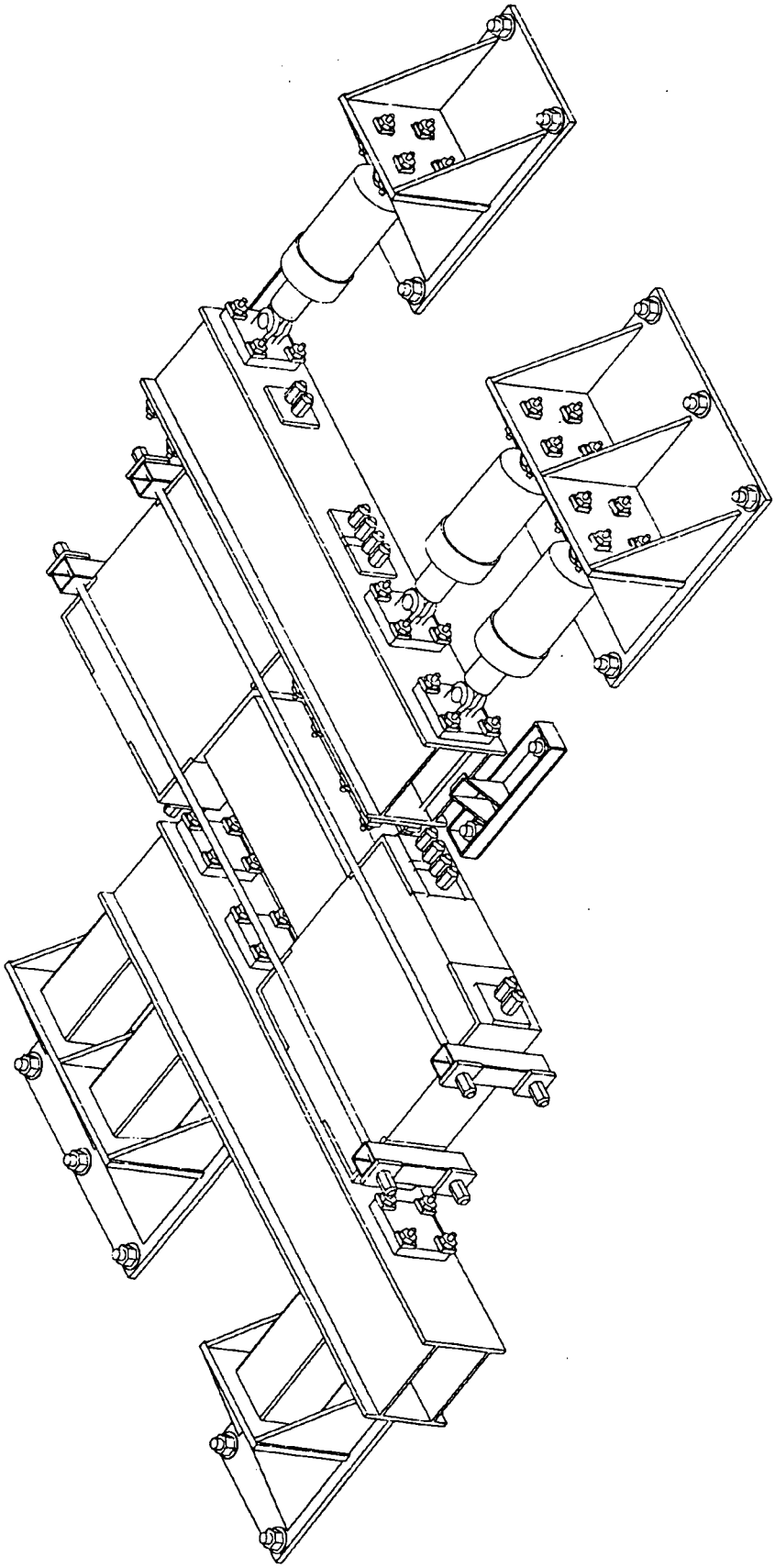

Figure 5.6: Test set-up.

to control the rotation of the wall and keep it zero to assure the two walls remained parallel to each other, as is the case in coupled shear walls under seismic loading.

Two 1 3/8 in. diameter Dywidag bars were attached longitudinally on each side of the coupling beam to simulate the axial stiffness of the flat slab, which is not constructed as part of the specimen.

The resulting force applied by the two actuators A and B coincides with the center of the coupling beam; therefore the coupling beam was subjected to double curvature with pure shear at the center, except when the actuator C applied some load. The loading and the resulting sectional forces are summarized in Figure 5.7.

5.1.5 Instrumentation

The measured pressures in the three actuators A, B and C were calibrated in terms of forces to calculate the shear force, V, applied to the coupling beam. The magnitude of the applied load (shear force, V) was determined by adding the forces in the three actuators.

Two LVDT's were attached to wall 2 and used to measure lateral displacements of wall 2 (loaded wall) as shown in Figure 5.8. An aluminum channel was mounted on wall 1 as a reference to measure lateral displacement of wall 2 relative to wall 1. The two LVDT's were connected to the aluminum channel as shown in Figure 5.8. LVDT1 is used to measure the lateral displacement (Δ as shown in Figure 5.7) between the two ends of the coupling beam since wall 1 is totally fixed. The difference between the readings of the two LVDT's was used to measure the rotation of wall 2.

The longitudinal strains in the diagonal reinforcements within the coupling beam were measured using six strain gauges as shown in Figure 5.9. In each diagonal direction, three strain gauges were attached to one diagonal bar: one at each end and one at the middle of the coupling beam. In order to measure the average strains in the concrete of

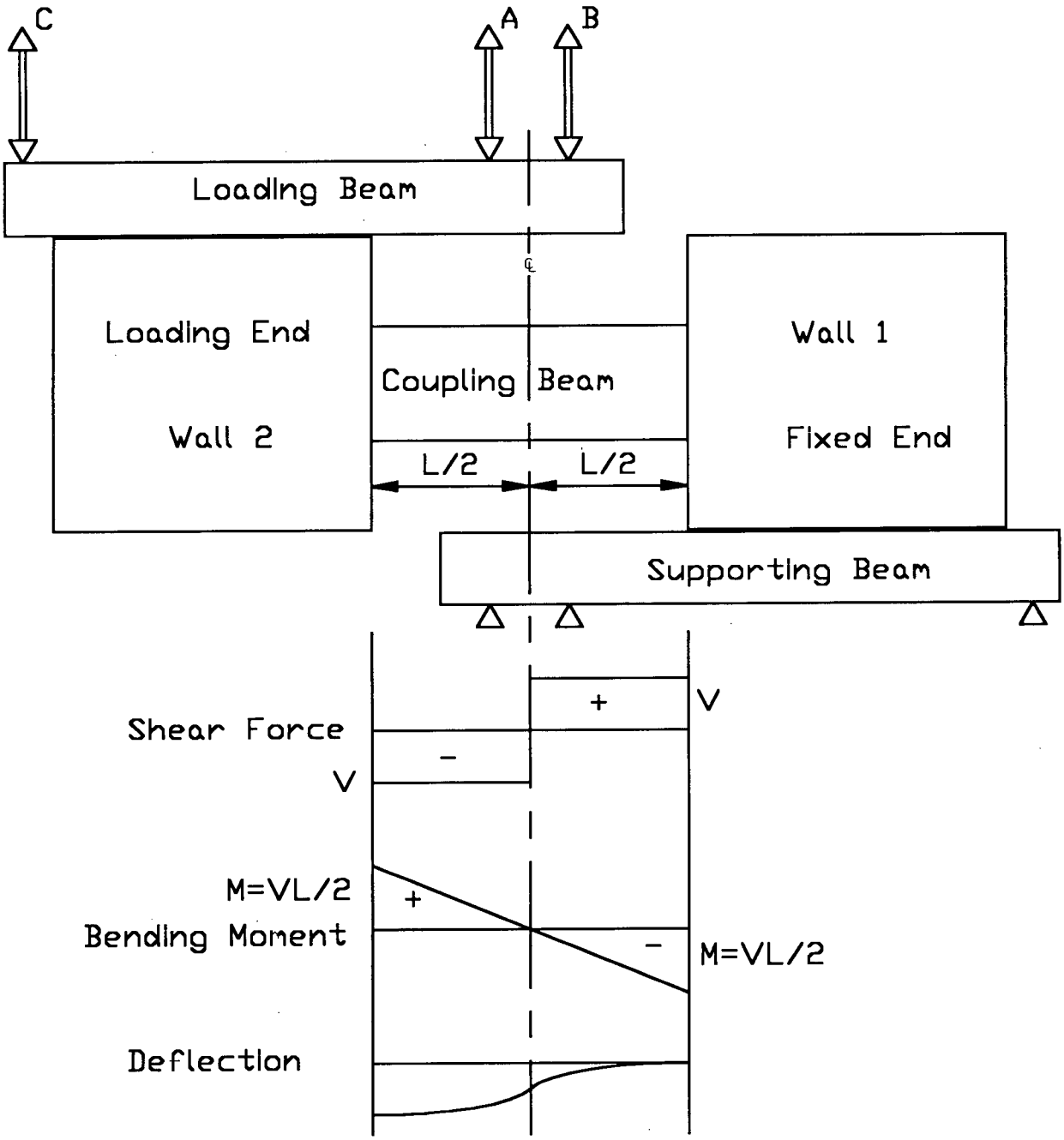

Figure 5.7: Loading and sectional forces.

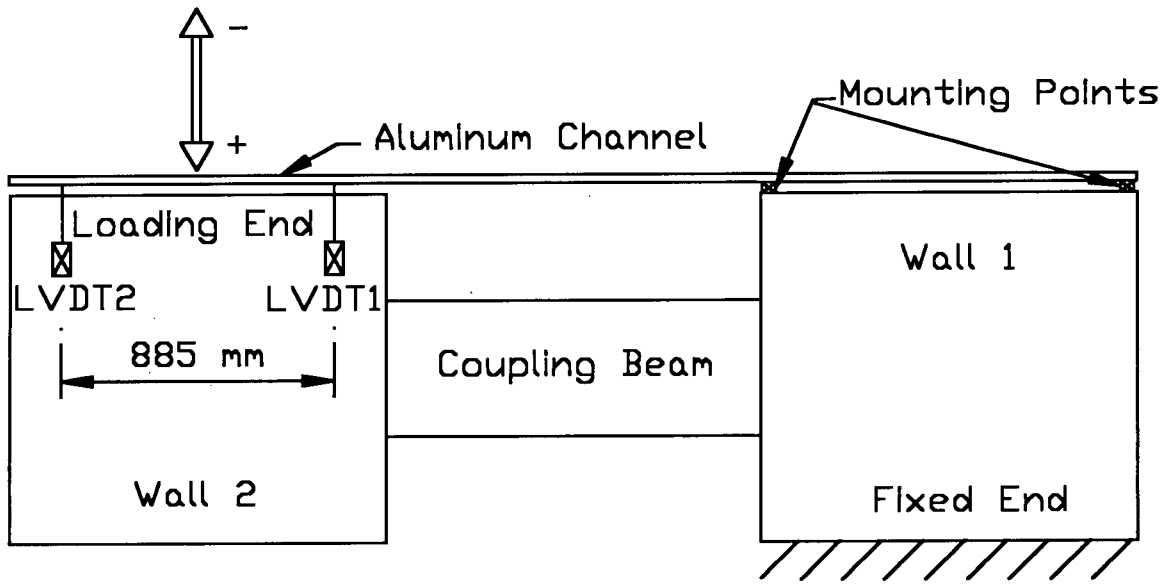

Figure 5.8: Location of the LVDT's.

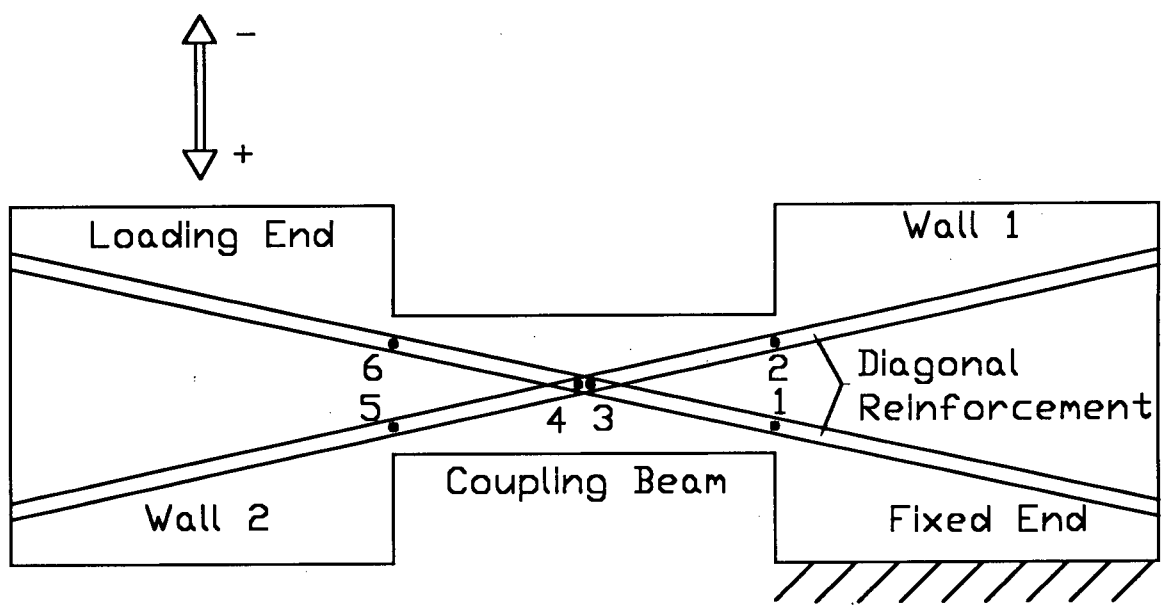

Figure 5.9: Location of the strain gauges.

the coupling beam, 9 targets were mounted as shown in Figure 5.10. The distances between these targets were measured using a digital caliper at numerous stages.

The axial loads in the Dywidag bars that provided the axial restraint were measured using four load cells as shown in Figure 5.11. One load cell was attached to each Dywidag bar.

The electronic signal from the pressure transducer, the six strain gauges, the two LVDT's and the four load cells were converted from analog to digital data, and recorded by a personal computer equipped with a data acquisition program. The data was recorded every second.

The cracks in the top face of the coupling beam and the walls were marked with lines adjacent to the cracks using a black pen. The crack widths were measured with a crack comparator. A sticker with the width in millimeters was attached to the concrete next to the crack and the crack patterns were photographed.

5.1.6 Testing Procedure

The Applied load was controlled by regulating the pressures in the three hydraulic actuators A, B and C. The hydraulic pressure was controlled using a "load maintainer", which is a mechanical device that works on the principle of a moment balance between a pressure acting on a differential area hydraulic piston and a moveable weight on a fulcrum arm (Kelsey Instruments, 1992). The load maintainer provided simple reliable load control of the actuators. In order to get equal hydraulic pressure in actuators A and B, the two actuators were connected to a common manifold, while actuator C was connected separately to a second manifold.

During the test, both the pressure in actuators A and B and the lateral displacement, Δ, were displayed on a computer screen. At several times during the test, it was decided to pause the loading in order to measure and manually record certain data or to check the

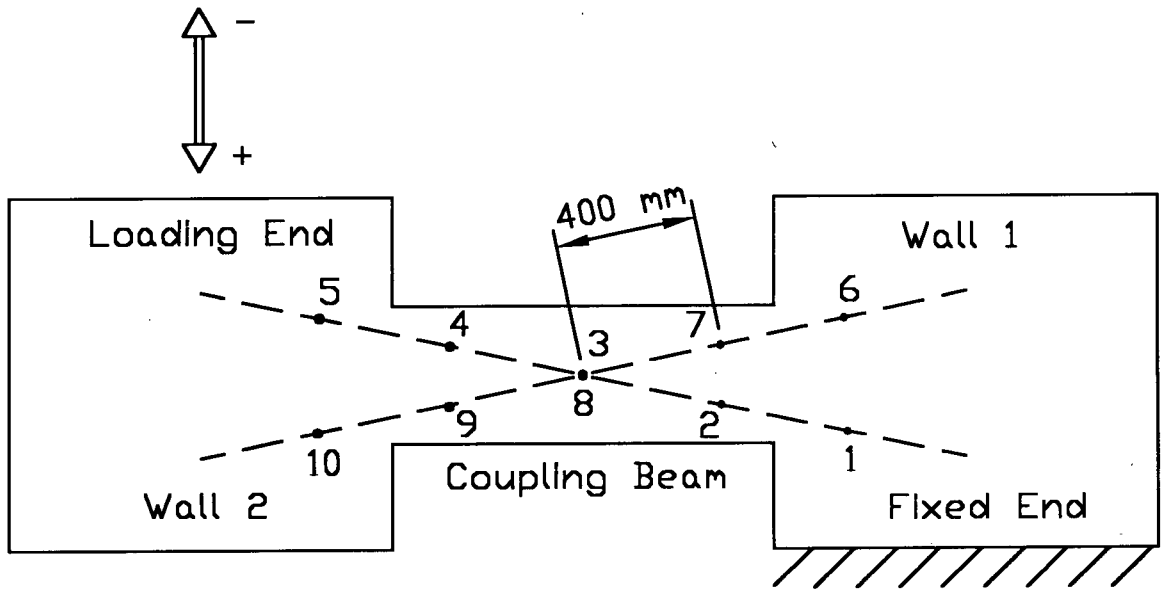

Figure 5.10: Location of the targets.

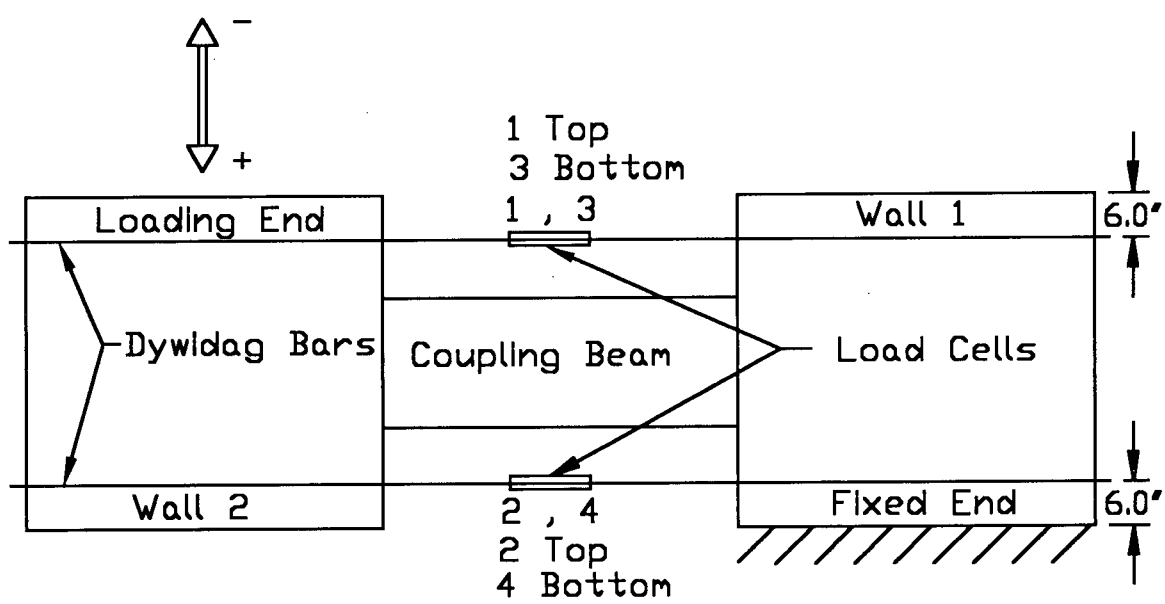

Figure 5.11: Axial restraints and load cells.

test set-up. During such cases, the displacements were maintained by reducing the applied load until the displacements stabilized.

During the load stages, the cracks in the concrete coupling beams and walls were marked, measured, and photographed as explained above. In addition, manual readings were taken of the distance between the target to calculate the average strain in the concrete coupling beam.

The initial readings in the four load cells were recorded as shown in Table 5.2. The initial axial loads in the Dywidag bars resulted from tightening the nuts.

Table 5.2: Initial axial loads in the load cells

Load Cell	Axial Load (kN)
1	77
2	93
3	74
4	77

The intended testing procedure was to cycle three times at every load or displacement level, starting with force-controlled loading until yielding is reached. Displacement-controlled loading would then be followed. The first loading stage was chosen at a load level of 320 kN, which does not produce any inelastic deformation. The specimen would then be loaded until yielding is reached. Then a displacement-controlled loading would be followed to load the specimen at different ductility levels. Each loading level was

chosen to consist of three complete reversal cycles as mentioned above. Due to a mistake during the test in calculating the total applied force by the hydraulic actuators, the first loading stage was over loaded and resulted in an applied force about twice that planned. This produced noticeable inelastic response in the first cycle of this stage. Thus, the specimen was subjected to force-controlled loading in the first stage, which consisted of four cycles as shown in Table 5.3. The loading was then controlled by the displacement as planned. Table 5.3 summarizes the loading cycles of all stages. Cycling was stopped at a maximum displacement of 80 mm. The specimen was then pushed monotonically from 80 mm until it failed at 156 mm.

5.1.7 Experimental Results and Observations

Figure 5.12 shows the hysteresis force-displacement loops obtained from the test with the load history as discussed above and shown in Table 5.3. For more clarity, Figure 5.13 shows the loops for the first four stages and the last four stages separately. Other results, such as strains in the diagonal reinforcement and axial forces in the axial restraints, are shown in Appendix A and can be found in detail in Adebar et al. (2001). It can be observed from Figure 5.12 that the specimen shows maximum shear strength of about 910 kN in the positive loading direction, while it shows a maximum of about 980 kN in the other loading direction (negative).

During the first loading stage, first flexural crack (very fine hair-line crack) occurred in the first cycle at a displacement and shear force of about 1.0 mm and 210 kN respectively. The first shear (diagonal) crack was also observed in the first cycle at a displacement and shear force of about 3.0 mm and 350 kN respectively. The cracks in the other direction of loading (negative loading) in this stage occurred at almost the same level of displacement and loading as above. Figure 5.14 shows the observed damage and the crack pattern of the first loading stage.

Table 5.3: Applied loading history.

Stage	Cycle	Displacement (mm)	Load (kN)	Stage	Cycle	Displacement (mm)	Load (kN)
1	1		662	5	14	42	
			-540			-41	
	2		516		15	40	
			-495			-42	
	3		511		16	41	
			-491			-41	
	4		516	6	17	51	
			-495			-50	
2	5	15			18	51	
		-14				-50	
	6	16			19	51	
		-11				-52	
	7	21		7	20	61	
		-8				-62	
3	8	21			21	70	
		-21				-71	
	9	21		8	22	81	
		-21				-80	
	10	21			PUSH	90	
		-23			PUSH	100	
4	11	34			PUSH	120	
		-30			PUSH	150	
	12	31			PUSH	156	
		-31					
	13	32					
		-31					

The cracks became significant at the end of the second stage at cycle number seven. The crack width of this stage was on the order of 0.3-0.8 mm as shown in Figure 5.15. Spalling of the concrete was initially observed at the third loading stage at approximately 20 mm lateral displacement. As shown in Figure 5.16, the spalling covered only two opposite corners of the coupling beam at its fixed ends. The cracks increased in frequency and width through this loading stage. A 1.5 mm wide shear crack was observed as shown in Figure 5.16. The concrete spalling expanded to cover all the four corners of the coupling beam at approximately 30 mm lateral displacement during the

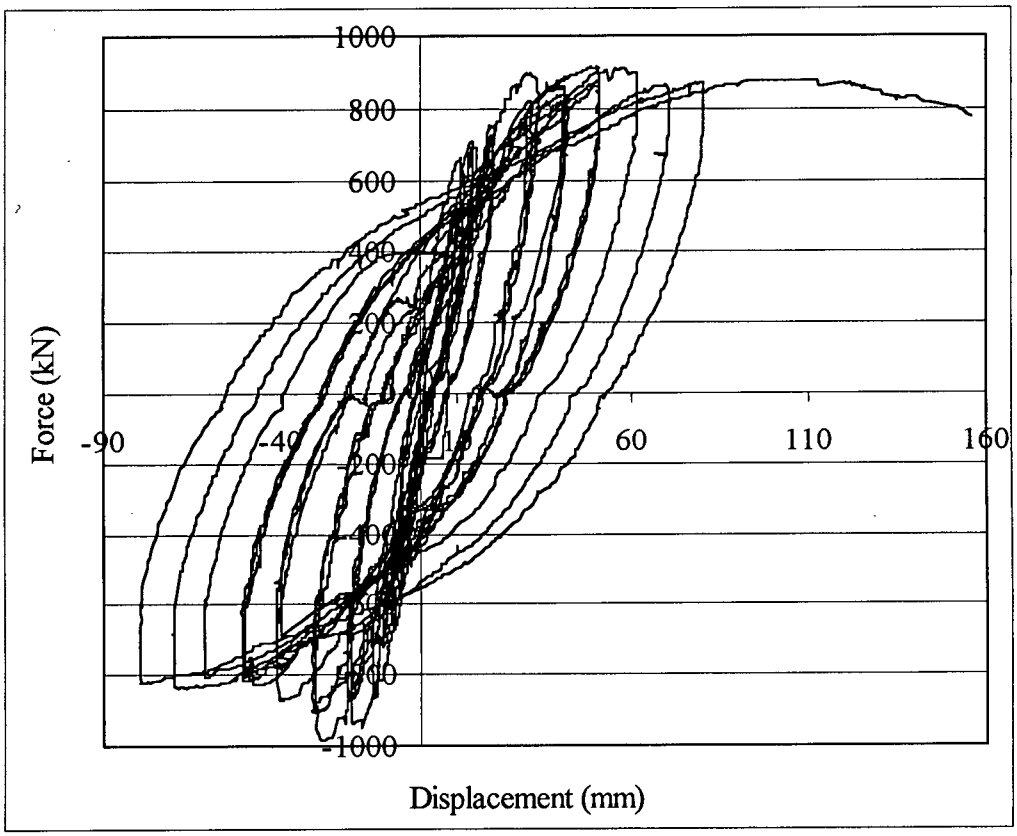

Figure 5.12: Experimental force-displacement hysteretic behavior.

forth loading stage. Figure 5.17 shows the crack pattern of this loading stage with crack width on the order of 1.0-3.0 mm. The damage, up to this point of loading as observed from the test, is still minor and would be easy to repair as shown in the previous photographs.

At stage No. 5, three complete cycles were performed at a lateral displacement of approximately 40 mm. The reinforcement started to be exposed and the concrete spalling became deeper as shown in Figure 5.18. The damage would still be repairable. At the end of cycle 19 at lateral displacement of 50 mm (stage No. 6), the spalling became significant and the shear cracks became wider as shown in Figure 5.19.

The spalling progressed through the last two stages (stages No. 7 and 8) as shown in Figures 5.20 and 5.21. The cycling stopped at the end of cycle 22 at a displacement of about 80 mm. The specimen was then pushed monotonically until it was considered

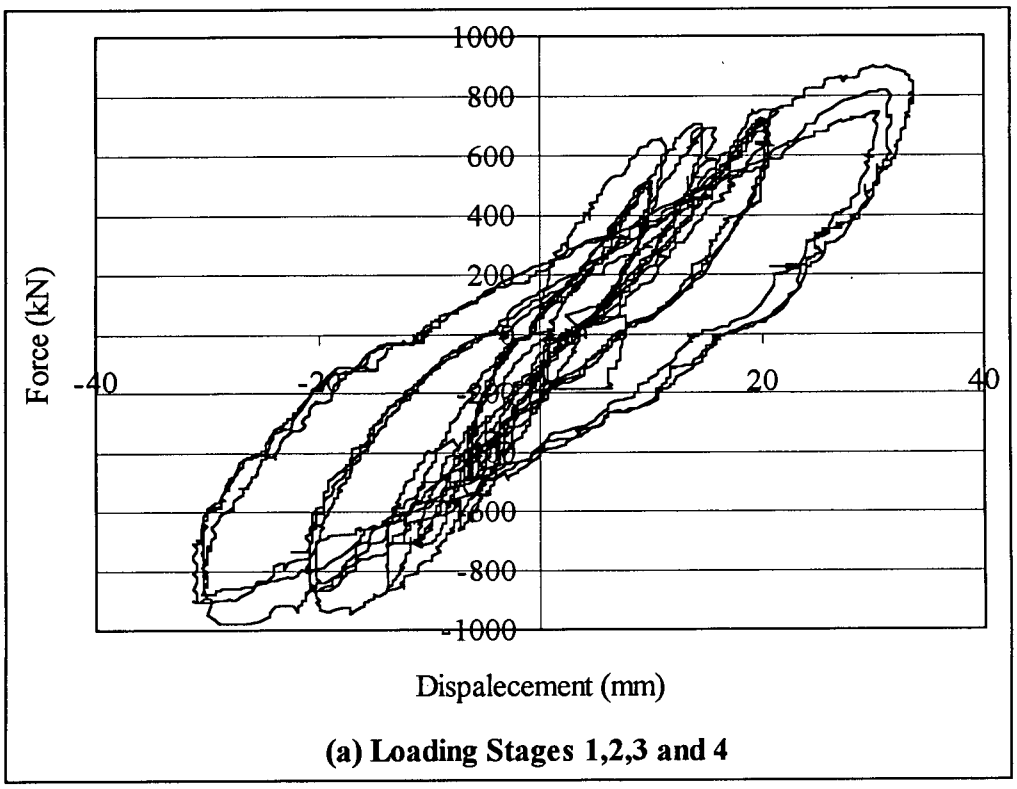

(a) Loading Stages 1,2,3 and 4

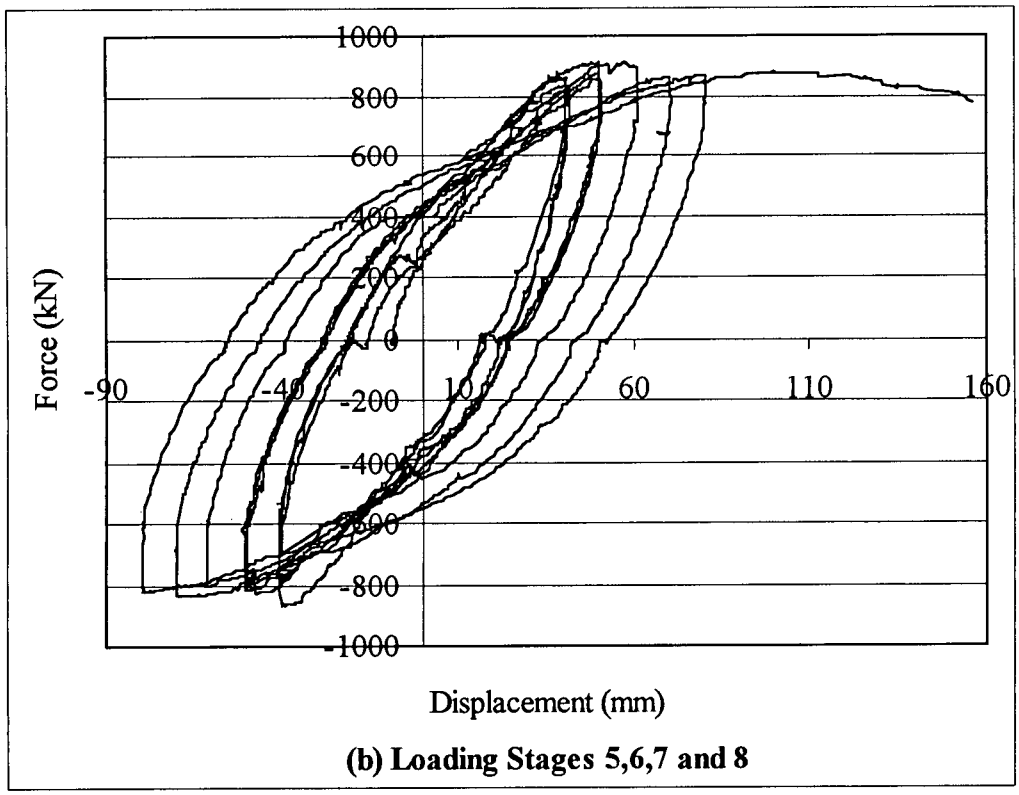

(b) Loading Stages 5,6,7 and 8

Figure 5.13: Experimental force-displacement hysteretic behavior.

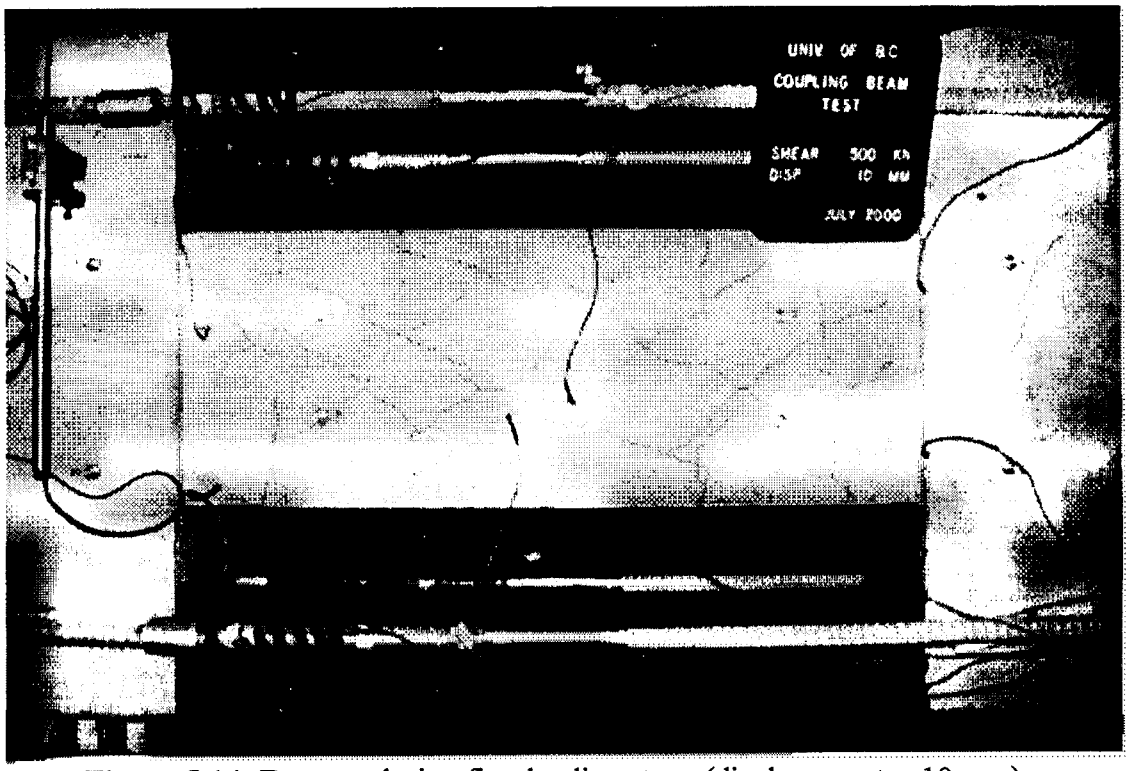

Figure 5.14: Damage during first loading stage (displacement = 10 mm).

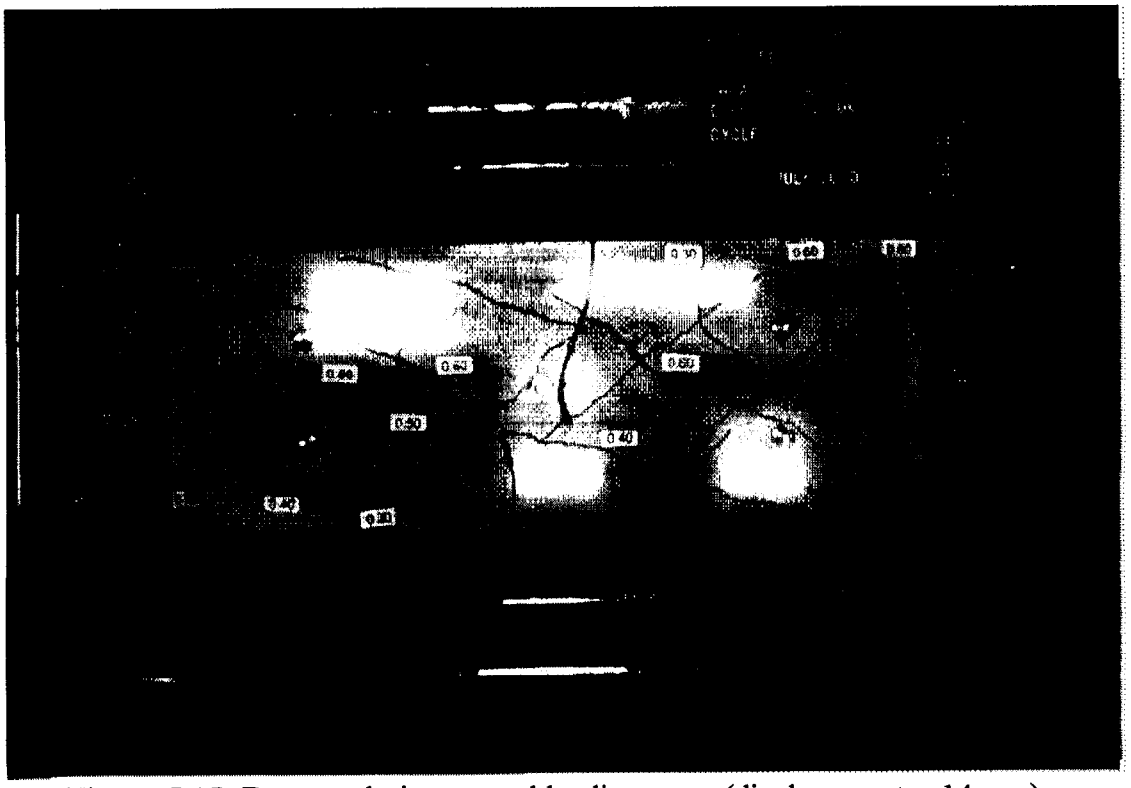

Figure 5.15: Damage during second loading stage (displacement = 14 mm).

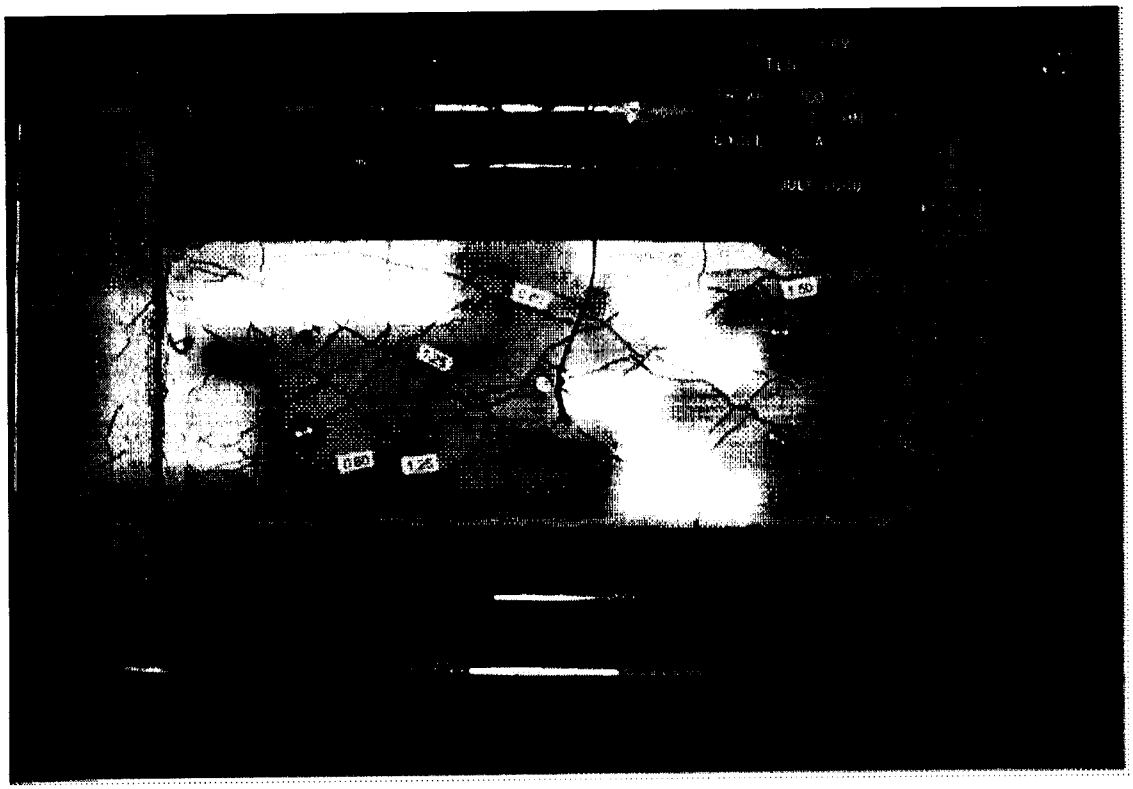

Figure 5.16: Damage during third loading stage (20 mm, concrete spalling).

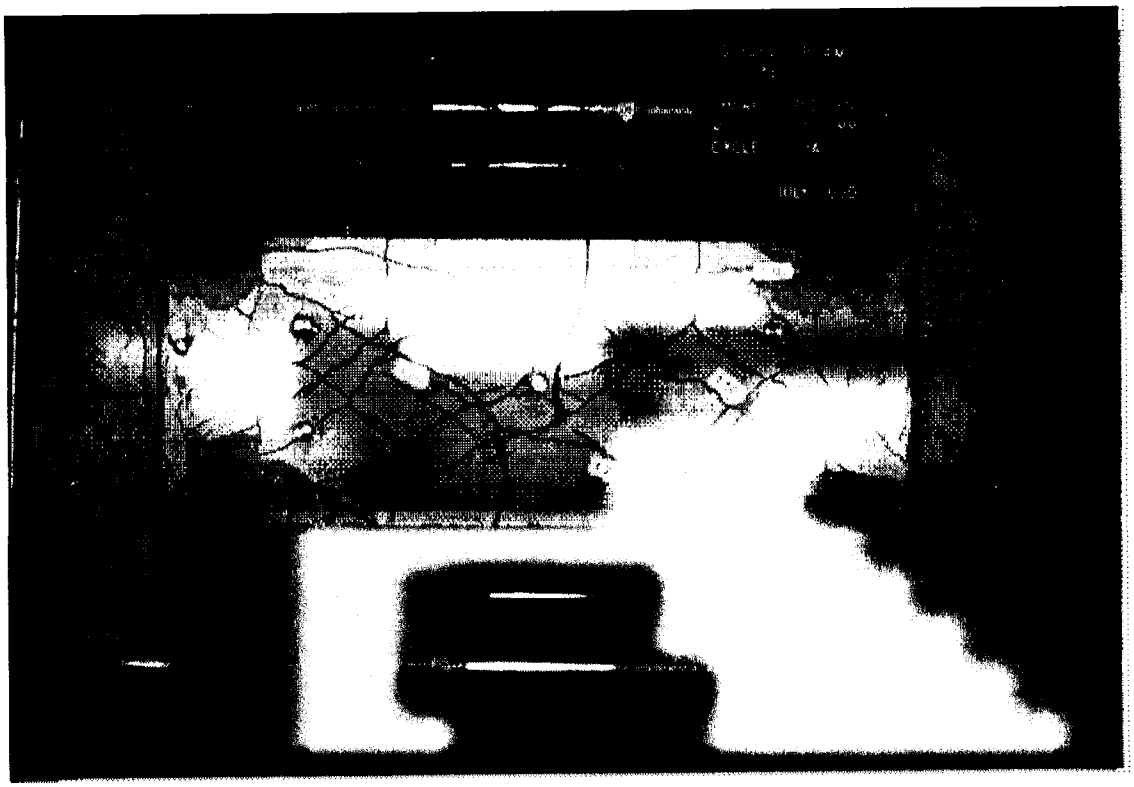

Figure 5.17: Damage during forth loading stage (displacement = 30 mm).

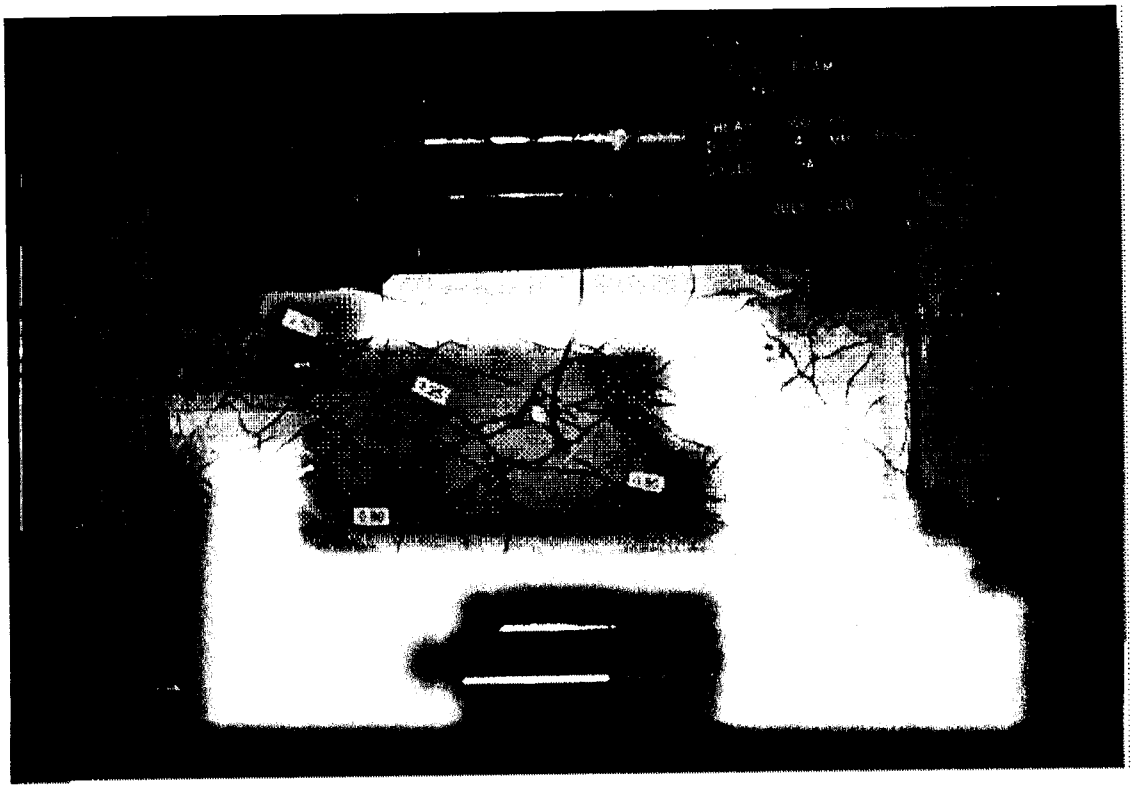

(a)

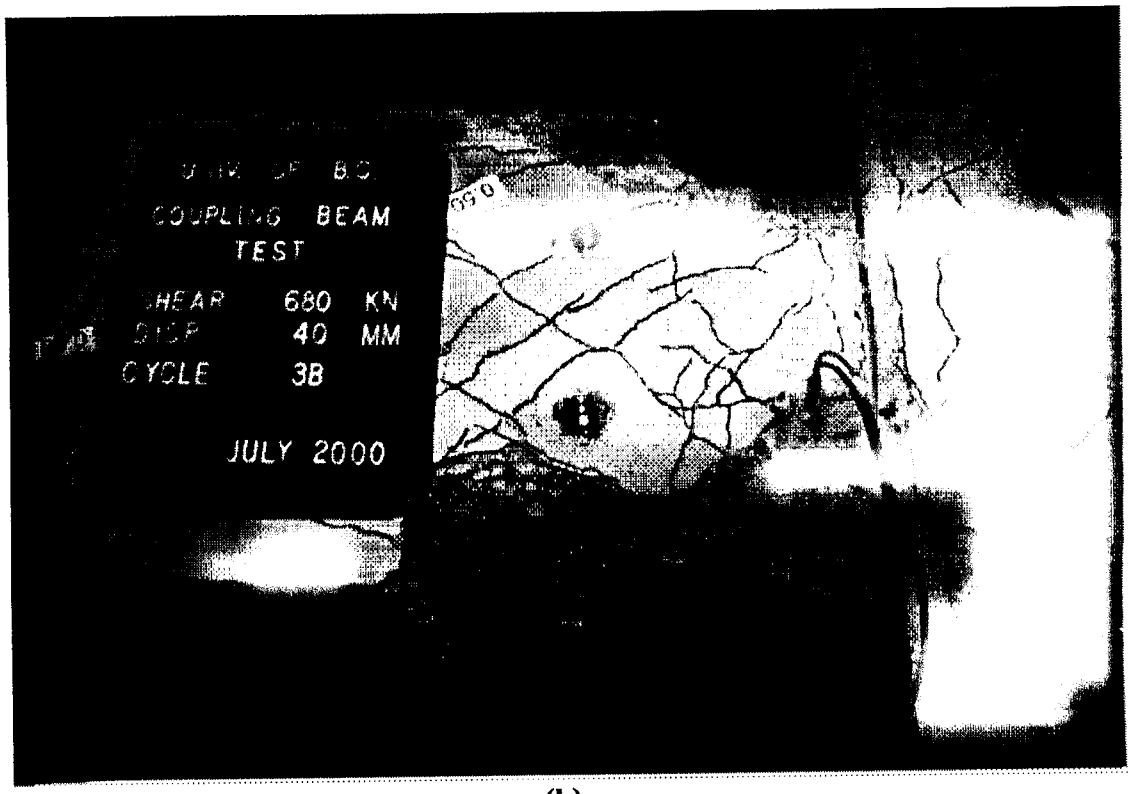

(b)

Figure 5.18: Damage during fifth loading stage (displacement = 40 mm).

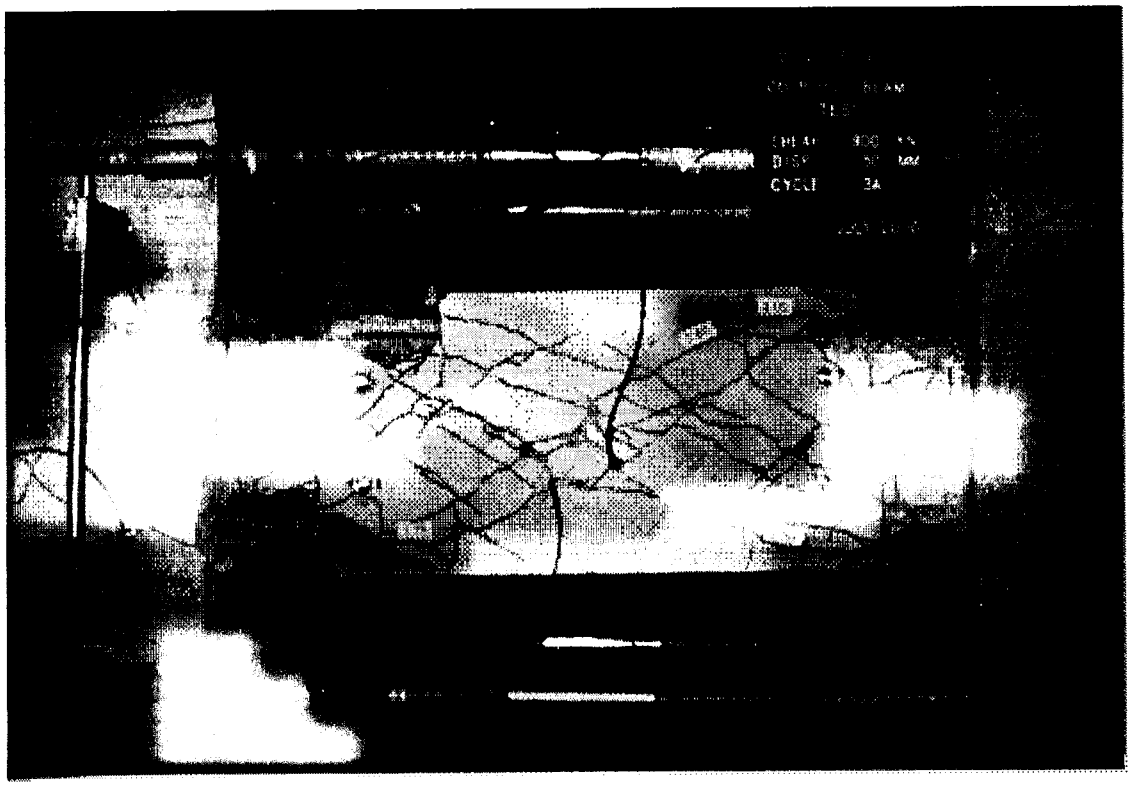

Figure 5.19: Damage during sixth loading stage (displacement = 50 mm).

failed at a lateral displacement of 156 mm, when the beam shear capacity dropped significantly. As shown in the photographs, the observed damage appeared repairable up to a lateral displacement of about 90 mm as shown in Figure 5.21. The damage became significant and irrepairable beyond that displacement in terms of very significant spalling, crushing of concrete, and buckling of the diagonal reinforcement. Buckling of the main diagonal reinforcement was noticed at a displacement of about 150 mm as shown in Figure 5.22.

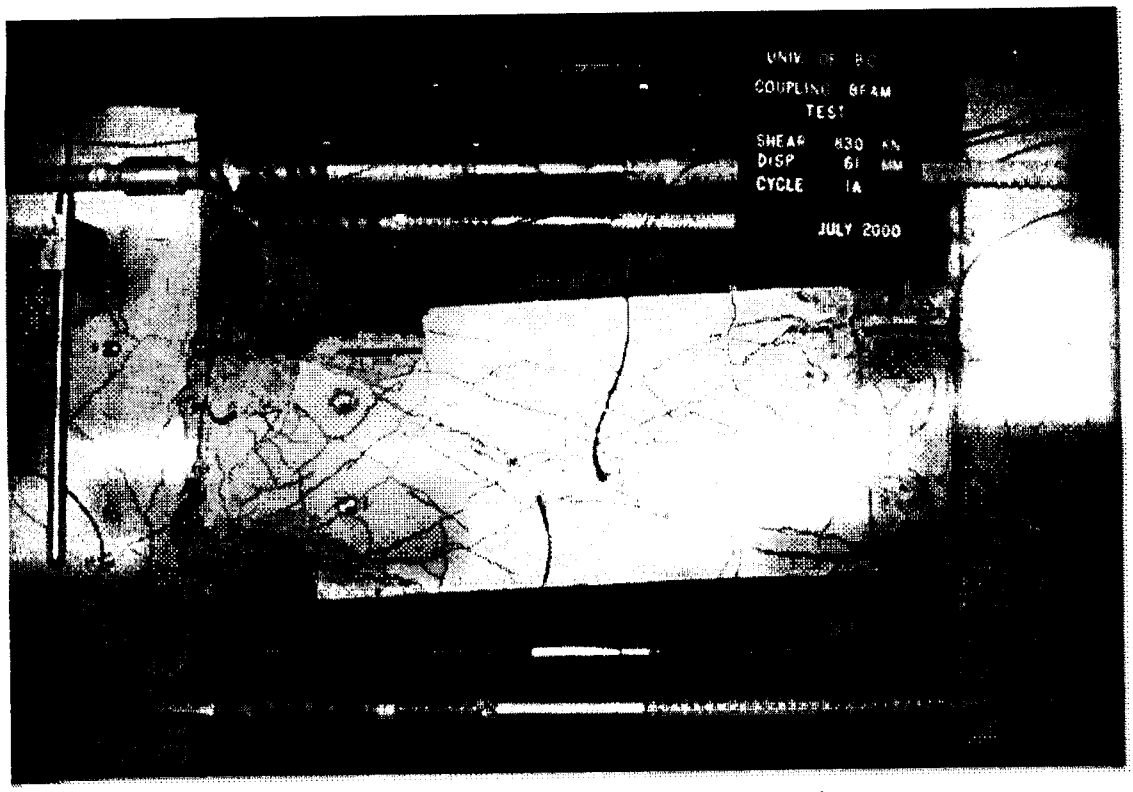

(a) Cycle No. 20 (displacement = 60 mm)

(b) Cycle No. 21 (displacement = 70 mm)

Figure 5.20: Damage during seventh loading stage.

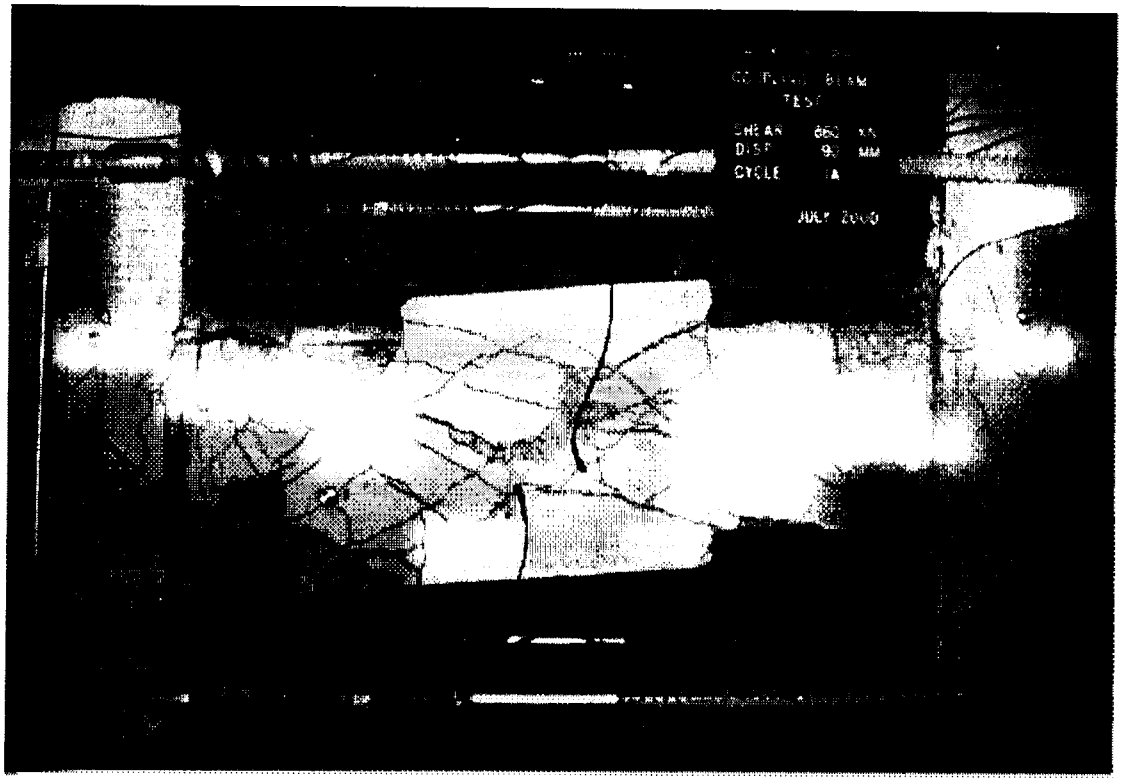

(a) Displacement = 90 mm

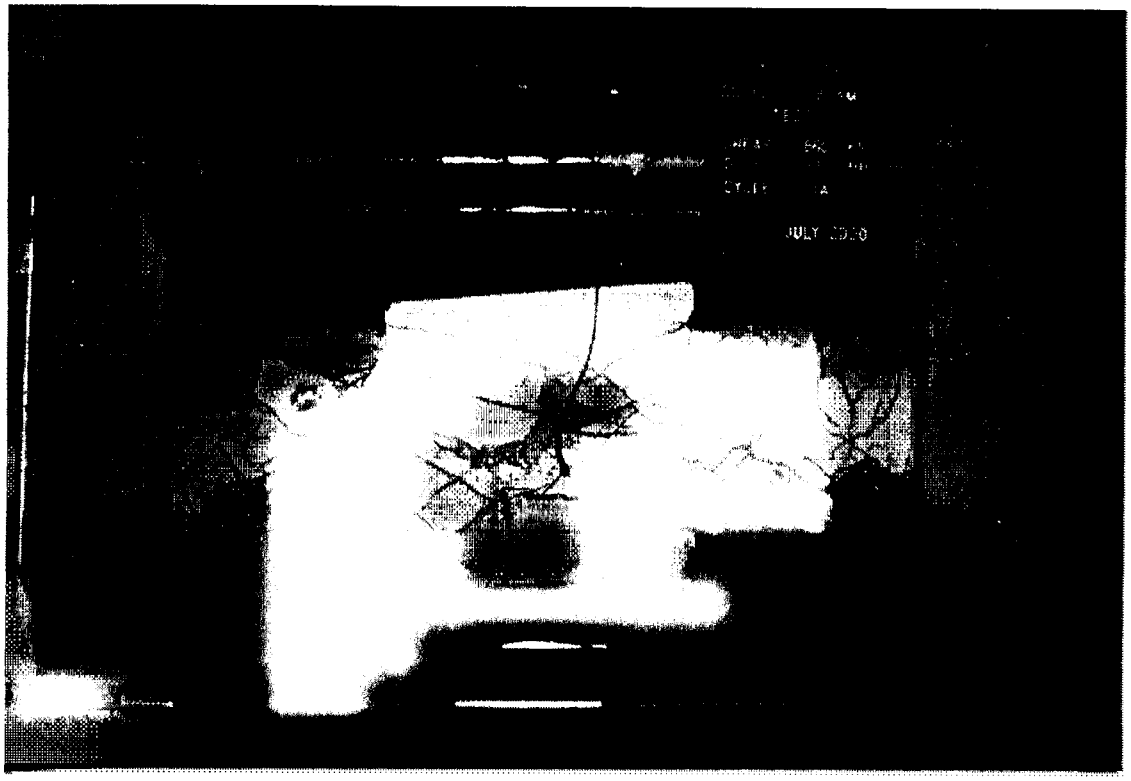

(b) Displacement = 100 mm

Figure 5.21: Damage during monotonic pushing (eighth stage, concrete crushing).

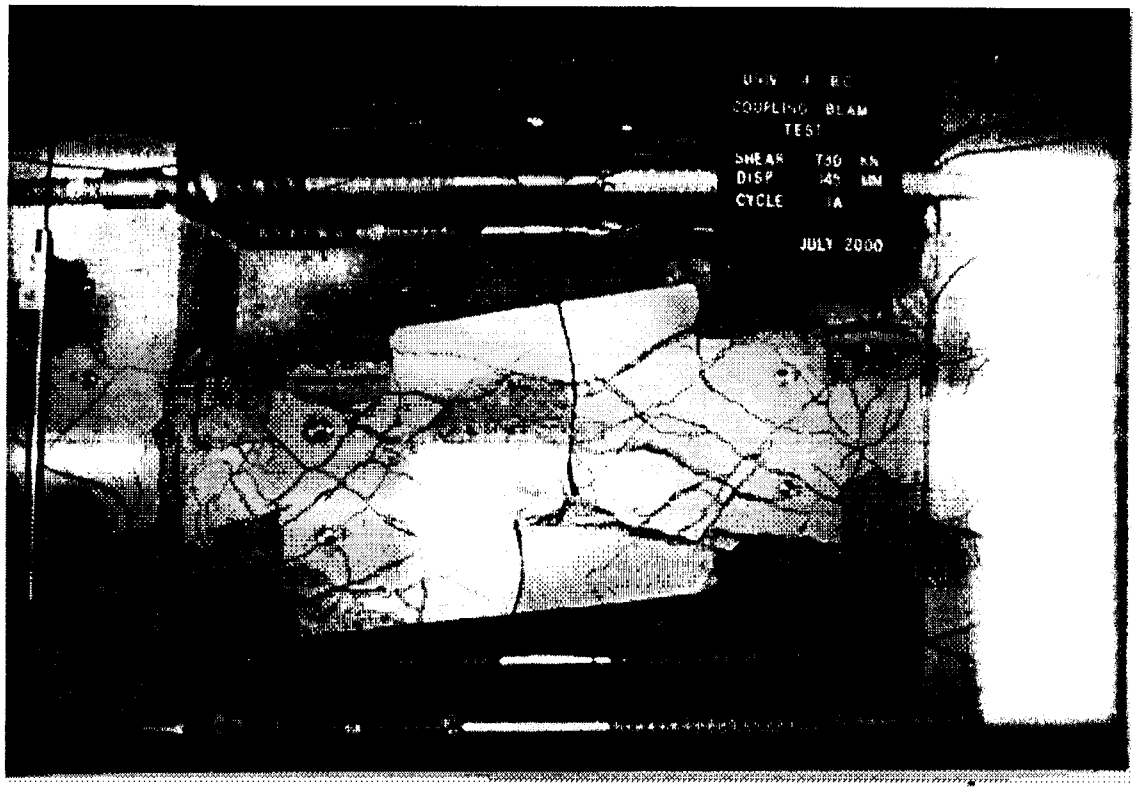

(a) Significant crushing (displacement = 145 mm)

(b) Buckling of 30M diagonal reinforcement (displacement = 156 mm)

Figure 5.22: Failure of the specimen (extensive crushing and buckling).

5.2 DAMAGE ANALYSIS AND COMPARISON

This section compares the observed damage to the predicted damage using the proposed damage model. A comparison between the predicted damage by the E1, E2 and P models is also presented. The E2 model is expected not suitable for this element since it was derived for flexural columns.

5.2.1 Monotonic Force-Displacement Envelope

The monotonic force-displacement envelope is needed to predict the damage using the proposed damage model as discussed in Chapter Three. The behavior and structural mechanics of a coupling beam with diagonal reinforcement is very different than a conventially reinforced element. Therefore, the procedures discussed in Chapter Three to predict the monotonic force-displacement for a regular reinforced column is not adequate here.

Paulay (1971) theoretically predicted the ultimate capacity of diagonally reinforced coupling beams based on the simple statically determinate model as shown in Figure 5.23. It was assumed that after the first yielding and load reversal only the diagonal reinforcement carries all the forces in tension and compression. According to Paulay (1971), the ultimate tensile, T_u, and compression, C_u, forces are identical at the development of yield strength as follows,

$$T_u = C_u = A_s f_y \tag{5-1}$$

Where A_s is the area of the diagonal reinforcement and f_y is the steel yield strength.

The resisting shear force of the beam, V_u, and the resisting moment at the supports of the coupling beam, M_u, can then be found according to the model shown in Figure 5.21,

$$\begin{aligned} V_u &= 2T_u \sin\alpha, \\ M_u &= (h - 2d')T_u \cos\alpha \end{aligned} \tag{5-2}$$

Where α (the diagonal angle), h and d′ are shown in Figure 5.23.

The above assumption can be very conservative if the concrete between the diagonal reinforcement in each direction is well confined and can contribute in resisting compressive forces. This is the case when the diagonal bars in each direction are well

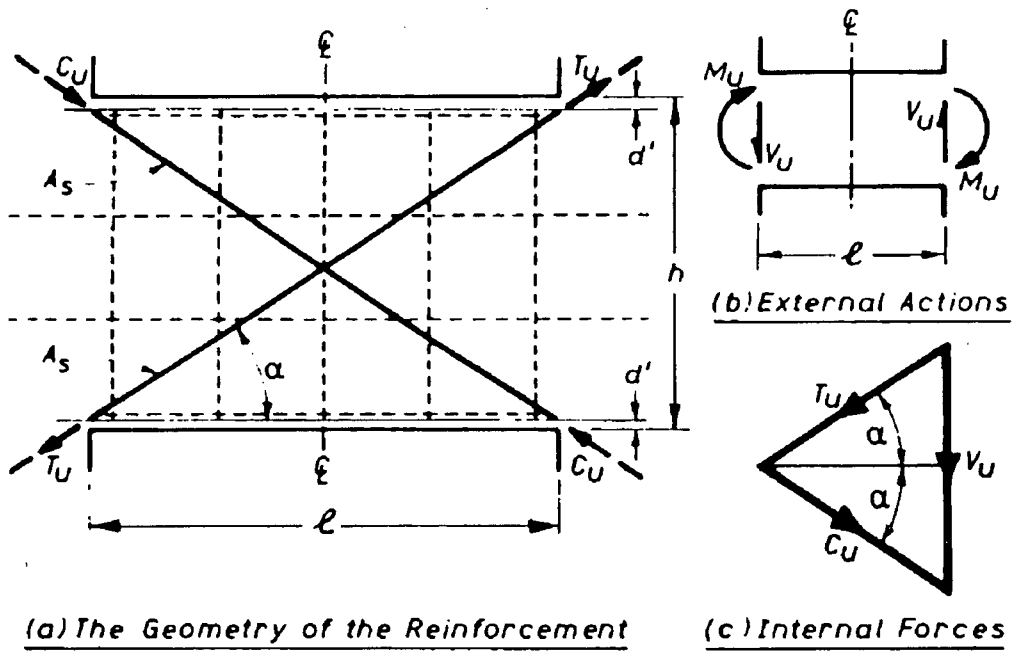

Figure 5.23: Simple determinate model (Paulay, 1971).

tied together. In order to come up with the complete monotonic force-displacement response we need to predict not only the ultimate shear capacity but also the yield displacement and the ultimate displacement of the coupling beam. The following is proposed to predict the complete force-displacement envelope for diagonally reinforced coupling beams.

It is assumed herein that the forces are carried by diagonal tension and compression as was assumed by Paulay (1971) and as shown in Figure 5.23. In order to consider the contribution of concrete core between the diagonal bars in each direction it is assumed that the diagonal compression force is carried by the diagonal reinforcement and the concrete core as shown in Figure 5.24. The tensile diagonal force is carried only by the diagonal reinforcement. Therefore, the diagonal tensile force, T, and the diagonal compressive force, C, at any strain, ε, can be written as,

$$T = A_s f_s = A_s f(\varepsilon_s),$$
$$C = A_s f_s + A_c f_c = A_s f(\varepsilon_s) + A_c f(\varepsilon_c) \tag{5-3}$$

Where A_c is the diagonal concrete core area, f_c and f_s are the concrete and steel stresses respectively, and ε_c and ε_s are the concrete and steel strains respectively. The total resisting shear force of the coupling beam, V, can then be written as,

$$V = (T + C)\sin\alpha \tag{5-4}$$

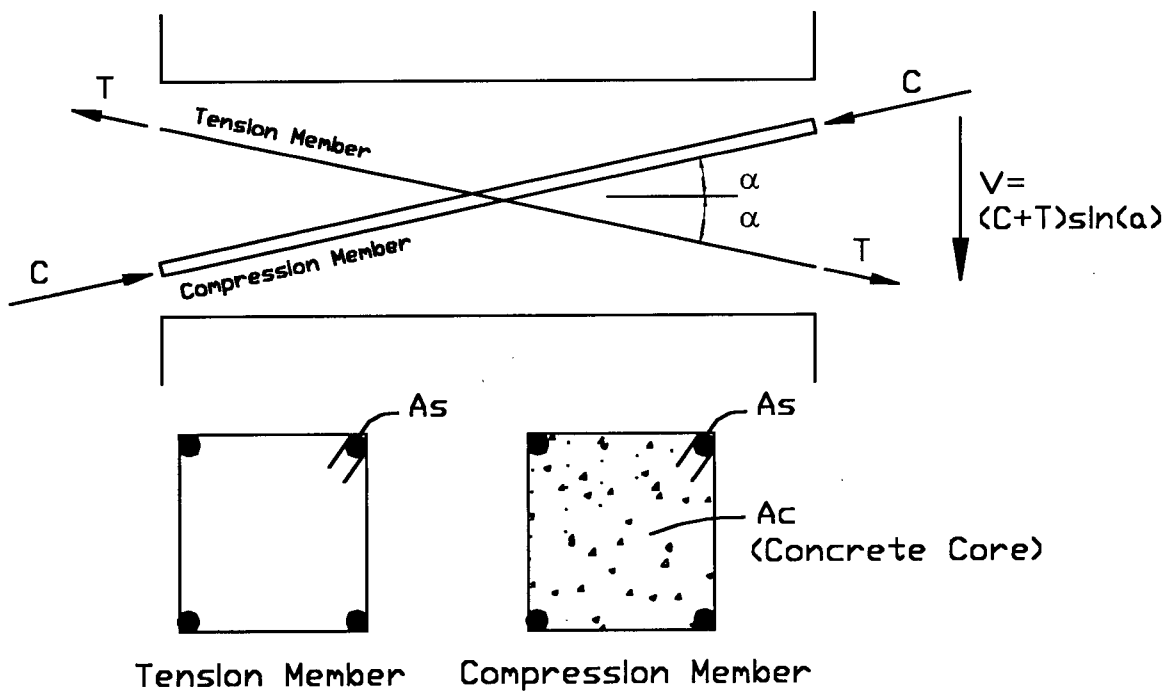

Figure 5.24: Proposed truss model.

This model as shown above is valid only when the coupling is axially restrained in order to satisfy force equilibrium in the beam direction because of the difference in value between T and C. The considered coupling beam here is restrained as shown in Figure 5.11. Coupling beams in a high-rise building are usually restrained by slabs on top of them.

The first yielding shear force and displacement are calculated when the reinforcing steel yields at ε_y which is almost the strain that gives the maximum compressive strength in unconfined concrete. It is assumed that the diagonal strains are equal in both directions; therefore, the first yielding shear force, V_y, can be written as,

$$\begin{aligned} V_y &= (T_y + C_y)\sin\alpha, \\ T_y &= A_s \varepsilon_y E_s, \\ C_y &= A_s \varepsilon_y E_s + A_c f'_c \end{aligned} \tag{5-5}$$

Where T_y and C_y are the first yield diagonal tensile and compressive forces respectively, and E_s is the steel modulus of elasticity.

The truss model theory is adopted herein to calculate the displacement at any strain level to predict the force-displacement envelope of the coupling beam. Following the principle of virtual work, the first yield lateral displacement, Δ_y, can be written as,

$$\Delta_y = \varepsilon_y \frac{L}{\cos\alpha \sin\alpha} \tag{5-6}$$

Where L is the length of the coupling beam.

After the diagonal reinforcement yields the concrete core in the diagonal compressive direction will start to carry more force due to increase of the concrete compressive strength because of the confinement until it reaches a compressive strength of f'_{cc} at a strain of ε'_{cc} [as defined by Mander confinement model (Mander et al., 1988)]. Therefore, the ultimate diagonal compressive force, C_u, at this loading stage, which gives the ultimate shear capacity, is,

$$C_u = A_s \varepsilon_y E_s + A_c f'_{cc} \tag{5-7}$$

The ultimate diagonal tensile force, T_u, at this stage of loading, is equal to the yield tensile force, T_y, as given in Equation 5-5 since only the diagonal reinforcement carries the tensile force and no strain hardening is accounted for (elastic perfect plastic behaviour). C_u can differ from one direction of loading to another depending on the area of the confined concrete and the confinement level in each direction. The ultimate shear

strength at this stage can be found following Equation 5-4. The corresponding displacement at this loading stage is calculated assuming the displacement is linearly proportional with the diagonal strain. The maximum strain reached at this stage is ε'_{cc} as discussed above; therefore, the displacement can be written as,

$$\Delta_{y2} = \frac{\Delta_y \varepsilon'_{cc}}{\varepsilon_y} \tag{5-8}$$

Also, at any displacement amplitude after yielding (Δ), the plastic strain in the diagonal reinforcement (ε_p), which is needed for the low-cycle accumulated damage calculation as discussed in Chapter Three, can be written as,

$$\varepsilon_p = \varepsilon_y \left(\frac{\Delta}{\Delta_y} - 1\right) \tag{5-9}$$

The ultimate displacement at failure can be determined either when the concrete core crushes or the diagonal reinforcement fractures whatever occurs first. In this case of a diagonally reinforced coupling beam the confined concrete core crushes way before the diagonal reinforcement fractures. The reinforcement steel is assumed to fracture at 10% strain, while the crushing strain of confined concrete, ε_{ccu}, is calculating according to the confinement formulas suggested by Mander et al. (1988). Therefore, the monotonic ultimate displacement at failure, Δ_f, is written as,

$$\Delta_f = \frac{\Delta_y \varepsilon_{ccu}}{\varepsilon_y} \tag{5-10}$$

Figure 5.25 summarizes the above calculated force-displacement points to predict the monotonic response.

Figure 5.26 shows the predicted monotonic force-displacement envelope following the above procedures. The monotonic envelope differs from one direction of loading to another because of the difference in the area of confined concrete in each direction. The predicted force-displacement envelope compares reasonably to the experimental results

as shown in Figure 5.26. The detailed calculation of the theoretical force-displacement envelope is given in Appendix A. The monotonic force-displacement envelope of the positive direction is considered for the damage calculation.

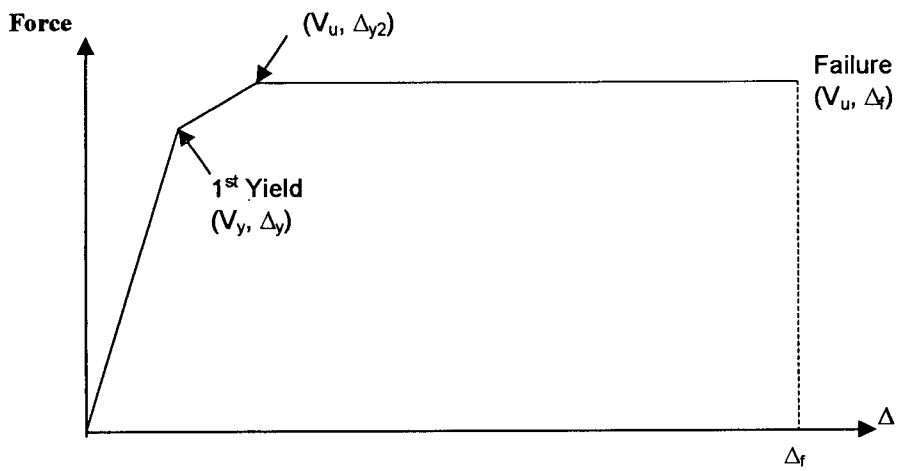

Figure 5.25: Key points of the monotonic force-displacement envelope.

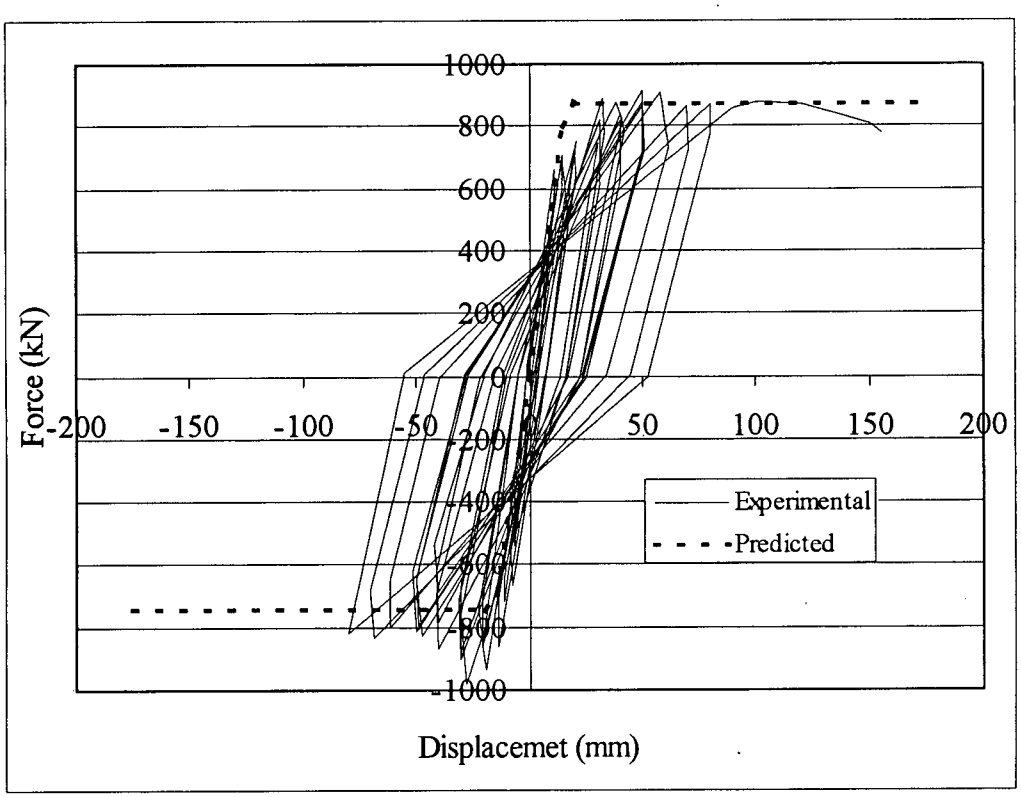

Figure 5.26: Monotonic force-displacement envelope.

5.2.2 Theoretical Damage

5.2.2.1 Comparison between the proposed model (P) and the observed damage

Table 5.4 and Figure 5.27 summarizes the observed damage and the predicted damage by the P model at all loading stages. The specimen showed almost no damage up to the end of cycle 10. The P model gave a damage of 0.06, which corresponds to no damage according to the damage classification as concluded at the end of Chapter 4. At the end of cycle 13, the observed damage became noticeable but it appeared to be minor. The P model estimated a damage of 0.12 and it corresponds to minor damage state. The spalling of concrete became more significant and the diagonal reinforcement started to be exposed at the end of cycle 16. At this stage, the P model gave a damage of 0.19, which is considered a minor damage. The damage progressed in terms of wider diagonal cracks and significant concrete spalling up to the end of cycle 21. This agreed with the P model since it gave a damage of 0.39 after 21 cycles as shown in Table 5.4. The observed damage became significant after cycle 22. It appeared difficult to repair after displacing the specimen monotonically to a 100 mm. This was also captured by the P model as it gave a damage of 0.56, which would be difficult to repair according to the concluded classification at the end of Chapter 4. The damage became very severe in terms of concrete crushing and buckling of the diagonal reinforcement at a monotonic displacement of 150 mm. At this displacement amplitude, a damage of 0.84 was estimated by the P model, which compares well with the test observation. Finally, the specimen failed monotonically at a displacement of 156 mm.

Since the specimen was loaded monotonically to failure after 22 cycle, it is a good idea to compare the predicted degraded monotonic response after 22 cycles using the proposed model with the observed one. Figure 5.28 shows this comparison. The P model gave a damage of 0.47 using the predicted monotonic response, while it gave a damage of 0.495 using the experimental monotonic response.

5.2.2.2 Comparison between the E1, E2 and P models

Figure 5.27 shows a comparison between the E1, E2, and P models. A value of 0.05 for the energy parameter, β_e, is assumed for the E1 model since the diagonal reinforced coupling beam is considered well reinforced and detailed as concluded from the high ductility capacity and minor strength deterioration throughout the cycling as shown in Figure 5.26.

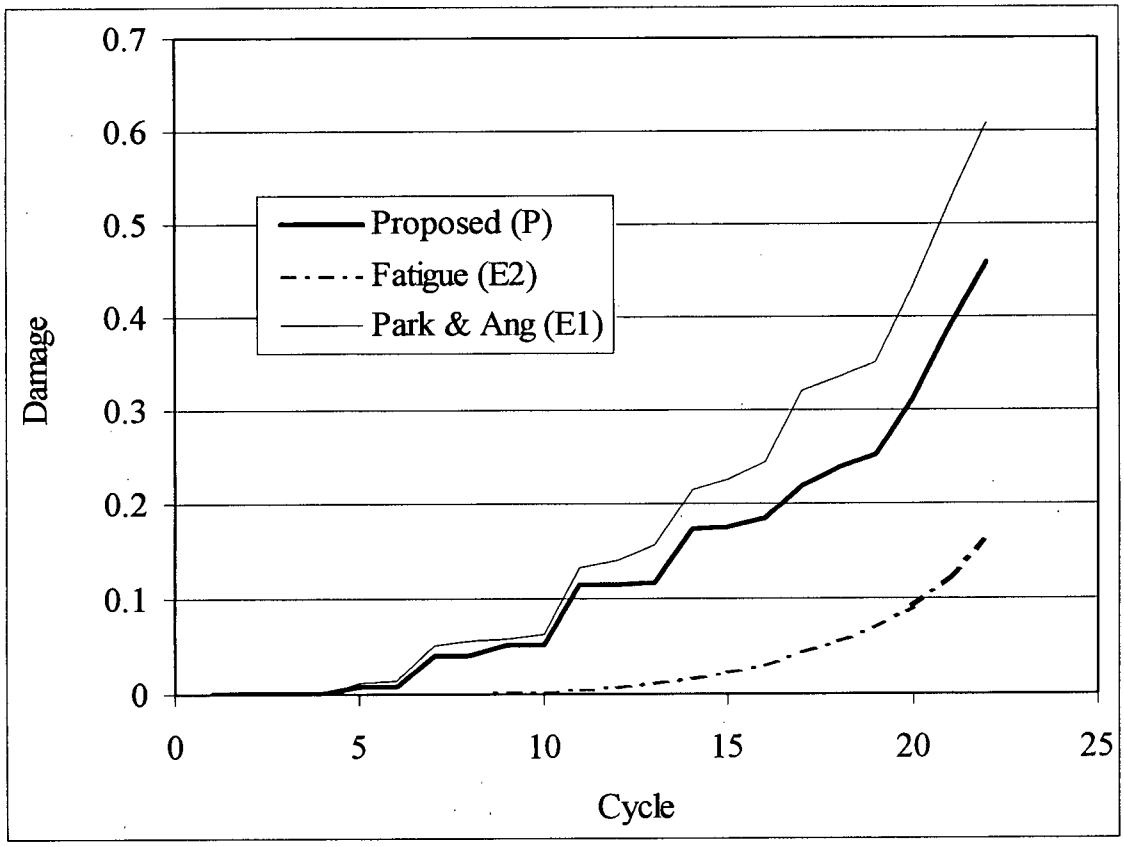

Figure 5.27: Damage of a coupling beam.

Table 5.4: Observed and predicted damage.

Cycle	Displacement (mm)	Comments	Proposed Damage
4	10	Hairy diagonal and flexure cracks, no damage	0.00
7	14	0.8 mm flexure cracks, 0.6 mm diagonal cracks, no damage	0.04
10	20	1.5 mm diagonal crack, spalling of cover at 2 opposite corners, no exposed diagonal reinforcement, minor damage	0.06
13	30	3.0 mm diagonal crack, cover spalling at all 4 corners, no exposed diagonal reinforcement, minor damage	0.12
16	40	3.0 mm diagonal crack, deeper spalling, diagonal reinforcement started to be exposed	0.19
19	50	Wider diagonal crack, significant spalling	0.25
20	60	Wider diagonal crack, significant spalling	0.27
21	70	Wider diagonal crack, significant spalling	0.39
22	80	Significant spalling, no signs of diagonal reinforcement buckling, significant damage	0.46
monotonic	90	Significant damage	0.51
monotonic	100	Significant damage	0.56
monotonic	150	Concrete crushing, buckling of diagonal reinforcement, severe damage	0.84
monotonic	156	Complete failure	0.90

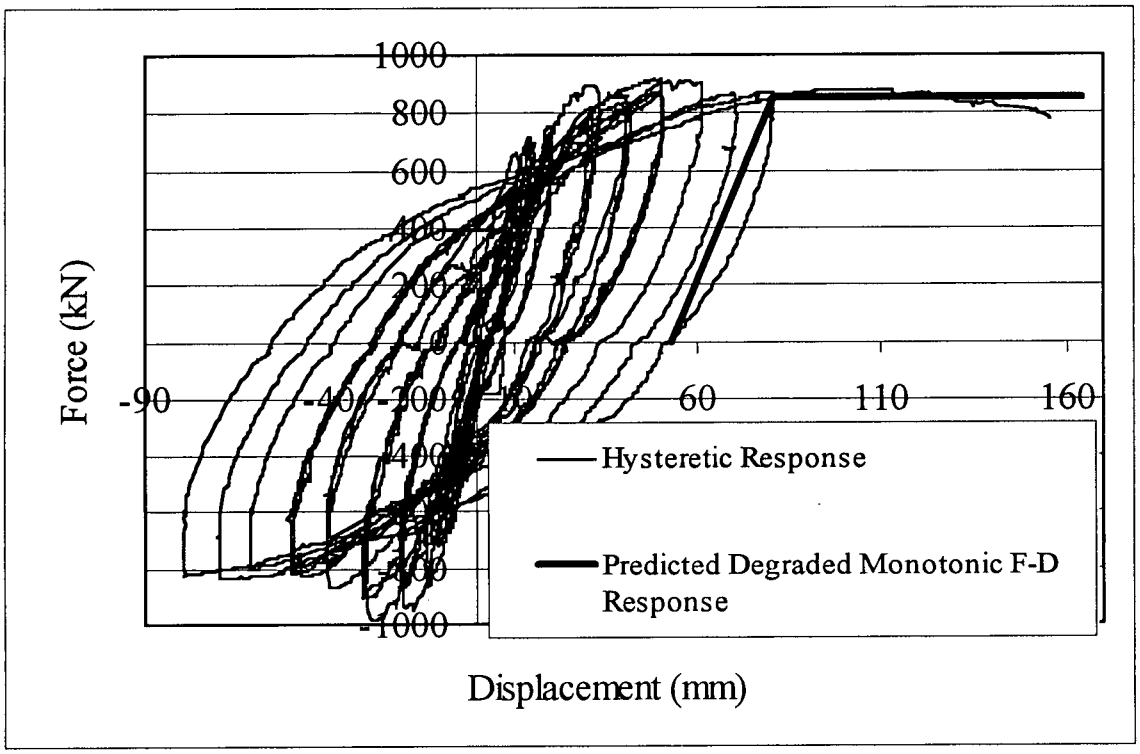

Figure 5.28: Predicted degraded monotonic force-displacement response.

The E2 model underestimated the damage because it was derived for flexural columns and the plastic strain demand in the diagonal reinforcement is low for such type of members since the failure was due to concrete crushing, which occurred at lower strain than the fracture strain of the diagonal reinforcement. The E1 model compared very well with the P model during the first 12 cycles, while it started to give higher damage after that. The E1 model gave a damage of 0.6 at the end of cycling (cycle 22 at 80 mm displacement), which means irrepairable state, while the specimen was able to monotonically displace to about 80 mm after cycling. This means that the E1 model overestimated the damage.

The P model provided results consistent with subjective observations of damage for the coupling beam test.

CHAPTER SIX

DAMAGE ANALYSIS OF EXISTING BRIDGE COLUMNS

This chapter presents the analysis of seismic damage of two bridges in the Greater Vancouver area. The objective of this study is to apply the proposed damage model to existing bridge columns that might experience real earthquake loading anytime in the future, and to evaluate the model's ability in describing the seismic damage progression of the bridge columns during earthquake loading. A comparison between the E1, E2 and P models is also presented in this chapter as part of the evaluation of the P model.

6.1 INTRODUCTION

The new Canadian Highway Bridge Design Code (CAN/CSA-S6-00) classifies bridges into three important categories; lifeline bridges, emergency-route bridges, and other bridges. Table 6.1 summarizes the performance requirements of the three important categories. These specifications are based on a single-level seismic design procedure. An analysis is required for the design earthquake (475-year return period event, 10% probability of exceedance in 50 years) and all forces and displacement are derived from this analysis. This approach focuses on collapse prevention during the design earthquake. Depending upon the importance of the bridge, different levels of damage are expected to occur as part of the mechanism for resisting the event. The code does not require any damage analysis to satisfy the above performance requirements.

It would be very useful to have damage descriptions and statements of repairability or lack of repairability, and even better if we could have damage values to achieve the code objectives.

Damage indices can contribute to more precise achievement of the code objectives since they are a way of quantifying the damage level after an earthquake. For example, a lifeline bridge under a large earthquake (1000 year return period, Table 6.1) could be required to show damage of less than 0.2 according to the P model as classified in

Chapter 4. While the damage should be less than 0.6 for an emergency-route bridge and less than 1.0 for other bridges. Therefore, damage indices would be a useful way to satisfy code performance criteria.

Table 6.1: Performance requirements (CAN/CSA-S6-00).

	Bridge		
Earthquake	**Lifeline**	**Emergency-Route**	**Other**
Small to Moderate	All traffic Immediate use	All traffic Immediate use	All traffic Immediate use
Design (475 year return period)	All traffic Immediate use	Emergency vehicles Immediate use	Repairable damage
Large (1000 year return period)	Emergence vehicles Immediate use	Repairable damage	No collapse

In order to evaluate the ability of the proposed damage model in describing the damage during an earthquake loading, two existing bridges were selected from Greater Vancouver area. The Garneau Flyover Bridge was designed in 1985. It was designed to the ATC-6 (Applied Technology Council, 1981) and is expected to have sufficient resistance to lateral earthquake loading. The second bridge, Clydesdale Street Underpass, was designed long before the ATC-6 (Applied Technology Council, 1981) and it is expected to show poor lateral earthquake resistance.

6.2 THE PROGRAM CANNY

CANNY-E, 1996 (Three Dimensional Non-linear Dynamic Structural Analysis) version was developed by CANNY CONSULTANTS PTE LTD, Singapore. Originally developed by Kang-Ning Li et al. (1988) at the University of Tokyo, Japan. The program is accompanied with detailed users and technical manuals in order to understand the details of the program.

6.2.1 CANNY Analysis Features

CANNY-E is a program for performing non-linear analysis of frame and shear-wall structures. It is applicable to structures that can be idealized by rigid nodes, linear elements and spring elements. It can be used to analyze most building structures, towers, trusses and some bridge structures. It deals with structures that have irregular shape and complicated geometrical configuration. It includes a number of different types of hysteresis models to represent the nonlinear behavior of various materials. All models have key parameters and options to be determined by the user; therefore, the program can be applied to reinforced concrete and steel structures. The program includes several types of structural elements. Each type of elements has its corresponding self-contained program units to formulate its stiffness matrix. The element models are arbitrarily oriented and express uniaxial tension and compression, uniaxial and biaxial flexure and shear, biaxial bending and axial, biaxial shear interaction, and torsion. Therefore, the program is able to perform structural analysis of two-dimensional plane frame and three-dimensional space frame structures. The program has no limits on number of nodes, elements, floor levels, and frames. The program is able to deal with material non-linearity and the P-Δ effect.

The analysis options available in CANNY are: mode shape, design load, static pushover, static cyclic and reversal, pseudo-dynamic, and dynamic analysis. The static and dynamic analysis options can include the effects of initial static loads.

6.2.2 CANNY Sophisticated Hysteresis Model

CANNY sophisticated hysteresis model is easy to use and capable of representing the complex and variable concrete hysteresis characteristics. It is designed to represent stiffness degradation, strength deterioration and pinching behavior. A trilinear or bilinear load-deformation envelope is needed for this hysteresis model. Figure 6.1 shows the parameters needed for the trilinear load-deformation envelope for CANNY.

Behavior under earthquake or cyclic loading is dealt with using seven dimensionless parameters. Stiffness degradation is governed by the parameters θ and δ as shown in Figure 6.2a. θ defines a target unloading point in term of the yield load, while δ defines the slope of the axis UU′ where the unloading ends.

The model presents the strength deterioration by directing the reloading towards a reduced strength level, $\overline{F}_{max}$, at the same displacement corresponding to the previous peak strength, F_{max}, as shown in Figure 6.2b. F_{max} is calculated depending on the ductility level and the dissipated hysteresis energy,

$$\overline{F}_{\max} = F_{\max}\left[1 - \lambda_e \frac{E_h}{F_y d_{\max} + F'_y d'_{\max}} - \lambda_\mu \left(1 - \frac{1}{\mu}\right)\right] \tag{6-1}$$

where E_h is the hysteretic energy, μ is the ductility and λ_e and λ_μ are the energy and ductility related strength deterioration parameters. While the softening of the post-yield envelope is controlled by another parameter, λ_3, as shown if Figure 6.2b,

$$\overline{K}_{py} = K_{py}\left[1 - \lambda_3 \left(1 - \frac{1}{\mu}\right)\right] \tag{6-2}$$

where K_{py} is the post-yield stiffness of the monotonic load-deformation envelope and $\overline{K}_{py}$ is the new post-yield stiffness.

The pinching behavior caused by opening and closing of cracks is modeled by two target points F_e and d_e as shown in Figure 6.2c. These target points are controlled by three parameters ε, λs, and δ,

The CANNY hysteresis model does not account for any degradation due to low-cycle accumulated damage. The effect of low-cycle damage is accounted for later when the damage is calculated using the P and E2 models.

Table 6.2: Value of CANNY hysteresis parameters

Parameter	Control	Comments
δ	Unloading	Range: 0.0 to ±0.05 Preferred equal to post-yield stiffness
θ	Stiffness degradation	Range: ≥ 1.0 0.0 = no stiffness degradation
λ_e	Energy-related strength deterioration	Range: 0.0 to 1.0 1.0 = severe deterioration
λ_μ	Ductility-related strength deterioration	Range: 0.0 to 1.0 1.0 = severe deterioration
λ_3	Post-yielding softening stiffness	Range: 0.0 to 1.0 1.0 = severe softening
ε	Pinching behavior	Range: 0.0 to 1.0 1.0 = severe pinching
λ_s	Pinching behavior	Range: 0.0 to 1.0 0.0 & 1.0 = no pinching

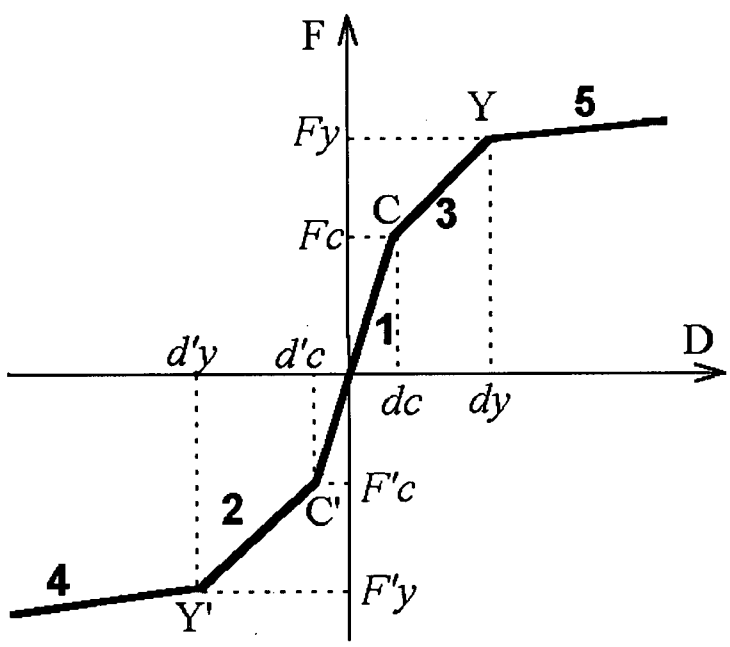

Figure 6.1: Trilinear load-deformation envelope.

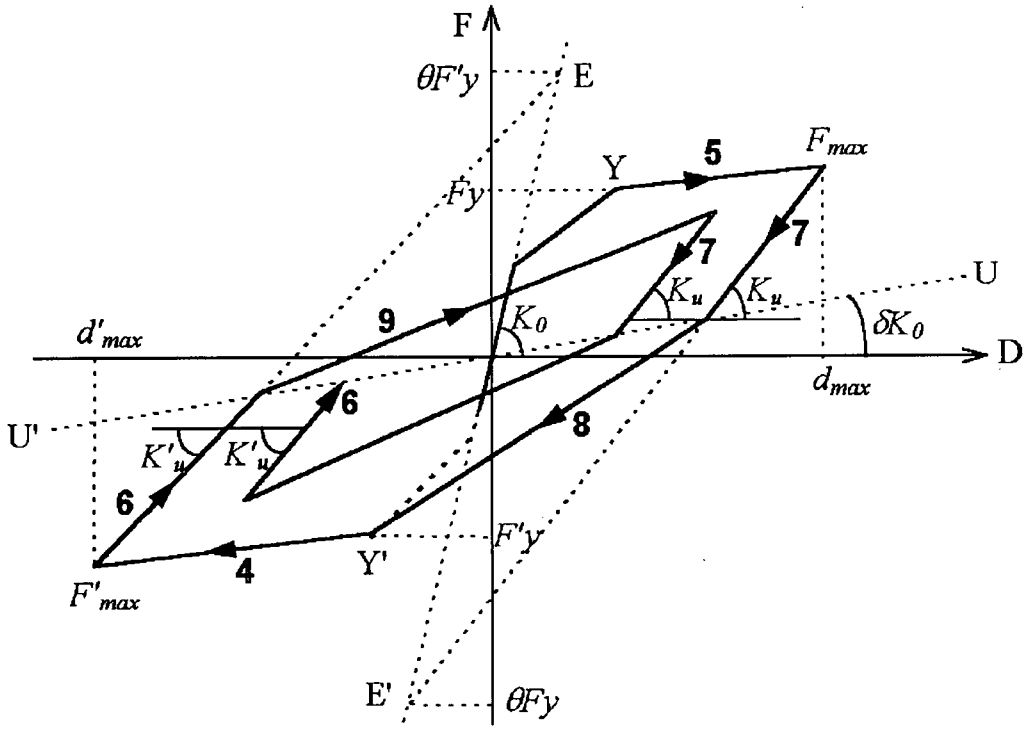

(a) Unloading Stiffness Degradation

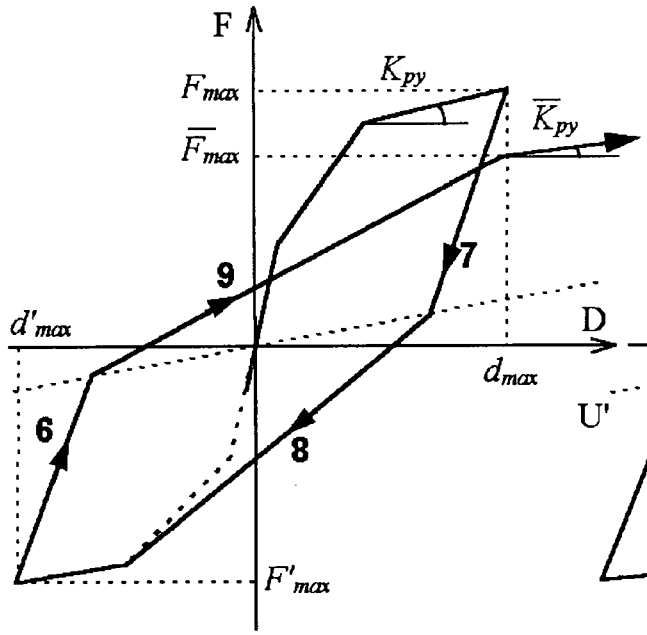

(b) Strength Deterioration

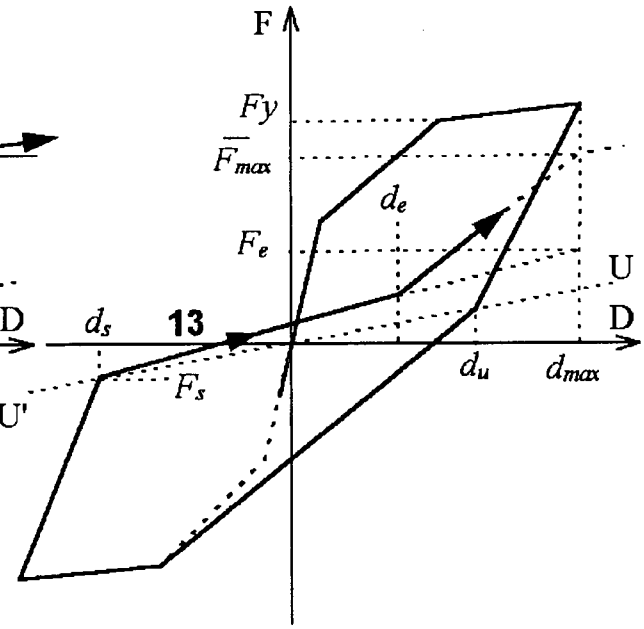

(c) Pinching Behavior

Figure 6.2: CANNY sophisticated hysteresis model.

$$
\begin{aligned}
d_e &= \varepsilon d_u \\
F_e &= \lambda_s\left(\overline{F}_{\max} - \delta K_o d_{\max}\right) + \delta K_o d_{\max}
\end{aligned}
\tag{6-3}
$$

Range values for the seven hysteresis parameters are shown in Table 6.2.

6.3 DESCRIPTION OF SELECTED BRIDGES

6.3.1 Garneau Flyover

The bridge is a three span structure, which carries two lanes of traffic to exit from the Richmond east west freeway to Knight Street in New Westminster district in Greater Vancouver. The bridge was designed and constructed in 1985-1986. It is owned by the British Columbia Ministry of Transportation and Highways (MoTH).

Figure 6.3 shows the bridge in plan, elevation and section. The concrete deck is 8.18 m wide. Bridge span lengths are 17.995 m in the west span, 26.00 m in the center span, and 17.995 m in the east span. The deck is 190 mm thick and supported on four 1473 mm deep prestressed concrete I stringers and had 1:12.5 super-elevation in the transverse direction. The substructure consists of two piers and two abutments. Each pier consists of a spread footing, a single circular column and a cap beam. The bearings are fixed-fixed on each pier and sliding on the abutments. The as-built reinforcement plan for the piers is reproduced in Figure 6.4. The footing is founded on loose soil.

The designed compressive strength for concrete used in the piers is 30 MPa and the reinforcement steel conforms to CSA G30.12 M, which has a yield strength of 400 MPa.

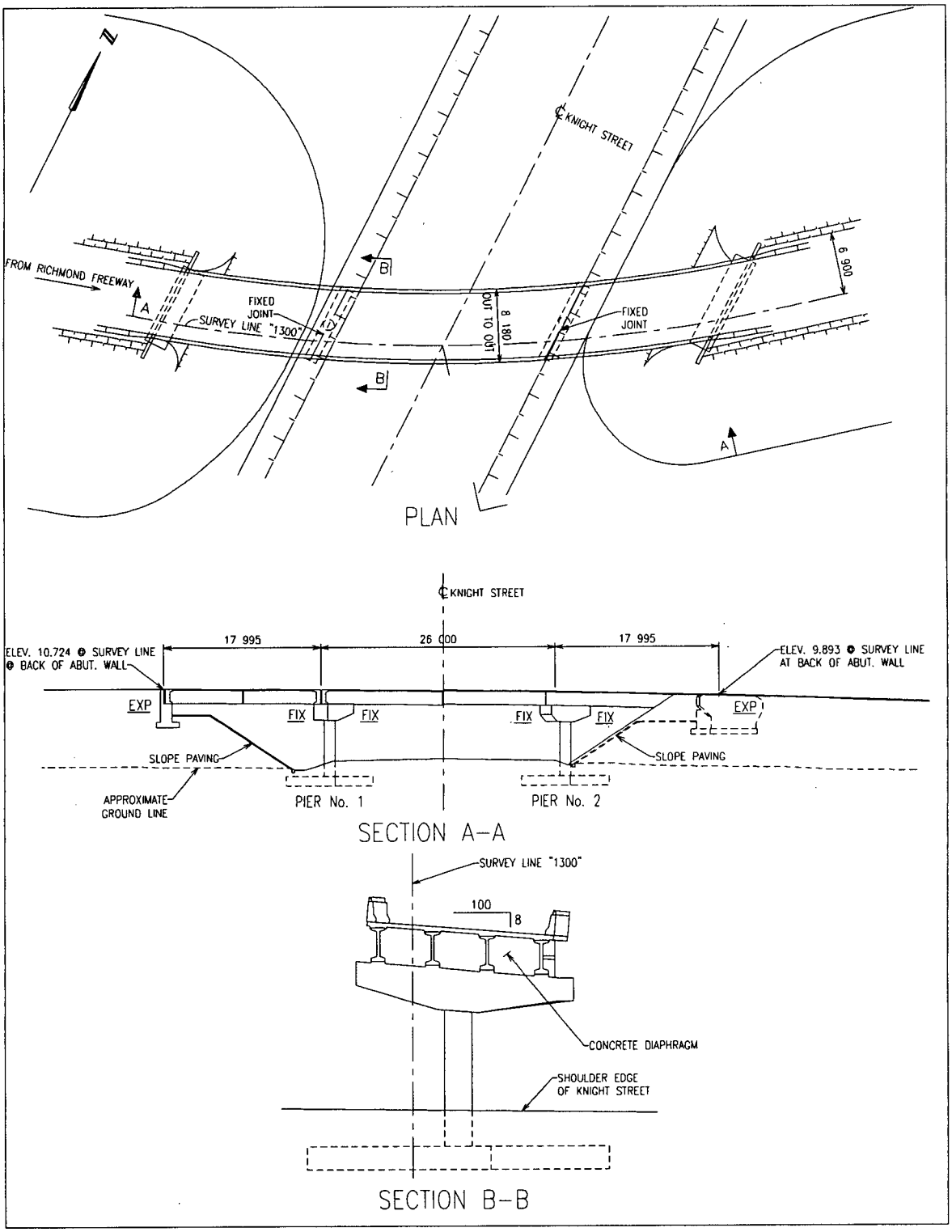

Figure 6.3: Configuration of Garneau Flyover.

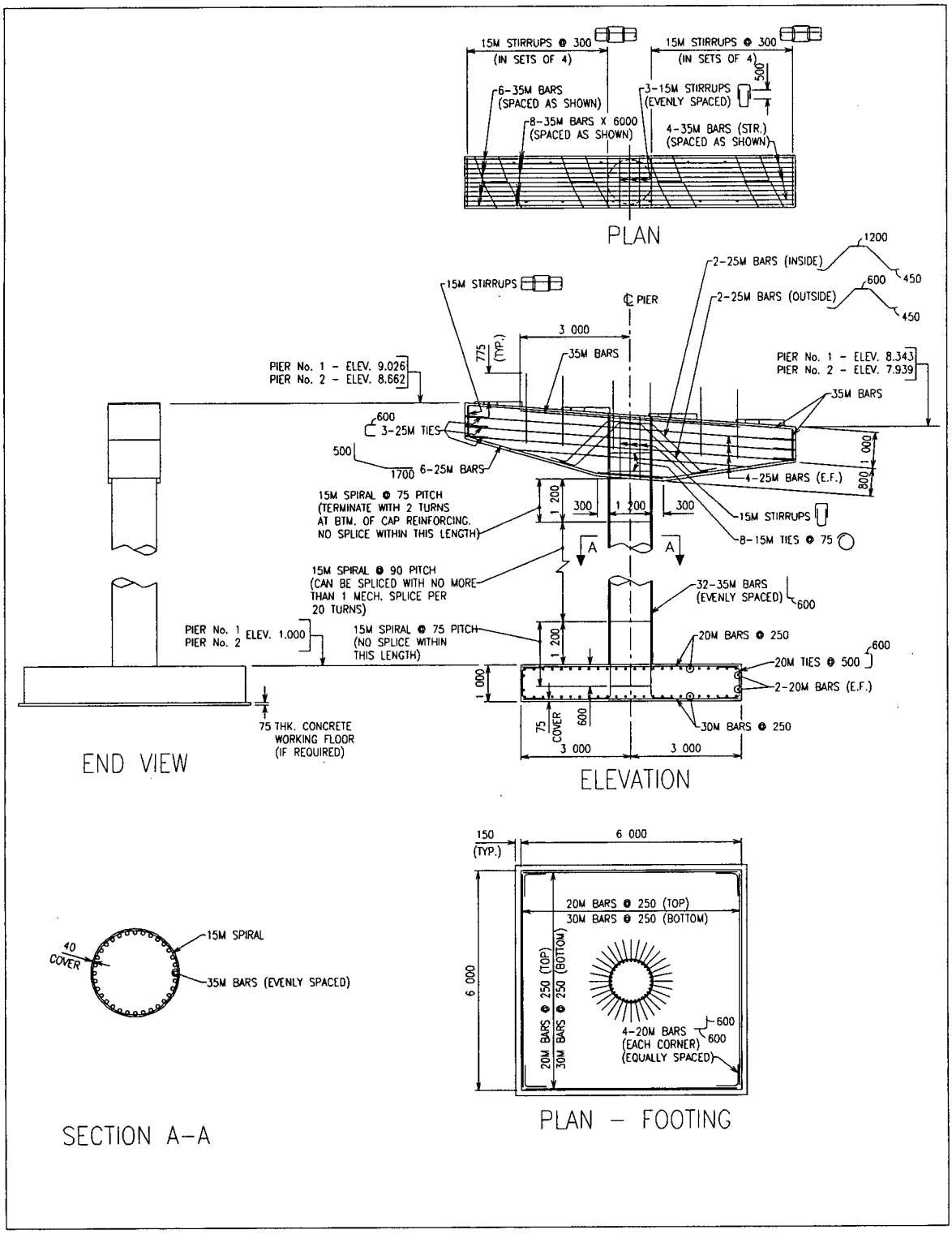

Figure 6.4: Piers as-built (Garneau Flyover).

6.3.2 Clydesdale Street Underpass

The bridge is a five span structure, which carries Clydesdale Street over Trans Canada Highway 1 in Greater Vancouver. The bridge was constructed in the early 1960's, and is owned by the British Columbia Ministry of Transportation and Highways (MoTH).

Figure 6.5 shows the bridge in plan, elevation and section. The width of the bridge is 14.63 m, consisting of 10.97 m roadway, and two 1.829 m wide sidewalks. Bridge span lengths starting from the west abutment are 13.64 m in the west span, 23.14 m in the second span, 13.64 m in the center span, 29.26 m in the fourth span, and 13.64 m in the fifth (east) span. The bridge consisted of eleven 1016 mm deep and 1212 mm wide prestressed concrete box stringers. The sidewalks are cast in place. The substructure consists of four piers and two abutments. Each pier consists of a spread footing, a single rectangular column and a cap beam. The rectangular column has a weak direction in the longitudinal direction of the bridge. The bearings are fixed-fixed on piers 2 and 3, sliding-sliding on piers 1 and 4, and fixed at the abutments. The as-built reinforcement plan for the piers is reproduced in Figure 6.6. The footing is founded on firm soil.

The compressive strength for concrete used in the piers is 30 MPa and the reinforcement steel conforms to CSA G30.12 M, which has a yield strength of 400 MPa.

6.4 MODELING OF COLUMNS

Several simplifications were made in modeling the columns of the two bridges investigated in this study. The bridges are transversally fixed at the abutments and the deck is assumed to be a rigid diaphragm. The columns are assumed cantilevered in the longitudinal direction of the bridges, while they are not totally free to rotate at the top in the transverse direction due to the strong cap beam, rigid deck and the distributed mass. Only the longitudinal direction is considered in this study.

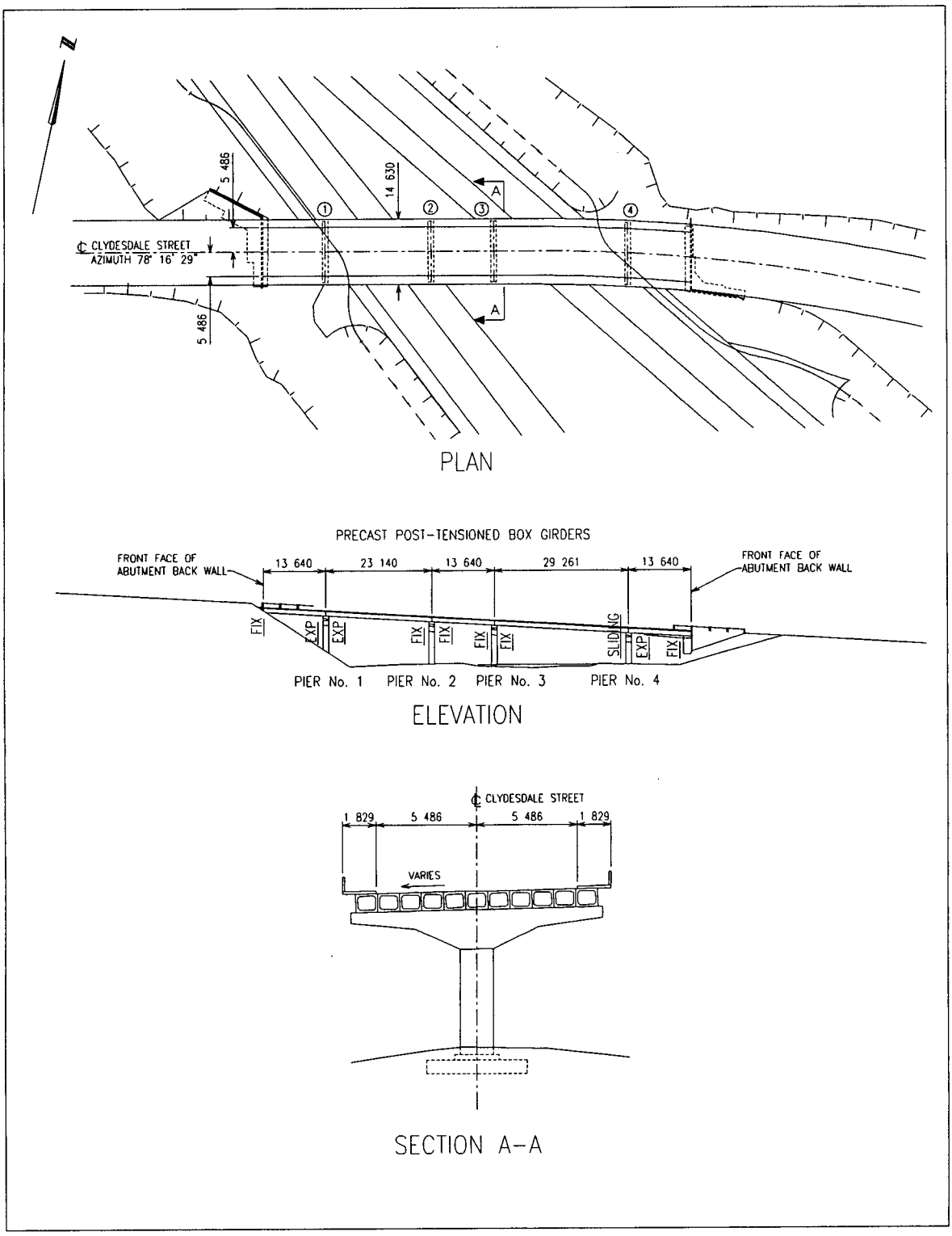

Figure 6.5: Configuration of Clydesdale Underpass.

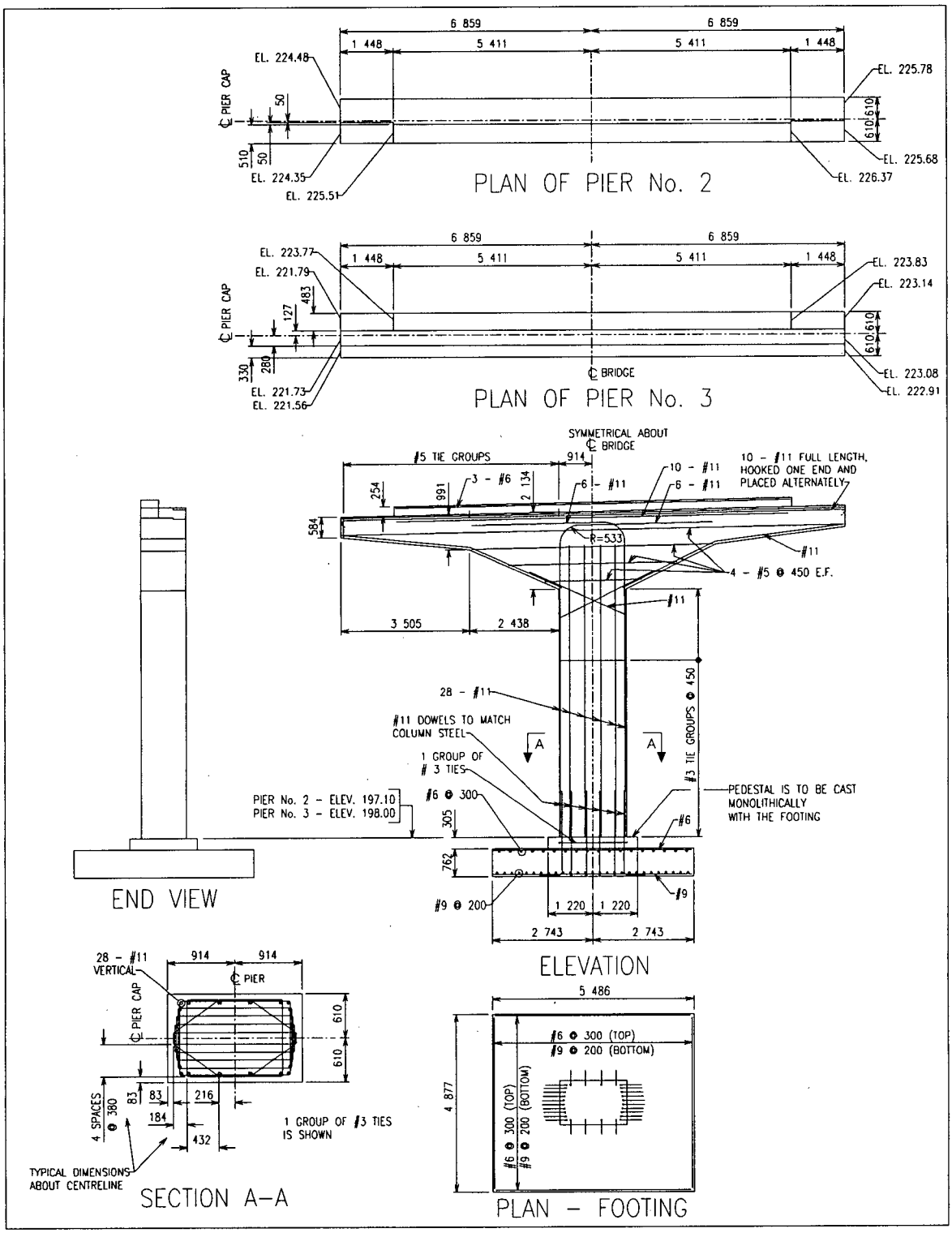

Figure 6.6: Piers as-built (Clydesdale Underpass).

The columns are modeled as cantilevers with lumped mass. The column is assumed to have two segments; the first one is modeled as a flexural column, L_F, from the top of footing to the bottom of the cap beam, the second segment is assumed rigid, L_R, to model the cap beam and the deck as shown in Figure 6.7. Three masses are considered in calculating the lumped mass (M): the mass of the superstructure (deck) (M_d), the mass of the cap beam (M_{cb}), and 50% of the mass of the column ($M_c/2$). The length of the rigid segment, L_R, is determined by finding the equivalent center of gravity of the above three masses. The mass of the superstructure, M_d, is calculated depending on the tributary area of the deck, which depends on the bearing conditions of the adjacent piers.

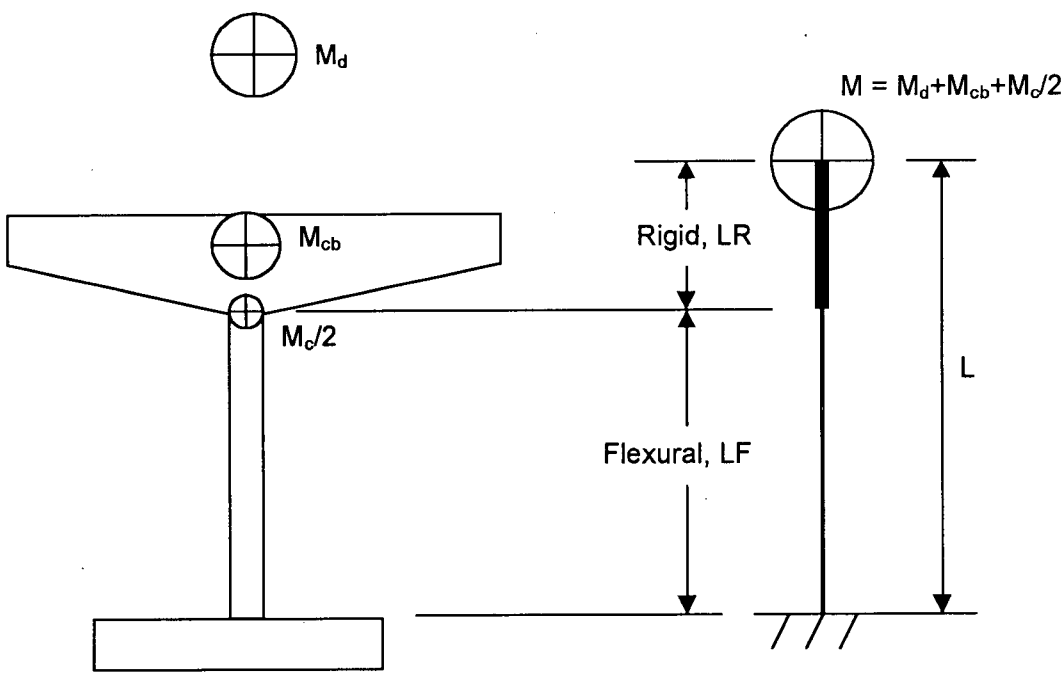

Figure 6.7: Column modeling.

The flexural segment, L_F, is divided into several flexural column elements. The axial load applied to the column is considered, which is equal to the dead load applied to the column. Simple modifications were made to the moment-curvature response of these column elements to consider shear and bond slip deformation as discussed later. A

bilinear moment-curvature response for the column element was predicted using layer analysis as discussed in Chapter Three taking into account the column concrete confinement and the axial load. A monotonic force-displacement envelope is generated for the columns from the moment-curvature response considering the rigid zone at the top of the column and shear and bond slip deformation. The shear capacity was also considered following Priestley et al. (1994) as discussed in Chapter Three.

6.4.1 Garneau Flyover

Only pier 1 is considered in this study, since both piers have the same mass, column properties, and boundary conditions. The only difference between the two piers is the length of the columns; column 1 is 5880 mm long and is 384 mm longer than column 2.

The bearings are fixed-fixed at the piers and sliding at the abutments; therefore, only the piers carry the lateral earthquake loading in the longitudinal direction. Each pier carries half the mass of the superstructure plus it's own mass; however, the axial load applied to the column is calculated according to the tributary area of the deck. The resulted mass and axial load are 3550 kN and 2800 kN respectively. Table 6.3 shows the magnitude and location of the individual masses and the equivalent mass. The center of gravity of the equivalent mass is located at 2745 mm, L_R, from the bottom of the cap beam, which is modeled as a rigid zone; therefore the total length of the column, L, including the rigid zone is 8625 mm.

Figure 6.8 shows the predicted monotonic bilinear moment-curvature response of the column section using layer analysis as discussed in Chapter Three. A monotonic bilinear force-displacement is generated by integrating the curvature distribution over the entire column as discussed in Chapter Three considering shear and bond slip deformation and the rigid zone at the top of the column as shown in Figure 6.9. This monotonic force-displacement envelope is needed for the damage calculation as discussed in Chapter three. The predicted yield and ultimate displacement are 125.5 and 870.5 mm respectively, while the yield shear force is 753 kN. This column has a high ductility capacity because of the good reinforcement detailing and confinement.

Table 6.3: Mass results (Garneau Flyover).

Mass	Magnitude (kN)	Location (mm) (from bottom of cap beam)
M_d	3020	3070
M_{cb}	450	1037
$M_c/2$	80	0
Total Mass (M)	3550	2745
Axial Load	2800	

The minimum shear capacity of the column at ultimate displacement (ductility capacity of about 7) as calculated following Priestley et al. (1994) is 3373 kN and is higher than the shear demand (753 kN).

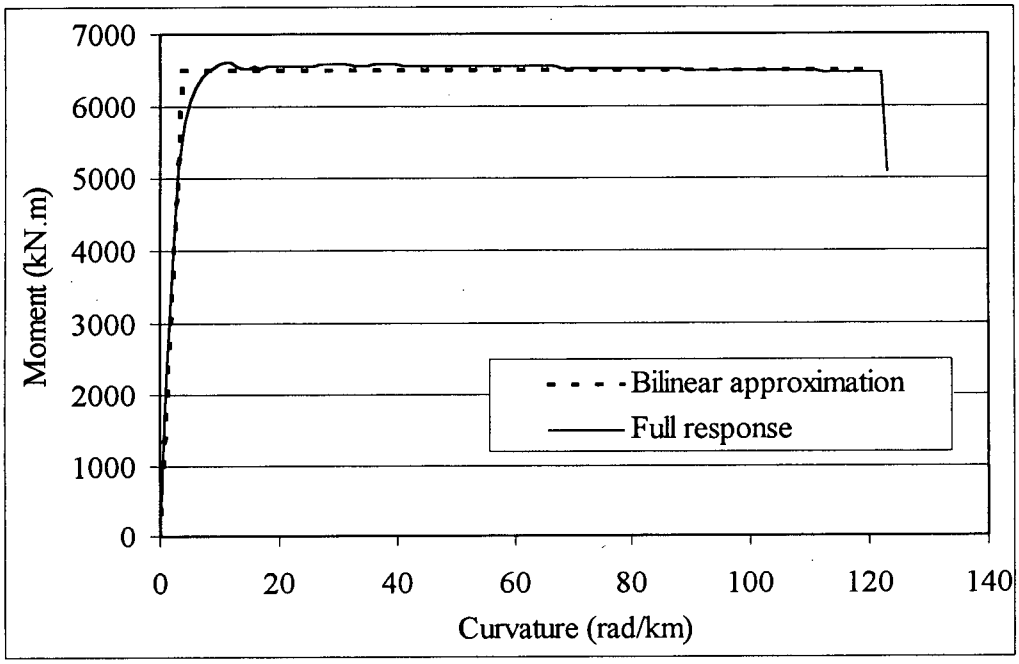

Figure 6.8: Predicted moment-curvature response (Garneau Flyover).

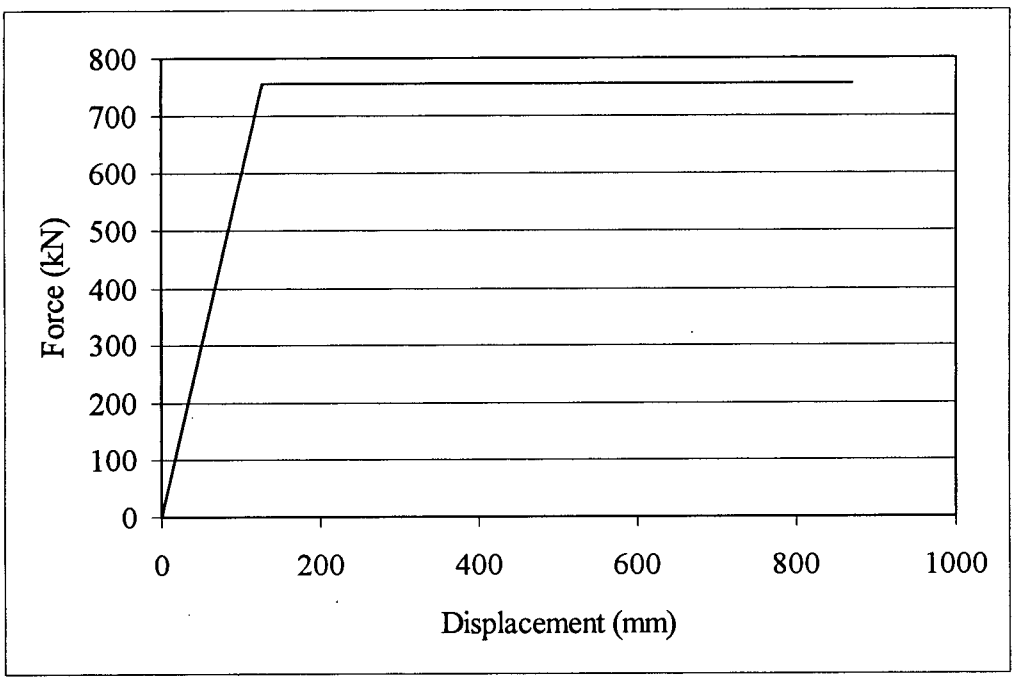

Figure 6.9: Bilinear force-displacement response (Garneau Flyover).

6.4.2 Clydesdale Street Underpass

Piers 2 and 3 are subjected to higher masses compared to other piers. All the four piers have the same column properties. The differences between pier 2 and 3 are the mass and the column length. The length of the column in pier 2 is 6690 mm and is 1090 mm longer than column 3.

The bearings are fixed-fixed at piers 2 and 3 and sliding at the adjacent piers; therefore, only the pier 2 and 3 carry the longitudinal earthquake loading for the middle 3 spans as shown in Figure 6.5. Pier 2 carries the mass of the 2nd span and half the 3rd span (middle span) of the superstructure plus it's own mass, while pier 3 carries half the mass of the 3rd span (middle span) and the entire 4th span of the superstructure. However, the axial load applied to columns 2 and 3 is calculated according to the tributary area of the deck. The resulting mass and axial load on both columns are shown in Table 6.4. Table 6.4 also shows the magnitude and location of the individual masses and the equivalent mass for piers 2 and 3. The center of gravity from the bottom of the cap beam, L_R, for columns 2 and 3 is located at 2582 and 2625 mm respectively. Therefore, the total length, L, of columns 2 and 3 including the rigid zone is 9272 and 8225 mm respectively.

Figure 6.10 shows the predicted monotonic moment-curvature response of the column section using layer analysis as discussed in Chapter Three. A monotonic bilinear force-displacement is generated for each of columns 2 and 3 by integrating the curvature distribution over the entire column as discussed in Chapter Three considering shear and bond slip deformation and the rigid zone at the top of the column. Figure 6.11 shows the bilinear force-displacement response of columns 2 and 3. These monotonic force-displacement envelopes are needed for the damage calculation as discussed in Chapter Three. The predicted yield and ultimate displacement for column 2 are 124.8 and 227.8 mm respectively, and for column 3 are 101 and 182.8 mm respectively. The yield shear force for columns 2 and 3 are 809 and 912 kN respectively as shown in Figure 6.11. The ductility capacity of these columns is low because of the poor reinforcement detailing and confinement.

The minimum shear capacity of the columns 2 and 3 at ultimate displacement (ductility capacity of about 1.8) as calculated following Priestley et al. (1994) is 943 kN and is higher than the shear demands of the two columns. However, the axial load, P, was not considered in calculating the shear capacity. Axial load would increase the shear capacity, as discussed in Chapter 3.

Table 6.4: Mass results (Clydesdale Underpass).

	Pier 2		**Pier 3**	
Mass	**Magnitude (kN)**	**Location (mm)** (from bottom of cap beam)	**Magnitude (kN)**	**Location (mm)** (from bottom of cap beam)
M_d	5480	2782	6700	2782
M_{cb}	520	1394	520	1394
$M_c/2$	185	0	156	0
Total Mass (M)	6185	2582	7376	2625
Axial Load	4240	—	4825	—

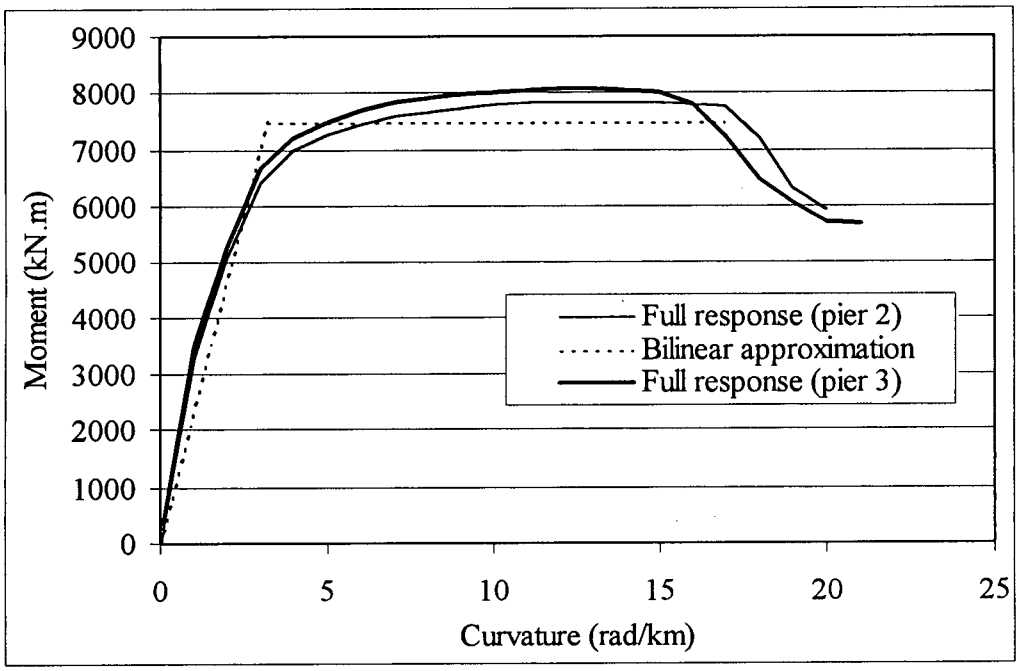

Figure 6.10: Predicted moment-curvature response (Clydesdale Underpass).

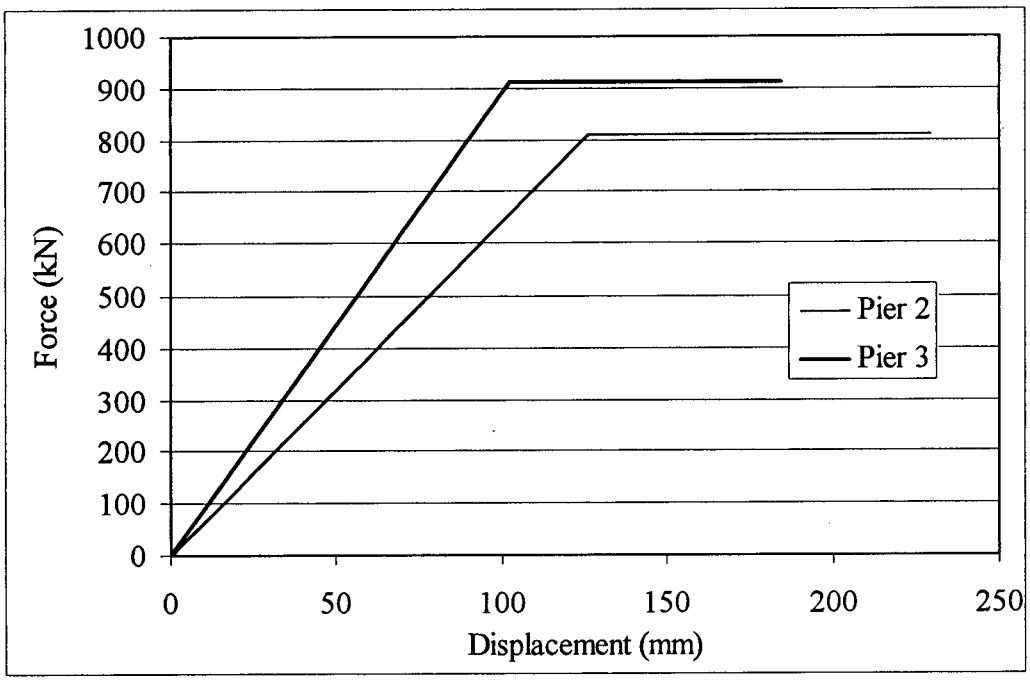

Figure 6.11: Bilinear force-displacement response (Clydesdale Underpass).

6.5 NONLINEAR DYNAMIC ANALYSIS

The nonlinear dynamic analysis is performed using CANNY structural program. A series of nonlinear dynamic analyses were performed using records from the 1971 San Fernando, 1989 Loma Prieta, 1978 Miyaki-Oki (Japan), and 1999 Taiwan earthquakes fitted to Vancouver firm ground spectrum with 2% probability of exceedance in 50 years, as shown in Figures 6.12 and 6.13. Table 6.5 summarizes the earthquakes used in this study. The frequencies, displacements and velocities of these earthquakes are not necessarily suitable for Vancouver, but they are selected mainly to examine the ability of the proposed model in predicting the damage of real bridges under real earthquake loading. These records were generated by Dr. Donald Anderson at the University of British Columbia using SYNTH program, which was written by Naumoski, 1985. The program computes the spectrum for the real acceleration time history. In order to match the computed spectrum with the target spectrum, raising and suppressing of the computed spectrum is performed iteratively by corresponding modification of the Fourier coefficients.

Garneau Flyover is located on loose soil in New Westminster District. The resulted firm ground acceleration was used in the SHAKE analysis program for till depths assumed as 200 m and 43 m, in order to examine the possible variation in damage for these two cases. These two depths were considered because they were generated and used by recognized consultants in projects in the vicinity of the bridge. Figures 6.14 and 6.15 show the ground acceleration time history at the surface.

A viscous damping equal to 2% is assumed for the nonlinear analysis. The P-Δ effect is considered in the analysis since the columns are subjected to axial loads of about $0.08f'_cA_g$. The predicted bilinear moment-curvature envelopes shown in Figures 6.8 and 6.10 were modified to include shear and bond slip deformation. This was done by increasing the yield curvature to give the yield displacement as shown in Figures 6.9 and 6.11. Table 6.6 summarizes the properties used in the analysis.

The columns are modeled as five column elements without any rigid zone and one column element with rigid zone at the top to model the rigidity of the cap beam and the superstructure between the top of the column and the center of gravity of the mass. A sample input file for CANNY program is shown in Appendix B.

Step by step analysis is done at a time interval of 0.02 second. Output of force and displacement at the top of the columns are generated at each analysis step.

Table 6.5: Earthquakes.

Eartquake	Direction	Explanation
Miyaew	East-West	1978 Miyaki-Oki Earthquake, Japan
TW078ew	East-West	1999 Taiwan Earthquake, Taiwan
LPew	East-West	1989 Loma Prieta Earthquake, California
LPns	Nort-South	1989 Loma Prieta Earthquake, California
SFew	East-West	1971 San Fernando Earthquake, California
SFns	North-South	1971 San Fernando Earthquake, California

6.6 HYSTERESIS PARAMETERS

While it is possible to make rough estimates of appropriate hysteresis parameters for a given concrete quality and structural type, these values are estimated depending on the reinforcement and the concrete confinement. Stone and Taylor (1993) established closed-form equations for hysteresis parameters for circular bridge columns using stepwise linear regression analysis on 65 digital test records. These equations are used in

this study to estimate the stiffness degradation, strength deterioration and pinching behavior with some modifications to accommodate the differences in their definition in CANNY.

Table 6.6: Columns properties.

	Garneau	**Clydesdale**	
	Pier 1 & 2	**Pier 2**	**Pier 3**
E (MPa)	30000	30000	30000
A (m^2)	1.1304	2.2326	2.2326
I (m^4)	0.0415	0.056	0.0545
Minimum Shear Capacity (kN) Priestley et al. (1994)	3373	943	943

A series of runs covering a range of the hysteresis parameters was carried out to determine the relative sensitivity of the column behavior to the parameters. The columns proved relatively insensitive to the values of δ, θ, λ_3, ε, and λs, while the behavior was quite sensitive to variations in parameters λ_e and λ_μ.

6.6.1 Garneau Flyover

The columns of this bridge are circular; therefore, the Stone and Taylor equations were used to estimate the hysteresis parameters. These columns are well confined and reinforced following the current standards for seismic design as shown in Figures 6.4 and 6.9. Therefore, the hysteresis parameters are expected to be very small. Table 6.7 shows the assumed hysteresis parameters for this case.

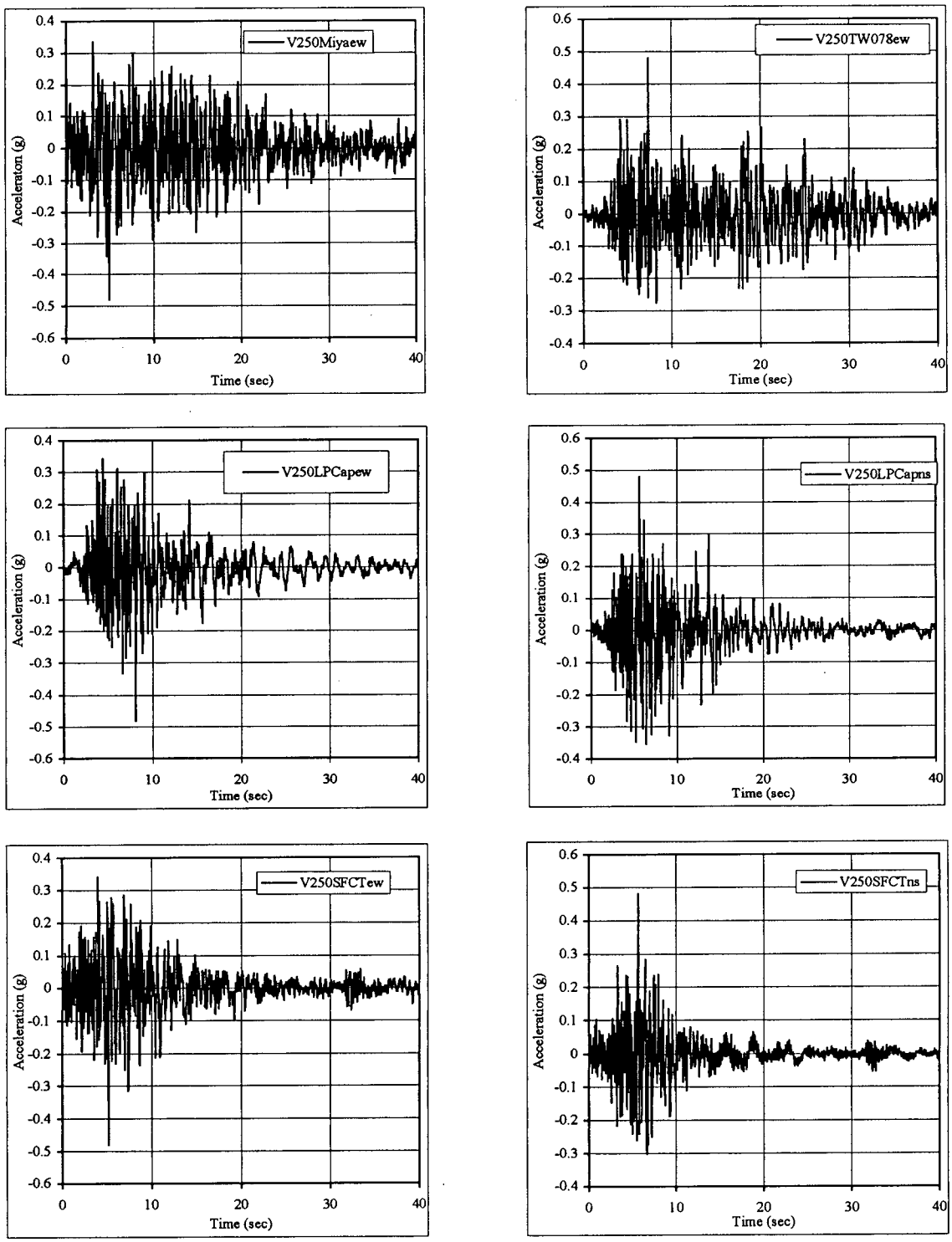

Figure 6.12: Earthquakes fitted to Vancouver firm ground spectrum.

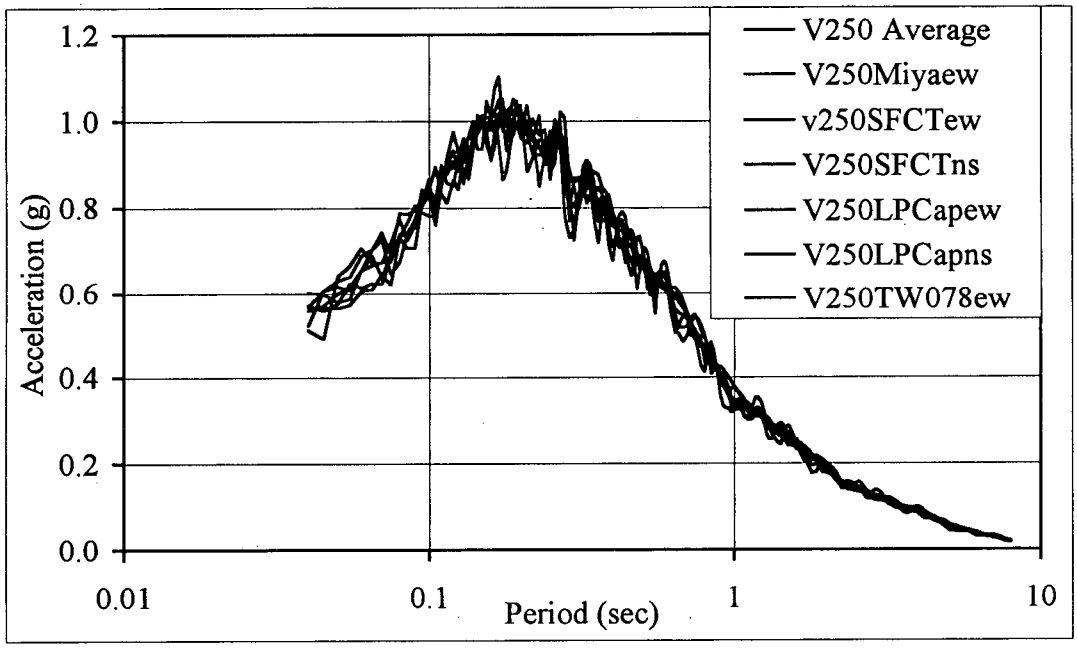

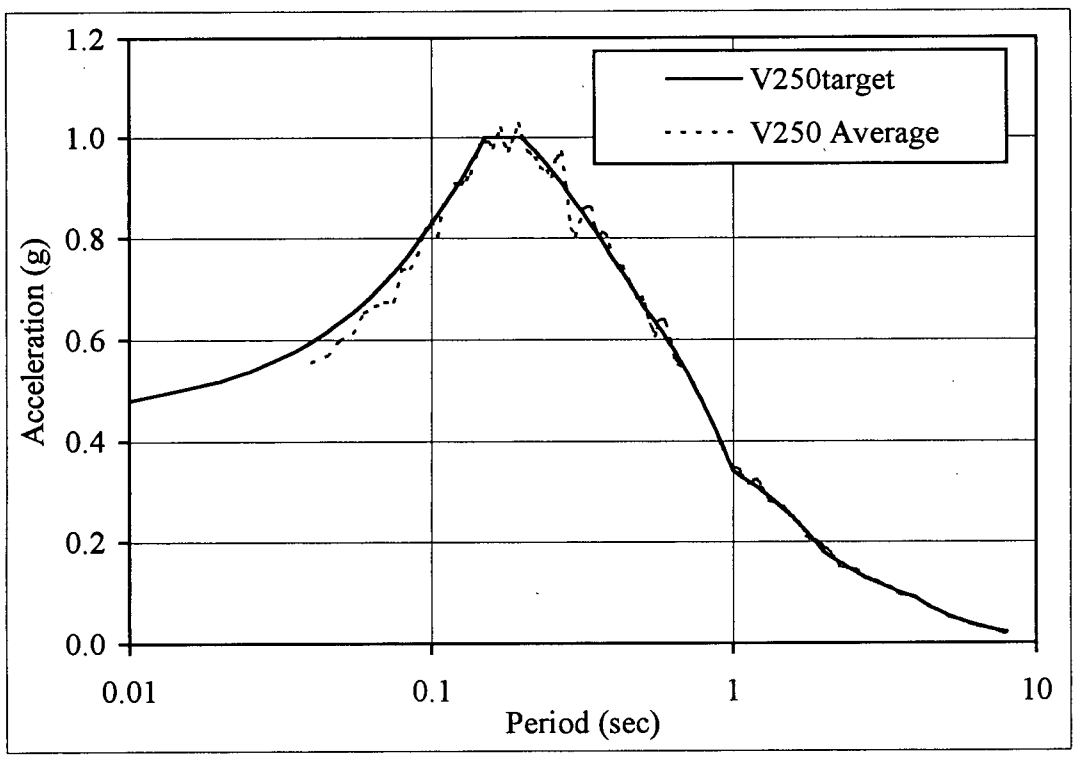

Figure 6.13: Vancouver firm ground spectrum 2% in 50 years.

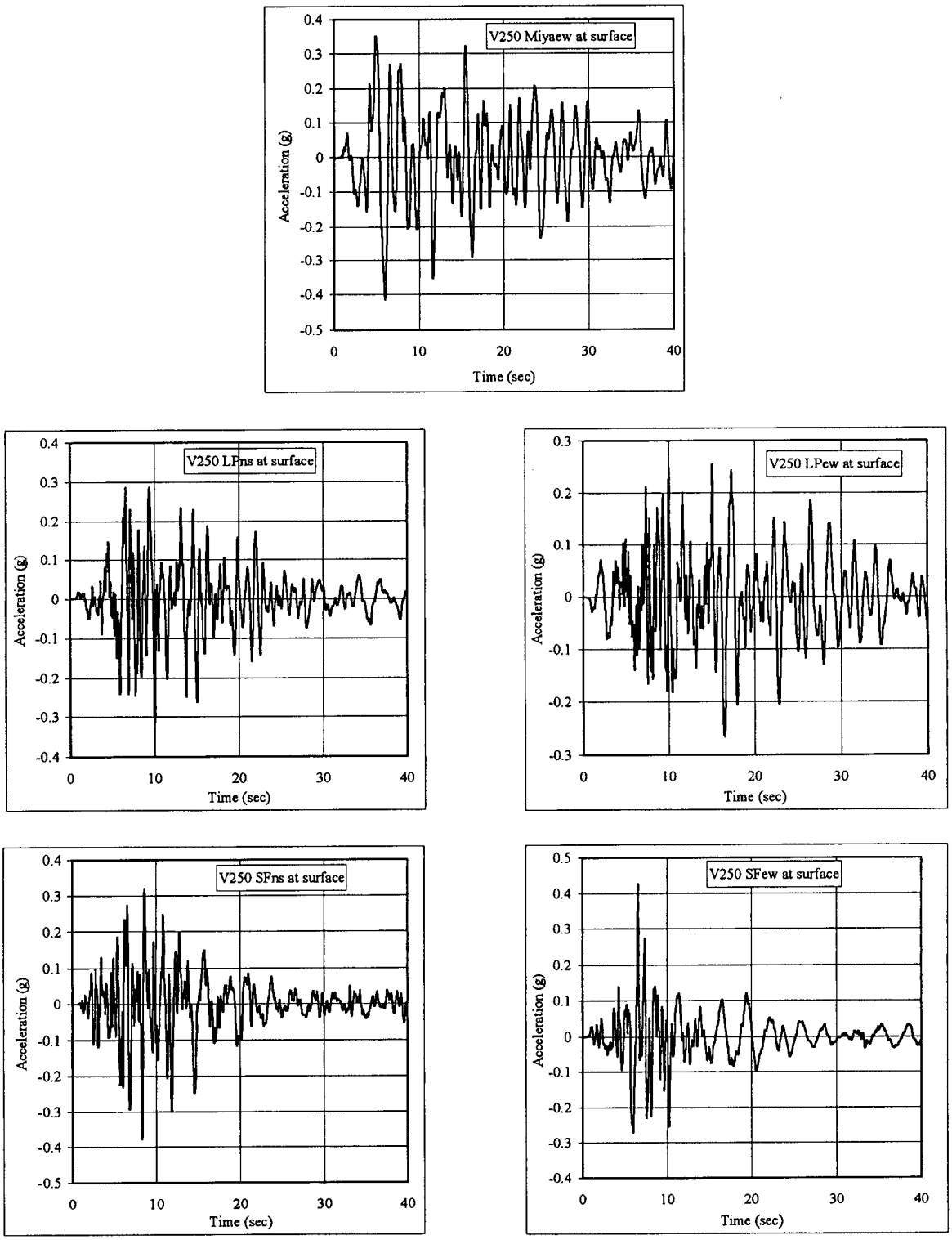

Figure 6.14: Ground motion records at surface (depth to rock = 200 m).

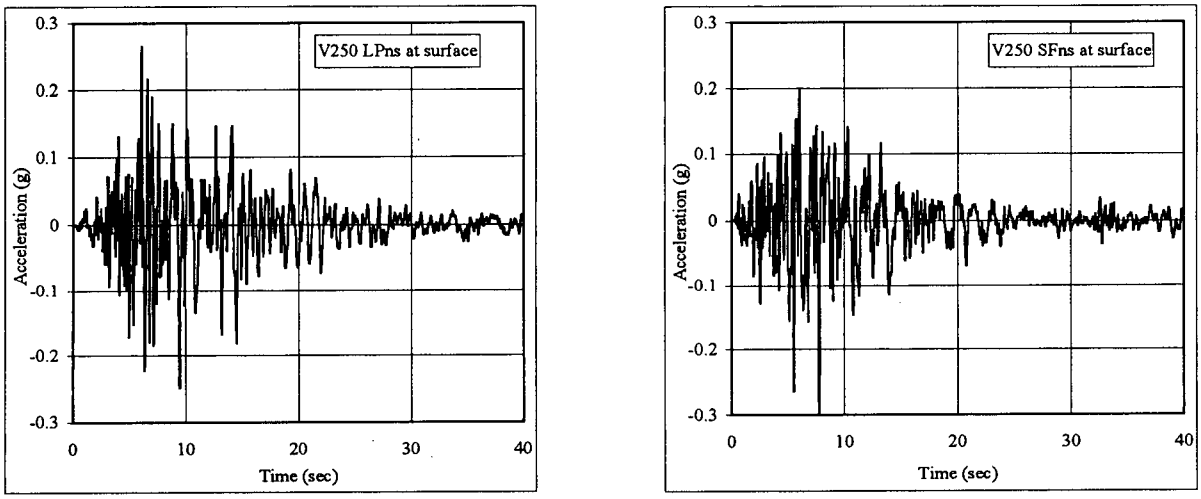

Figure 6.15: Ground motion records at surface (depth to rock = 43 m).

6.6.2 Clydesdale Street Underpass

The columns of this bridge are rectangular; therefore, the Stone and Taylor equations are not applicable here. The ductility capacity of these columns is low (less than 2.0 as shown in Figure 6.11) which makes the hysteresis parameters less important since the effect of these parameters is very small in the early loading stages. Therefore, the same hystersis parameters used in Garneau Flyover as shown in Table 6.7 are also assumed for this bridge.

6.7 DAMAGE ANALYSIS

In order to apply the damage models to earthquake responses, which have unsymmetrical hysteresis loops unlike the cyclic responses used in the previous application chapters where the loading consisted of symmetric cycles, a modification is needed to apply the E2 model. As shown in previous chapters, the E2 damage model was considered for each cycle of loading since the cycle has equal and opposite displacement amplitude in each direction, while this is not necessarily the case in earthquake loading, as shown in Figure 6.16.

Table 6.7: Estimated hysteresis parameters (Garneau Flyover).

Parameter	Estimated Value	Comments
δ	0.0	Preferred equal to post-yield stiffness
θ	5	Small stiffness degradation
λ_e	0.02	Small deterioration
λ_μ	0.01	Small deterioration
λ_3	0.0	No softening
ε	0.0	No pinching
λ_s	1.0	No pinching

Therefore, each range (r) as shown in Figure 6.16, i.e. the difference between successive peak values or between a peak and zero value, is counted as a quarter cycle, the amplitude of which is the range. A similar technique with a slight difference was used by others and summarized by Dowling (1972). The damage is then predicted at every quarter cycle by the E1, E2, and P models.

Unsymmetrical earthquake responses might produce a follower cycle with displacement amplitude less than a primary cycle (earlier cycle with maximum displacement). For example, the displacement reached in the second cycle (end of r7) is less than the maximum displacement reached prior to this point (end of r3) as shown in Figure 6.16. Therefore, the predicted stiffness and starting location of the degraded monotonic response that is needed to calculate A_n at the end of r3 is used to calculate the damage at the end of r7. However, the predicted ultimate deformation at the end of r7 will be

different than the one at the end of r3 because of low-cycle accumulated damage due to r4, r5, r6 and r7 as shown in Figure 6.16.

A modified version of the E1 model as suggested by Kunnath et al. (1992) is used in this application, where the yield deformation is removed from the first term, as discussed in Chapter 2. Equation 2-24 is therefore adapted here by substituting displacement δ for curvature ϕ, hence

$$D = \frac{\delta_m - \delta_y}{\delta_u - \delta_y} + \beta_e \frac{\int dE}{F_y \delta_u} \tag{6-4}$$

The energy constant, β_e, was identified directly from the estimated hysteresis parameters.

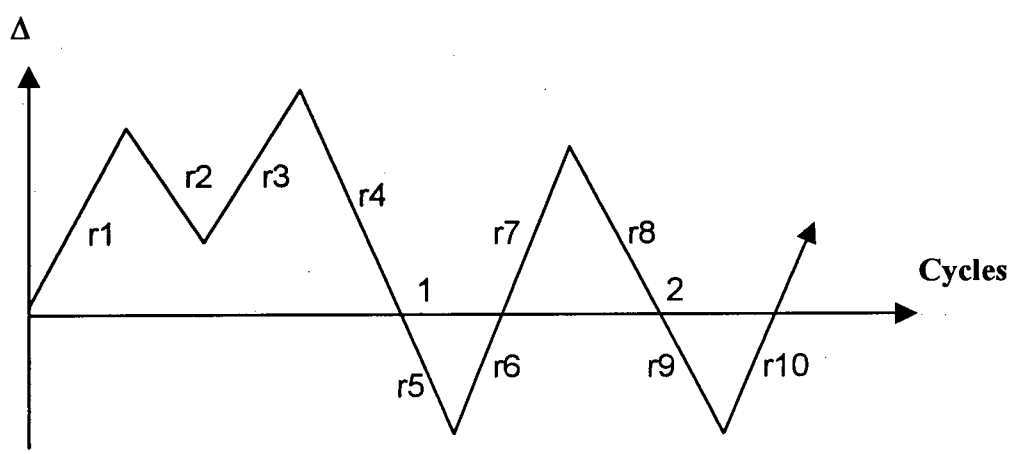

Figure 6.16: Cycle counting method.

6.7.1 Garneau Flyover

The bridge as discussed is situated on loose soil; however, the damage analysis is performed for the two cases of firm and loose soil. This is considered to evaluate the bridge column behavior in different soil properties. Two alternative fill depths (200 m and 43 m) are considered for the analysis in loose soil, as discussed earlier in this chapter.

All the monotonic force-displacement parameters needed for the damage prediction by the E1, E2, and P models are obtained for the monotonic force-displacement response as

shown in Figure 6.9. Figures 6.17 to 6.28 show the damage progression estimated by the three damage models (E1, E2, and P) and the CANNY output for the force-displacement hysteresis loops and the time-displacement response. The E1 and P models predicted the damage very closely and showed damage progression during the time history of the ground motions. The E2 gave low damage compared to E1 and P models.

The bridge column behaved really well to the earthquake records if the bridge was built on firm ground or loose soil of about 43 m deep. Figures 6.17, 6.19, 6.21, 6.22, 6.24, 6.24 and 6.28 show that these earthquake records produced insignificant inelastic cycles. The E1 and P models showed very little damage of less than 0.1 under these earthquake records as shown in the damage figures. This damage corresponds to the no damage state as concluded by the proposed damage model at the end of Chapter 4. This was expected since the bridge was designed with sufficient detailing and lateral earthquake resistance. The E2 model showed almost zero damage for this case because of the low ductility demands that induced very low plastic strains in the longitudinal reinforcement of the column.

On the other hand, the bridge column showed significant damage under the selected earthquake records if the bridge was built on fill of about 200 m deep as shown in Figures 6.18, 6.20, 6.23, 6.25, and 6.27. These figures show that this case produced few significant inelastic cycles. The 1978 Miyaki-Oki earthquake (Figure 6.23) produced a complete collapse of the column as estimated by the E1 and P models (D=1.0). The entire damage happened during one cycle only because of the high displacement demand induced during that cycle as shown in Figure 6.23. Other earthquakes produced significant damage between 0.5 and 0.8 as shown in the damage figures. Although the E2 model gave damage less than the E1 and P models, it is still significant.

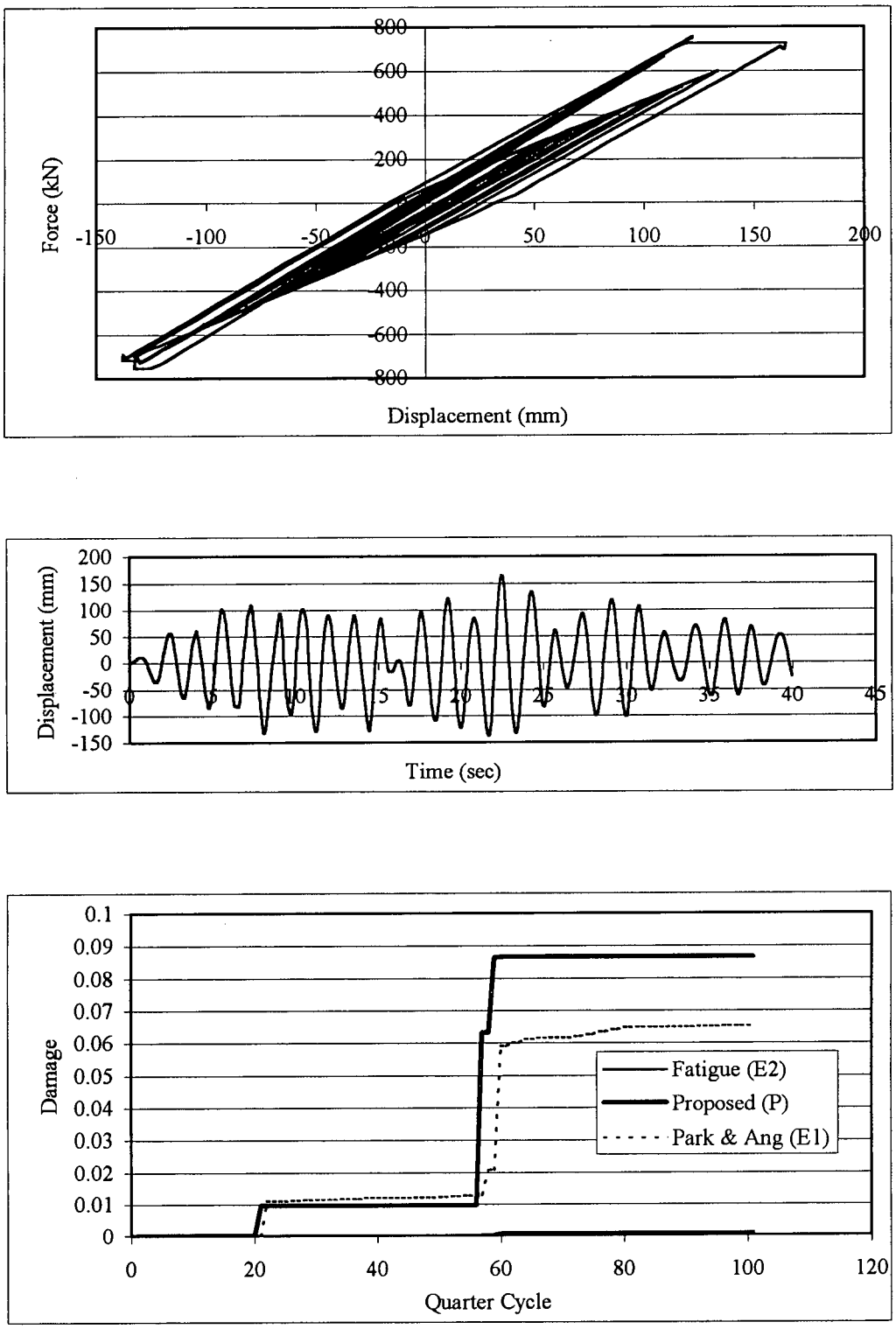

Figure 6.17: Garneau behavior to Loma Prieta east-west (firm ground).

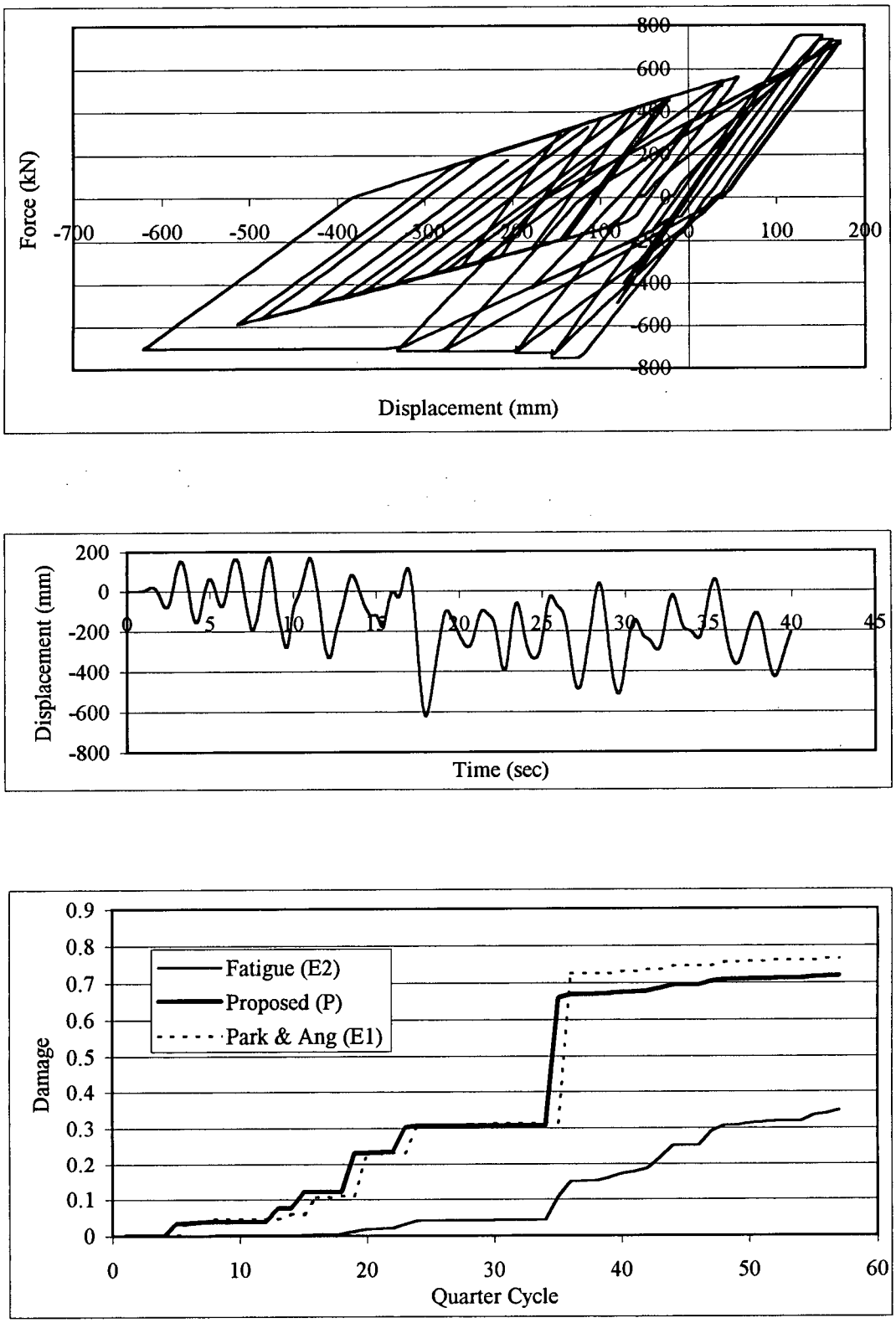

Figure 6.18: Garneau behavior to Loma Prieta east-west (fill of 200 m).

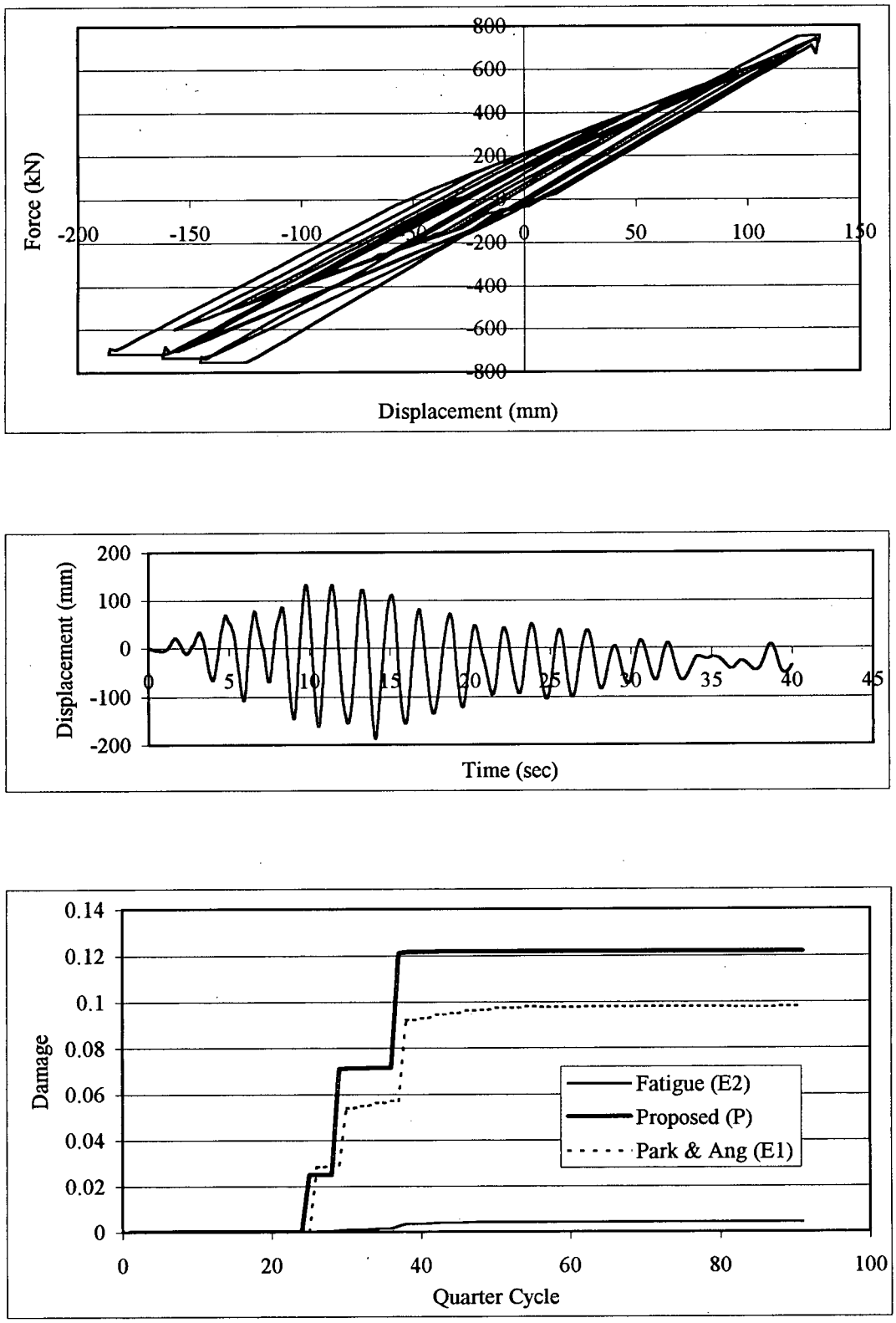

Figure 6.19: Garneau behavior to Loma Prieta north-south (firm ground).

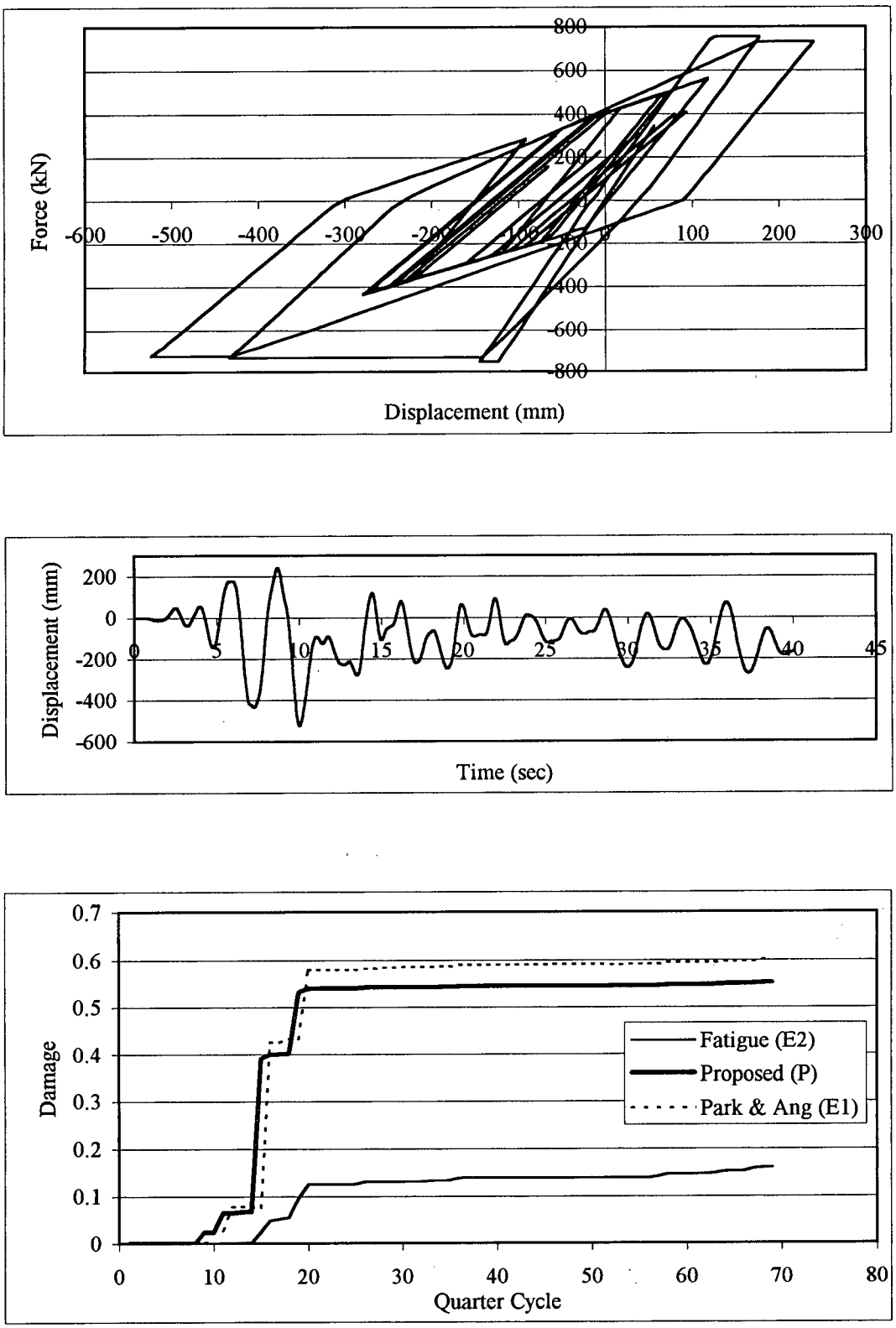

Figure 6.20: Garneau behavior to Loma Prieta north-south (fill of 200 m).

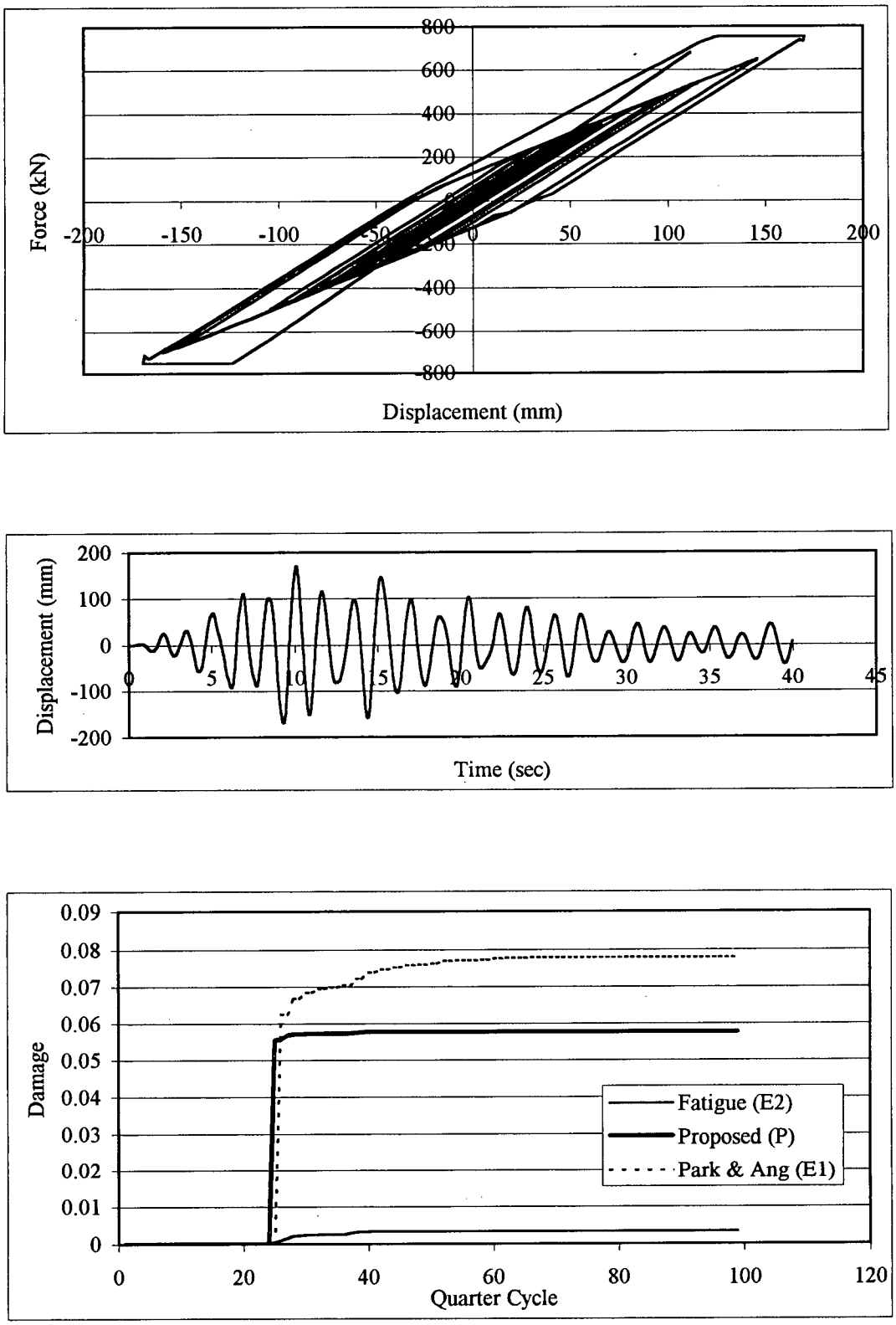

Figure 6.21: Garneau behavior to Loma Prieta north-south (fill of 43 m).

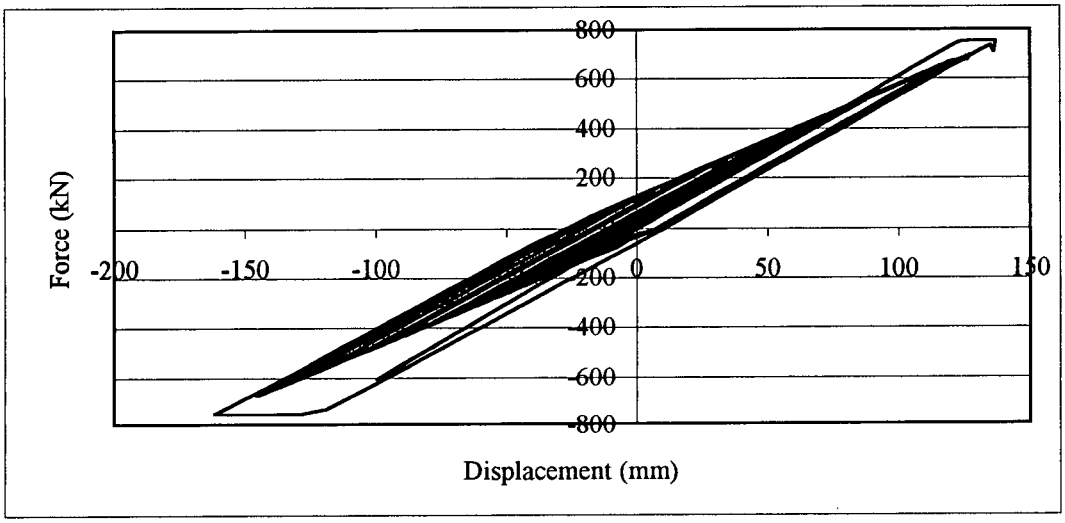

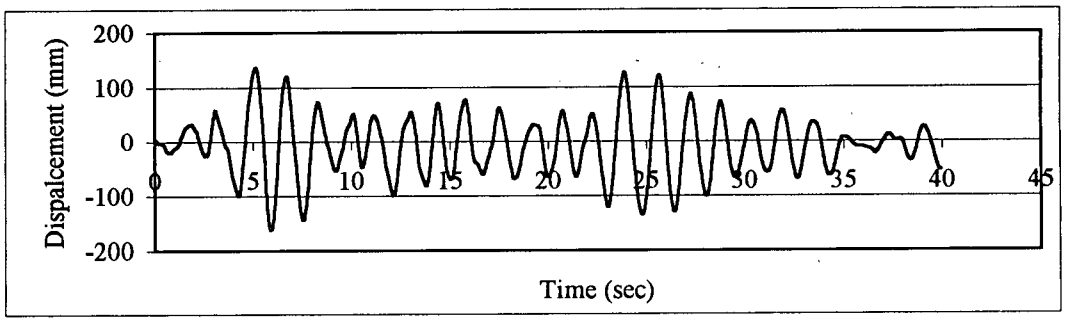

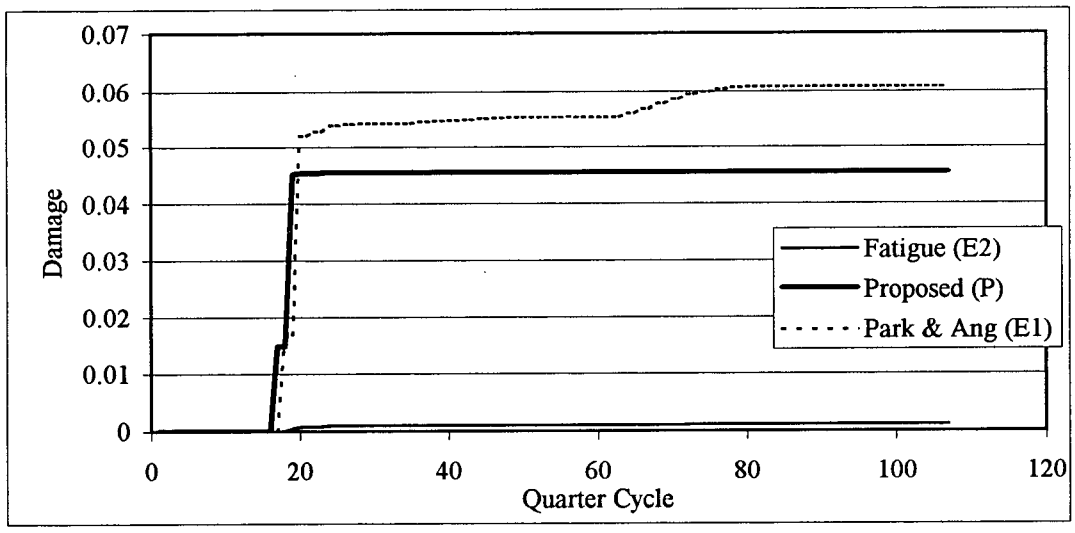

Figure 6.22: Garneau behavior to 1978 Miyaki-Oki east-west (firm ground).

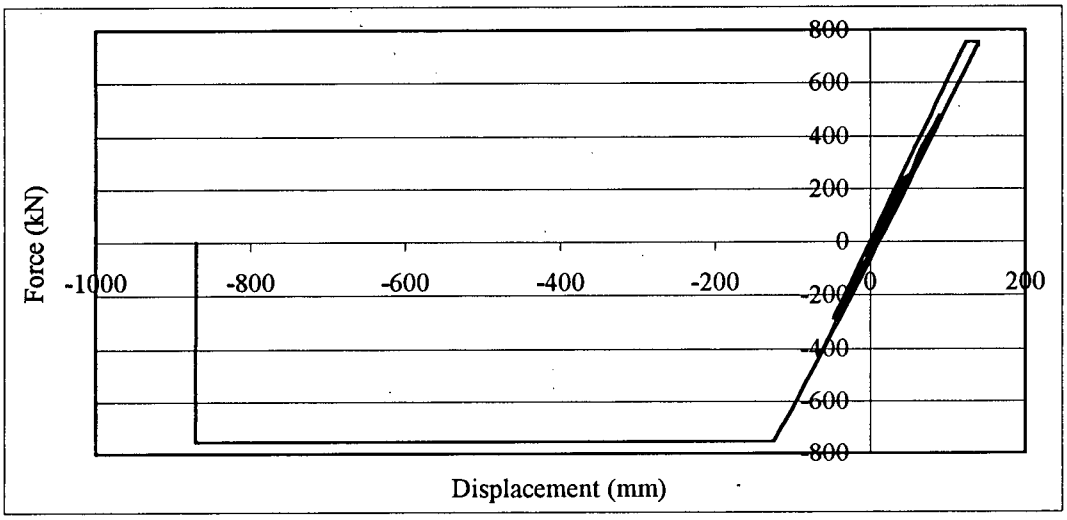

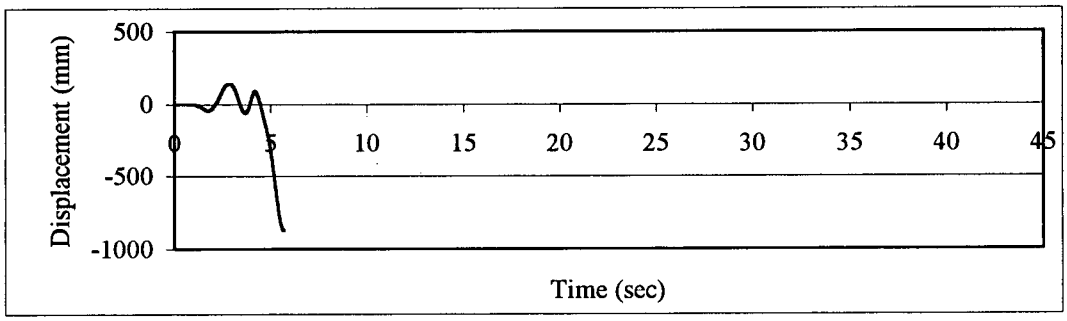

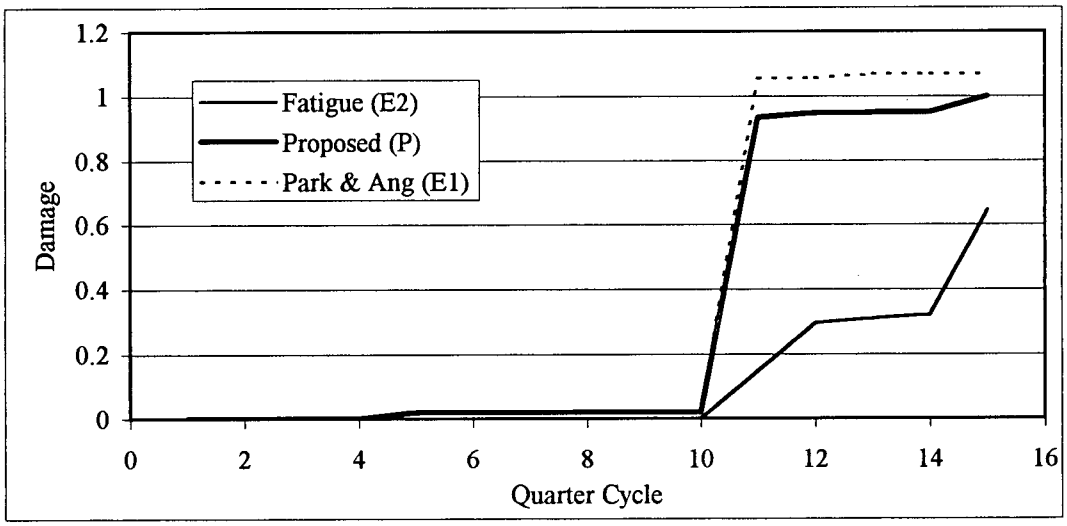

Figure 6.23: Garneau behavior to 1978 Miyaki-Oki east-west (fill of 200 m).

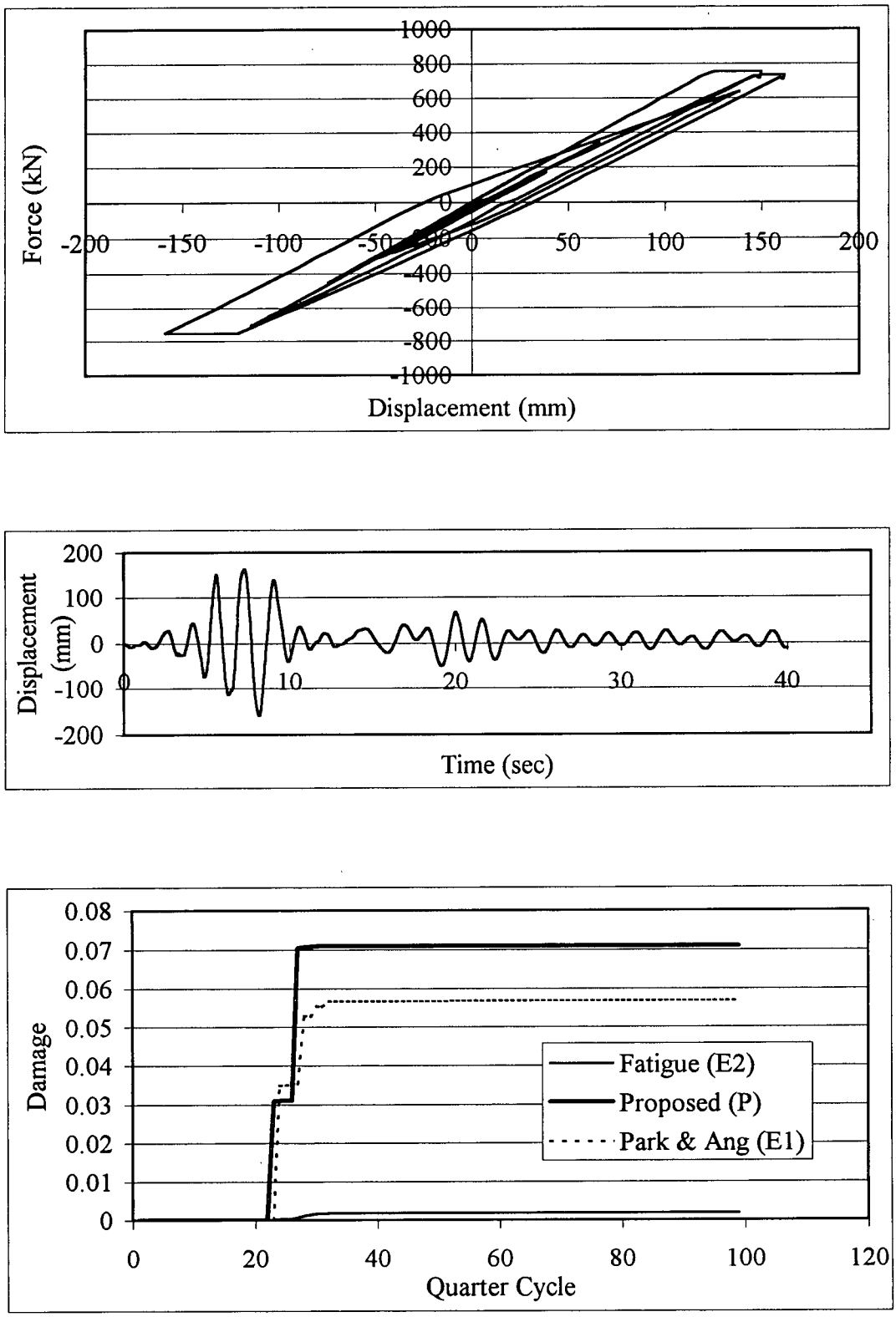

Figure 6.24: Garneau behavior to 1971 San Fernando east-west (firm ground).

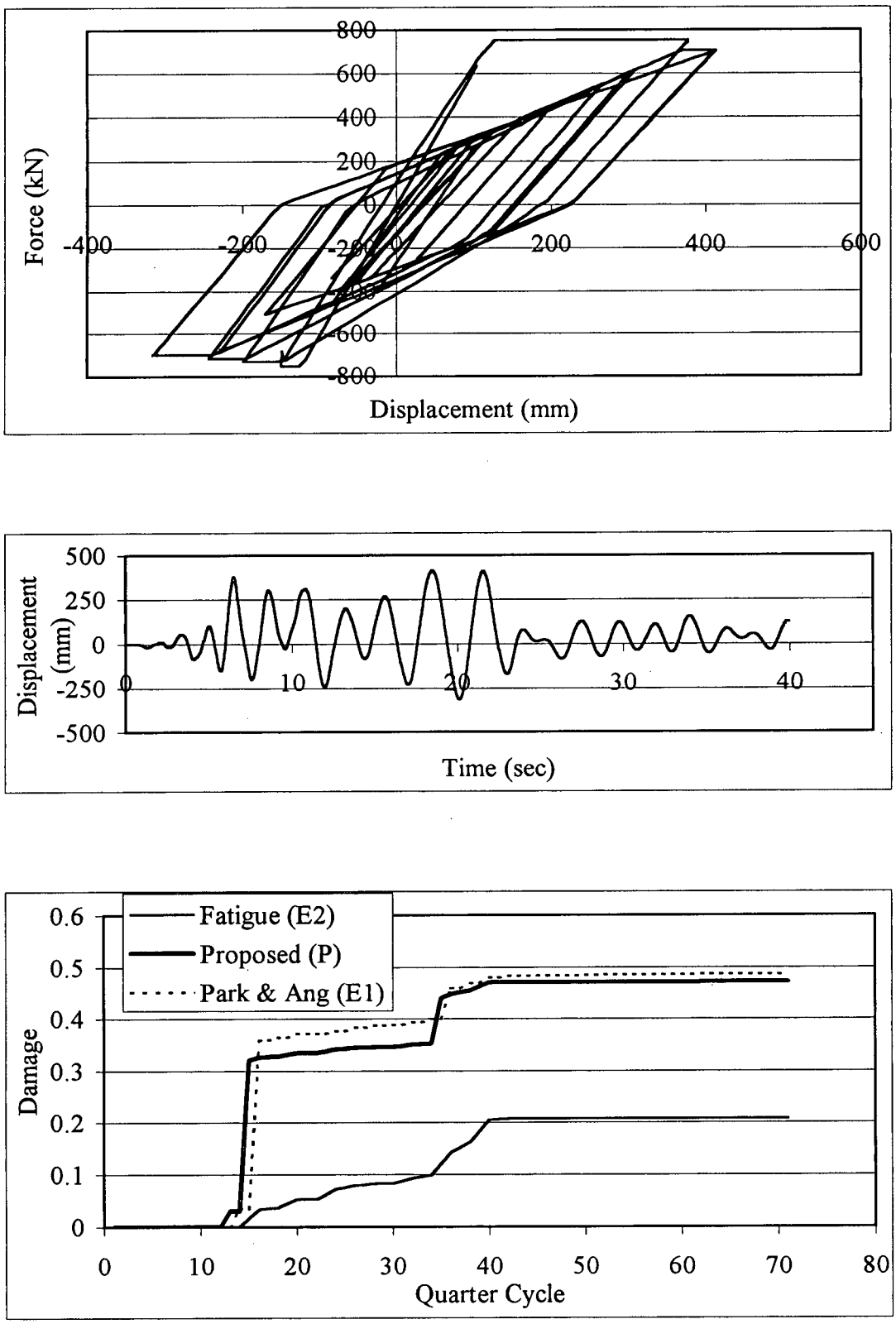

Figure 6.25: Garneau behavior to 1971 San Fernando east-west (fill of 200 m).

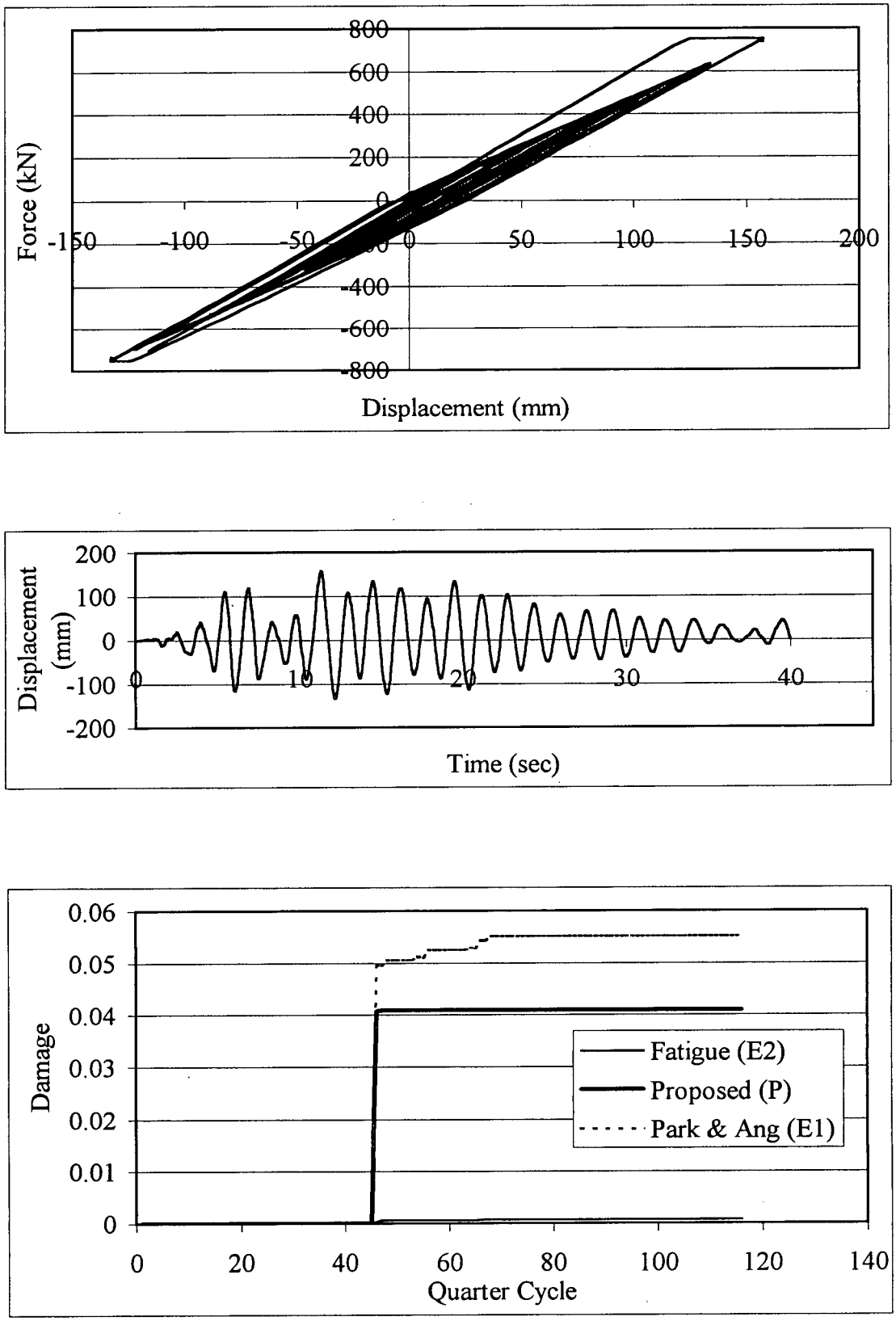

Figure 6.26: Garneau behavior to 1971 San Fernando north-south (firm ground).

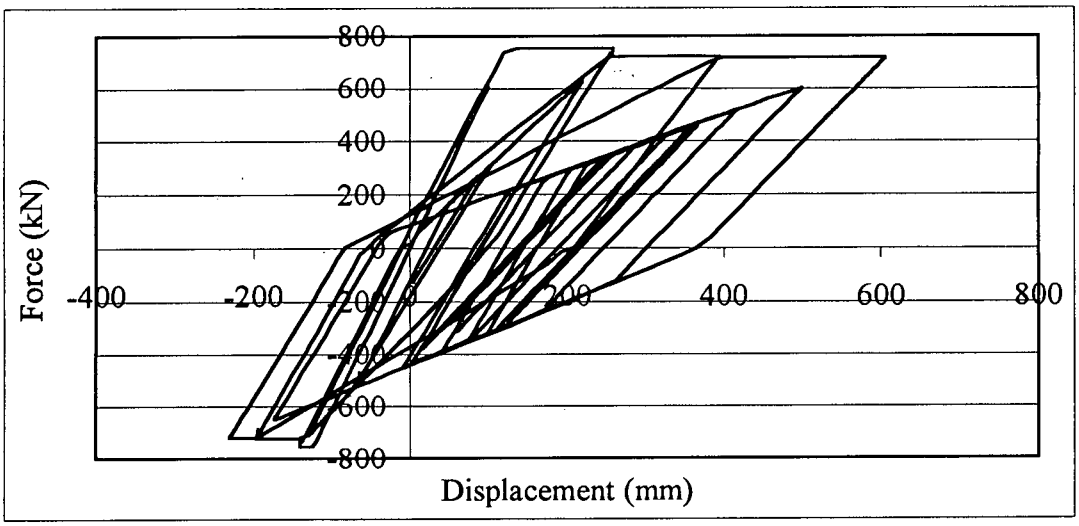

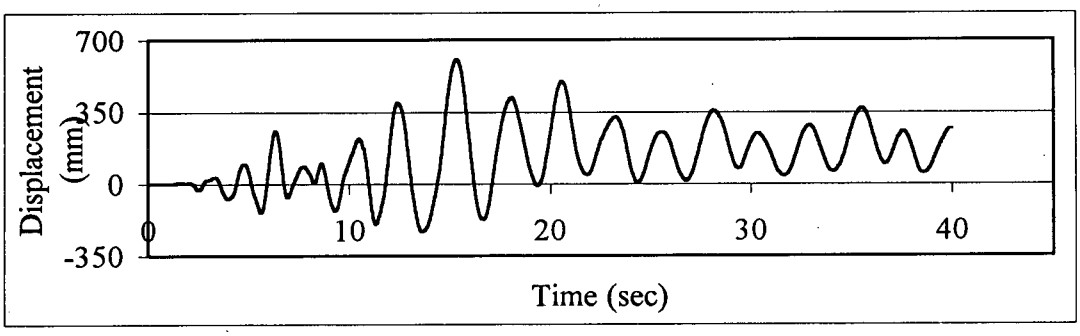

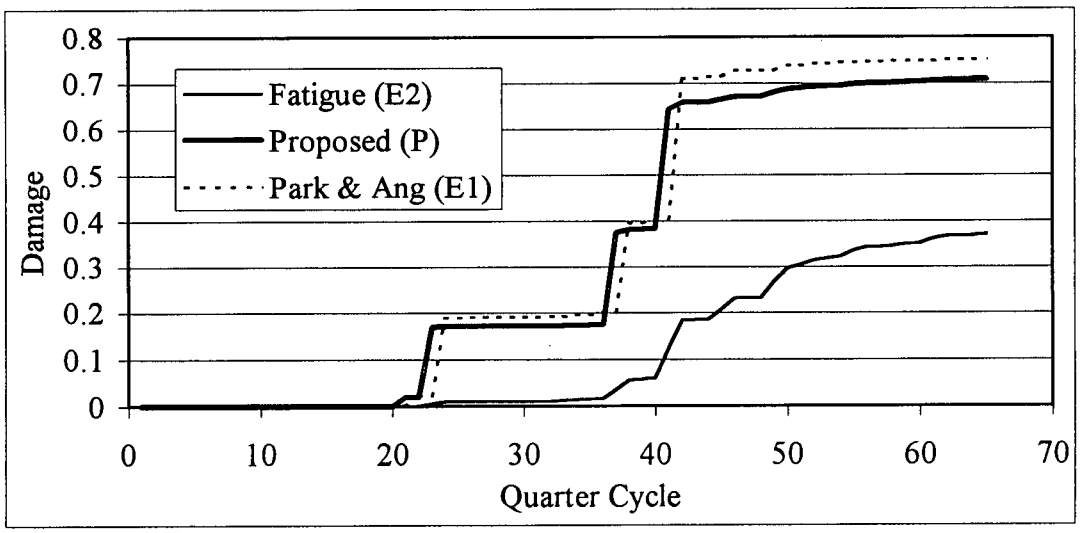

Figure 6.27: Garneau behavior to 1971 San Fernando north-south (fill of 200 m).

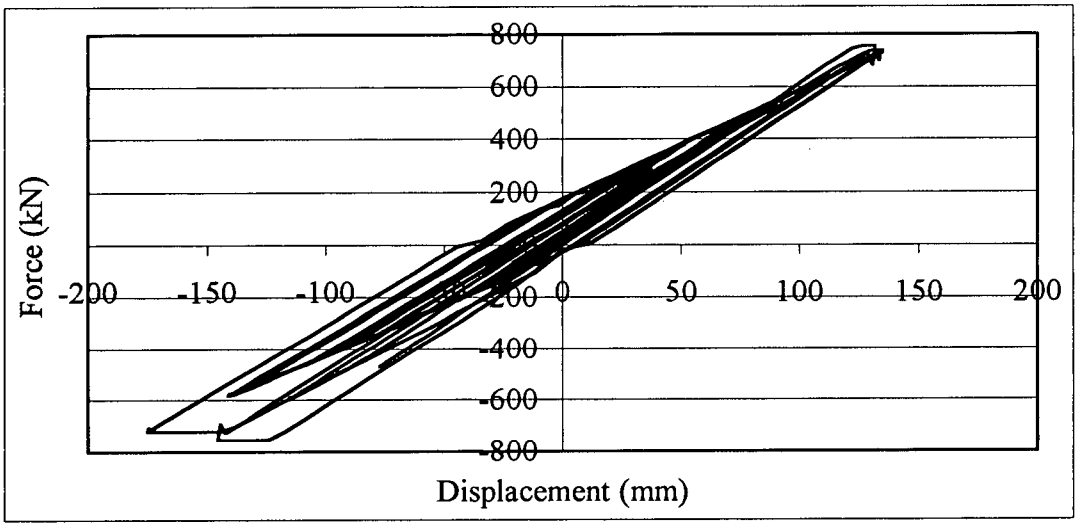

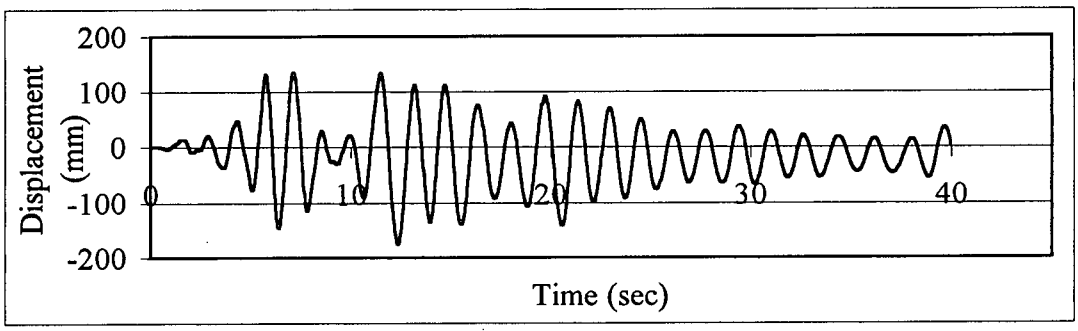

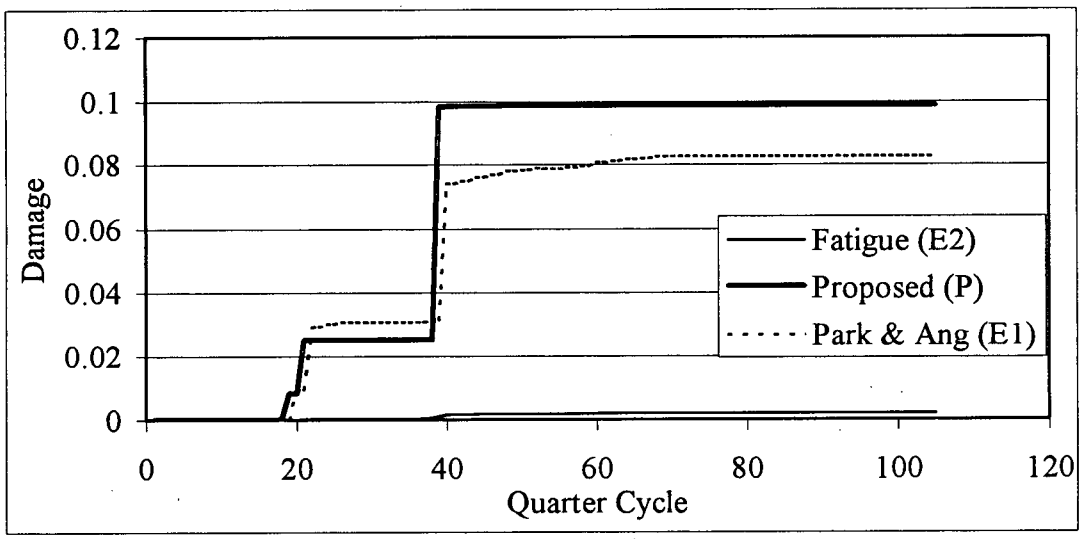

Figure 6.28: Garneau behavior to 1971 San Fernando north-south (fill of 43 m).

6.7.2 Clydesdale Street Underpass

The bridge as discussed is situated on firm ground; therefore, only firm ground motion records are considered for this bridge.

All the monotonic force-displacement parameters needed for the damage prediction by the E1, E2, and P models are obtained for the monotonic force-displacement response as shown in Figure 6.11. Figures 6.29 to 6.34 show the damage progression estimated by the three models and the CANNY output for the force-displacement hysteresis loops and the time-displacement response for pier 2. The results of pier 3 are shown in Appendix B.

As shown in the damage figures, the E1 model gave damage higher than the P model through the loading history. This is because of the low ductility capacity, which influences the E1 prediction as shown in Equation 6.4. The 1971 San Fernando north-south and 1999 Taiwan earthquakes produced complete failure (D=1.0) to pier 2 as estimated by the E1 and P models as shown in Figures 6.33 and 6.34. Pier 3 showed the same damage (D=1.0) under these earthquakes as shown in the figures in Appendix B. This is happened during the first inelastic cycle, as it had a ductility demand higher than the capacity. The E2 model predicted almost no damage because of the small plastic displacement induced during these earthquakes. Although the ductility demand was higher than the ductility capacity, the induced plastic displacement was considerably small because of the low displacement capacity for both piers as shown in Figure 6.11. The E1 and P models estimated a damage of 1.0 (complete collapse) to pier 3 under 1989 Loma Prieta east-west earthquake as shown in Figure B.1 in Appendix B. Other earthquake records produced damage of less than 1.0 as estimated by the P model as shown in the damage figures; however, the damage is considered significant and sometimes beyond repair according to the damage classification as concluded by the P model at the end of chapter 4. This confirms to what was expected since the columns of this bridge are poorly reinforced and detailed.

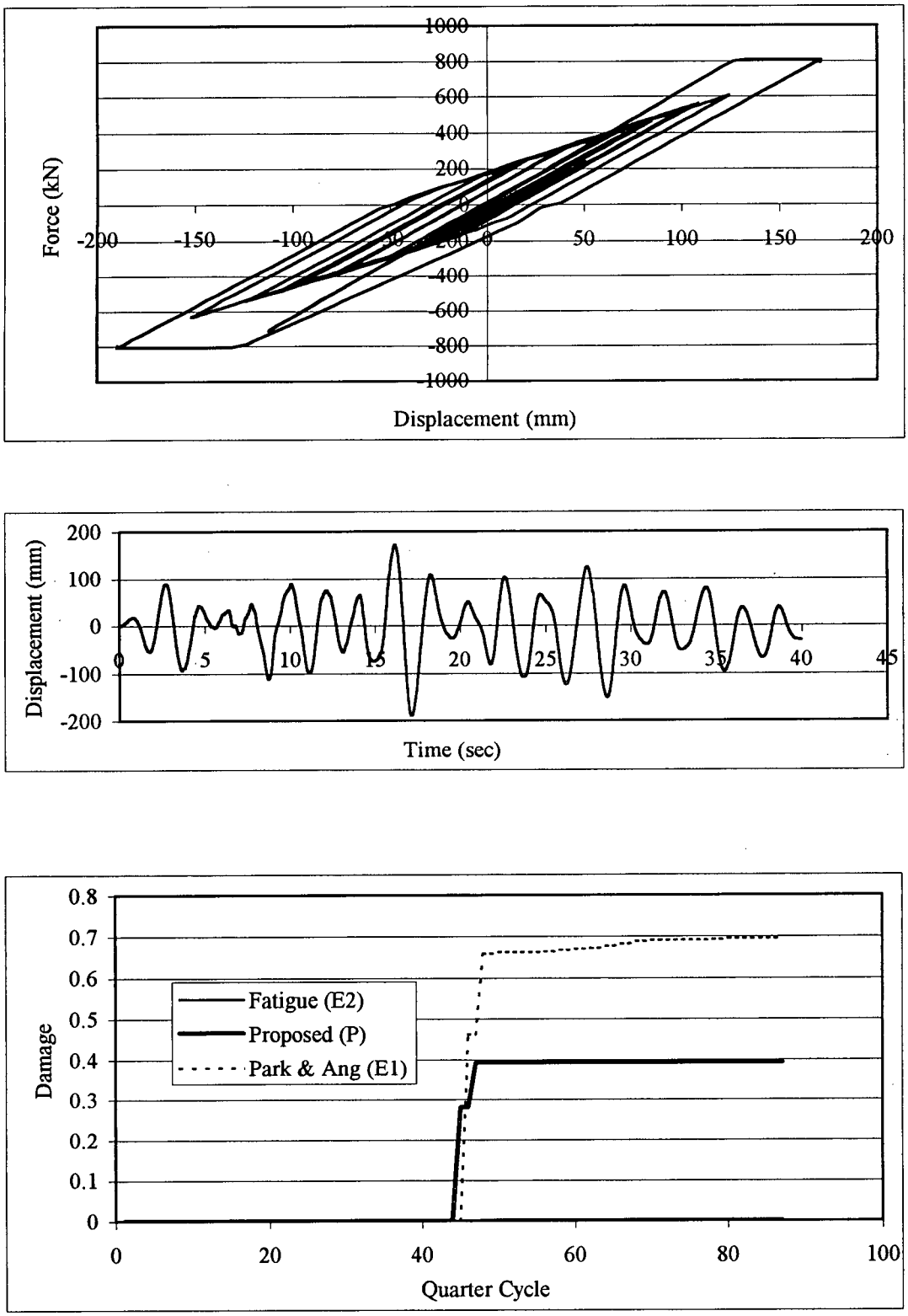

Figure 6.29: Clydesdale behavior to 1989 Loma Prieta east-west (pier 2).

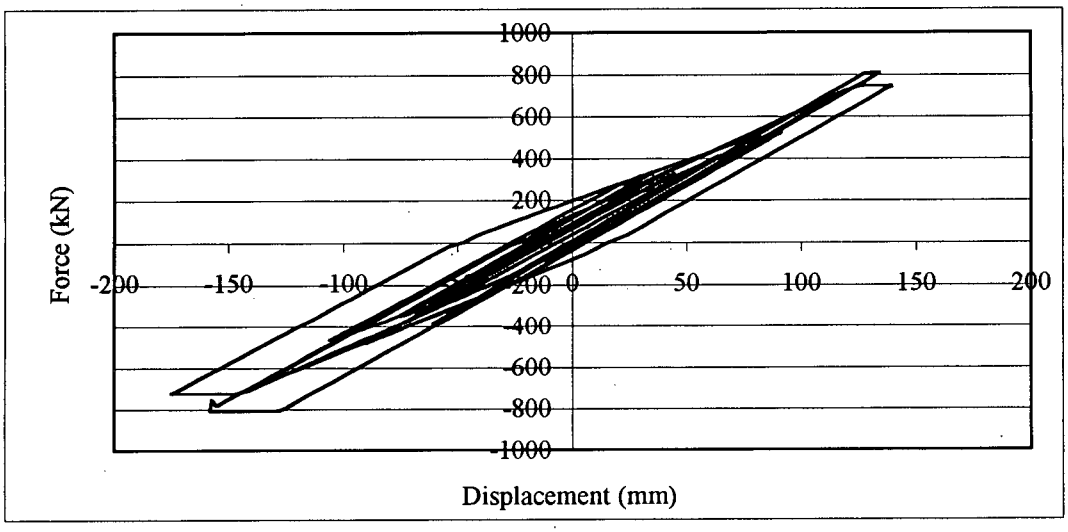

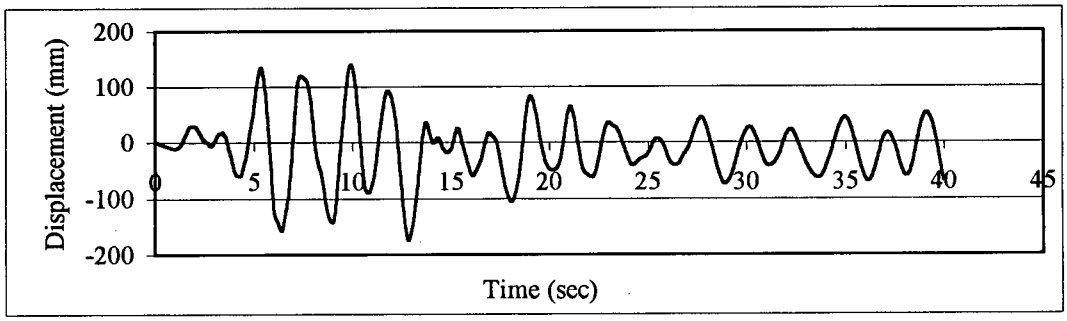

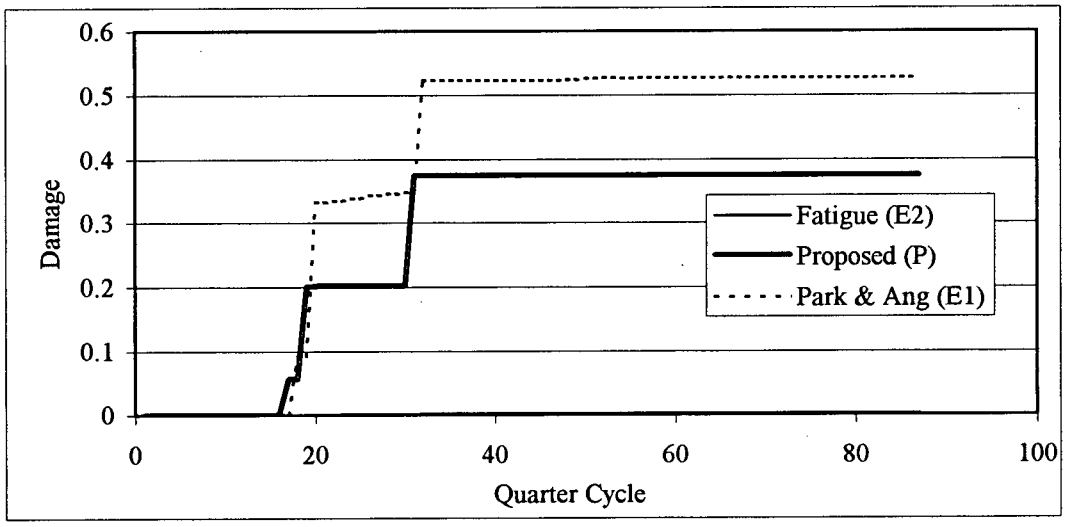

Figure 6.30: Clydesdale behavior to 1989 Loma Prieta north-south (pier 2).

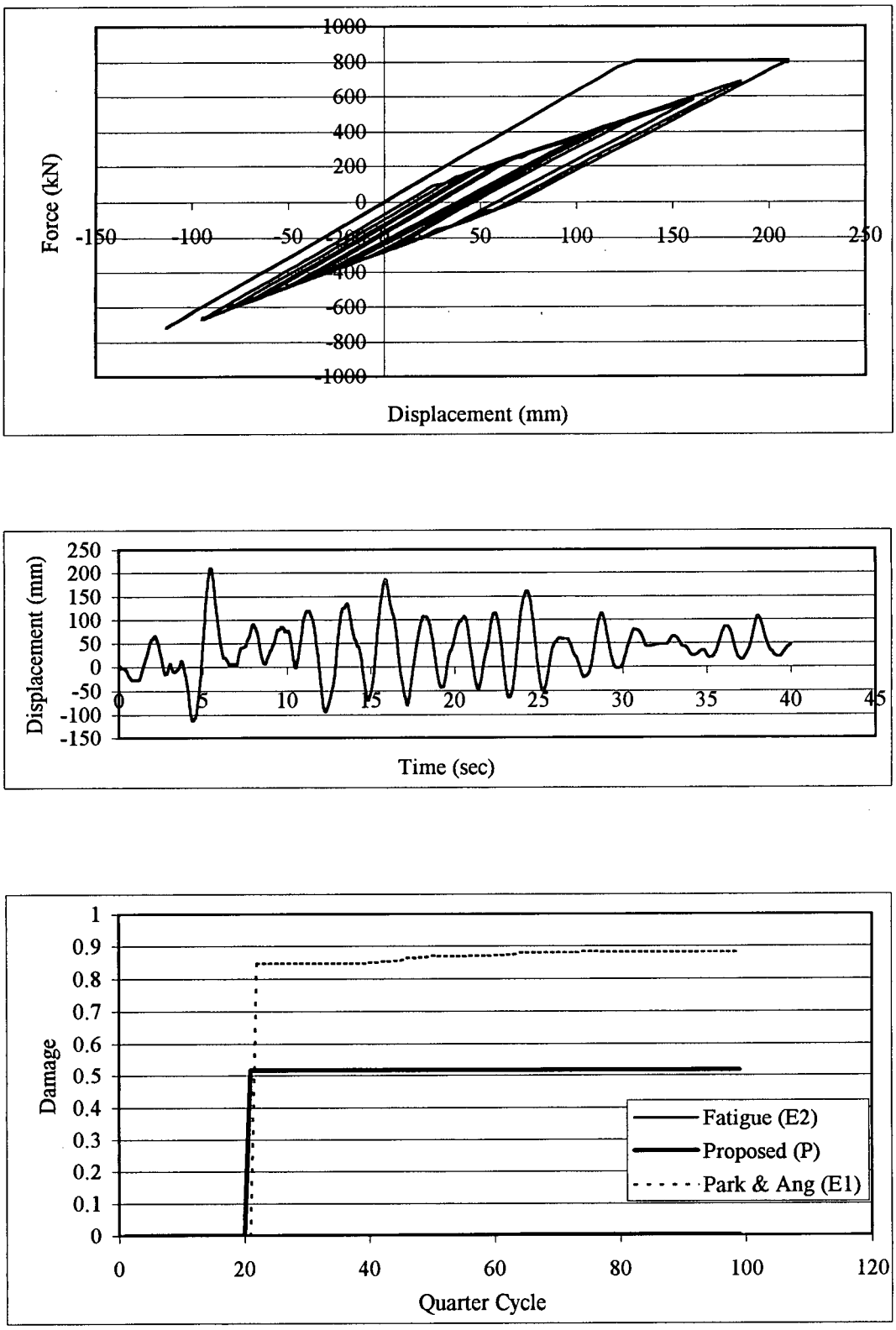

Figure 6.31: Clydesdale behavior to 1978 Miyaki-Oki east-west (pier 2).

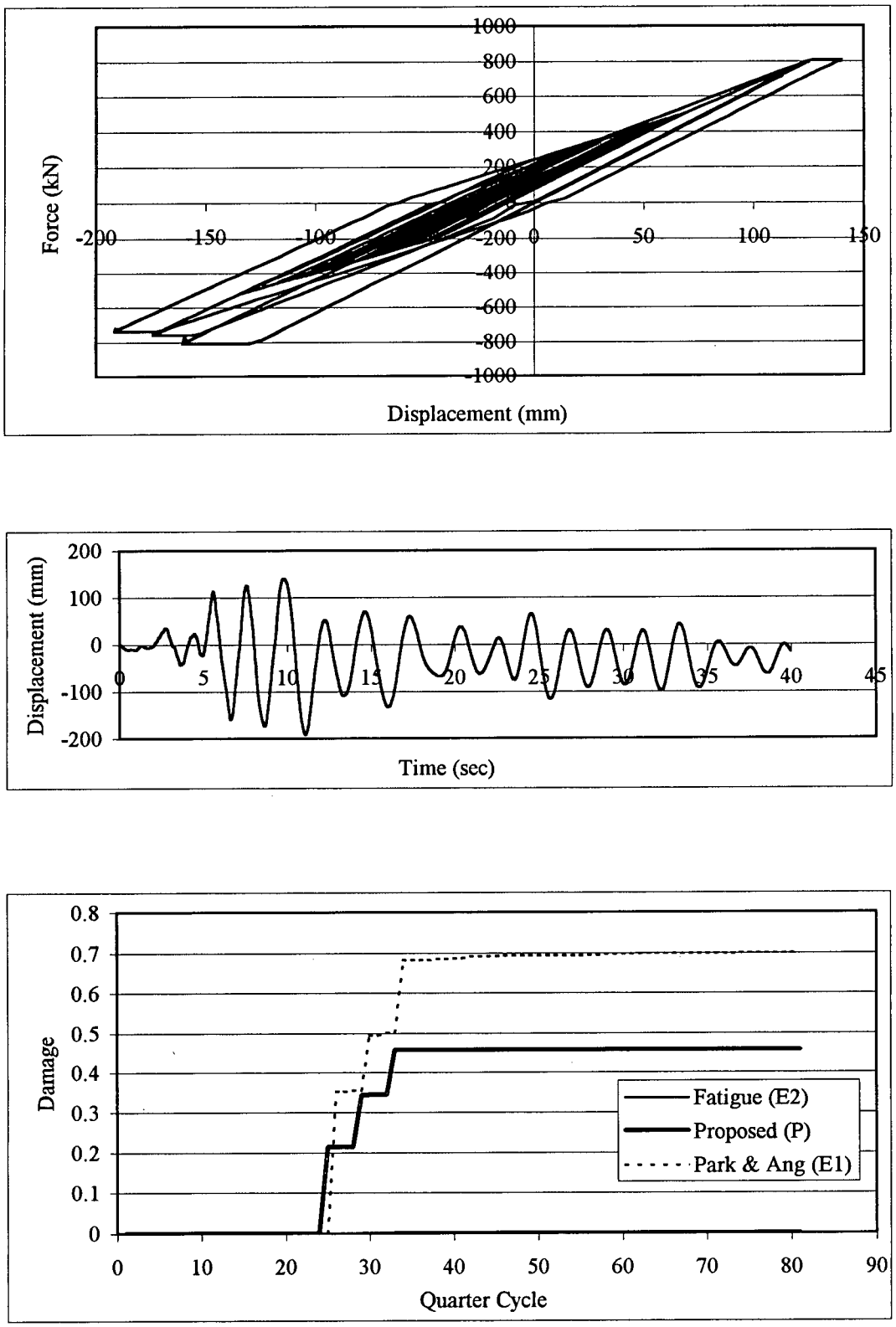

Figure 6.32: Clydesdale behavior to 1971 San Fernando east-west (pier 2).

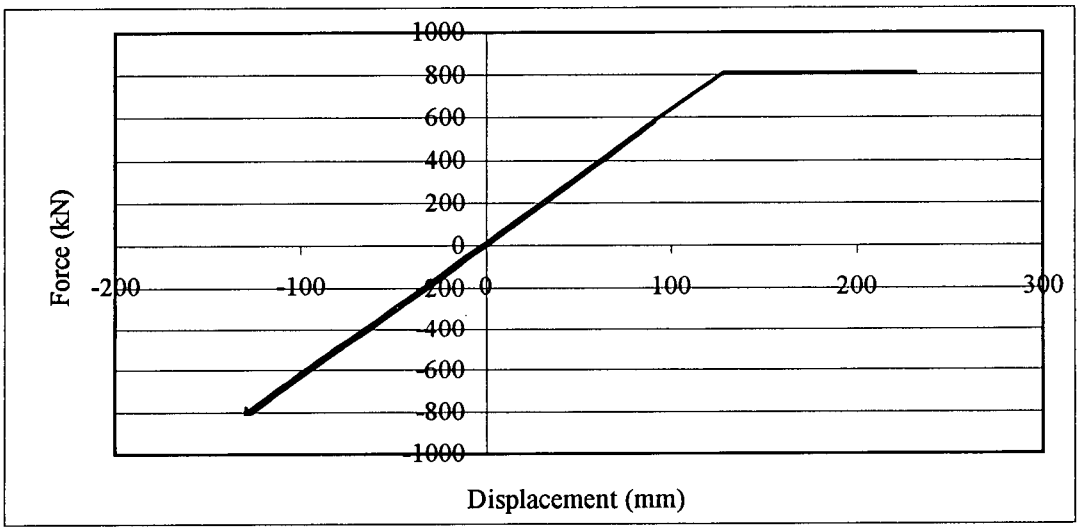

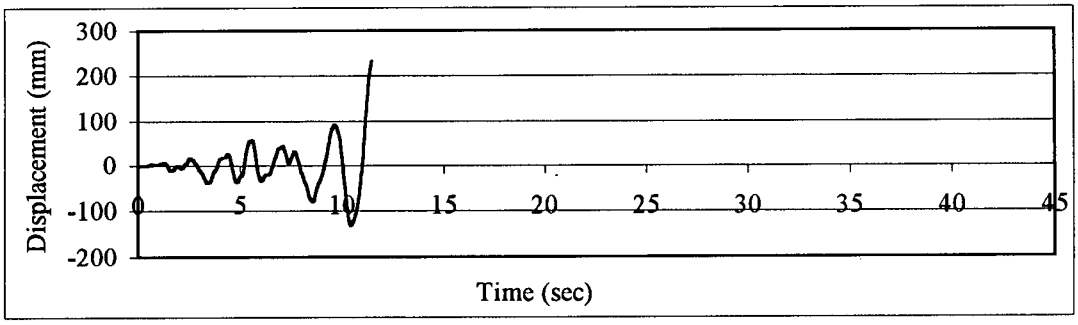

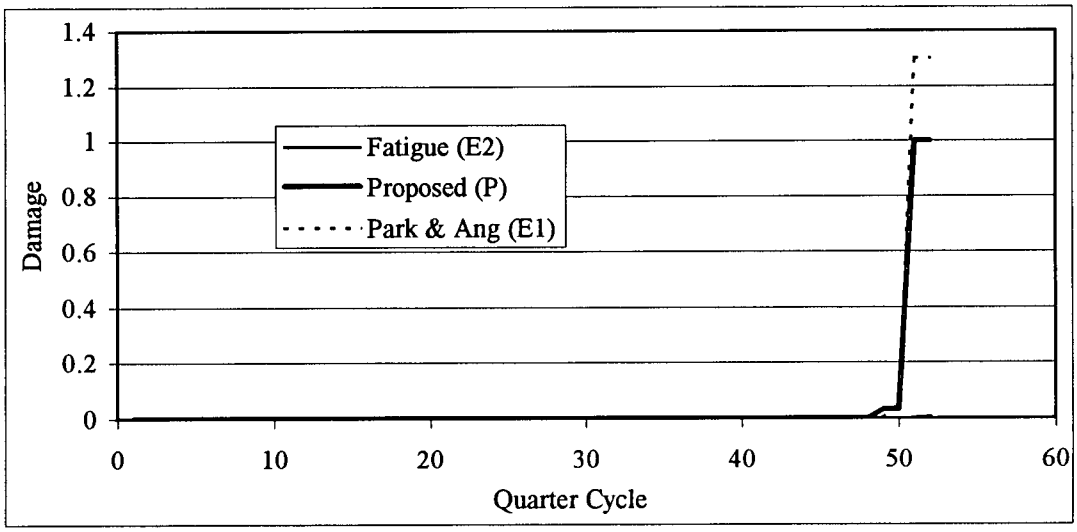

Figure 6.33: Clydesdale behavior to 1971 San Fernando north-south (pier 2).

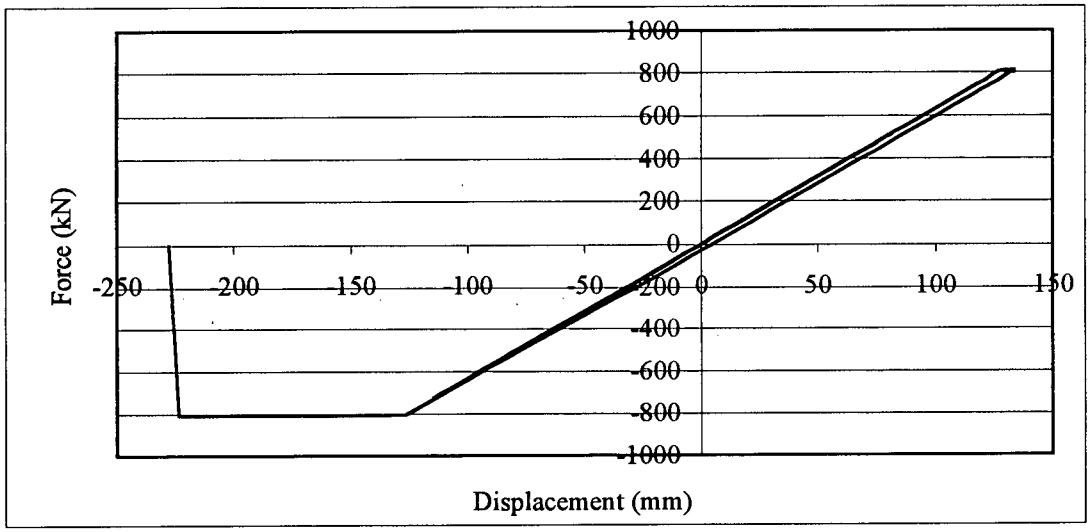

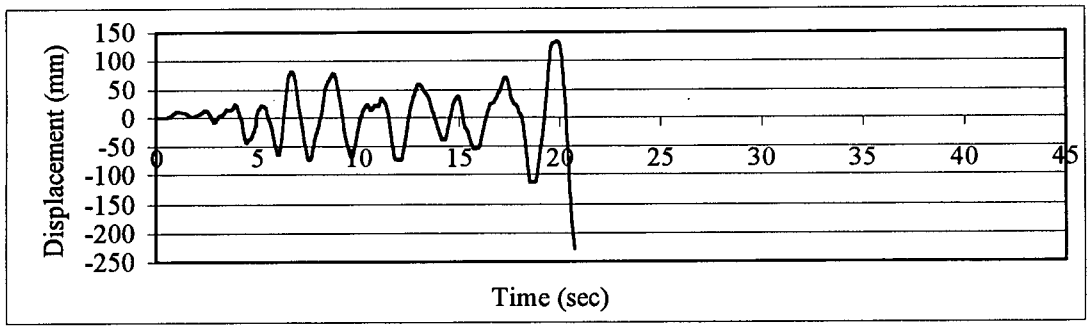

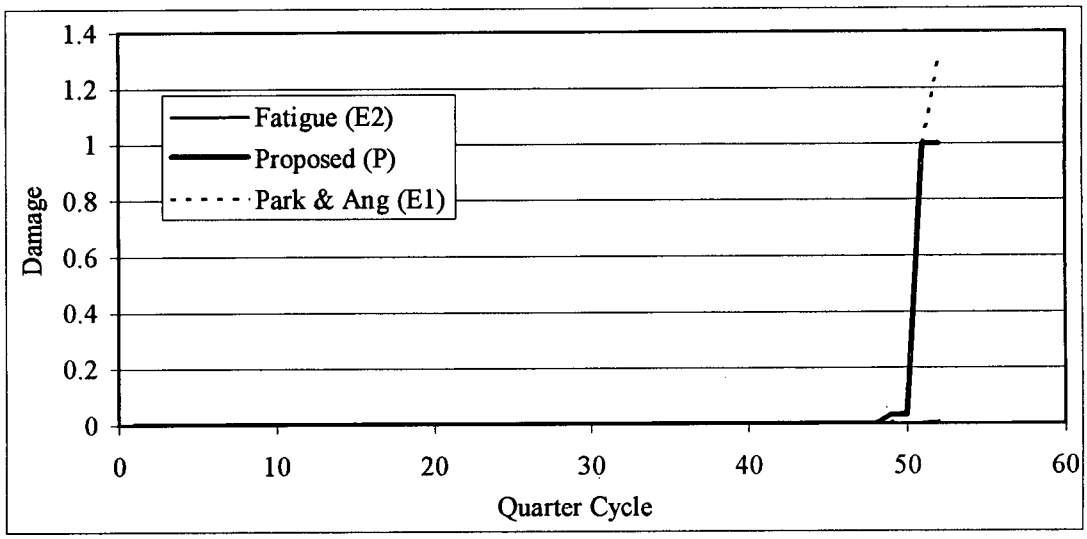

Figure 6.34: Clydesdale behavior to 1999 Taiwan east-west (pier 2).

CHAPTER SEVEN

DECISION ANALYSIS

The object of this chapter is to briefly demonstrate a seismic retrofit decision analysis for bridges using the proposed damage model as a tool. This is done to demonstrate how the damage model can be used as a measure of consequences.

In order to demonstrate the use of the damage index as a measure of consequences, a simple decision model is used to consider the retrofit options for the Clydesdale Underpass since it showed poor lateral resistance to seismic loading as discussed in Chapter 6. This decision will consider two options; no retrofit (do nothing) or fully effective retrofit.

A decision analysis model is diagrammed as a decision tree with two actions, retrofit and no retrofit, as shown in Figure 7.1. For the no retrofit option, various earthquake levels are considered. Each earthquake level is associated with a damage cost, which depends on the seismic damage level as calculated in Chapter 6.

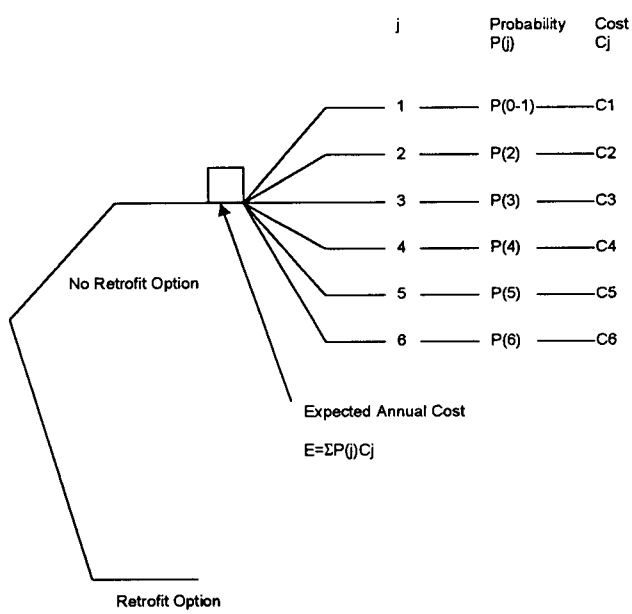

Figure 7.1: Decision tree.

In this study, six earthquake records with different probability of exceedance in 50 years are selected as shown in Table 7.1. The PGA's of these records were calculated for the Vancouver area. The annual probability of these earthquakes are calculated following Poisson Process and assuming that the annual occurrence rate of each event j is the same as the annual probability, P(j), of that event since probability of 2 or more events in one year is negligible. Table 7.1 summarizes the annual earthquake probabilities.

Table 7.1: Annual earthquake probabilities and damage indices.

j	Probabilty of Exceedance in 50 Years P(1 or more\50)	PGA (g)	P(0\50)	Annual Occurrence Rate, v	Return Period (1/v) (year)	Damage Index D
1	>0.5		<0.50	0.975466		0.00
2	0.5	0.0075	0.50	0.013863	72	0.00
3	0.3	0.0424	0.70	0.007133	140	0.00
4	0.1	0.2400	0.90	0.002107	475	0.00
5	0.05	0.3701	0.95	0.001026	975	0.35
6	0.02	0.4800	0.98	0.000404	2475	1.00
			Total=	1.000000		

7.1 DAMAGE ANALYSIS

For this study the 1971 San Fernando (North-South) earthquake record is used. It would have caused collapse of piers 2 and 3 of Clydesdale Underpass according to the analysis in Chapter 6. The San Fernando (North-South) earthquake record fitted to Vancouver ground spectrum with 2% probability of exceedance in 50 years was scaled to obtain the records for earthquakes with other probabilities of exceedance according to their PGA's as shown in Table 7.1.

The damage analysis of Clydesdale Underpass is shown in detail in Chapter 6. The analysis was repeated here to calculate the damage due to earthquakes with other probabilities of exceedance as shown in Table 7.1. Only the proposed damage model (P model) is considered in this study. A damage of zero was obtained from earthquakes with probabilities of exceedance equal or higher than 10% (j from 1 to 4) as shown in Table 7.1.

7.2 LOSS ESTIMATE

In general, damage costs can be divided into two categories: direct costs and indirect costs.

The direct costs are subdivided into the following two items: facilities repair and/or replacement, and deaths and injuries. Only the first item will be considered herein since occupancy is typically small for bridges and can be expected to be proportional to the repair and replacement costs.

According to MoTH experience and the experience of several senior bridge engineers in Vancouver, it was assumed that the average replacement costs for bridges is 1,200 Canadian dollars per square meter of deck area including removal cost, which is about 20%.

In assigning direct damage costs to damage states, a relationship between the damage index, D, and the dollar damage index, DD, must be established. In this case, the D corresponds to the proposed damage model as discussed earlier. In this study, the DD is defined as the ratio between the cost of repair and the total cost of removal and replacement; it can therefore take any value between 0.0 and 1.0.

The range of the repair costs are derived based on the damage classification given by the proposed damage model to associate the D values with a damage cost. According to this damage classification as given at the end of Chapter 4, a damage of less or equal 0.1 means no physical damage, while a damage of higher that 0.6 is considered irrepairable. A linear realtionship is assumed here between the D and DD as shown in Figure 7.2.

The total area of Clydesdale Underpass is 1366 m^2; therefore, the total direct replacement cost including removal of the existing bridge is $1.64 millions. Table 7.2 shows the estimated direct damage cost for the Clydesdale Underpass.

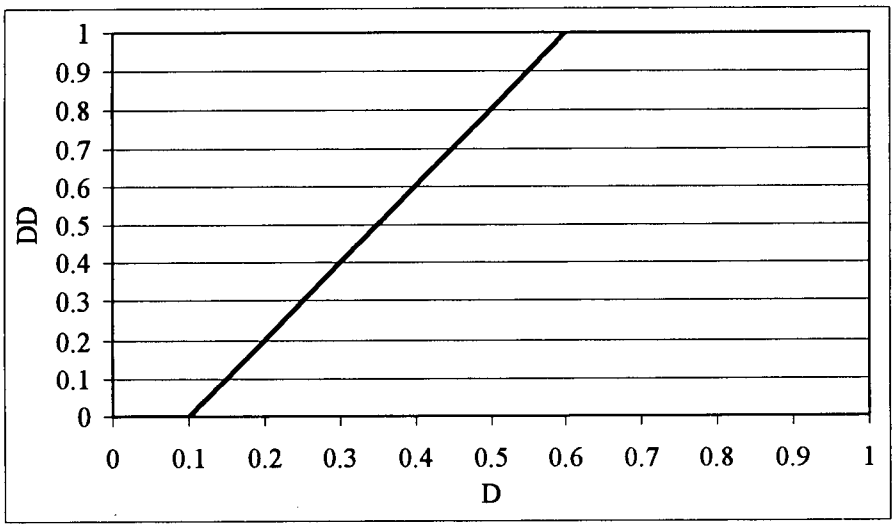

Figure 7.2: Relationship between D and DD.

Table 7.2: Estimated cost (Clydesdale Underpass).

j	Damage Index D	Dollar Damage Index DD	Direct Cost DC (millions of $CAD)	Indirect Cost IC (millions of $CAD)
1	0.00	0.00	0.00	0.00
2	0.00	0.00	0.00	0.00
3	0.00	0.00	0.00	0.00
4	0.00	0.00	0.00	0.00
5	0.35	0.50	0.82	1.50
6	1.00	1.00	1.64	3.00

The indirect costs consist of economic impacts and social impacts. Economic impacts may include business interruption, unemployment and tax impact. Social impacts may include individual pain and loss, and disruption to the community. An indirect cost of $30,000 per day is assumed here for this bridge. This assumption is based on the number of vehicles crossing such a bridge per day and how much will cost each motorist in order to find another route. It is also assumed that 100 days is a reasonable construction time

for such a bridge. Table 7.2 shows the estimated indirect damage costs for Clydesdale Underpass.

7.3 DECISION CALCULATIONS

The net present cost, NPC, of damage due to seismic event is the sum of the initial cost of the rehabilitation and the present value of the annual expected damage value of costs, taken over the bridge life.

In the event that failure occurs, there are consequences, which have to be expressed in units such as dollars in order to have comparisons with other costs such as retrofit costs. The consequences occur in the future; therefore, they have to be discounted to the present for comparison with retrofit costs. A discount rate of 5% is used here to bring future costs to the present. The net present cost, NPC, is written as,

$$NPC = C_r + C_p \tag{7-1}$$

Where C_r is the retrofit cost, C_p is the present cost of the no retrofit action.

Logically, the retrofit process is expected to improve the seismic performance of the bridge depending on the level of retrofit. The reduction in the damage index from its present state (no retrofit) will totally depend on the level of retrofit chosen for the bridge. For each level of retrofit, the C_r and C_p values can be estimated, as discussed above, and the total present cost value can be calculated using Equation 7-1.

It is assumed here that the retrofit is fully effective and it will reduce the damage index of each earthquake, as given in Table 7.1, to a maximum value of 0.1 in which no damage will be expected due to such a seismic event. In the case of Clydesdale Underpass, the assumed retrofit level should reduce the damage from 1.0 to 0.1 in order to expect no repair during the remaining life of the bridge. Therefore, The C_p value in Equation 7-1 for such a retrofit level is zero. In this case, the NPC of the retrofit option is simply the cost of retrofit,

$$NPC(r) = C_r \tag{7-2}$$

For the no retrofit option, the NPC can be also calculated using Equation 7-1. In this case, the retrofit cost, C_r, is zero,

$$NPC(nr) = C_p \tag{7-3}$$

Table 7.3 shows the direct and total costs associated with no retrofit option of Clydesdale Underpass.

Table 7.3: NPC for the no retrofit option in millions of $CAD.

Direct Cost	Indirect Cost	Total Cost
0.0275	0.0502	0.0777

As shown in Table 7.3, the total cost of the no retrofit option ($CAD 77,700) is about 5.0% of the replacement cost ($CAD 1,640,000). Therefore, if the retrofit option for this bridge, in order to reduce the seismic damage index from 1.0 to 0.1, costs more than 5.0% of the replacement cost it should not be considered and the no retrofit option will be the optimal option.

CHAPTER EIGHT

SUMMARY AND CONCLUSIONS

8.1 SUMMARY

Existing damage models for reinforced concrete elements were reviewed. The review focused on local damage indices since they are the basis for most available global indices. Existing damage models were classified into four categories: non-cumulative models, deformation-based cumulative models, energy-based cumulative models, and combined models.

A new damage model (P model) was proposed for reinforced concrete elements. The model yields a damage index at a point in the time history for the load on the element, based on the predicted monotonic response from the point in time to failure. It accounts for stiffness degradation, strength deterioration, and ultimate displacement reduction. The model is cumulative and it combines energy, ductility, and low-cycle accumulation. Layer analysis technique was utilized to predict the monotonic force-displacement response of a reinforced concrete column in order to process the damage models.

The P model was compared with two of the often-used existing models E1 and E2 for a number of different cases:

a) 12 tested columns by others under controlled reversed cyclic loading. These columns covered different aspects that play major role in the seismic behavior of bridge columns, such as; shear, flexure, confinement, axial load, stirrups spacing, number of cycles, and displacement amplitude.

b) A full-scale coupling beam, which was experimentally tested as part of this thesis, under controlled reversed cycles. This application was to evaluate the P model in describing the damage of structural elements other than bridge columns.

c) Two existing bridges in Greater Vancouver area. This was to evaluate the P model in describing the seismic behavior of real bridge columns.

An experimental test of a full-scale coupling beam was carried out in order to observe the seismic damage of reinforced concrete elements other than bridge columns. A trilinear monotonic force-displacement response was proposed in order to measure the needed parameters for the damage models.

The CANNY program was utilized in performing the nonlinear dynamic analysis of the two existing bridges in Vancouver. A computer program was written to process the damage models from CANNY output.

The use of the P model was demonstrated in the context of a simple bridge retrofit problem. A risk-based retrofit was demonstrated through Clydesdale Underpass in Vancouver.

8.2 CONCLUSIONS

The damage analysis and comparison of 12 tested bridge columns presented in Chapter 4 showed that the E1 model sometimes overestimates damage at small inelastic cycles and underestimates damage at large inelastic cycles. The E2 and P models performed better than the E1 model at small inelastic cycles. On the other hand, the E2 model accounts only for low-cycle accumulated damage at the longitudinal steel due to flexure and sometimes underestimates the damage at small inelastic cycles. The E2 and P models showed good ability in predicting the number of complete cycles to failure due to low-cycle accumulation at the longitudinal reinforcement. However, both models overestimated the number of cycle to failure when the failure is due to low-cycle accumulated damage in the confinement. The P model provided results consistent with subjective observations of damage for the specimens, while the E1 and E2 model were not consistent. It is concluded that the proposed damage model is a reasonable combination between ductility, energy and low-cycle accumulation and it showed good

agreement with the observed damage for both flexure and shear dominated tests because it appears to follow subjective classification for degree of damage.

It is concluded from the observed damage of the 12 column specimens that a damage of 0.4 as suggested by Park et al. (1987) as a threshold value between repairable and irrepairable damage is considered conservative. The following damage scale is concluded from the comparison between the P model and the observed damage, which suggests a value of 0.6 for the irrepairable damage.

$D < 0.1$	No damage.
$0.1 \leq D < 0.2$	Minor damage–light cracking–very easy to repair.
$0.2 \leq D < 0.4$	Moderate damage–severe cracking, cover spalling–repairable.
$0.4 \leq D < 0.6$	Severe damage–extensive cracking, reinforcement exposed–repairable with difficulties.
$0.6 \leq D < 1.0$	Severe damage–concrete crushing, reinforcement buckling–irrepairable.
$D = 1.0$	Complete collapse.

The P model predicted the ultimate displacement after cyclic loading due to low-cycle accumulated damage at the longitudinal reinforcement. Specimen SR4 (Adebar and Roux, 1998) failed monotonically at a displacement of 46 mm after it was cycled 18 cycles at different displacement amplitudes. The P model gave a monotonic ultimate displacement of 43 mm after cycling, while it gave a monotonic ultimate displacement of 48 mm for the virgin state. This reduction (from 48 mm to 43 mm) in the ultimate displacement due to low-cycle accumulation at the longitudinal reinforcement, reasonably agreed with the experimental result (46 mm).

The P model showed ability in describing the progression of damage during the cyclic loading of elements other than bridge columns. This was concluded based on the damage analysis of a diagonally reinforced coupling beam presented in Chapter 5. The mechanical behavior of such a structural element is very different than a reinforced concrete column; therefore, the P model shows promise as a way to predict damage of other structural elements. The proposed truss model to predict the monotonic force-displacement of a diagonally reinforced coupling beam showed good agreement with the experimental results.

The P model predicted the ultimate displacement after cyclic loading due to low-cycle accumulation at the diagonal reinforcement of the coupling beam. The coupling beam (Adebar et al., 2001) failed monotonically due to concrete crushing and reinforcement buckling at 156 mm displacement after it was cycled 22 cycles at different displacement amplitude. The P model gave a monotonic ultimate displacement of 164 mm after cycling, while it gave a monotonic ultimate displacement for the virgin state of 175 mm. This reduction (from 175 mm to 164 mm) in the ultimate displacement is due to low-cycle accumulated damage at the diagonal reinforcement and it reasonably agreed with the test result (156 mm).

Chapter 6 showed that the P model is applicable to existing bridge columns under real seismic loading. The proposed method in dealing with the unsymmetrical cycles worked well in describing the low-cycle accumulated damage. This chapter showed that the model could be applied in real life and to any structural element if the monotonic force-displacement behavior can be generated. The model compared well with the expected damage of the considered columns and with the E1 model. The E1 model gave damage higher than the P model through the loading history for Clydesdale Underpass. This is because of the low ductility capacity of this bridge, which influenced the E1.

It is concluded from this study that the P model is easy to use and minimizes the number of parameters that have to be assumed by the engineers. The P model always ranges from zero for the original state (never loaded element) to 1.0 for the collapsed state.

The following tasks are recommended for future research:

- Using more sophisticated material models, i.e. include strain hardening of the reinforcement, confinement model, and bond slip model to predict the force-displacement behavior.
- Conducting more reinforced concrete columns testing by pushing the columns monotonically after they are cycled to compare the results with the proposed reduction in the ultimate monotonic displacement.
- Investigate the low-cycle accumulated damage at the confinement and include it in predicting the number of complete cycles to failure.
- Applying the model to structures with more than one element to evaluate the model ability in describing the global damage.
- Apply the model to define a state of damage as a target to create a performance-based seismic design criteria for bridges.
- Conducting a reliability analysis to evaluate the effect and sensitivity of all the random variables that define the proposed model.
- The P model does not address the shear issue properly and future work is needed to calibrate the model that includes the effect of shear.

REFERENCES

Adebar, P., and Roux S., 1998, Seismic shear response of RC members with varying ductility, *Technical Report,* Department of Civil Engineering, University of British Columbia, Vancouver, Canada.

Adebar, P., Hindi, R. A., and Gonzalez, E, 2001, Seismic behavior of a full-scale diagonally reinforced slender coupling beam, *Technical Report,* Department of Civil Engineering, University of British Columbia, Vancouver, Canada.

American Concrete Institute, 1989, *ACI Building Code Requirements For Reinforced Concrete (ACI 318-89) And Commentary (ACI 318R-89)*, Detroit, MI, revised 1992, 347.

Ang, A. H-S., Kim, W. J., and Kim, S. B., 1993, Damage estimation of existing bridge structures, *Structural Engineering in Natural Hazards Mitigation, ASCE Structures Congress, , Irvine, CA, Proceedings*, **2**, 1137-1142.

Applied Technology Council, 1981, *Seismic Guidelines For Highway Bridges,* Report ATC-6.

Applied Technology Council, 1983, *Seismic Retrofitting Guidelines For Highway Bridges,* Report ATC-6-2, Palo Alto, CA, August.

Applied Technology Council, 1985, *Earthquake Damage Evaluation Of Seismic Regulations For Buildings,* Report ATC-13.

Applied Technology Council, 1999, *Evaluation of Earthquake Damaged Concrete and Masonry Wall Buildings, Basic Procedures Manual,* prepared by Applied Technology Council (ATC 43 Project) for the Partnership for Response and Recovery, published by the Federal Emergency Management Agency, *FEMA 306*, Washington, DC.

Applied Technology Council, 1999, *Evaluation of Earthquake Damaged Concrete and Masonry Wall Buildings, Technical Resources*, prepared by Applied Technology Council (ATC 43 Project) for the Partnership for Response and Recovery, published by the Federal Emergency Management Agency, *FEMA 307*, Washington, DC.

Banon, H., Biggs, J. M., and Irvine, H. M., 1981, Seismic damage in reinforced concrete frames, *Journal of Structural Engineering*, ASCE, **107**, (9), September, 1713-1729.

Benjamin, J. R. and Cornell, C. A., 1970, *Probability, Statistics, and Decision for Civil Engineering*, McGraw-Hill Book Company, New York.

Bracci, J. M., Reinhorn, A. M., Mander, J. B., and Kunnath, S. K., 1989, Deterministic model for seismic damage evaluation of RC structures, *MCEER Report 89-0033*, State University of New York at Buffalo, NY.

CAN/CSA-S6, 1983, *Canadian Highway Bridge Design Code, Canadian Standards Association,* Rexdale, Ontario, Canada.

CAN/CSA-S6, 2000, *Canadian Highway Bridge Design Code, Canadian Standards Association,* Rexdale, Ontario, Canada.

CANNY-E, 1996, *Three-Dimensional Nonlinear Dynamic Structural Analysis Computer Program Package*, Canny Consultants PTE Ltd., Singapore.

Chang, G. A. and Mander, J. B., 1994, Seismic Energy Based Fatigue Damage Analysis of Bridge Columns, *NCEER Report 94-0006*, State University of New York at Buffalo, NY.

Chung, Y. S., Meyer, C., and Shinozuka, M., 1987, Seismic Damage Assessment of RC Members, *NCEER Report 87-0022*, State University of New York at Buffalo, NY.

Chung, Y. S., Meyer, C., and Shinozuka, M., 1989a, Modeling of concrete damage, *ACI Structural Journal*, **86**, (3), May-June, 259-271.

Chung, Y. S., Meyer, C., and Shinozuka, M., 1989b, Automated damage-controlled design of RC buildings, *5th International Conference on Structural Safety and Reliability (ICOSSAR 89), San Francisco, California, Proceedings*, **I**, 383-390.

Chung, Y. S., Meyer, C., and Shinozuka, M., 1990, Automatic seismic design of reinforced concrete building frames, *ACI Structural Journal*, **87**, (3), May-June, 326-340.

Ciampoli, M., Giannini, R., Nuti, C., and Pinto, P. E., 1989, Seismic reliability of non-linear structures with stochastic parameters by directional simulation, *5th International Conference on Structural Safety and Reliability (ICOSSAR 89), San Francisco, California, Proceedings*, **II**, 1121-1128.

Coffin, L. F., Jr., 1954, A study of the effects of cyclic thermal stresses on a ductile metal, *Transactions of the American Society of Mechanical Engineers*, New York, NY, **76**, 931-950.

CSA-A23.3, 1994, *Canadian Concrete Code, Canadian Standards Association*, Rexdale, Ontario, Canada.

Darwin, D. and Nmai, C. K., 1986, Energy dissipation in RC beams under cyclic load, *Journal of Structural Engineering*, ASCE, **112**, (8), August, 1829-1846.

Dowling, N. E., 1972, Fatigue failure predictions for complicated stress-strain histories, *Journal of Materials*, JMLSA, **7**, (1), March, 71-87.

Gonzalez, E., 2001, Seismic response of diagonally reinforced slender coupling beams, *M.A.Sc. thesis*, Department of Civil Engineering, University of British Columbia, Vancouver, Canada.

Gosain, N. K. Brown, R. H., and Jirsa, J. O., 1977, Shear requirements for load reversals on RC members, *Journal of Structural Engineering*, ASCE, **103**, (7), July, 1461-1476.

Gunturi, S.K.V. and Shah, H. C., 1993, Mapping structural damage to monetary damage, *Structural Engineering In Natural Hazard Mitigation*, Proceedings, ASCE Structures Congress, Irvine, CA, **2**, 1331-1336.

Kratzig, W. B. and Meskouris, M., 1987, Nonlinear seismic analysis of reinforced concrete frames, *Earthquake Prognostics*, Vogel and Brandes (editors), Verlag Friedr, Vieweg and Sohn, Braunschweig, 453-462.

Kunnath, S. K., EL-Bahy, A., Taylor, A., and Stone, W., 1997, Cumulative Seismic Damage of Reinforced Concrete Bridge Piers, *NCEER Report 97-0006*, State University of New York at Buffalo, NY.

Kunnath, S. K., Reinhorn, A. M., and Lobo, R. F., 1992, IDARC version 3.0: A Program for the Inelastic Damage Analysis of RC Structures, *NCEER Report 92-0022*, State University of New York at Buffalo, NY.

Kunnath, S. K., Reinhorn, A. M., and Park, Y. J., 1990, Analytical modeling of inelastic seismic response of R/C structures, *Journal of Structural Engineering*, ASCE, **116**, (8), August, 996-1017.

Li, Kang-Ning, Aoyama, H., and Otani, S., 1988, Reinforced concrete columns under varying axial load and bi-directional lateral load reversals, *9th World Conference on Earthquake Engineering, Tokyo, Proceeding*, 537-544.

Mander, J. B, Dutta, A., and Kim, J. H., 1998, Fatigue Analysis of Unconfined Concrete Columns, *MCEER Report 98-0009*, State University of New York at Buffalo, NY.

Mander, J. B, Priestley, M.J.N., and Park R., 1988, Theoretical stress-strain model for confined concrete, *Journal of Structural Engineering*, ASCE, **114**, (8), August, 1804-1826.

Mander, J. B. and Cheng, C.-T., 1995, Renewable hinge detailing for bridge columns, *Pacific Conference on Earthquake Engineering, Melbourne, Australia, Proceedings*, November 20-22, 197-206.

Mander, J. B., Panthaki, F. D., and Kasalanati, A., 1994, Low cycle fatigue behavior of reinforcing steel, *Journal of Material in Civil Engineering*, ASCE, **6**, (4), April.

Manson, S. S., 1953, Behavior of materials under conditions of thermal stress, *Heat Transfer Symposium, Proceedings*, University of Michigan Engineering Research Institute, Ann Arbor, Michigan, 9-75.

Miner, M. A., 1945, Cumulative damage in fatigue, *Journal of Applied Mechanics*, **12**, A-159.

Naumoski, N., 1985, SYNTH Program, Generation of artificial acceleration time history compatible with a target spectrum, *McMaster Eartquake Engineering Software Library*, Department of Civil Engineering, McMaster University, Hamilton, Canada.

Nishimura, K. S., 1997, Risk-based retrofit decision model for bridges, *M.A.Sc. Thesis*, Department of Civil Engineering, University of British Columbia, Canada.

Park, R. and Paulay, T., 1975, *Reinforced Concrete Structures*, John Wiley and Sons, New York.

Park, Y. J. and Ang, A.H-S., 1985, Mechanistic seismic damage model for reinforced concrete, *Journal of Structural Engineering*, ASCE, **111**, No. ST4, 722-739.

Park, Y. J., Ang, A.H-S., and Wen, Y. K., 1985, Seismic damage analysis of reinforced concrete buildings, *Journal of Structural Engineering*, ASCE, **111**, No. ST4, 740-757.

Park, Y. J., Ang, A.H-S., and Wen, Y. K., 1987, Damage-limiting seismic design buildings, *Earthquake Spectra*, **3**, (1), 1-26.

Paulay, T. and Priestley, M.J.N., 1992, *Seismic Design of Reinforced Concrete and Masonry Buildings*, John Wiley and Sons, New York.

Paulay, T., 1971, Coupling beams of reinforced concrete shear walls, *Journal of Structural Engineering*, ASCE, **97**, (3), March, 843-862.

Priestley, M.J.N., Seible, F., and Benzoni, G., 1994a, Seismic response of columns with low longitudinal steel ratios, *Structural System Research Project, Report SSRP-08*, University of California, San Diego, June, 79 pp.

Priestley, M.J.N., Seible, F., and Calvi, G. M., 1996, *Seismic Design and Retrofit of Bridges*, John Wiley and Sons, New York.

Priestley, M.J.N., Verma, R., and Xiao, Y., 1994b, Seismic shear strength of reinforced concrete columns, *Journal of Structural Engineering*, ASCE, **120**, (8), August, 2310-2329.

Rao, P. S., Sarma, B. S., Lakshmanan, N., and Stangenberg, F., 1998, Damage model for reinforced concrete elements under cyclic loading, *ACI Structural Journal*, **95**, (6), November-December, 682-690.

Roufaiel, M.S.L. and Meyer, C., 1987, Analytical modeling of hysteretic behavior of R/C frames, *Journal of Structural Engineering*, ASCE, **113**, (3), 429-444.

Saatcioglu, M. and Raszi, S. R., 1992, Strength and ductility of confined concrete, *Journal of Structural Engineering*, ASCE, **118**, (6), June, 1590-1606.

Sexsmith, R. G., 1983, Bridge risk assessment and protective design for ship collision, *Introductory Report, International Association for Bridge and Structural Engineering Colloquium on Ship Collision with Bridges and Offshore Structures*, Copenhagen, Denmark, 425-433.

Sexsmith, R. G., 1994, Seismic risk management for existing structures, *Canadian Journal of Civil Engineering*, **21**, (2), 180-185.

Singhal, A. and Kiremidjian, A. S., 1995, Method for Developing Motion Damage Relationships for Reinforced Concrete Frames, *NCEER Report 95-0008*, State University of New York at Buffalo, NY.

Stephens, J. E. and Yao, J.T.P., 1987, Damage assessment using response measurement, *Journal of Structural Engineering*, ASCE, **113**, (4), April, 787-801.

Stone, W. C. and Cheok, G. S., 1989, Inelastic behavior of full-scale bridge columns subjected to cyclic loading, *NIST Building Science Series Report No. 166*, U.S. Department of Commerce, National Institute of Standards and Technology, Gaithersburg, MD, 252 pp.

Stone, W. C. and Taylor, A. W., 1993, Seismic performance of circular bridge columns designed in accordance with AASHTO/CALTRANS standards, *NIST Building Science Series Report No. 170*, National Institute of Standards and Technology, Gaithersburg, MD, 119 pp.

Toussi, S. and Yao, J.T.P., 1983, Hysteresis identification of existing structures, *Journal of Engineering Mechanics*, ASCE, **109**, (5), May, 1189-1203.

Wang, M. L. and Shah, S. P., 1987, Reinforced concrete hysteresis model based on the damage concept, *Earthquake Engineering and Structural Dynamics*, **15**, (8), 993-1003.

Wang, M. L., 1994, Responses of various non-linear reinforced concrete models, *12 International Modal Analysis Conference, Honolulu, Proceedings,* **II**, 1512-1519.

Williams, M. S. and Sexsmith, R. G., 1994, Review of methods assessing seismic damage in concrete structures, *Technical Report 94-02,* Earthquake Engineering Research Facility, University of British Columbia, Vancouver, Canada.

Williams, M. S., Villemure, I., and Sexsmith, R. G., 1997, Evaluation of seismic damage indices for concrete elements loaded in combined shear and flexure, *ACI Structural Journal*, **94**, (3), May-June, 315-322.

APPENDIX A

COUPLING BEAM

The design and construction of the coupling beam specimen were done by the author as part of this thesis, while the testing was done in collaboration with Emilio Gonzalez (Adebar et al., 2001). This Appendix shows in tables and figures the results of the experiment, which were prepared by Emilio Gonzalez and can be found in detail in Adebar et al. (2001).

Table A.1 Force-displacement (Load History)

Stage	Cycle	Transv. Displ. (mm)	Shear Force (kN)
1	1A	11	662
	1B	-7	-540
	2A	10	516
	2B	-7	-495
	3A	10	511
	3B	-7	-491
	4A	10	516
	4B	-7	-495
2	1A	15	708
	1B	-14	-710
	2A	16	695
	2B	-11	-719
	3A	21	753
	3B	-8	-668
3	1A	21	635
	1B	-21	-862
	2A	21	726
	2B	-21	-867
	3A	21	723
	3B	-23	-855
4	1A	34	890
	1B	-30	-983
	2A	31	746
	2B	-31	-881
	3A	32	822
	3B	-31	-907
5	1A	42	837
	1B	-41	-869
	2A	40	819
	2B	-42	-689
	3A	41	880
	3B	-41	-782
6	1A	51	915
	1B	-50	-829
	2A	51	877
	2B	-50	-797
	3A	51	863
	3B	-52	-816
7	1A	61	913
	1B	-62	-803
	2A	70	865
	2B	-71	-837
	3A	81	870
	3B	-80	-824
8	1A	156	779

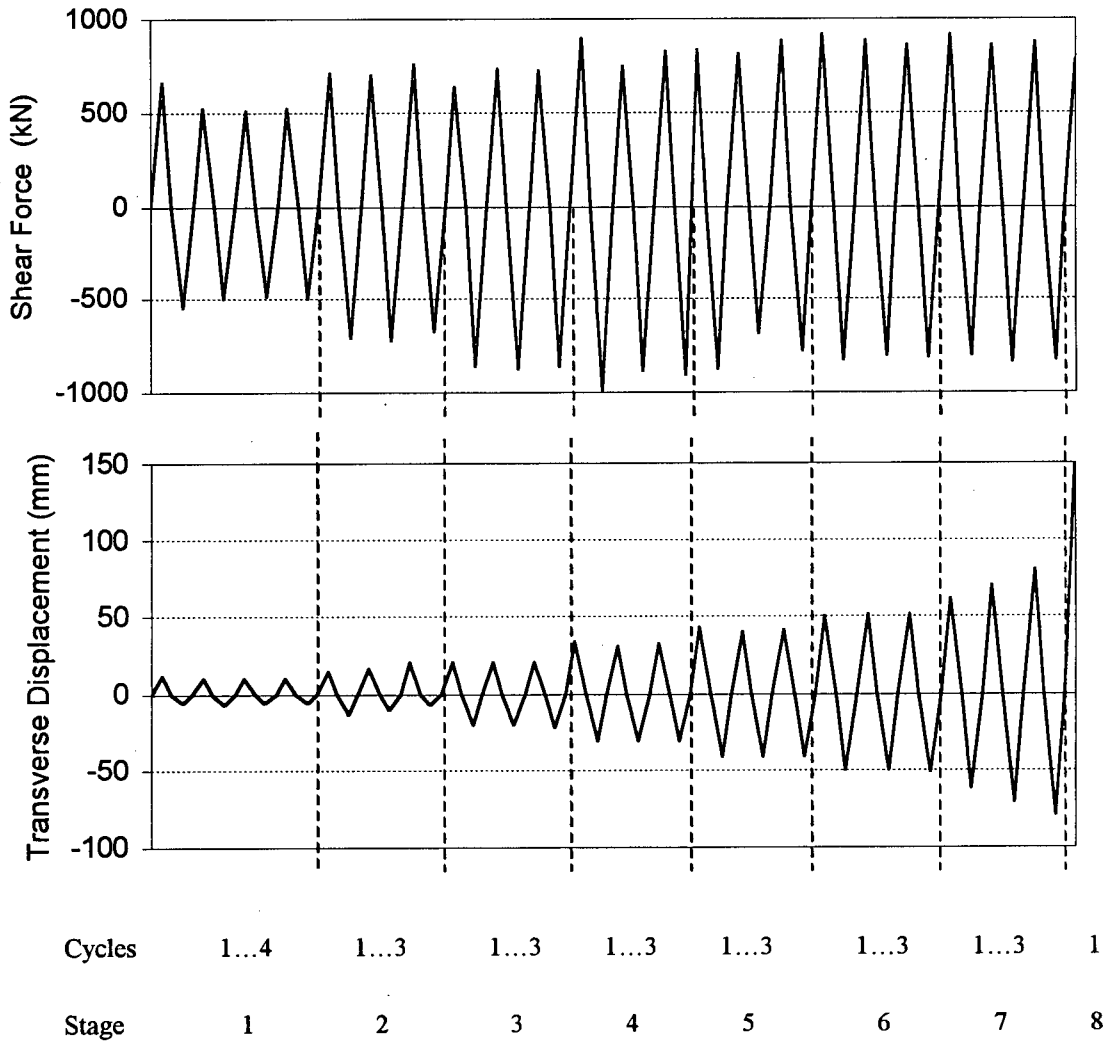

Figure A.1 Load History of Experiment

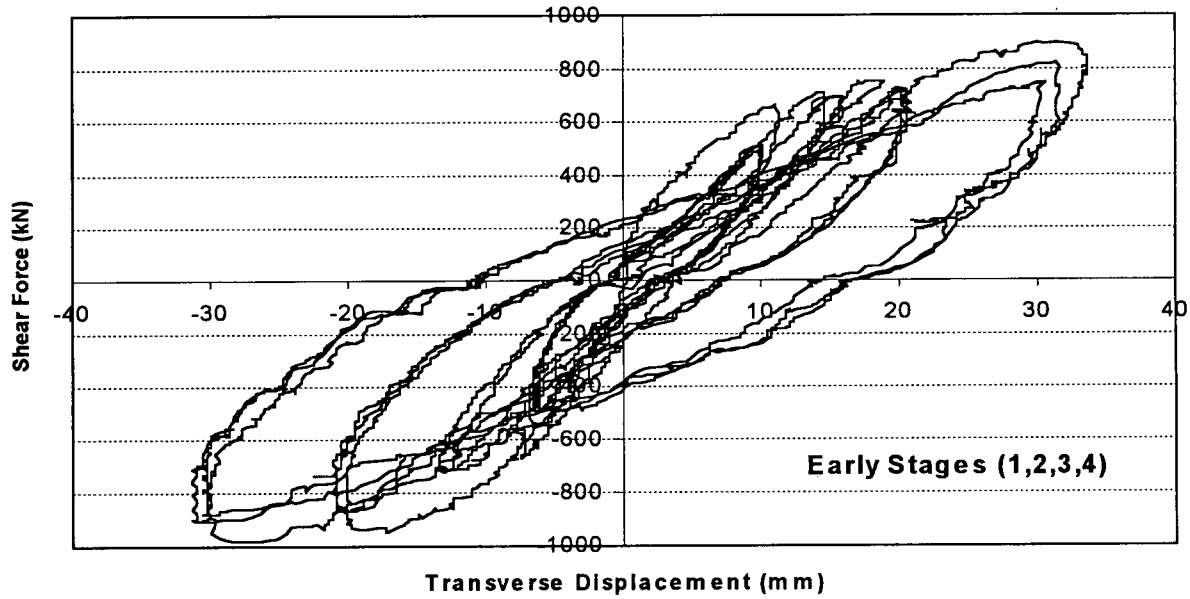

(a)

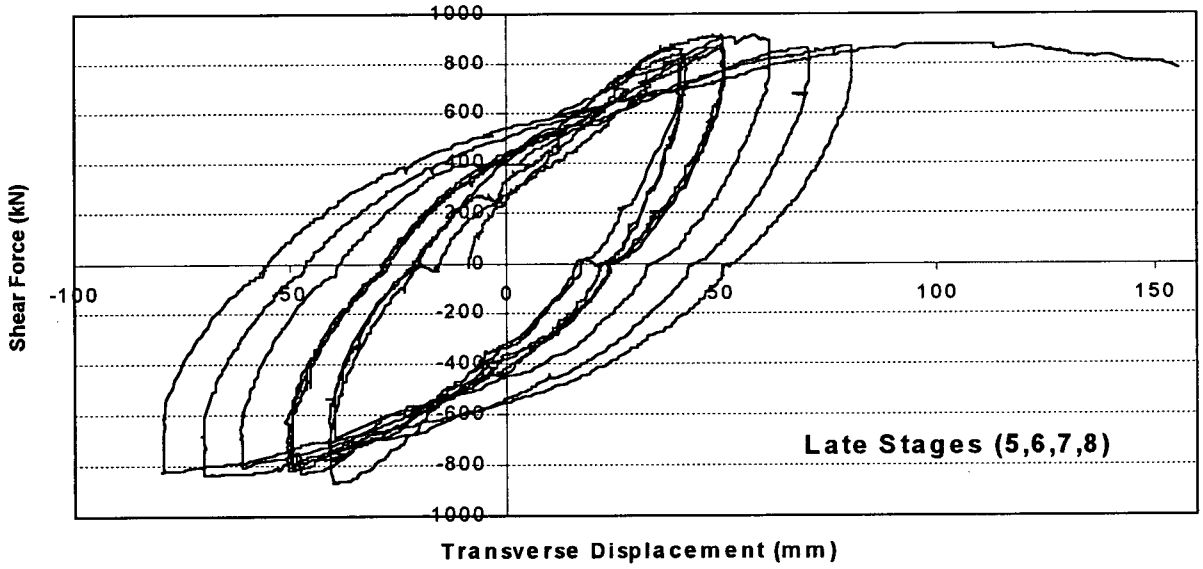

(b)

Figure A.2: Force-displacement behaviour; (a) early stages and (b) late stages.

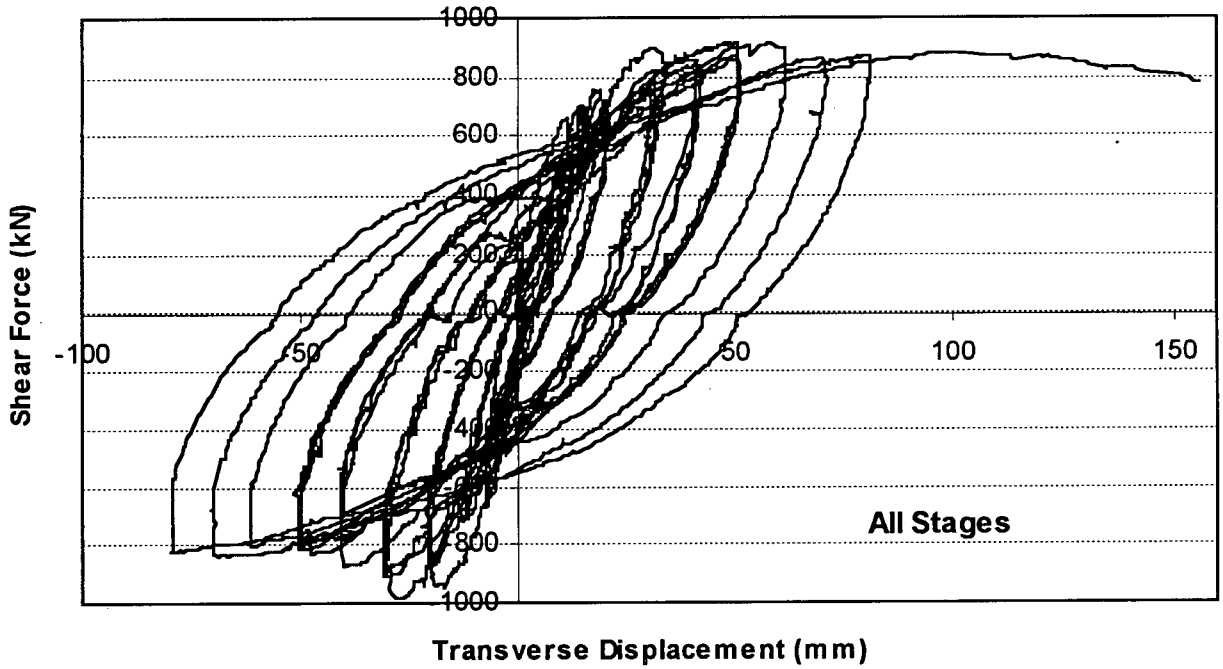

Figure A.3: Force-displacement behaviour (all stages).

Axial Restraint

Figures A.4 and A.5 show the behaviour of the axial restraint with respect to the transverse displacement. These figures indicate that the Dywidag bars were prestressed to an initial value of 320 kN. On the late stages of the test, it is noted that the axial restraint presents a very unsymmetrical behaviour.

Measured Diagonal Strains

Table A.2 shows the caliper readings converted to strains at certain peak loads. Table A.3 shows a summary of the diagonal strains measured at the peak loads in each cycle as indicated.

Table A.2: Caliper readings.

Stage	Cycle	Trans. Displ. (mm)	Shear Force (kN)	Average Strain ($x10^6$)							
				1-2	2-3	3-4	4-5	6-7	7-8	8-9	9-10
1	2A	10	558	-368	-363	-256	-611	1874	666	978	1911
2	2B	-11	-656	2313	1584	2106	3086	-2397	-1303	-1122	-1390
3	2B	-20	-852	5171	2456	825	6462	-3181	-1476	-2847	-3185
4	3A	30	805	-1134	3269	-1167	3173	7510	-318	-259	3880
5	1A	40	839	-958	-363	-1622	-1485	8789	-666	-1122	8830
6	2A	50	885	-4375	-2775	-1480	-4716	14890	-1332	647	16083
6	3B	-50	-807	14245	2049	1195	16330	-7743	-2837	-4659	-3532

Table A.3: Peak strain readings.

Stage	Cycle	Trans. Displ. (mm.)	Shear Force (kN)	Strain Measurements ($x10^{-6}$) 1	2	3	4	5	6
1	1A	11	662	-1481	1444	-385	1508	2334	188
	1B	-7	-540	1669	-133	1165	-367	-1128	1151
	2A	10	516	-1165	1155	-348	1251	1825	74
	2B	-7	-495	1499	-151	1082	-372	-1032	1050
	3A	10	511	-1174	1174	-380	1260	1820	74
	3B	-7	-491	1481	-156	1078	-376	-1027	1037
2	1A	15	708	-1706	1669	-587	1806	2535	92
	1B	-14	-710	2398	-266	1761	-638	-1683	1491
	2A	16	695	-1729	1651	-642	1838	2508	74
	2B	-11	-719	2425	-371	1798	-729	-1811	1555
	3A	21	753	-2183	1898	-825	1889	2467	5
	3B	-8	-668	1641	-431	1504	-798	-1811	1454
3	1A	21	635	-2384	1715	-811	1664	2114	-91
	1B	-21	-862	9550	-596	2490	-1569	-6034	3095
	2A	21	726	-679	1972	-1045	2044	2852	-128
	2B	-21	-867	9550	-729	2417	-1656	-6680	2972
	3A	21	723	-463	1962	-1077	2049	2645	-128
	3B	-23	-855	9550	-770	2398	-1701	-6855	2939
4	1A	34	890	-5805	9385	-1549	2636	7074	-187
	1B	-30	-983	8675	986	2549	-1940	-2348	1271
	2A	31	746	-3929	2806	-1637	2416	2673	464
	2B	-31	-881	7212	963	2481	-1954	-1756	963
	3A	32	822	-4920	3255	-1756	2585	3503	431
	3B	-31	-907	7098	990	2503	-2210	-1990	853
5	1A	42	837	-5369	3058	-1852	2737	2141	441
	1B	-41	-869	7872	967	2687	-2068	-2114	771
	2A	40	819	-4195	3058	-1971	2737	1449	372
	2B	-42	-689	3741	1288	2316	-1848	-1032	647
	3A	41	880	-4466	2315	-2035	2723	880	468
	3B	-41	-782	3434	912	2568	-1990	-2843	743
6	1A	51	915	-5850	2348	-2201	2792	9582	542
	1B	-50	-829	3081	1091	2742	-2142	9582	638
	2A	51	877	-4411	2366	-2201	2792	9582	431
	2B	-50	-797	2292	1027	2751	-2151	9582	638
	3A	51	863	-3888	2375	-2228	2796	9582	441
	3B	-52	-816	2242	995	2912	-2192	-1907	670
7	1A	61	913	-3187	2366	-2810	3007		519
	1B	-62	-803	1174	1215	3219	-2243		615
	2A	70	865	-2659	2407	-3796	3131		413
	2B	-71	-837	1554	862	5007	-2618		638
	3A	81	870	-1293	2334	-8317	3631		381
	3B	-80	-824	692	1178	7139	-3210		624
8	1A	156	779	-156	2187	-8477	4181		564

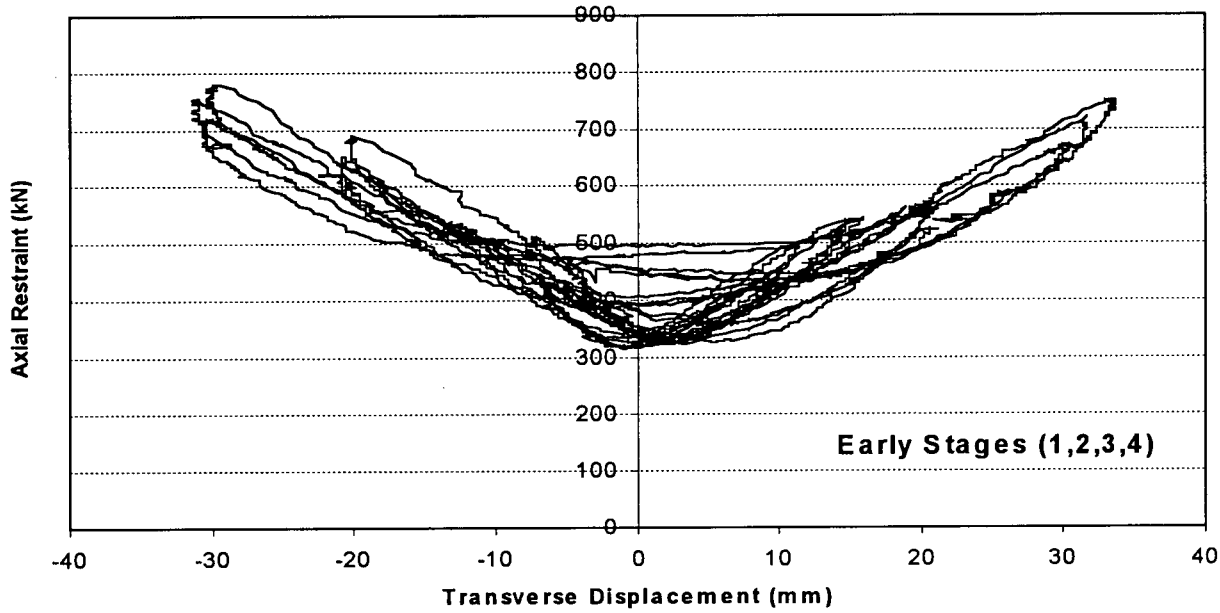

(a)

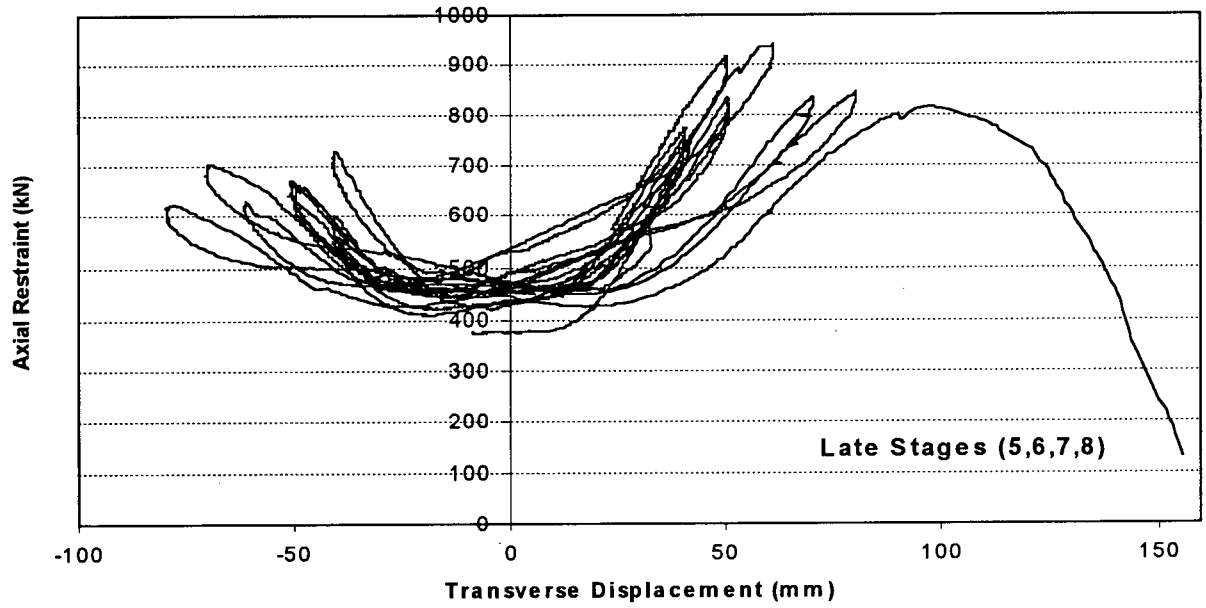

(b)

Figure A.4: Axial restraint history; (a) early stages and (b) late stages.

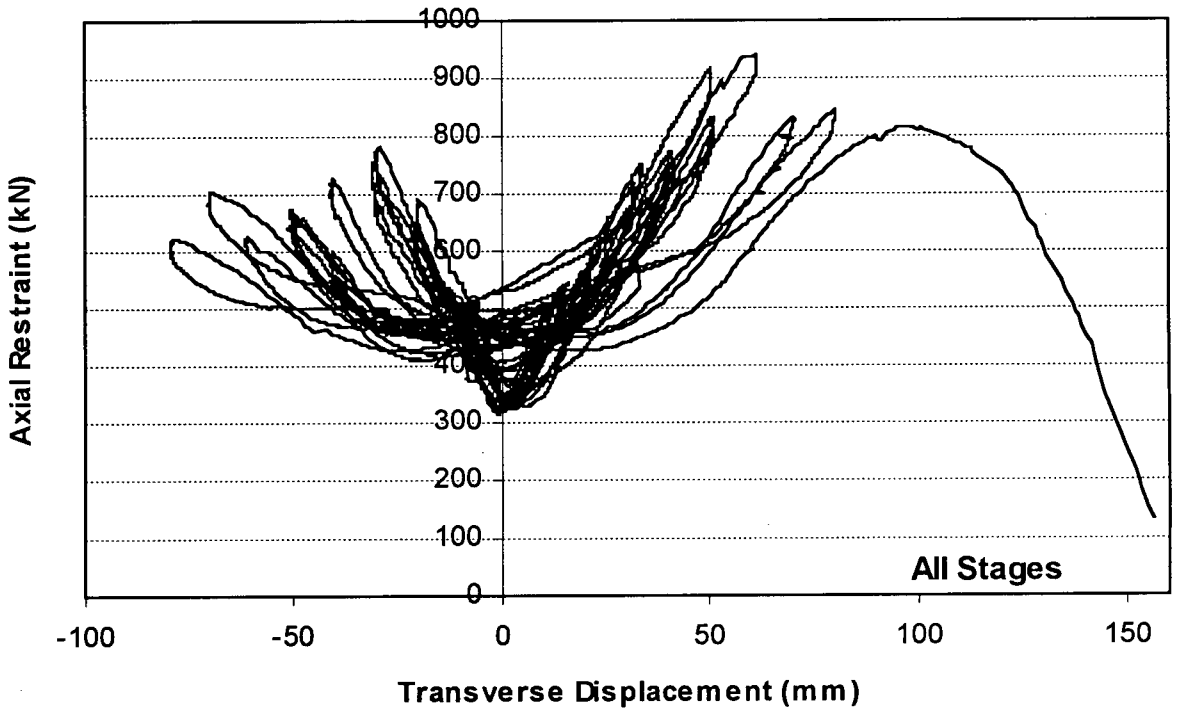

Figure A.5: Axial restraint history (all stages).

Force-Displacement Calculation of A Coupling Beam

Large Direction

f'c=	35	fy=	464	Ab=	700	Concrete:	
K=	1.327898	Ey=	0.00232	No. Bars=	4	b=	216
E'c=	0.00232	Angle (deg)=	12.34	Asteel=	2800	d=	140
		L=	1220	Aconcrete=	27440		
f'cc=	46.47644	Ties Area=	100	Fty=	1299.2	*w1*=	146
E'cc=	0.003192	Ties Spacing=	100	Fcy1=	2259.6	*w2*=	70
Ecu=	0.03	fyh (ties)=	400	Fcy2=	2574.513		

Rowx=	0.014286	Ae=	11550.6	
Rowy=	0.009259	Acc=	27440	
		ke=	0.42094	**Confinement**
kx=	0.068725			
ky=	0.044544	r=	0.64815	
		x=	0.05663	
K=	1.41084	A=	6.42336	
K=	1.279389	B=	2.17348	
Kave=	1.345114			
K=	**1.327898**			

Small Direction

f'c=	35	fy=	464	Ab=	700	Concrete:	
K=	1.446555	Ey=	0.00232	No. Bars=	4	b=	115
E'c=	0.00232	Angle (deg)=	12.34	Asteel=	2800	d=	140
		L=	1220	Aconcrete=	13300		
f'cc=	50.62942	Ties Area=	100	Fty=	1299.2	*w1*=	45
E'cc=	0.003621	Ties Spacing=	100	Fcy1=	1764.7	*w2*=	70
Ecu=	0.03	fyh (ties)=	400	Fcy2=	1972.571		

Rowx=	0.014286	Ae=	5696.56	
Rowy=	0.017391	Acc=	13300	
		ke=	0.42831	**Confinement**
kx=	0.069929			
ky=	0.08513	r=	0.82143	
		x=	0.07753	
K=	1.417083	A=	6.64291	
K=	1.493721	B=	2.23541	
Kave=	1.455402			
K=	**1.446555**			

	Displ	Force	
	-175.2423	-699.4953	
	-18.64795	-699.4953	small
	-13.55207	-655.053	
	0	0	
1st Yield	13.55207	760.8612	
2nd Yield	18.64795	828.1888	large
Ultimate	175.2423	828.1888	

APPENDIX B

DAMAGE OF EXISTING BRIDGES

CANNY sample input file (Garneau Flyover):

```
// analysis assumptions and output options

title : SINGLE COLUMN Garneau Flyover, Vancouver, BC
force unit = kN
length unit = m
time unit = sec

gravity acceleration g = 9.805

analysis in Y-direction
including P-Delta effect
output of overall responses
output of nodal displacement, velocity and acceleration
output all of column, beam response

// dynamic response control data

integration every 1-step
start time 0, end time 40.0
damping constant 0.02 to [M]
Newmark method, Beta-value 0.25
/*scale factor 0.012 to X-EQ file = c:\canny\cannye\elcentro.ew
/*scale factor 0.01 to Y-EQ file = d:\canny99\program\elcentro.ns
/*scale factor 9.81 to Y-EQ file = d:\canny99\program\V250SFCTns.lac
/*scale factor 9.81 to Y-EQ file = d:\canny99\program\V250SFCTew.lac
scale factor 9.81 to Y-EQ file = d:\canny99\program\V250LPCapew.lac
/*scale factor 9.81 to Y-EQ file = d:\canny99\program\V250LPCapns.lac
/*scale factor 9.81 to Y-EQ file = d:\canny99\program\V250Miyaew.lac
/*scale factor 9.81 to Y-EQ file = d:\canny99\program\V250TW078ew.lac
master DOFs for analysis control : Y-translations, 7-node
response limit 10
binary-formatted output at every 1-step

// node locations
node 1 to 6 every 1, (0 0 0), Zi=0.98
node 7 (0 0 8.63)

// node degrees of freedom
general degrees of freedom : 5-components
node 1 eliminate all components

// node weight
node 7 , w= 3550
node 6 , w= 0.0001

//master DOFs for mode analysis
add master DOFs Y-translation for all nodes with weight

//master DOFs for mode extraction
add master DOFs of Y-translation of all nodes

// element data : column
1 2 BU100 TU100 AU90
```

```
2 3 BU100 TU100 AU90
3 4 BU100 TU100 AU90
4 5 BU100 TU100 AU90
5 6 BU100 TU100 AU90
6 7 BU100 TU100 AU90 r(0  2.75)

// stiffness and hysteresis parameters

U90 EL1 3.0e+7  10.1304
U100 CA7 3.0e+7 4.15e-2 C(300 300) Y(6500 6500) A(1 1) B(0.000001
0.000001) P(0 5 .02 .01 0 0 1)

// initial load
node 7 , Pz=2800, positive is compression
```

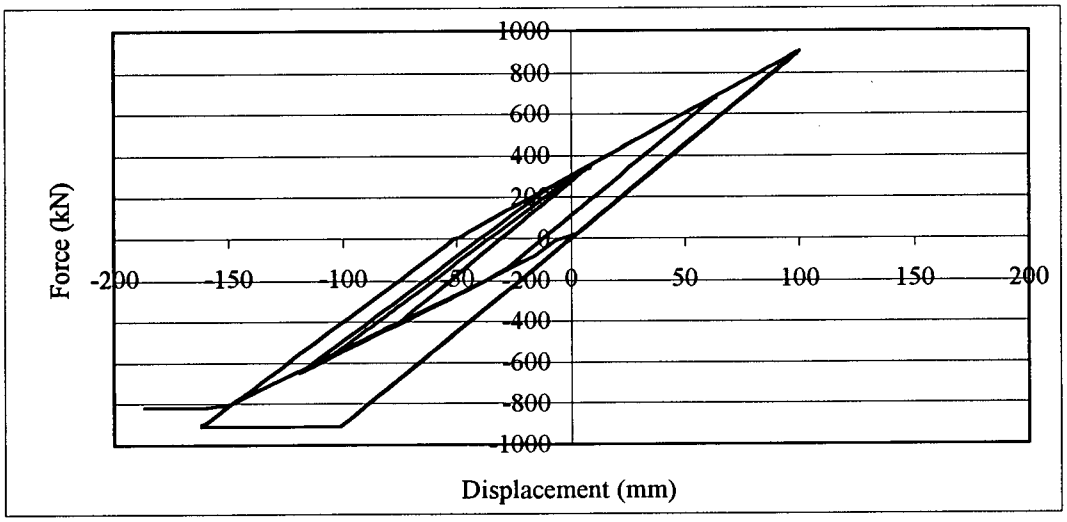

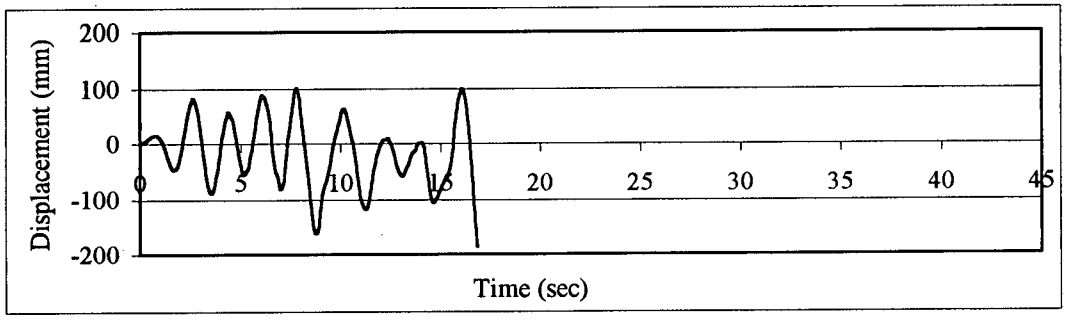

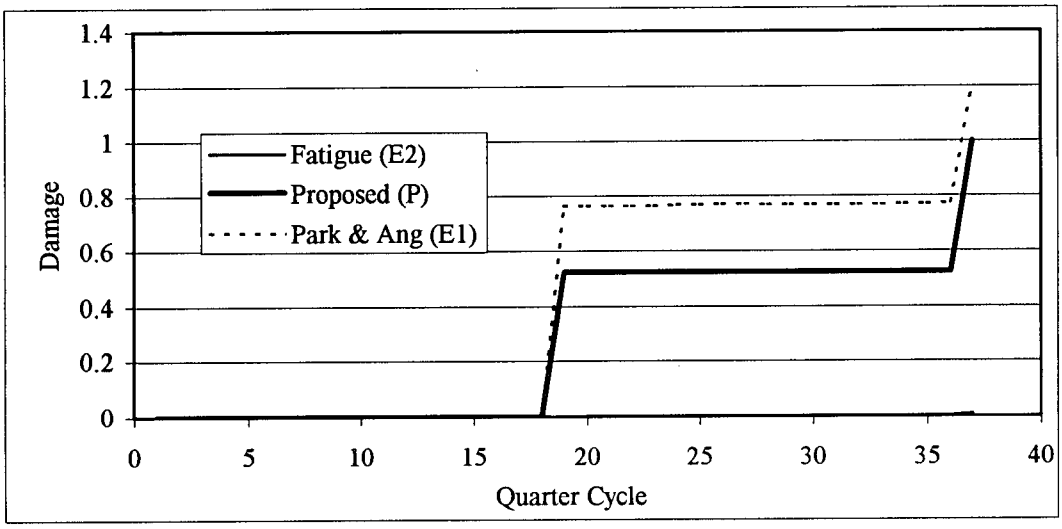

Figure B.1: Clydesdale behavior to 1989 Loma Prieta east-west (pier 3).

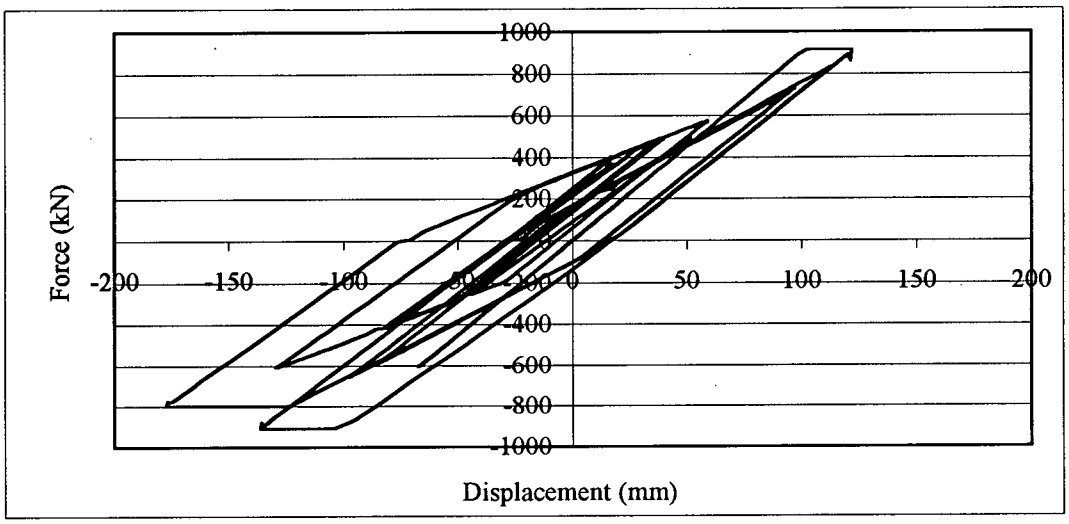

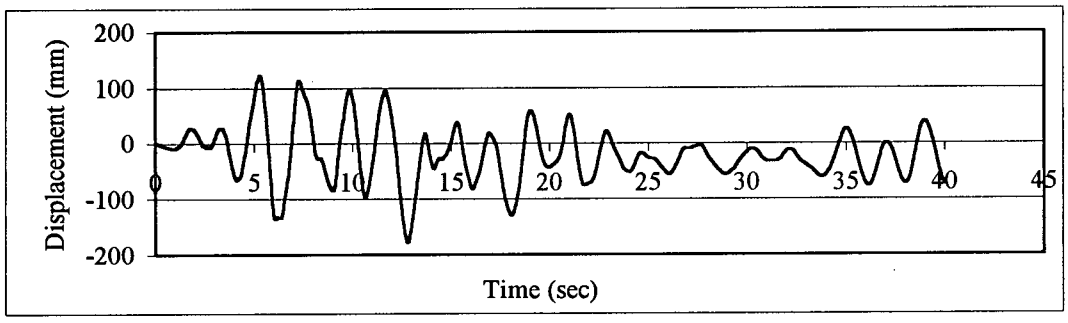

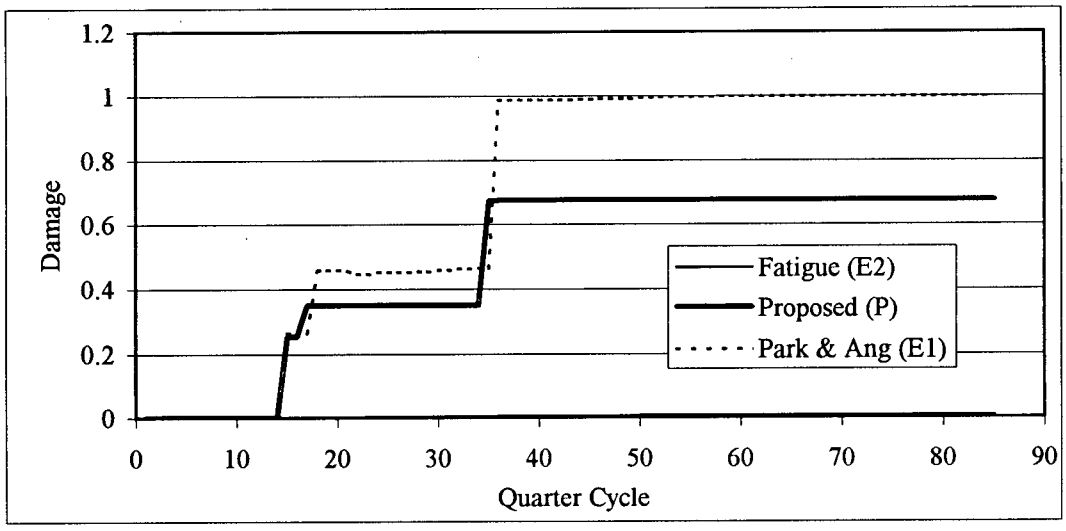

Figure B.2: Clydesdale behavior to 1989 Loma Prieta north-south (pier 3).

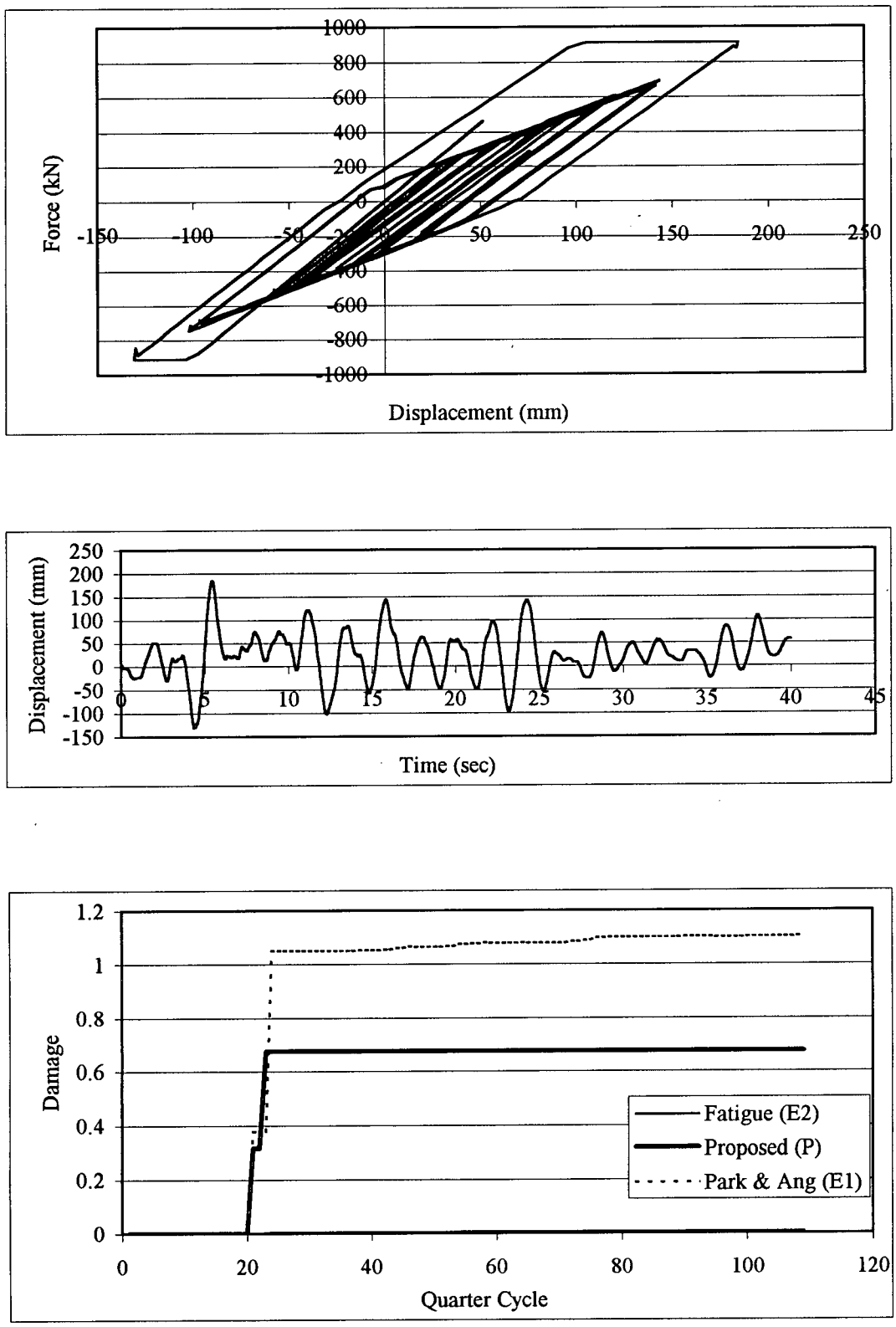

Figure B.3: Clydesdale behavior to 1978 Miyaki-Oki east-west (pier 3).

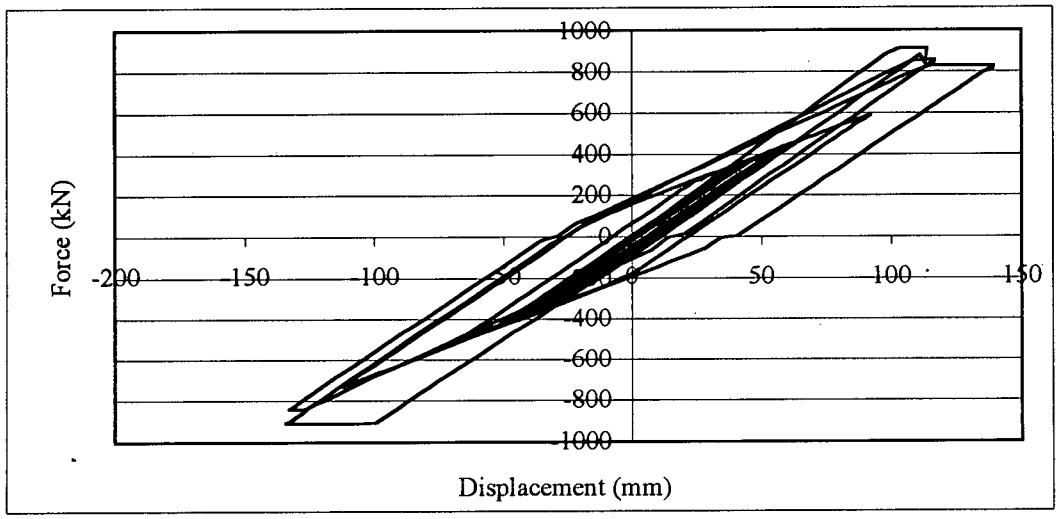

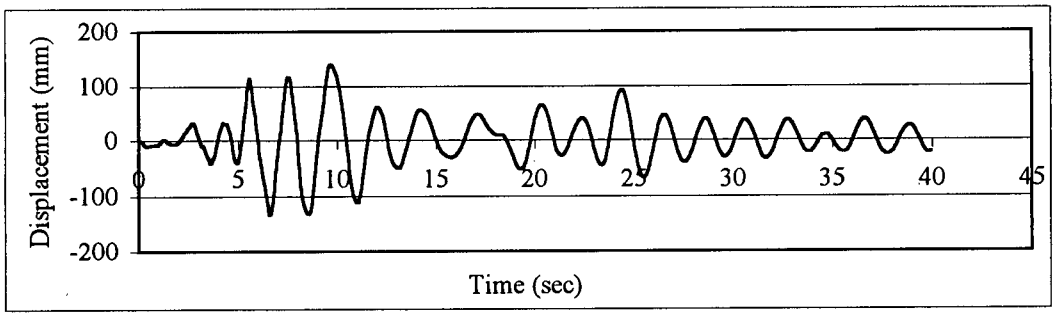

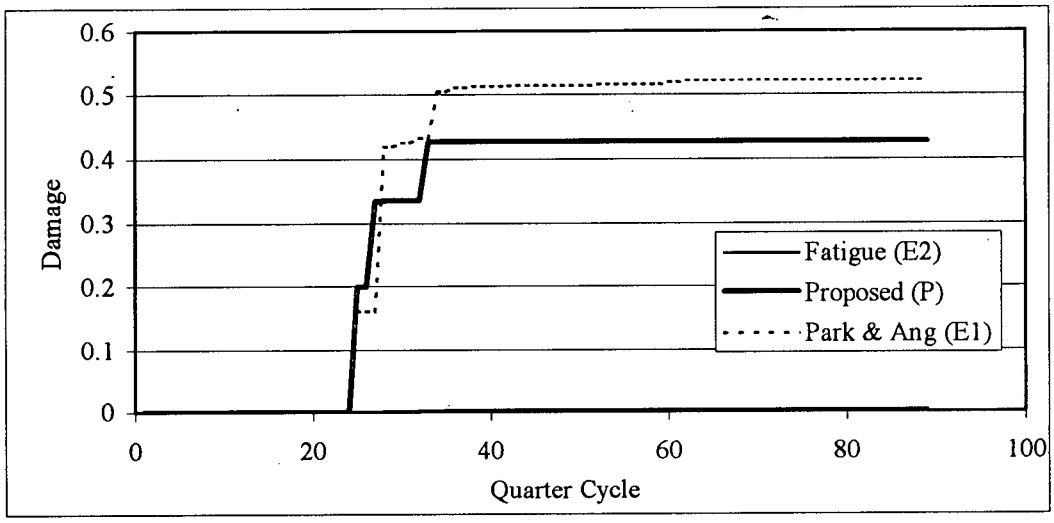

Figure B.4: Clydesdale behavior to 1971 San Fernando east-west (pier 3).

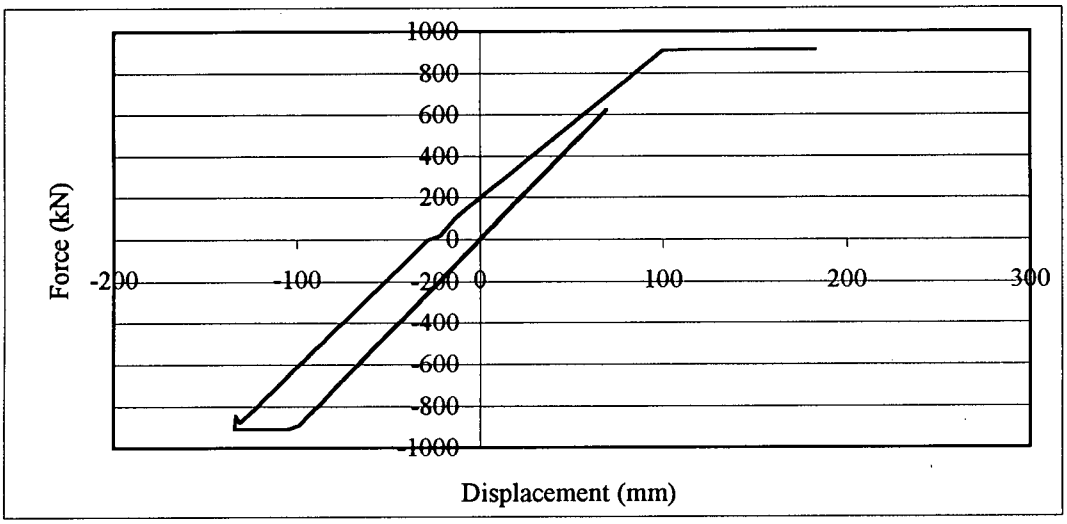

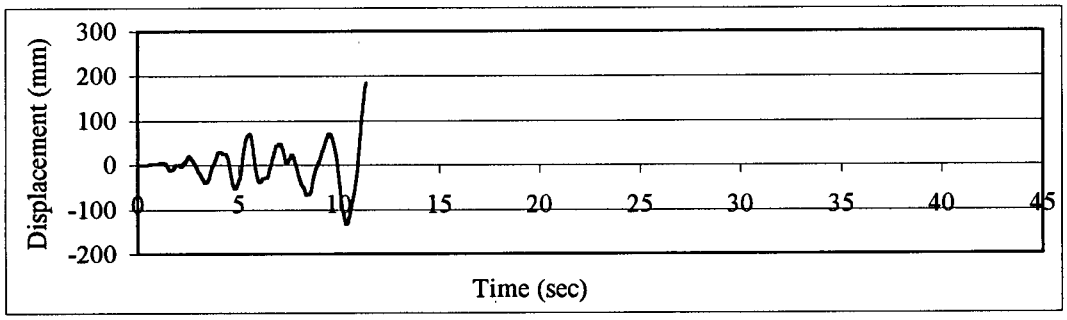

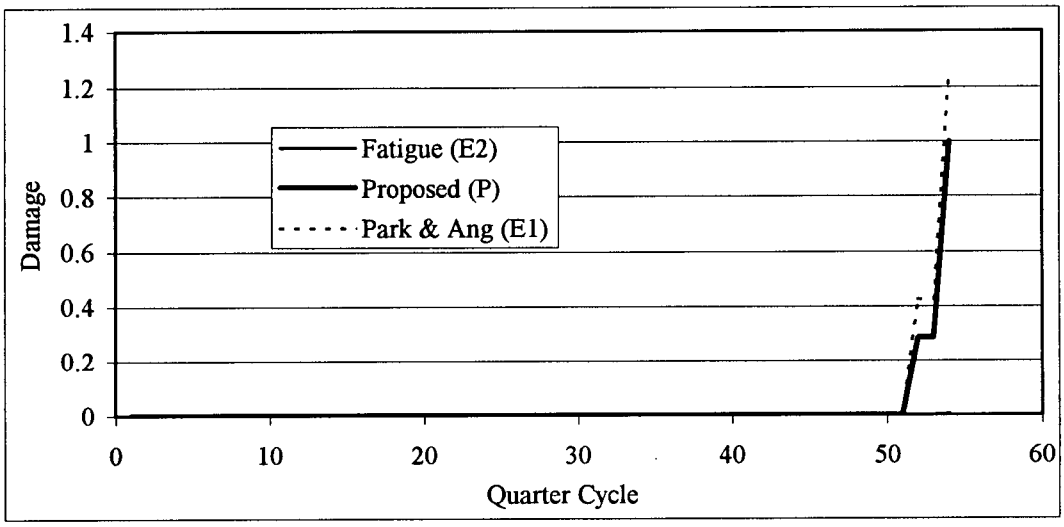

Figure B.5: Clydesdale behavior to 1971 San Fernando north-south (pier 3).

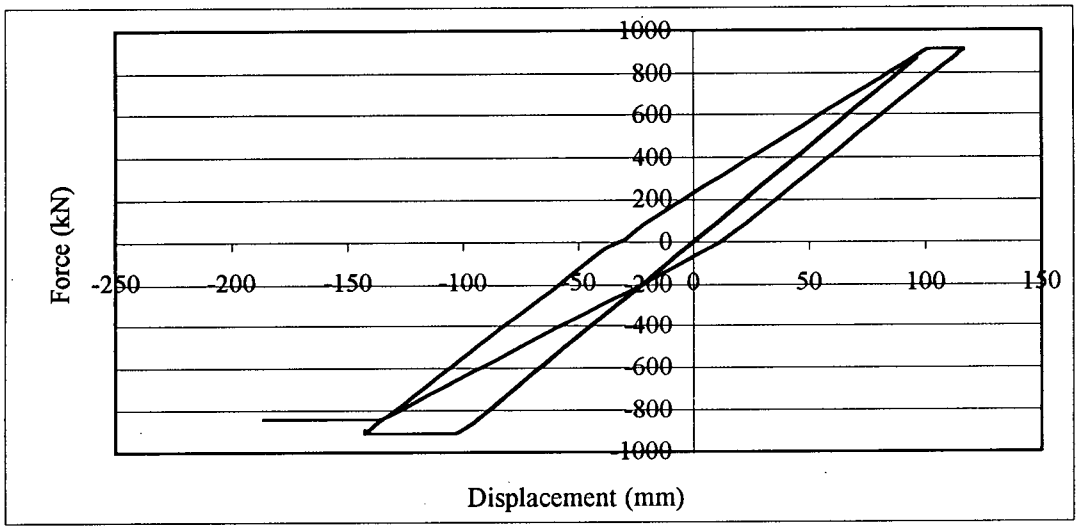

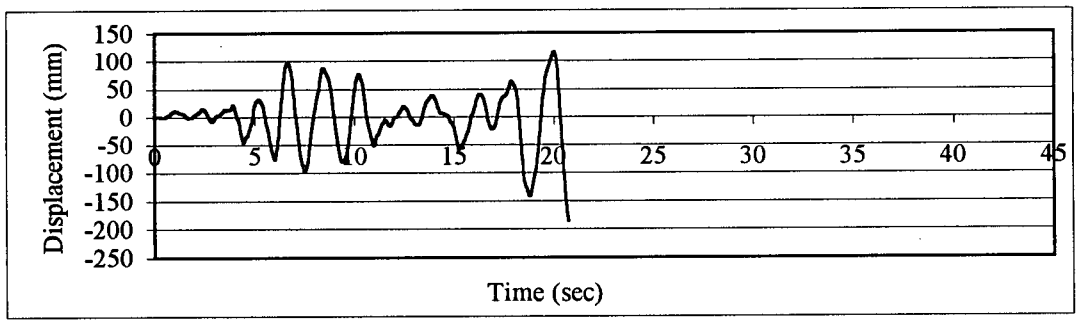

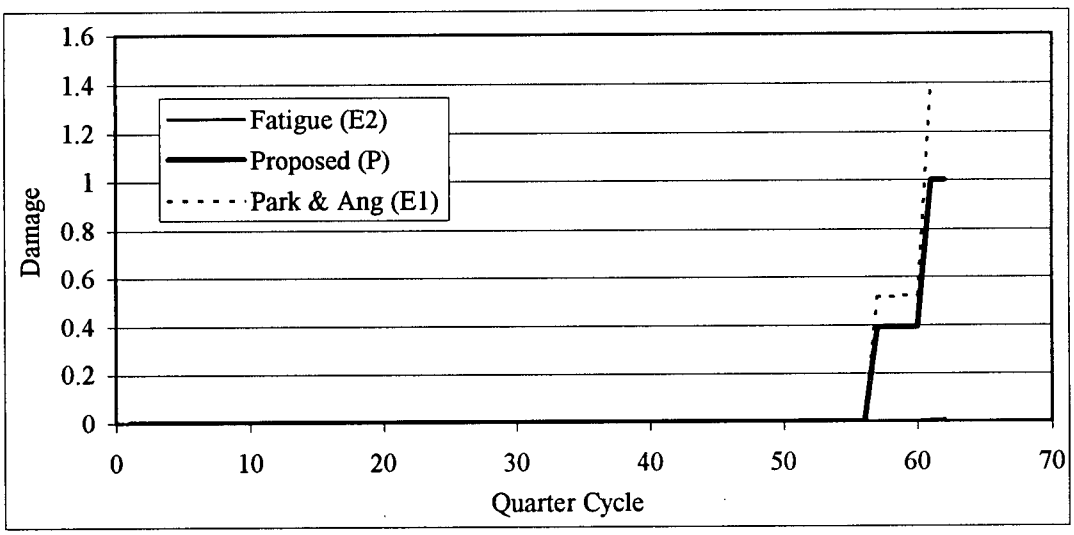

Figure B.6: Clydesdale behavior to 1999 Taiwan east-west (pier 3).